

Université de Montréal

**Analyse et modélisation d'étoiles naines blanches de type
DB dans le Sloan Digital Sky Survey et le relevé *Gaia***

par

Cynthia Genest-Beaulieu

Département de Physique
Faculté des arts et des sciences

Thèse présentée à la Faculté des études supérieures et postdoctorales
en vue de l'obtention du grade de
Philosophiæ Doctor (Ph.D.)
en Physique

30 avril 2019

Université de Montréal

Faculté des études supérieures et postdoctorales

Cette thèse intitulée

Analyse et modélisation d'étoiles naines blanches de type DB dans le Sloan Digital Sky Survey et le relevé *Gaia*

présentée par

Cynthia Genest-Beaulieu

a été évaluée par un jury composé des personnes suivantes :

René Doyon

(président-rapporteur)

Pierre Bergeron

(directeur de recherche)

Gilles Fontaine

(membre du jury)

Pierre Chayer

(examinateur externe)

René Doyon

(représentant du doyen de la FESP)

Thèse acceptée le :

3 juillet 2019

Sommaire

L'étude des naines blanches repose principalement sur la détermination de leurs paramètres atmosphériques et physiques, tels que la température effective, la gravité de surface, la composition chimique de l'atmosphère, la masse, l'âge et la luminosité. Grâce aux grands relevés, le Sloan Digital Sky Survey (SDSS) et *Gaia* en particulier, qui ont rendu accessibles des données photométriques, spectroscopiques ainsi que la parallaxe trigonométrique pour des milliers de naines blanches, il est maintenant possible de déterminer ces quantités pour un très grand nombre de naines blanches. Une analyse comparative des paramètres atmosphériques des naines blanches DA et DB dans le SDSS et *Gaia* est présentée dans cette thèse. Cette analyse permet d'identifier certaines lacunes au niveau des modèles d'atmosphère, notamment les profils d'élargissement Stark dans les modèles d'atmosphère riches en hydrogène ainsi que les profils d'élargissement van der Waals dans ceux riches en hélium qui ne semblent pas tout à fait satisfaisants. Cette analyse permet aussi de révéler la présence de plusieurs systèmes binaires non-résolus de types DA+DA, DA+DC, DA+DB ainsi que DB+DB.

Comme les techniques photométrique et spectroscopique ne permettent pas de déterminer tous les paramètres directement, il faut faire appel à la relation masse-rayon pour obtenir les autres quantités d'intérêt. Les parallaxes trigonométriques du relevé *Gaia* permettent de mettre à l'épreuve cette relation et de conclure à sa validité.

Les naines blanches de type DB sont moins bien comprises du fait de leur rareté, donc une attention particulière leur est accordée. L'analyse des distributions de gravité de surface, de masse et d'abondance d'hydrogène révèle la présence de plusieurs objets d'intérêt, tels que des DB massives ou magnétiques. En particulier, la distribution des abondances d'hydrogène montre des naines blanches ayant des quantités bien différentes de cet élément dans leur atmosphère, ce qui suggère qu'elles ont suivi des canaux évolutifs différents.

La fraction de naines blanches de type DB en fonction de la température reste relativement constante entre 40,000 K et 25,000 K, puis augmente graduellement jusqu'à atteindre son maximum à 15,000 K. Cette fluctuation est cohérente avec les deux canaux évolutifs et le scénario de dilution convective, c'est-à-dire que certaines DB ont conservé leur atmosphère riche en hélium durant toute leur évolution tandis que d'autres sont d'anciennes DA qui se sont transformées lorsque la mince couche superficielle d'hydrogène est diluée dans la couche convective d'hélium située en dessous.

L'origine de l'hydrogène atmosphérique est cependant toujours sujette à débat. La plupart des DBA montrent des abondances beaucoup trop élevées pour pouvoir être expliquées par une origine résiduelle. Ces abondances élevées ne cadrent pas non plus dans le scénario de dilution convective, mettant un doute sur l'origine résiduelle. Une solution possible à ce dilemme serait qu'une couche d'hydrogène flotte à la surface de la naine blanche, donnant ainsi l'illusion d'une plus grande abondance. Cette hypothèse est testée à l'aide de nouveaux modèles chimiquement stratifiés.

Mots clés : étoiles : paramètres fondamentaux - naines blanches - techniques photométrique et spectroscopique, étoiles : évolution spectrale

Summary

The study of white dwarf stars relies heavily on the determination of their atmospheric and physical parameters, such as effective temperature, surface gravity, chemical composition, mass, age and luminosity. Thanks to surveys like the Sloan Digital Sky Survey (SDSS) or *Gaia*, photometric and spectroscopic data, as well as trigonometric parallaxes were made publicly available for a large number of white dwarfs, making it possible to determine the parameters listed above for very large samples. A comparative analysis of the atmospheric parameters of type DA and type DB white dwarfs from the SDSS and *Gaia* is presented in this thesis. This analysis reveals that the Stark broadening profiles in pure hydrogen model atmospheres as well as the van der Waals broadening treatment in helium-rich atmospheres need to be revisited. The comparison of photometric and spectroscopic effective temperatures and masses unveils the presence of DA+DA, DA+DC, DA+DB, as well as DB+DB unresolved double degenerate systems.

The photometric and spectroscopic techniques can only determine a few parameters directly. To obtain the other quantities of interest, one must rely on evolutionary models and the mass-radius relation. The exquisite *Gaia* trigonometric parallaxes offer the opportunity to put this relation to the test for a large number of white dwarfs. It is found that the theoretical mass-radius relation is valid.

The DB white dwarfs are less well understood than their hydrogen-rich counterpart since they are rarer. Therefore, a thorough analysis of the DB white dwarf population is presented. The analysis of the surface gravities and mass distribution reveals the presence of several objects of particular interest, massive or magnetic DB stars for example. The hydrogen abundance distribution also reveals that white dwarfs have very different quantities of that element in their atmosphere, in the same temperature range, suggesting that they must have followed different evolutionary channels.

The fraction of DB stars remains somewhat constant between 40,000 K and 25,000 K and steadily increases below this temperature, reaching its peak value around 15,000 K. This is in line with the two evolutionary channels and the convective dilution scenario, where some DA transform into DB stars when the thin hydrogen layer at the surface is mixed in the underlying helium convection zone, while some DB stars retain their helium-rich atmosphere throughout their evolution.

The origin of this photospheric hydrogen, however, is still up for debate. Most DBA white dwarfs have hydrogen abundances way too high to have a residual origin resulting from the convective dilution scenario. One possible solution to this dilemma is that a small residual hydrogen layer still floats on the surface, thus giving the illusion of a higher hydrogen content. This hypothesis is tested with new chemically stratified model atmospheres.

Keywords: stars: fundamental parameters - stars: evolution - techniques: photometric and spectroscopic - white dwarfs

Table des matières

Sommaire	v
Summary	vii
Liste des tableaux	xiii
Table des figures	xv
Liste des sigles et des abréviations	xix
Notation	xxi
Remerciements	xxv
Chapitre 1. Introduction	1
1.1. Les étoiles naines blanches	1
1.2. Types de naines blanches	2
1.2.1. Type DA	3
1.2.2. Type DB	5
1.2.3. Autres types spectraux.....	9
1.3. Évolution spectrale	12
1.3.1. Modèle d'évolution spectrale de Fontaine & Wesemael (1987).....	12
1.3.2. Nouvelles avancées sur la théorie de l'évolution spectrale	14
1.4. Origine de l'hydrogène dans l'atmosphère des DBA.....	16
1.5. Modélisation des atmosphères de naines blanches.....	18
1.5.1. Modèles de DA	18

1.5.2. Modèles de DB/DBA	19
1.6. Obtention des paramètres atmosphériques.....	21
1.6.1. Relation Masse-Rayon	21
1.6.2. Technique photométrique	23
1.6.3. Technique spectroscopique	25
1.6.3.1. Technique spectroscopique pour les DA	25
1.6.3.2. Technique spectroscopique pour les DB	26
1.6.4. Avantages et inconvénients de chaque technique	28
1.7. Relevés SDSS et <i>Gaia</i>	30
1.7.1. <i>Sloan Digital Sky Survey</i>	30
1.7.2. Le relevé <i>Gaia</i>	31
1.8. Objectifs et structure de la thèse	32
1.9. Déclaration de l'étudiante	33

**Chapitre 2. A Comprehensive Spectroscopic and Photometric Analysis of
DA and DB White Dwarfs from SDSS and *Gaia*.....** 35

2.1. Abstract	36
2.2. Introduction	36
2.3. Sample	38
2.4. Theoretical Framework.....	39
2.4.1. DA Model Atmospheres.....	40
2.4.2. DB/DBA Model Atmospheres.....	41
2.5. Photometric Analysis	42
2.5.1. Photometric Technique.....	43
2.5.2. Effect of the Presence of Hydrogen on the Photometric Solutions	46
2.5.3. Photometric Results	49

2.6. Spectroscopic Analysis	51
2.6.1. Spectroscopic Technique	51
2.6.1.1. DA White Dwarfs.....	52
2.6.1.2. DB/DBA White Dwarfs	53
2.6.2. van der Waals Broadening in DB White Dwarfs	55
2.6.3. Spectroscopic Results	58
2.7. Comparison of Photometric and Spectroscopic Atmospheric Parameters	60
2.7.1. Effective Temperatures.....	60
2.7.2. Stellar Masses	65
2.8. The Mass-Radius Relation for White Dwarfs	73
2.9. Conclusion	78
Chapitre 3. A Photometric and Spectroscopic Investigation of the DB White Dwarf Population in the SDSS and <i>Gaia</i>	81
3.1. Abstract	82
3.2. Introduction	82
3.3. DB White Dwarf Sample.....	86
3.3.1. Spectroscopic Sample	86
3.3.2. Photometric and Astrometric Sample	86
3.4. Theoretical Framework.....	88
3.5. Error Estimation.....	90
3.5.1. Photometric Errors	90
3.5.2. Spectroscopic Errors	93
3.6. Atmospheric and Physical Parameters of DB White Dwarfs	95
3.6.1. Surface Gravity Distributions	95
3.6.2. Mass Distributions	101

3.6.3.	Hydrogen Abundance Distribution	108
3.6.4.	Comparison with Koester & Kepler (2015)	109
3.6.5.	Accuracy and Precision of the Fitting Techniques	112
3.7.	Objects of Particular Astrophysical Interest	113
3.7.1.	Double Degenerate Candidates	113
3.7.2.	DBA White Dwarfs with Large Hydrogen Abundances	117
3.7.3.	DBZ White Dwarfs	119
3.7.4.	Magnetic White Dwarfs	119
3.8.	Spectral Evolution of DB White Dwarfs	122
3.8.1.	Evolution of the DB-to-DA Ratio	123
3.8.2.	Origin of Hydrogen in DBA white dwarfs	127
3.9.	Chemically Stratified Atmospheres	131
3.10.	Discussion	137
Chapitre 4.	Conclusion	141
Bibliographie	147	
Annexe A.	Systèmes binaires de type DA+DB du Chapitre 3	A-i
Annexe B.	Procédure de stratification	B-i
B.1.	Profil d'abondance en équilibre diffusif	B-i
B.2.	Méthode de Newton	B-iii
B.3.	Implémentation du profil d'abondance d'hydrogène dans le code de modèle d'atmosphère	B-iv
Annexe C.	Paramètres atmosphériques et physiques des naines blanches de type DB de l'échantillon du Chapitre 3	C-i

Liste des tableaux

1.1	Limites de détection de H α et H β	28
3.1	List of DA+DB double degenerate candidates.....	115
3.2	List of DB+DB double degenerate candidates.....	117
3.3	Distribution of the different spectral subtypes in the DA and DB samples	124
C.1	Liste des paramètres atmosphériques et physiques.....	C-i

Table des figures

1.1	Spectre d'une naine blanche de type DA	3
1.2	Distribution de masse des DA de Genest-Beaulieu & Bergeron (2014)	5
1.3	Spectres de naines blanches de type DB et DBA	6
1.4	Distribution de masse des DB de Bergeron et al. (2011)	8
1.5	Autres types de naines blanches.....	10
1.6	Zone convective dans l'atmosphère d'une DB.....	14
1.7	Relation masse-rayon théorique	22
1.8	Spectres synthétiques de DA	27
1.9	Spectres synthétiques de DB	29
2.1	Distribution of signal-to-noise ratios	40
2.2	Distribution of parallactic distances	41
2.3	Example of the photometric technique	45
2.4	Magnitude differences between SDSS u , r , i and z and the SDSS g band	46
2.5	Spectroscopic hydrogen abundance of DB white dwarfs.....	47
2.6	Effect of the hydrogen abundance on the photometric solution.....	48
2.7	Photometric and spectroscopic stellar mass of DA white dwarfs	50
2.8	Photometric and spectroscopic stellar mass of DB white dwarfs	51
2.9	Example of the spectroscopic technique for DA white dwarfs	53
2.10	Example of the spectroscopic technique for DB white dwarfs	55
2.11	Spectroscopic mass distribution of DB white dwarfs using different van der Waals broadening theories	57

2.12	Comparison of the atmospheric parameters obtained using different van der Waals theories.....	58
2.13	Differences between spectroscopic and photometric effective temperatures for DA and DB white dwarfs as a function of spectroscopic temperature	61
2.14	Differences between spectroscopic and photometric effective temperatures for DA and DB white dwarfs as a function of parallactic distance	63
2.15	Differences between spectroscopic and photometric effective temperature for DA white dwarfsm using different dereddening procedures.....	64
2.16	Photometric and spectroscopic fits of a double degenerate DA+DC candidate ...	66
2.17	Differences between spectroscopic and photometric masses for DA and DB white dwarfs	67
2.18	Photometric and spectroscopic fits of a DA+DA double degenerate candidate ...	68
2.19	Photometric and spectroscopic fits of a DB+DA double degenerate binary.....	70
2.20	Photometric and spectroscopic fits of a DB+DB double degenerate candidate ...	71
2.21	Photometric and spectroscopic cumulative mass distribution of DA and DB white dwarfs	73
2.22	Comparison between the parallactic distance and the distance inferred from the mass-radius relation	74
2.23	Radius as a function of mass for the DA and DB white dwarfs	76
3.1	Distribution of signal-to-noise ratios of our sample	87
3.2	Distribution of parallactic distances for the photometric sample	89
3.3	Photometric errors.....	91
3.4	Eddington fluxes as a function of wavelenght	92
3.5	Internal spectroscopic errors	94
3.6	External spectroscopic errors.....	96
3.7	$\log g$ distribution, with and without 3D corrections.....	97

3.8	White dwarfs with similar T_{eff} , but different $\log g$	99
3.9	Theoretical 3D corrections for pure helium atmospheres	101
3.10	Photometric and spectroscopic mass distribution as a function of effective temperature	102
3.11	Photometric and spectroscopic cumulative mass distributions	103
3.12	Photometric and spectroscopic fits of massive DB white dwarfs.....	105
3.13	Cumulative mass distributions, with and without 3D corrections.....	107
3.14	Hydrogen abundance as a function of effective temperature.....	109
3.15	Cool DB white dwarfs showing no H α	110
3.16	Comparison with Koester & Kepler (2015)	111
3.17	Photometric and spectroscopic fits SDSS J011356.38+301514.62.....	116
3.18	Location of the unresolved double degenerates in the masse distribution	118
3.19	Photometric and spectroscopic fits of high H abundance DBA white dwarfs	120
3.20	Spectroscopic fits of DBZ white dwarfs.....	121
3.21	Photometric and spectroscopic fits of magnetic DB white dwarfs	122
3.22	Number of DA and DB white dwarfs as a function of T_{eff}	126
3.23	Ratio of DB white dwarfs as a function of T_{eff}	127
3.24	Theoretical hydrogen abundance in the convective dilution scenario	129
3.25	Hydrogen abundance profile in chemically stratified atmospheres	133
3.26	Temperature and pressure structure of stratified model atmospheres.....	134
3.27	Synthetic spectra obtained from chemically stratified atmospheres.....	135
3.28	Observed and synthetic spectra for WD 1822+410	136
A.1	SDSS J0113+3015	A-i
A.2	SDSS J0744+3022	A-ii
A.3	SDSS J0847+4842	A-iii

A.4	SDSS J0910+2105	A-iv
A.5	SDSS J1013+0759	A-v
A.6	SDSS J1036+1938	A-vi
A.7	SDSS J1127+3252	A-vii
A.8	SDSS J1136+3204	A-viii
A.9	SDSS J1406+5627	A-ix
A.10	SDSS J1505+3830	A-x

Liste des sigles et des abréviations

Ca	Calcium
DA	Naine blanche dont le spectre ne montre que des raies d'hydrogène
DB	Naine blanche dont le spectre ne montre que des raies d'hélium neutre
DBA	Naine blanche dont le spectre montre de fortes raies d'hélium ainsi que des raies plus faibles d'hydrogène
DBZ	Naine blanche dont le spectre montre de fortes raies d'hélium ainsi que des raies de métaux
DR x	<i>Data Release x</i>
ETL (LTE)	Équilibre Thermodynamique Local (<i>Local Thermodynamic Equilibrium</i>)
FWHM	<i>Full Width at Half-Maximum</i> ou pleine largeur à mi-hauteur
H	Hydrogène
H α	Raie d'absorption située à 6563 Å correspondant à une transition entre les niveaux 2 et 3 de l'atome d'hydrogène
H β	Raie d'absorption située à 4861 Å correspondant à une transition entre les niveaux 2 et 4 de l'atome d'hydrogène
He	Hélium
He I	Hélium neutre
He II	Hélium ionisé une fois
MLT	<i>Mixing-Length Theory</i> ou théorie de la longueur de mélange
MWDD	<i>Montreal White Dwarf Database</i>

NLTE	<i>Non-Local Thermodynamic Equilibrium</i> ou hors-équilibre thermodynamique local
O	Oxygène
Pan-STARRS	<i>Panoramic Survey Telescope and Rapid Response System</i>
PG	Relevé Palomar-Green
SDSS	<i>Sloan Digital Sky Survey</i>
TLUSTY	Code de modèle d'atmosphère de Hubeny & Lanz (1995)
USNO	<i>United States Naval Observatory</i>
YPC	<i>Yale Parallax Catalog</i>
vdW	van der Waals

Notation

A_x	Extinction interstellaire
Ca/He	Rapport des abondances en nombre de calcium et d'hélium
D	Distance entre la Terre et une étoile
D_{MR}	Distance obtenue à partir de la relation masse-rayon
D_π	Distance parallactique
$E(B - V)$	Excès de couleur
f_ν	Flux monochromatique
f_ν^m	Flux moyen dans la bande-passante de fréquence médiane ν
g	Gravité de surface
H	Hauteur caractéristique de pression
$\text{H}/\text{He}, N(\text{H})/N(\text{He})$	Rapport des abondances en nombre d'hydrogène et d'hélium
H_ν	Flux d'Eddington monochromatique
H_ν^m	Flux d'Eddington moyen dans la bande-passante de fréquence médiane ν
λ	Longueur d'onde
L	Luminosité de l'étoile
L_\odot	Luminosité solaire
M, M_\star	Masse de l'étoile
M_{H}	Masse totale d'hydrogène
M_{He}	Masse totale d'hélium
M_\odot	Masse solaire
m_ν	Magnitude observée dans la bande-passante de fréquence médiane ν

ν	Fréquence
P	Pression
$\pi(R/D)^2$	Angle solide
π	Parallaxe trigonométrique
$q(x) \equiv M_x/M_\star$	Rapport de la masse totale de l'élément x sur la masse de l'étoile
R_\odot	Rayon Solaire
R	Rayon de l'étoile
R_x	Facteur de rougissement dans la bande passante x
$S_m(\nu)$	Fonction de transmission de la bande-passante m
S/N	Rapport signal-sur-bruit
σ	Constante de Stefan-Boltzmann
σ_x	Erreur associée au paramètre x
T	Température
T_{eff}	Température effective
τ_R	Profondeur optique de Rosseland
ω	Largeur du profile de Lorentz
z	Distance entre l'étoile et le plan galactique

À Jocelyn et à ma famille, les étoiles de mon quotidien

Remerciements

J'aimerais tout d'abord remercier mon directeur de recherche, Pierre Bergeron, qui m'a épaulée et guidée durant les cinq années qu'a duré mon doctorat. Durant mon parcours aux études graduées, il a su me transmettre sa passion pour les étoiles naines blanches et leur modélisation et, grâce à ses conseils constructifs, j'ai pu accomplir la présente thèse de doctorat.

J'aimerais aussi remercier ma famille qui m'a soutenue tout au long de mes études, dans les moments joyeux tout comme dans les périodes plus sombres. J'aimerais tout particulièrement remercier mes parents qui m'ont toujours encouragée et poussée à donner le meilleur de moi-même, tant dans mes études que dans tout ce que j'entreprends. Un merci tout spécial à Jocelyn qui pris soin de moi et qui a su m'apaiser lorsque le stress de fin d'études prenait le dessus.

Je me dois aussi de remercier Frédérique et Marie-Lou, avec qui j'ai vécu mes études doctorales. Sans vous, l'étude pour les cours et l'examen général (prédoc) aurait été beaucoup plus ardue et, il va sans dire, beaucoup plus ennuyeuse. Je n'oublierai pas nos cours de yoga (connectons avec l'univers !) et tous ces dîners, parfois en compagnie de Mirjam et Benoit, durant lesquels nous avons parlé de tout et de rien, nous avons ri, nous nous sommes vidé le coeur et pendant lesquels nous nous sommes cassé la tête sur des mots croisés (volcan européen en quatre lettres ?).

Un gros merci à la «*team* naine blanche », passée et présente, avec qui j'ai adoré discuter de science, et parfois de tout et de rien lorsque le coeur le demandait. Un merci particulier à mes collègues actuels : Antoine, Benoit, François, Maude, Simon B. et Simon C. Vous avez été une équipe formidable, où l'entraide règne et avec qui j'ai passé d'inoubliables soirées à jouer à des jeux de société (lire jouer à Avalon) lors des conférences du CRAQ et des European White Dwarfs Workshop. J'aimerais souligner l'aide particulière de Simon B. qui a répondu

à mes questions concernant les métaux et à Antoine pour nos discussions sur l'obscur calcul d'erreur (en particulier pendant les trajets en métro).

Finalement, j'aimerais aussi saluer Gilles Fontaine qui, toujours souriant et prêt à partager sa passion des naines blanches, m'a donné le goût d'entreprendre des études graduées dans le domaine.

Chapitre 1

Introduction

1.1. Les étoiles naines blanches

La dernière phase évolutive des étoiles ayant une masse entre $0.07 M_{\odot}$ et $8.0 M_{\odot}$ est le stade de naine blanche. Ces étoiles représentent environ 97% des astres de notre galaxie. La fin de la phase de la branche asymptotique des géantes est caractérisée par l'expulsion des couches externes de l'étoile, ce qui crée une nébuleuse planétaire. Lorsque la fusion nucléaire cesse complètement au sein de l'objet, l'étoile (le cœur de la nébuleuse planétaire) atteint la phase de naine blanche. Comme il n'y a plus de fusion nucléaire, il n'y a plus de source d'énergie, donc les naines blanches ne font que se refroidir. Les plus jeunes ont une température effective de l'ordre de 150,000 K, alors que les plus vieilles connues ont une température avoisinant les 3000 K. Ce grand intervalle de température occasionne aussi un grand intervalle de luminosité ($L_{\star} = 4\pi\sigma R_{\star}T_{\text{eff}}^4$), soit de $10^3 > L/L_{\odot} > 10^{-4.7}$. En moyenne, ces objets ont un rayon de $0.01 R_{\odot}$, ce qui est comparable à la taille d'une planète¹. Leur petite taille, combinée avec une gravité de surface élevée ($\log g = 8.0$ en moyenne²) en fait des objets compacts.

Le cœur d'une naine blanche est composé de carbone et d'oxygène, qui sont les produits du brûlage nucléaire de l'hydrogène et de l'hélium. La fusion du carbone et de l'oxygène ne s'est jamais amorcée, puisque la masse du progéniteur n'était pas assez élevée pour que la température en son cœur atteigne la valeur nécessaire à ce processus. Reposant sur ce cœur de carbone et d'oxygène se trouve une mince couche d'hélium, elle-même recouverte

1. Le diamètre de la Terre (12 742 km) est environ 109 fois plus petit que celui du Soleil (1 391 016 km).

2. En unité cgs, soit en cm s^{-2} . Par comparaison, la gravité de surface du Soleil est $\log g = 4.4$.

d'une mince couche d'hydrogène. Selon les théories évolutives, la quantité d'hélium maximale pouvant survivre à la phase de nébuleuse planétaire est $M_{\text{He}} \sim 10^{-2} M_\star$ (Fontaine et al., 2001). Pour l'hydrogène, la fraction est encore plus petite, soit $M_{\text{H}} \sim 10^{-4} M_\star$ (Fontaine et al., 2001). Une naine blanche a donc une structure en «pelure d'oignon». Il est important de mentionner que la quasi-totalité de la masse de l'objet est comprise dans le cœur et que l'atmosphère ne représente qu'une très faible fraction de la masse totale ($M \sim 10^{-14} M_{\text{tot}}$ au maximum).

1.2. Types de naines blanches

Les naines blanches ne forment pas un groupe homogène : il en existe plusieurs types. Dans la nomenclature, un objet dégénéré est identifié par la lettre D. Par conséquent, tous les types spectraux de naines blanches commencent par cette lettre, suivie d'une autre définie selon les raies d'absorption visibles dans son spectre. Dû à la gravité élevée, le tri gravitationnel est extrêmement efficace, c'est-à-dire que si des éléments lourds sont accrétiés à la surface, ils sombrent très rapidement vers les couches plus profondes de l'atmosphère, les rendant ainsi indétectables. C'est pourquoi la plupart des spectres de naines blanches ne portent la signature que d'un seul élément. Il se peut cependant que des raies d'absorption de plusieurs éléments différents soient détectés. Dans ce cas, la nomenclature veut que l'élément visible dominant soit identifié le premier, suivi des autres, en ordre décroissant de la force des raies spectrales.

Il est toutefois important de noter que le type spectral est basé *uniquement* sur les raies d'absorption présentes dans le spectre et n'est pas synonyme de composition atmosphérique. Par exemple, une naine blanche froide pourrait avoir une atmosphère riche en hélium, mais un spectre ne montrant que des raies d'hydrogène, la température étant trop faible pour que les raies d' He I soient présentes (voir la figure 23 de Bergeron et al. 1997 et la section 2.2 de Rolland et al. 2018).

La présente étude porte sur les deux types de naine blanche les plus communs, soient les DA et les DB. Cependant, comme les DB sont bien moins comprises que les DA, elles font l'objet d'une étude plus approfondie.

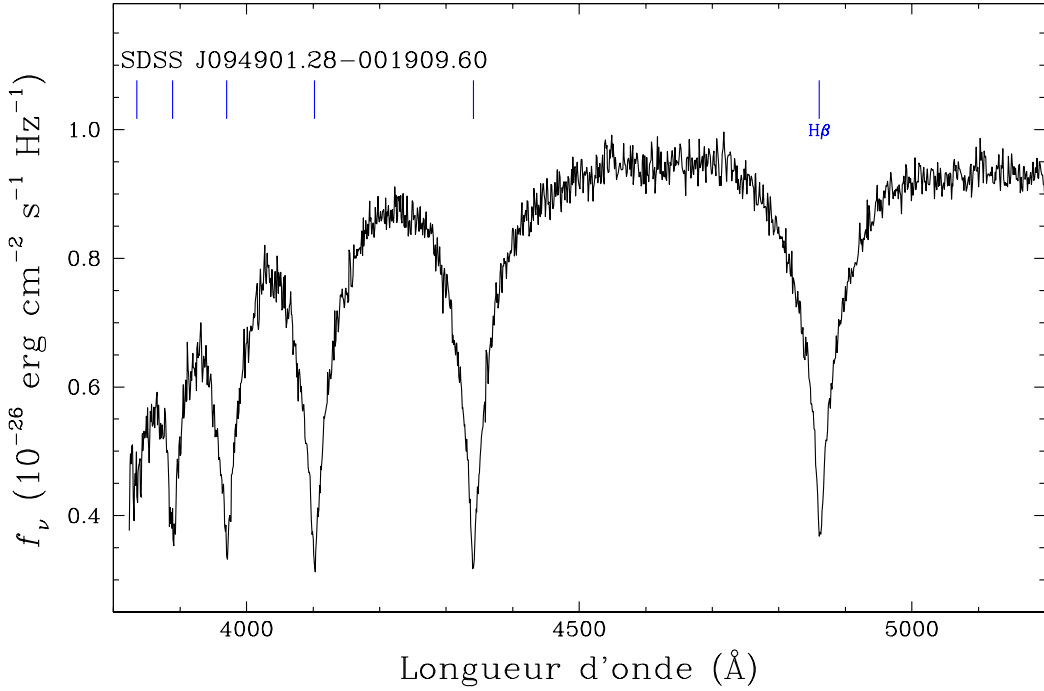


FIGURE 1.1. Exemple de spectre observé de naine blanche de type DA (SDSS J094901.28-001909.60). Le spectre est caractérisé par la présence de raies d'hydrogène, dont l'emplacement est marqué par les traits bleus. $H\beta$ est aussi identifiée.

1.2.1. Type DA

Le type de naine blanche le plus commun, et le mieux compris, est le type DA. Ces objets représentent environ 80% des naines blanches connues et leur spectre ne montre que des raies d'hydrogène. Un exemple typique de spectre de DA est présenté à la figure 1.1.

Les DA couvrent un très grand intervalle de température. L'une des DA les plus chaudes connues est PG 0948+534, qui a une température effective de 110,000 K (Preval & Barstow, 2017). À l'autre extrême, les DA les plus froides connues ont une température d'environ 5000 K, puisqu'en deçà de cette température, les raies de Balmer disparaissent (Wesemael et al., 1993).

Il existe une région en température dans laquelle on retrouve des DA pulsantes, appelées les ZZ Ceti ou DAV. Cette région, la bande d'instabilité, se situe entre $T_{\text{eff}} = 12,460$ K et $T_{\text{eff}} = 11,160$ K (modèles avec $ML2/\alpha=0.6$, Bergeron et al. 1995b). Les limites exactes de cette bande d'instabilité dépendent fortement de la physique implémentée dans les modèles,

plus particulièrement de l'efficacité convective utilisée. On connaît environ 200 objets de ce type (Van Grootel et al., 2017).

Un problème bien connu survient lors de l'analyse des DA froides : le *high-log g problem*, ou le problème des gravités de surface élevées. Lorsqu'on tente de déterminer la gravité de surface de DA ayant une température effective plus faible que 13,000 K à l'aide de données spectroscopiques, les valeurs obtenues sont systématiquement plus élevées que la valeur moyenne déterminée pour les objets plus chauds ($\langle \log g \rangle \sim 8.0$). Plusieurs théories ont été avancées pour tenter de résoudre ce problème. La plus populaire invoquait la présence d'une quantité indétectable d'hélium dans l'atmosphère de ces DA froides, résultat de la convection ($T_{\text{eff}} < 15,000$ K, Koester 1976; Vauclair & Reisse 1977; Dantona & Mazzitelli 1979; Bergeron et al. 1991). Il s'est cependant avéré que la cause de ce problème est l'utilisation de modèles d'atmosphère dits 1D, qui emploient la théorie de la longueur de mélange pour traiter la convection (voir la section 1.5.1). Tremblay et al. (2013a) ont donc calculé des modèles 3D, qui traitent la convection selon l'hydrodynamique radiative et qui tiennent aussi compte du dépassement convectif (*convective overshoot* en anglais) et d'effets hors équilibre hydrostatique. L'utilisation de ces nouveaux modèles, ou l'application des corrections 1D → 3D appropriées, permettent de corriger le problème des gravités de surface élevées. La figure 1.2 montre bien l'effet des corrections 3D sur la distribution de masse des DA. À gauche, les corrections pour les effets 3D n'ont pas été appliquées. On peut voir que la distribution de masse des objets froids ($T_{\text{eff}} < 13,000$ K, histogramme hachuré rouge) tend vers des masses plus élevées que celle des objets plus chauds ($T_{\text{eff}} > 13,000$ K, histogramme hachuré bleu). Lorsque les corrections 3D sont appliquées (panneau de droite), les distributions de masse pour les objets chauds et froids sont en bien meilleur accord.

La distribution de masse corrigée est centrée sur la valeur moyenne $\langle M \rangle = 0.609 M_{\odot}$ (Genest-Beaulieu & Bergeron, 2014), valeur corroborée par plusieurs études, dont Liebert et al. (2005) et Tremblay et al. (2011a). Une particularité de cette distribution est la présence de DA très massives ($M \gtrsim 0.8 M_{\odot}$). On explique souvent la présence de ces naines blanches comme le résultat de la fusion d'étoiles (Iben, 1990; Kilic et al., 2018) ou encore comme une conséquence évolutive, telle que décrit par la relation entre la masse du progéniteur et la masse de la naine blanche (*initial-final mass relation*, El-Badry et al. 2018). À l'autre extrême, on compte aussi un certain nombre de DA de très faibles masses ($M \lesssim 0.5 M_{\odot}$). Le

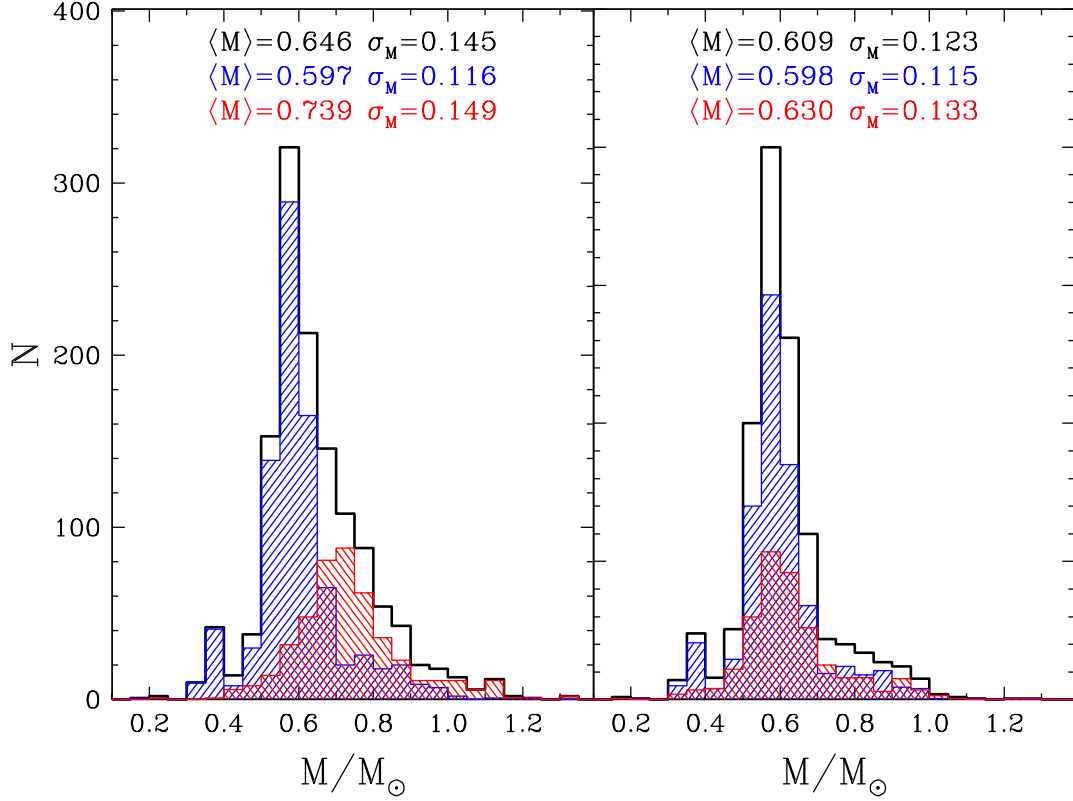


FIGURE 1.2. Figure 17 de Genest-Beaulieu & Bergeron (2014) montrant la distribution de masse de leur échantillon de DA du SDSS sans (gauche) et avec (droite) les corrections 3D de Tremblay et al. (2013a). Les histogrammes noirs représentent l'échantillon complet, tandis que les histogrammes bleus (rouge) montre le sous-échantillon avec $T_{\text{eff}} > 13,000$ K ($T_{\text{eff}} < 13,000$ K). Les masses moyennes ainsi que les écarts-types sont aussi indiqués avec les couleurs correspondantes.

mécanisme souvent évoqué pour expliquer la présence de ces objets est l'évolution dans un système binaire à enveloppe commune (*common envelope evolution* en anglais), puisque la galaxie est trop jeune pour avoir produit des naines blanches avec $M \lesssim 0.5 M_{\odot}$.

1.2.2. Type DB

Les naines blanches de type DB sont beaucoup plus rares que les DA. Elles ne représentent qu'environ 20% de la population de naines blanches (Beauchamp et al., 1996) et sont moins bien comprises que leur homologues riches en hydrogène.

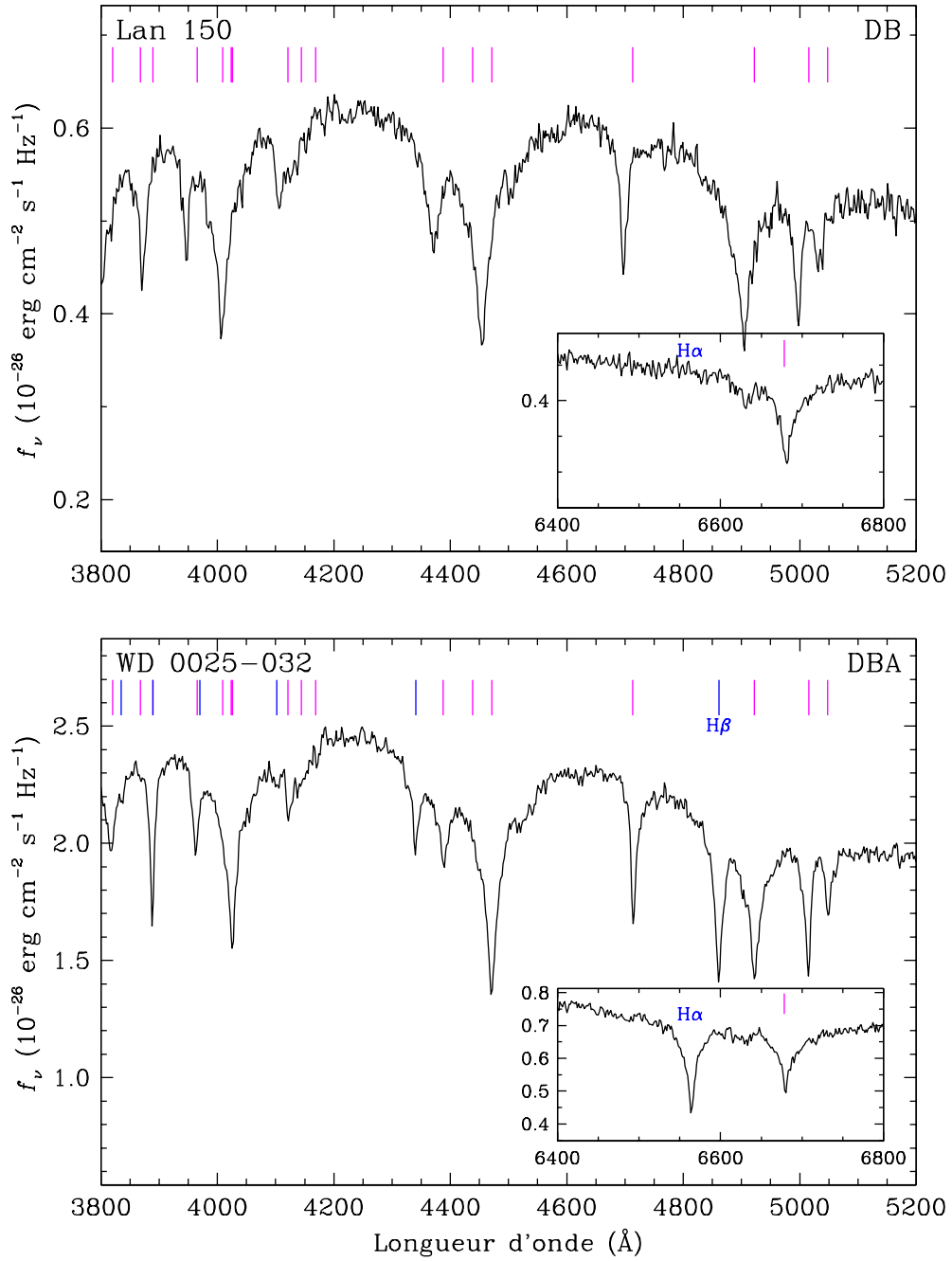


FIGURE 1.3. Exemples de spectre de naine blanche de type DB (Lan 150, panneau du haut) et DBA (WD 0025–032, panneau du bas) (Bergeron et al., 2011). Leur spectre est caractérisé par la présence de raies d'hélium neutre, identifiées par les traits magenta, et, dans le cas de la DBA, de raies d'hydrogène, identifiées par les traits bleus. Les raies H α et H β sont aussi identifiées.

Le spectre d'une naine blanche de type DB est caractérisé par la présence de raies d'hélium neutre seulement, comme on peut le voir à la figure 1.3 (panneau du haut). S'il y a aussi présence de raies de l'He II, la naine blanche est alors classifiée DO. La transition entre ces deux types se produit aux alentours de $T_{\text{eff}} = 40,000$ K. Comme les raies d'hélium neutre disparaissent sous $T_{\text{eff}} \sim 10,000$ K, on ne retrouve des DB que dans l'intervalle $40,000\text{K} > T_{\text{eff}} > 10,000$ K.

Il se peut que le spectre de ces objets montre, en plus des raies d'hélium, de faibles raies d'hydrogène, comme il est montré à la figure 1.3 (panneau du bas). Dans ce cas, on dit que la naine blanche est de type DBA³. Ce phénomène n'est pas rare ; Koester & Kepler (2015) et Rolland et al. (2018) obtiennent que la fraction de DBA dans leur échantillon de DB est de 75% et 63%, respectivement. Évidemment, cette fraction dépend fortement des limites de détection de l'hydrogène (du rapport signal-sur-bruit des spectres observés de la région H α , voir la section 1.6.3.2). Typiquement, l'abondance d'hydrogène dans ces atmosphères est de l'ordre de H/He $\sim 10^{-6} - 10^{-3}$ (Bergeron et al., 2011; Rolland et al., 2018). Bergeron et al. (2011) notent que les DBA apparaissent en grand nombre à des températures plus basses que 20,000 K. Au-delà de cette température, elles se font plutôt rares et presque toutes les naines blanches à atmosphère riche en hélium sont de type DB. Dans leur échantillon, seuls trois objets sont classés DBA au-delà de 20,000 K et ceux-ci ne montrent qu'une très faible quantité d'hydrogène ($M_{\text{H}} \sim 10^{-16} M_{\odot}$).

On a longtemps pensé qu'il existait une région en température, soit entre 45,000 K et 30,000 K, où on ne retrouvait aucune DB (DO). Cet intervalle de température est maintenant connu sous le nom de brèche des DB (ou *DB gap* en anglais). Les relevés à grandes échelles, en particulier le Sloan Digital Sky Survey (SDSS, voir la section 1.7.1), ont cependant permis de confirmer la présence de DB (DO) ayant des températures effectives entre 45,000 K et 30,000 K (Eisenstein et al., 2006a), quoique beaucoup moins que ce qui est attendu. Eisenstein et al. (2006a) ont déterminé que le rapport du nombre de DB sur le nombre de DA était 2.5 fois plus faible à 30,000 K qu'à 20,000 K, suggérant que la brèche des DB était plutôt une déficience de DB.

Une autre région d'intérêt en température est la région où l'on retrouve les DB variables, aussi appelées V777 Her ou DBV. Elles se trouvent entre $\sim 22,000$ K et 30,000 K, si l'on

3. Lorsqu'on discute de naines blanches de type DB, cela inclut généralement les objets de type DBA.

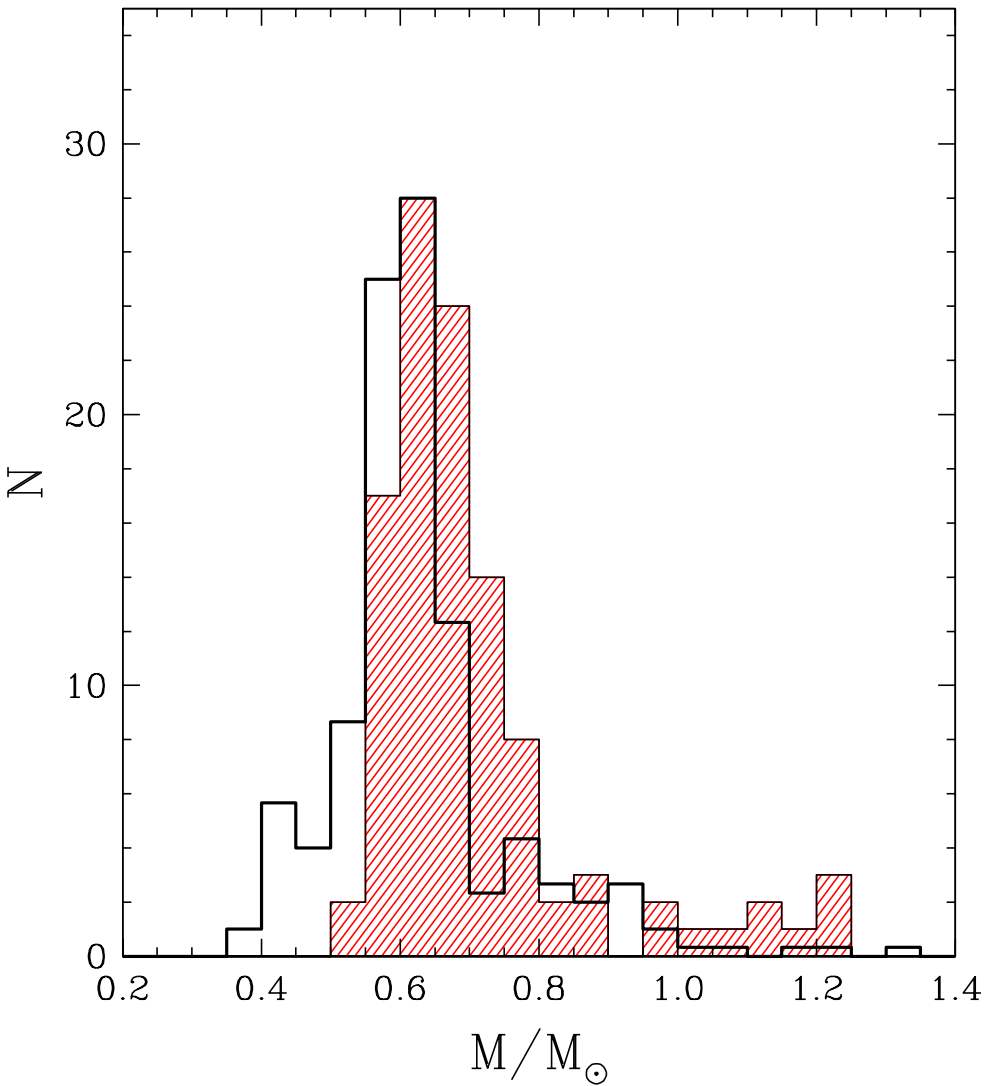


FIGURE 1.4. Figure 23 de Bergeron et al. (2011) comparant la distribution de masse des DB et DBA de leur échantillon (histogramme hachuré rouge) à celle des DA de Liebert et al. (2005) (histrogramme noir). La distribution de masse pour les DA a été normalisée afin que le maximum corresponde à celui de la distribution des DB.

suppose une efficacité convective $ML2/\alpha = 1.25$ et $\log g = 8.0$ (Van Grootel et al., 2017). Tout comme pour les DA, les limites exactes de la bande d’instabilité dépendent fortement de l’efficacité convective utilisée dans les modèles. Ces DB pulsantes sont bien moins nombreuses que les ZZ Ceti : on connaît environ 20 V777 Her contre ~ 200 DAV (Van Grootel et al., 2017).

La figure 23 de Bergeron et al. (2011), reproduite ici à la figure 1.4, compare les distributions de masse des DA et des DB. Il est à noter que certaines DB très massives (et froides) ont été exclues de cette figure, puisque les raies spectrales étaient trop faibles pour que les valeurs de $\log g$ soient fiables (voir les sections 2.6.1.2 et 3.6.1). Bergeron et al. (2011) notent que, bien que les sommets des deux distributions concordent, la distribution de DB tend vers des masses plus élevées ($\langle M_{\text{DB}} \rangle = \langle M_{\text{DA}} \rangle + \sim 0.03 M_{\odot}$). Les auteurs trouvent aussi que certaines DB de leur échantillon sont très massives, jusqu'à $M \sim 0.9 M_{\odot}$. Beuchamp et al. (1996), Koester & Kepler (2015) et Rolland et al. (2018) obtiennent aussi des distributions de masses similaires. Ces naines blanches massives se retrouvent toutes dans l'intervalle $18,000 \text{ K} > T_{\text{eff}} > 13,000 \text{ K}$. L'hypothèse ayant été avancée pour expliquer ces masses élevées est que le traitement de l'élargissement des raies par les particules neutres, plus particulièrement l'élargissement van der Waals, n'est pas tout à fait au point (voir la section 1.5.2). Ce type d'élargissement devient important pour $T_{\text{eff}} < 16,000 \text{ K}$, alors qu'au-delà de cette température, c'est l'élargissement Stark qui domine. Bergeron et al. (2011) notent cependant que certaines DB dans ce même intervalle de température ont des masses normales, soit autour de $M = 0.6 M_{\odot}$, ce qui pourrait signifier que ces valeurs élevées sont peut-être réelles.

Le problème des masses élevées mentionné ci-dessus rend la détermination de la masse moyenne des DB ardue. On retrouve dans la littérature plusieurs valeurs différentes de $\langle M_{\text{DB}} \rangle$: $0.596 M_{\odot}$ (Voss et al. 2007, basée sur les données SPY), $0.671 M_{\odot}$ (Bergeron et al., 2011) ou encore $0.706 M_{\odot}$ (Koester & Kepler 2015, basée sur les données du SDSS). Il est toutefois difficile de comparer ces valeurs, puisqu'elles ont été obtenues à l'aide de modèles et de techniques différentes.

La figure 1.4 montre aussi une absence marquée de DB de faible masse ($M < 0.5 M_{\odot}$). Ceci semble suggérer que le mécanisme produisant des DA peu massives, l'évolution dans un système binaire à enveloppe commune, ne forme pas de DB.

1.2.3. Autres types spectraux

Tel que mentionné à la section précédente, si le spectre d'une naine blanche montre des raies de He II ou une combinaison de raies de He I et He II, elle sera classifiée DO. Un

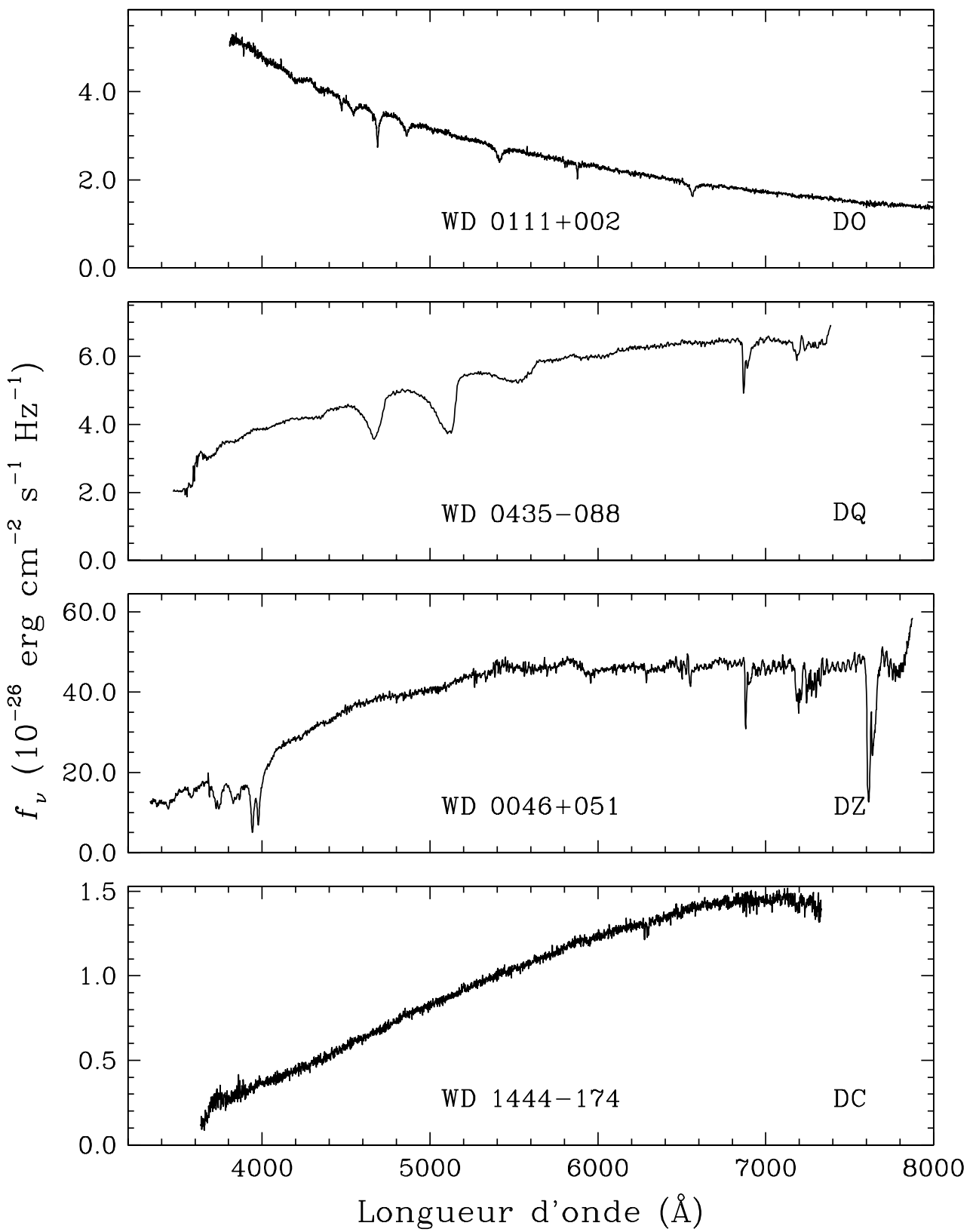


FIGURE 1.5. Exemples de spectres observés de DO (WD 0111+002, SDSS), DQ (WD 0435–088, Giannicchele et al. 2012), DZ (WD 0046+051, Limoges et al. 2015) et DC (WD 1444–174, Giannicchele et al. 2012), de haut en bas.

exemple de spectre de ce type d'objet est montré à la figure 1.5. On retrouve ces objets dans l'intervalle $120,000 \text{ K} < T_{\text{eff}} < 40,000 \text{ K}$.

Certaines naines blanches montrent des raies de carbone, et parfois de faibles raies d'hélium : ce sont les DQ. Un exemple de spectre de DQ est présenté à la figure 1.5. Ces objets ont des températures $T_{\text{eff}} \lesssim 16,000 \text{ K}$. La présence de carbone dans l'atmosphère est expliquée par le dragage convectif. Le dragage convectif se produit lorsque le bas de la cellule convective de l'hélium plonge assez profondément pour atteindre la zone de transition entre l'hélium et le carbone qui est formée à la fin de la phase où l'hélium est brûlé. Le carbone est alors entraîné vers la surface grâce à la convection (Pelletier et al., 1986). Dans le cas des DQ les plus chaudes, le carbone atmosphérique pourrait aussi être expliqué par la présence d'un vent stellaire résiduel, qui viendrait contrer le tri gravitationnel, permettant ainsi au carbone de flotter à la surface (Fontaine & Brassard, 2005).

Il ne faut pas confondre ces étoiles avec les DQ chaudes (*hot DQ* en anglais), qui ont des atmosphères riches en carbone et non en hélium (Dufour et al., 2007). Bergeron et al. (2011) mentionnent que ces étoiles, comme elles apparaissent autour de 24,000 K, devraient avoir des atmosphères complètement dépourvues d'hydrogène, donc doivent nécessairement avoir des étoiles de type DB comme progéniteurs. D'autres études suggèrent aussi qu'elles seraient le résultat de la fusion de deux naines blanches (Dunlap & Clemens, 2015).

Il est aussi possible de détecter la présence de métaux⁴ (autre que le carbone) dans le spectre de certaines naines blanches. Cette catégorie d'objets constitue les DZ. Un exemple de spectre de DZ est montré à la figure 1.5. Ces objets font leur apparition autour de $T_{\text{eff}} \sim 10,000 \text{ K}$, là où l'hélium devient spectroscopiquement invisible. Ces métaux proviendraient du disque de débris d'un ancien système planétaire ayant une composition similaire à celle du système solaire (Zuckerman et al., 2007; Dufour et al., 2012; Gänsicke et al., 2012). Il y aurait alors accrétion de ce matériel sur la naine blanche, polluant ainsi son atmosphère. L'accrétion doit se faire de manière continue, sans quoi le tri gravitationnel ferait disparaître ces métaux trop rapidement pour qu'ils puissent être observés.

Finalement, le spectre de certaines naines blanches ne montre aucune raie d'absorption, du fait de leur trop basse température effective : c'est la classe des DC. Comme ces objets

4. Dans le domaine de l'astrophysique, les deux éléments les plus communs sont l'hydrogène et l'hélium. Par simplicité, le terme métaux est utilisé pour désigner tout autre élément du tableau périodique.

ne montrent aucune raie spectrale, il est impossible de déterminer leur composition atmosphérique à partir de leur spectre. Un exemple de spectre de DC est présenté à la figure 1.5. Ces objets ont une température maximale d'environ 10,000 K.

1.3. Évolution spectrale

Comme les réactions nucléaires au cœur d'une naine blanche sont éteintes, on pourrait croire que si elle commence sa vie en montrant un certain type spectral, elle conservera ce même type pour le reste de son évolution. Il semble toutefois que la situation soit plus complexe, car, comme il a été mentionné à la section 1.2.2, la proportion de DB (DO) n'est pas constante en fonction de la température, donc de l'âge.

Pour tenter d'expliquer ce fait, un modèle a été proposé par Fontaine & Wesemael (1987) (voir aussi Liebert et al. 1987). Bien que les nouvelles avancées dans la recherche des naines blanches aient contredit certains points de ce modèle, il constitue néanmoins la base de la théorie de l'évolution spectrale.

1.3.1. Modèle d'évolution spectrale de Fontaine & Wesemael (1987)

Dans ce scénario, on suppose que toutes les naines blanches, ou du moins une grande majorité, ont le même progéniteur : les étoiles de type PG1159. Ces étoiles sont les objets de transition entre la phase post-AGB (la phase suivant la branche asymptotique des géantes) et la phase de naine blanche. Ceci est supporté par le fait que la région du diagramme Hertzsprung-Russell où on retrouve les PG1159 et celle où se trouvent les DO se superposent en partie (Hügelmeyer et al., 2005). Le spectre de ces objets est dominé par des raies d'hélium ionisé, de carbone ionisé (C IV) ainsi que d'oxygène ionisé et est dépourvu de raies d'absorption d'hydrogène (Hügelmeyer et al., 2005). Les PG1159 ont des gravités de surface entre $\log g = 5.5$ et $\log g = 8.0$ et des températures effectives élevées, dans l'intervalle 200,000 K $> T_{\text{eff}} >$ 65,000 K (Hügelmeyer et al., 2005).

Avec le temps, ces étoiles se refroidissent et le tri gravitationnel fait sombrer le carbone et l'oxygène atmosphériques vers les couches plus profondes, ce qui la convertit en naine blanche de type DO à $T_{\text{eff}} \sim 120,000$ K, lorsque la fusion nucléaire cesse. Avec le temps, la naine blanche se refroidit et le tri gravitationnel continue de séparer les éléments, ce qui fait remonter l'hydrogène à la surface. Après un certain temps, la couche d'hydrogène ainsi créée

est assez épaisse pour que le spectre ne montre que des raies d'hydrogène et la naine blanche apparaît alors comme une DA. Ceci permettait d'expliquer le fait qu'à l'époque, aucune naine blanche de type DA plus chaude que $T_{\text{eff}} \sim 80,000$ K n'était connue. L'hydrogène continue ensuite de diffuser vers la surface pour qu'à $T_{\text{eff}} = 45,000$ K, soit à la limite chaude de la brèche qu'on croyait totalement dépourvue de DB, toutes les DO se soient transformées en DA.

La présence de DO jusqu'à une température de 45,000 K ainsi que l'absence de DA à $T_{\text{eff}} > 80,000$ K permet d'estimer la quantité d'hydrogène contenue dans l'enveloppe des naines blanches. L'enveloppe d'une DO à $\approx 80,000$ K doit avoir au maximum $\sim 6 \times 10^{-18} M_{\odot}$ d'hydrogène, sans quoi les raies d'hydrogène sont trop fortes et la naine blanche est alors classifiée DOA (MacDonald & Vennes, 1991). D'un autre côté, la quantité minimale nécessaire pour qu'une naine blanche ait un spectre ne montrant pas de raie d'hélium à 45,000 K est $M_{\text{H}} = 5 \times 10^{-16} M_{\odot}$ (MacDonald & Vennes, 1991). Après sa transformation en DA, la naine blanche se refroidit de $T_{\text{eff}} \sim 45,000$ K à $T_{\text{eff}} \sim 30,000$ K en conservant son type spectral.

Pour les naines blanches de type DB (DO), l'atmosphère devient convective à $T_{\text{eff}} \sim 60,000$ K, mais ce n'est qu'à 30,000 K que cette zone de convection devient importante, comme le montre la figure 1.6. La zone convective d'hélium devient alors assez grande pour atteindre la couche superficielle d'hydrogène qui s'est formée grâce au tri gravitationnel et la dilution convective⁵ a lieu : le spectre montre maintenant des raies d'hélium neutre, ce qui explique la réapparition des DB autour de $T_{\text{eff}} \sim 30,000$ K. La température exacte à laquelle la dilution convective se produit dépend de l'épaisseur de la couche d'hydrogène (MacDonald & Vennes, 1991; Rolland et al., 2018). Il est à noter que si la fraction de masse d'hydrogène dans l'atmosphère est supérieure à $\sim 10^{-14}$, la dilution convective ne se produira pas et la naine blanche restera de type DA (Rolland et al., 2018).

Vers 10,000 K, le nombre de naines blanches à atmosphère d'hélium augmente de nouveau. À cette température, à la fois la couche superficielle d'hydrogène et l'enveloppe d'hélium située en dessous sont convectives. Le bas de la zone convective d'hydrogène devient de plus en plus profond lorsque la naine blanche se refroidit et, ultimement, entre en contact avec

5. Il y a dilution convective lorsque la zone *convective* d'hélium atteint la couche *radiative* d'hydrogène, ce qui a pour effet de diluer l'hydrogène dans l'enveloppe d'hélium.

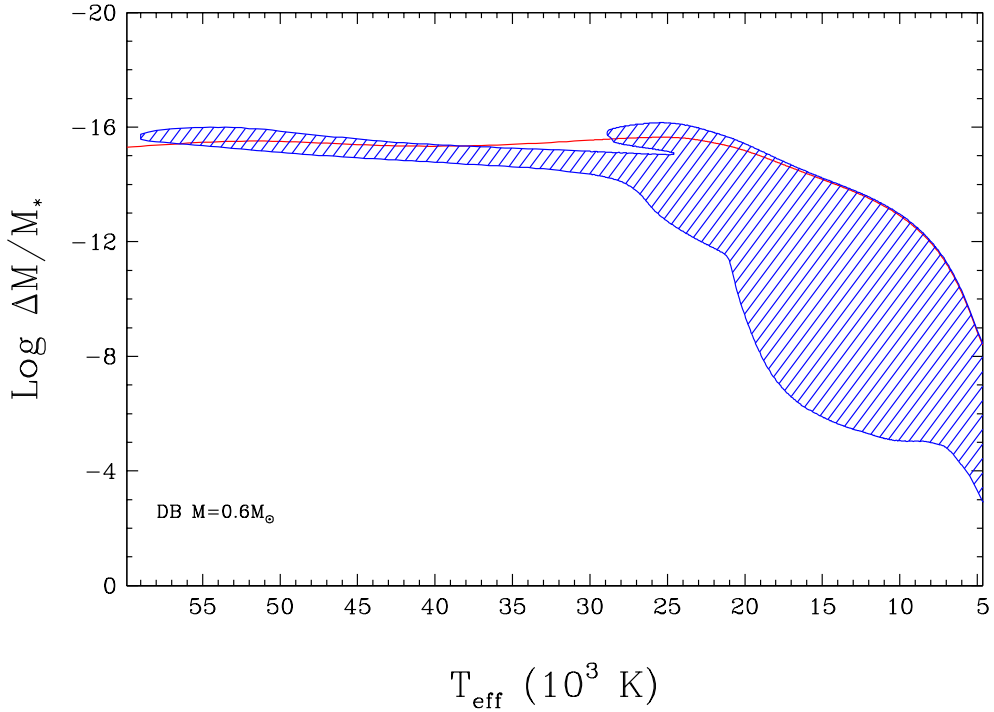


FIGURE 1.6. Emplacement de la zone convective (région hachurée) dans l'enveloppe pure en hélium d'une naine blanche de $0.6 M_{\odot}$, en fonction de la température effective et de la profondeur (exprimée en fraction de masse), selon les calculs de Rolland et al. (2018). Le calcul a été effectué à l'aide de la version $ML2/\alpha = 0.6$ de la théorie de la longueur de mélange et la courbe rouge représente la photosphère ($\tau_R \sim 1$).

la zone convective de l'hélium, augmentant ainsi la quantité d'hélium atmosphérique. Selon Rolland et al. (2018), le mélange convectif⁶ a lieu entre $\sim 12,000$ K et ~ 7000 K pour des valeurs de M_H entre $10^{-13} M_{\odot}$ et $10^{-8} M_{\odot}$. La température exacte à laquelle ce phénomène se produit dépend de M_H : plus il y a d'hydrogène, plus la température à laquelle le mélange convectif a lieu est basse.

1.3.2. Nouvelles avancées sur la théorie de l'évolution spectrale

Le modèle d'évolution spectrale décrit à la section 1.3.1 permettait de bien expliquer les rapports N_{DB}/N_{DA} observés à l'époque, mais il échoue à expliquer certaines découvertes faites depuis.

6. Il y a mélange convectif lorsque la zone *convective* d'hélium atteint la couche *convective* d'hydrogène, ce qui force le mélange de l'hydrogène et de l'hélium.

Par exemple, ce scénario n'explique pas la présence de naines blanches de type DB dans la brèche (Eisenstein et al., 2006a), car on suppose que toutes les naines blanches se sont converties en DA à $T_{\text{eff}} = 45,000$ K. Il a donc été proposé par Bergeron et al. (2011) qu'il n'existerait non pas un, mais deux canaux évolutifs pour les naines blanches. Le premier est celui décrit par Fontaine & Wesemael (1987) et le second se produit lorsqu'il n'y a tout simplement pas assez d'hydrogène dans l'enveloppe pour que la naine blanche effectue la conversion DO→DA. La présence de ce deuxième canal évolutif se base sur le fait que la plupart des DB de leur échantillon ayant $T_{\text{eff}} > 20,000$ K ne montrent pas, ou très peu, d'hydrogène. Eisenstein et al. (2006a) mentionnent qu'environ 10% des DA doivent subir une transformation entre 30,000 K et 20,000 K pour expliquer le rapport $N_{\text{DB}}/N_{\text{DA}}$ observé.

Bergeron et al. (2011) ont déterminé que pour qu'une naine blanche apparaisse DB à cette température, la quantité d'hydrogène dans son atmosphère ne devait pas excéder $M_{\text{H}} = 10^{-17} M_{\odot}$. Ils mentionnent aussi que les 3 DBA de leur échantillon ayant des températures plus élevées que 20,000 K avaient $M_{\text{H}} \sim 10^{-16} M_{\odot}$. Dans un cas comme dans l'autre, M_{H} est trop faible pour que la naine blanche ait eu une atmosphère riche en hydrogène au cours de son évolution.

Bergeron et al. (2011) (voir aussi Rolland et al. 2018) font mention de la possibilité d'un troisième canal évolutif produisant des DB ayant très peu d'hydrogène impliquant les DQ chaudes (voir la section 1.2.3). Comme ce type d'objet n'existe pas sous $T_{\text{eff}} \sim 18,000$ K (Dufour et al., 2008; Bergeron et al., 2011), elles se transformeraient en DB à cette température. Le mécanisme convertissant les DQ chaudes en DB est toutefois inconnu et, comme on ne connaît que très peu de ce type de naine blanche, ce canal évolutif serait numériquement peu important.

La dilution convective invoquée dans le modèle d'évolution spectrale pose aussi certains problèmes. À partir de leurs modèles, Rolland et al. (2018) ont déterminé la température effective à laquelle la dilution convective avait lieu en fonction de la quantité d'hydrogène présente dans l'atmosphère, ainsi que l'abondance résultante. Par exemple, pour $M_{\text{H}} = 10^{-15} M_{\odot}$, il y aurait dilution complète à 31,500 K, pour une efficacité convective $\text{ML2}/\alpha = 2.0$. L'abondance d'hydrogène serait alors $\log \text{H/He} = -0.3$, ce qui est beaucoup plus élevé que les limites observées pour les DB, qui se situent autour de $\text{H/He} \sim 10^{-4} - 10^{-5}$ (Bergeron et al., 2011). Ceci suggère encore une fois que ces naines blanches doivent avoir maintenu

leur atmosphère d'hélium durant leur évolution, ce qui est cohérent avec la découverte de DB chaudes ($45,000 \text{ K} > T_{\text{eff}} > 30,000 \text{ K}$) par Eisenstein et al. (2006a).

1.4. Origine de l'hydrogène dans l'atmosphère des DBA

Tel que mentionné à la section 1.2.2, entre 63% et 75% (Koester & Kepler, 2015; Rolland et al., 2018) des naines blanches de type DB contiennent une certaine quantité d'hydrogène dans leur atmosphère. L'origine de cet hydrogène atmosphérique n'est toutefois pas claire.

On pourrait penser que l'hydrogène dans l'atmosphère des DBA est d'origine résiduelle. Dans le scénario d'évolution spectrale décrit à la section 1.3, on suppose que lorsqu'il y a dilution convective de la couche superficielle d'hydrogène, la dilution est *complète*, c'est-à-dire qu'après cet épisode, l'hydrogène est distribué de façon uniforme dans la couche d'hélium. Il se trouve cependant que les abondances mesurées dans les DBA ayant $T_{\text{eff}} < 20,000 \text{ K}$ sont beaucoup plus élevées que ce qui est attendu après la dilution convective (voir Rolland et al. 2018). Bref, il y a trop d'hydrogène.

Pour expliquer ce surplus, certaines études proposent que l'hydrogène ait été accrétré du milieu interstellaire (MacDonald & Vennes, 1991) ou de comètes (Veras et al., 2014). Rolland et al. (2018) ont cependant montré que l'épaisseur de la couche d'hydrogène accumulée sur une étoile ayant une atmosphère pure en hélium au commencement de sa vie de naine blanche serait suffisamment épaisse à $30,000 \text{ K}$ pour empêcher la conversion DA→DB, et ce, même si le taux d'accrétion est faible. Il semble donc que l'accrétion ne soit pas la solution au problème. Il a aussi été proposé que l'hydrogène dans les DBA pourrait provenir de l'accrétion de disques de débris planétaires (Raddi et al., 2015; Gentile Fusillo et al., 2017). Cependant, cette conclusion se base sur l'étude de quelques naines blanches ayant des abondances atypiques ($\log \text{H/He} \sim -3.6$ et très riches en métaux). Cette théorie s'applique difficilement aux DB ne montrant pas de raies métalliques et ayant une très faible abondance d'hydrogène.

Un point soulevé par Bergeron et al. (2011) est la présence de naines blanches DB et DBA dans la même région de température ($T_{\text{eff}} < 20,000 \text{ K}$) montrant des abondances d'hydrogène très différentes (voir leur figure 25). La limite supérieure dans le cas des DB est $\log \text{H/He} < -6.0$, tandis que les DBA dans cette région ont plutôt des abondances 100 fois plus élevées (de l'ordre de $\log \text{H/He} \sim -4$). La plupart des analyses semblent montrer que les

masses moyennes des DB et des DBA ne sont pas significativement différentes l'une de l'autre (Voss et al., 2007; Bergeron et al., 2011; Falcon et al., 2012). Si tel est effectivement le cas, on pourrait alors supposer que ces deux types d'objets forment un seul groupe homogène (Voss et al., 2007) et que les DBA soient à l'extrême d'une distribution d'abondance d'hydrogène continue (Falcon et al., 2012).

Les masses similaires ainsi que le grand écart entre les quantités d'hydrogène dans l'atmosphère des DB et des DBA, soulève une autre question, à savoir pourquoi l'accrétion, qui semble nécessaire pour expliquer les valeurs de M_{H} observées dans les DBA froides, est efficace pour certaines étoiles, mais ne l'est pas du tout pour d'autres et ce, dans la même région de température (Bergeron et al., 2011). Certaines DB montrent très peu d'hydrogène, même à basse température : elles doivent nécessairement avoir évolué de DB plus chaudes n'ayant pas accrétié durant leur évolution (Bergeron et al., 2011). Ceci devrait aussi être vrai pour certaines DC, DQ et DZ ne montrant aucune trace d'hydrogène à des températures où celui-ci devrait être visible ($T_{\text{eff}} > 5000$ K).

Une hypothèse proposée par Rolland et al. (2018) est que l'abondance d'hydrogène mesurée ne corresponde pas à la quantité *réelle* d'hydrogène contenue dans l'enveloppe de la naine blanche. Dans le scénario d'évolution spectrale (section 1.3), l'hydrogène présent dans l'enveloppe des DO remonte à la surface par tri gravitationnel, jusqu'à ce que la couche superficielle soit assez épaisse pour que la naine blanche apparaisse de type DA. On suppose alors que *tout* l'hydrogène qui était contenu dans l'enveloppe de la naine blanche se trouve maintenant à la surface. Il se pourrait cependant que ce ne soit pas le cas et qu'une fraction de M_{H} provenant des profondeurs n'ait tout simplement pas eu le temps de remonter à la surface. Avec le temps, cet hydrogène remonte jusqu'à la zone convective (voir la figure 1.6), puis finalement se fait redistribuer dans l'atmosphère. Selon cette théorie, une DBA à $\sim 18,000$ K montrant de fortes raies d'hydrogène pourrait avoir été une DB, ou DBA, avec un faible $\log \text{H/He}$, à $\sim 25,000$ K (Rolland et al., 2018).

Une autre hypothèse est de remettre en cause la dilution *complète* de la couche superficielle d'hydrogène dans la zone convective d'hélium. Tel que mentionné plus haut, on suppose qu'à la suite d'un épisode de dilution convective, l'hydrogène est distribué uniformément dans l'enveloppe. Bergeron et al. (2011) ont suggéré que ce processus ne diluait peut-être pas complètement l'hydrogène, mais qu'une mince couche d'hydrogène subsisterait

toujours à la surface de la naine blanche (voir aussi Genest-Beaulieu & Bergeron 2017). Dans ce cas, l'abondance d'hydrogène mesurée serait supérieure à la quantité réelle contenue au sein de la naine blanche.

Ces deux dernières hypothèses supposent que l'hydrogène aurait une origine résiduelle et pourraient potentiellement résoudre le mystère des abondances apparemment trop élevées observées dans l'atmosphère des DBA, mais elles demeurent à être vérifiées.

1.5. Modélisation des atmosphères de naines blanches

Afin de bien pouvoir caractériser les naines blanches, il est impératif d'avoir des modèles d'atmosphère représentatifs de ces objets. Tel que mentionné à la section 1.2, cette thèse se concentre sur les deux types de naines blanches les plus communs, soient les DA et les DB. Comme ces deux types d'objets ont des caractéristiques physiques différentes, il est nécessaire de calculer une grille de modèles pour chacun d'eux.

1.5.1. Modèles de DA

Les conditions physiques dans l'atmosphère d'une DA varient grandement selon la température effective de la naine blanche, c'est pourquoi la grille de modèles utilisée pour ce type d'objet a été calculée à l'aide de deux codes différents.

Pour les modèles ayant $T_{\text{eff}} < 30,000$ K, les calculs ont été effectués à l'aide du code détaillé dans Tremblay & Bergeron (2009), où l'approximation de l'équilibre thermodynamique local (ETL) est utilisée. La convection atmosphérique, qui devient importante pour $T_{\text{eff}} < 15,000$ K, est traitée selon la théorie de la longueur de mélange (*mixing-length theory* ou MLT en anglais). Brièvement, on fait l'approximation qu'une bulle de matière conserve ses caractéristiques sur une distance l , la longueur de mélange, avant de se thermaliser avec le gaz environnant. Différentes paramétrisations de la théorie de la longueur de mélange permettent d'ajuster l'efficacité convective (plus la convection est efficace, plus la quantité d'énergie transportée est grande).

Pour les modèles à $T_{\text{eff}} > 30,000$ K, l'approximation de l'équilibre thermodynamique local n'est plus valide. Par conséquent, les modèles sont calculés à l'aide du code TLUSTY, décrit dans Hubeny & Lanz (1995).

La détermination des paramètres atmosphériques des naines blanches repose grandement sur la force et la forme des raies d'absorption (voir la section 1.6.3). C'est pourquoi une part importante des modèles d'atmosphère est de tenir compte des sources d'élargissement des raies d'absorption : l'élargissement thermique, ou Doppler, qui est causé par la distribution de vitesse de l'atome émetteur selon la ligne de visée de l'observateur, et l'élargissement par pression. Ce dernier est causé par les interactions entre les différentes particules du gaz et l'atome émetteur. Ces interactions créent un champ électrique variable qui perturbe les niveaux d'énergie de l'atome émetteur. Le profil de raie résultant est obtenu en faisant la convolution des profils dus à l'élargissement thermique et à l'élargissement par pression.

Dans le cas des atmosphères pures en hydrogène, le type d'élargissement par pression le plus important est l'élargissement Stark, qui se produit lorsque l'atome perturbateur est une particule chargée. Les profils d'élargissement Stark utilisés dans les présents modèles ont été calculés et implémentés par Tremblay & Bergeron (2009). Ceux-ci sont une amélioration par rapport aux anciens profils (décrits dans Lemke 1997), puisqu'ils tiennent compte des effets non idéaux dus aux perturbations sur l'émetteur par les photons et les électrons.

La grille de modèles couvre de 1500 K à 120,000 K en température, pour des gravités de surface entre $\log g = 6.5$ et $\log g = 9.0$.

1.5.2. Modèles de DB/DBA

Les modèles d'atmosphère de DB utilisés dans cette thèse sont similaires à ceux décrits dans Bergeron et al. (2011) (voir aussi le chapitre 2). La convection dans les modèles de DB est aussi traitée selon la théorie de la longueur de mélange, plus particulièrement avec la version $ML2/\alpha=1.25$. Contrairement aux DA, l'approximation de l'ETL est valide jusqu'à environ $T_{\text{eff}} \sim 40,000 - 45,000$ K (Dreizler & Werner, 1996). Au delà de cette température, les effets hors-ETL deviennent importants et doivent être considérés. Cependant, comme il a été mentionné à la section 1.2, la transition DO→DB se produit à environ 40,000 K. Par conséquent, l'approximation ETL peut être utilisée dans tout l'intervalle de température couvert par les DB.

Tout comme pour les DA, il est important d'inclure les sources d'élargissement des raies. Les profils de raies décrits dans Beauchamp et al. (1997) sont utilisés pour l'élargissement

Stark. Pour l’élargissement des raies dû aux particules neutres, qui dominent dans l’atmosphère des DB froides ($T_{\text{eff}} < 16,000$ K), la situation est plus complexe. Les théories utilisées pour décrire l’élargissement par les particules neutres sont souvent pointées du doigt pour expliquer l’augmentation de la masse moyenne des DB à basse température (voir la section 1.2.2).

Les élargissements par résonance et van der Waals sont traités conjointement. La procédure complète est détaillée dans Beauchamp (1995). L’élargissement par résonance est traité selon le formalisme de Ali & Griem (1965). Il est à noter qu’à cause des règles de sélection pour le spin ($\Delta S = 0$), seules certaines raies sont élargies par résonance. En particulier, comme il est supposé que les atomes perturbateurs sont dans l’état fondamental⁷, seules les transitions entre les niveaux i et j ayant un spin nul⁸ créent une raie sujette à l’élargissement par résonance. Le tableau VIII de Beauchamp (1995) donne une liste des principales raies élargies par résonance.

Pour l’élargissement van der Waals, la largeur du profil Lorentzien est calculée selon deux théories différentes. La première est celle de Unsold (1955) et la seconde est celle de Deridder & van Rensbergen (1976). Cette dernière théorie prédit systématiquement des profils plus larges que la théorie de Unsold (1955), sauf lorsque les nombres quantiques initiaux et finaux de la transition sont plus grands que 2 ou 3. De plus, la théorie de Deridder & van Rensbergen (1976) n’est plus valide en deçà de ces nombres quantiques, puisqu’elle a été développée à l’aide du potentiel de Smirnov. Par conséquent, la largeur due à l’élargissement van der Waals adoptée dans les modèles est :

$$\omega_{\text{vdW}} = \max(\omega_{\text{Unsold}}, \omega_{\text{Deridder}}) \quad (1.1)$$

Les deux seules exceptions sont les raies $\lambda = 4121$ Å et $\lambda = 4713$ Å, pour lesquelles $\omega_{\text{vdW}} = \omega_{\text{Unsold}}$.

Lewis (1967) a déterminé que la combinaison de l’élargissement van der Waals et de résonance donnait un profil d’une largeur égale à $\omega_{\text{neutre}} \sim 0.6 - 0.8(\omega_{\text{resonance}} + \omega_{\text{vdW}})$. Cependant,

7. Cette supposition est valide puisque l’élargissement par les particules neutres ne domine que dans les modèles de DB froids, dans lesquels les atomes d’hélium sont majoritairement dans l’état fondamental (voir Beauchamp 1995).

8. Le spin du niveau fondamental de l’hélium neutre est nul.

ces résultats ne sont valides que pour des températures de l'ordre de 100 K, difficilement applicables aux atmosphères de naines blanches. C'est pourquoi la valeur conservatrice

$$\omega_{\text{neutre}} = \max(\omega_{\text{resonance}}, \omega_{\text{vdW}}) \quad (1.2)$$

est adoptée pour la largeur des profils d'élargissement dus aux particules neutres.

Faute de meilleures théories, c'est la procédure décrite plus haut qui est utilisée dans les modèles d'atmosphère, bien qu'elle soit loin d'être idéale. Il ne fait aucun doute que cette procédure doit être révisée et grandement améliorée.

La grille de modèles de DB(A) couvre de 11,000 K à 50,000 K en température effective, pour des gravités de surface entre $\log g = 7.0$ et 9.0 et des abondances d'hydrogène entre $\log H/He = -6.0$ à -2.0 . Une grille de modèles d'atmosphère constituée d'hélium pur couvrant les même intervalles en température et gravité de surface est aussi utilisée.

1.6. Obtention des paramètres atmosphériques

Afin de pouvoir étudier les naines blanches, il faut connaître leurs paramètres atmosphériques et physiques, qui sont la température effective, la gravité de surface, le rayon, la masse, la luminosité, la composition atmosphérique et l'âge. Les méthodes les plus couramment utilisées pour obtenir ces paramètres sont les techniques photométrique et spectroscopique. La technique photométrique permet d'obtenir la température effective T_{eff} ainsi que l'angle solide $\pi(R/D)^2$ en comparant la distribution d'énergie observée aux prédictions des modèles. La technique spectroscopique, quant à elle, permet de déterminer T_{eff} , la gravité de surface $\log g$ ainsi que l'abondance d'hydrogène $\log H/He$, si applicable, en comparant les spectres observés et synthétiques. Dans les deux cas, les autres paramètres doivent être obtenus de façon indirecte en faisant appel à la relation masse-rayon provenant de modèles évolutifs.

1.6.1. Relation Masse-Rayon

Il existe une relation entre le rayon et la masse d'une naine blanche, car la structure de ces objets est gouvernée par la pression due aux électrons dégénérés. De façon simpliste, la relation entre la masse et le rayon d'une naine blanche est $MR^3 = \text{constante}$. Donc, plus une naine blanche est massive, plus son rayon est petit et vice versa. Ceci implique qu'il existe

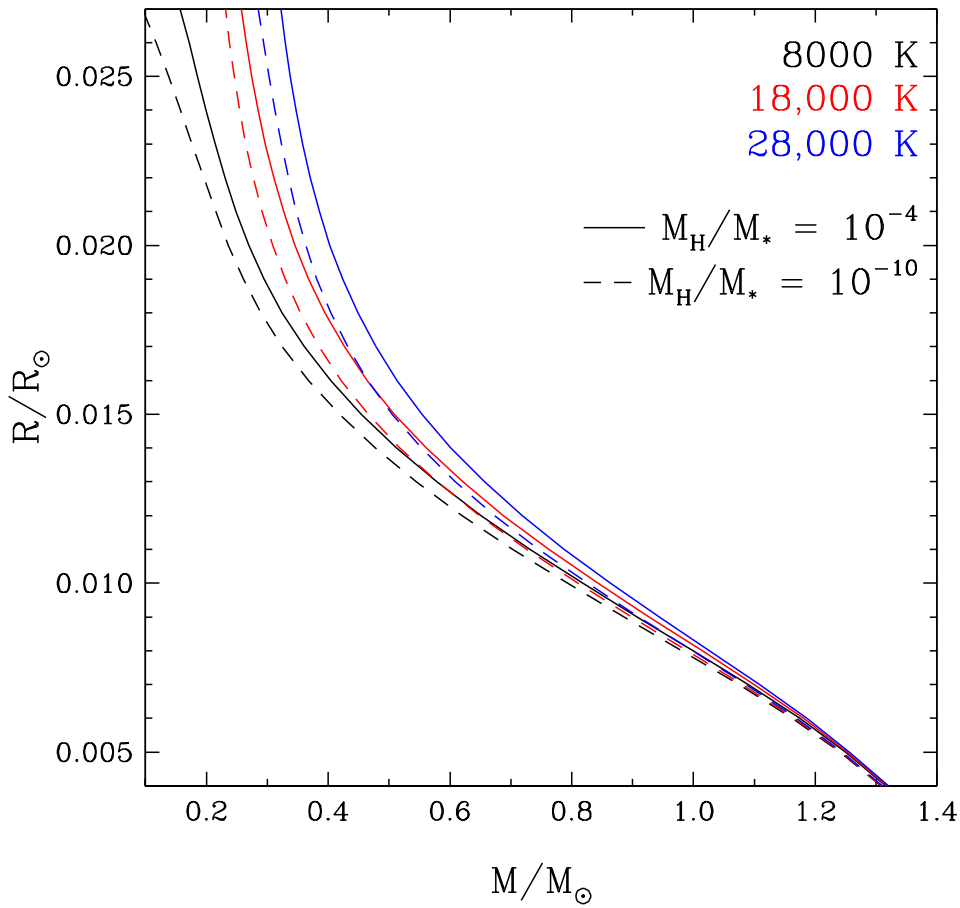


FIGURE 1.7. Relations masse-rayon théoriques pour $T_{\text{eff}} = 8000 \text{ K}$ (noir), $18,000 \text{ K}$ (rouge) et $28,000 \text{ K}$ (bleu), pour une couche d'hydrogène épaisse ($q(\text{H}) \equiv M(\text{H})/M_{\star} = 10^{-4}$, trait plein) et mince ($q(\text{H}) = 10^{-10}$, tirets).

une masse pour laquelle le rayon de la naine blanche devient théoriquement nul. Cette masse limite, appelée la masse de Chandrasekhar, est $M_C = 1.4 M_{\odot}$.

Comme les naines blanches continuent de se contracter en se refroidissant, pour obtenir une relation masse-rayon réaliste, il faut prendre en considération, entre autres, l'âge, ou la température effective, et l'épaisseur de l'atmosphère, c'est pourquoi elle est normalement combinée à des modèles évolutifs. Dans le cadre de cette thèse, les modèles évolutifs utilisés sont similaires à ceux décrits dans Fontaine et al. (2001). Ces modèles supposent un cœur de carbone et d'oxygène ainsi qu'une couche épaisse d'hydrogène ($M_{\text{H}}/M_{\star} = 10^{-4}$) dans le cas des DA, ou une couche beaucoup plus mince ($M_{\text{H}}/M_{\star} = 10^{-10}$) représentative de l'enveloppe

des DB. La Figure 1.7 montre la relation entre la masse et le rayon d'une naine blanche pour différentes températures effectives et épaisseur de la couche d'hydrogène.

Tel que mentionné plus haut, les techniques photométrique et spectroscopique ne permettent de déterminer directement que deux ou trois des paramètres d'intérêt, et il est nécessaire d'invoquer la relation-masse pour obtenir les paramètres manquants. Cette relation est donc cruciale pour l'étude des naines blanches.

La relation masse-rayon théorique à été mise à l'épreuve à quelques reprises (Holberg et al., 2012; Tremblay et al., 2017; Parsons et al., 2017; Bédard et al., 2017), mais seulement pour des échantillons comportant un nombre restreint d'objets. Bien que ces études aient conclu que la relation masse-rayon est valide, il serait bénéfique de la remettre à l'épreuve en utilisant un échantillon plus volumineux.

1.6.2. Technique photométrique

La technique photométrique compare la distribution d'énergie aux prédictions des modèles afin d'obtenir la température effective T_{eff} ainsi que l'angle solide $\pi(R/D)^2$. La procédure est décrite dans Bergeron et al. (1997). Cette technique peut être utilisée pour tous les types de naines blanches.

La première étape est de dérougir les données. Lorsque la lumière de l'étoile parcourt la distance la séparant de la Terre, elle rencontre des nuages de poussière qui la dévie/l'absorbe. Ce phénomène n'affecte pas toutes les longueurs d'ondes de la même façon, la lumière bleue étant la plus affectée, faisant apparaître l'étoile plus rouge (ou froide) qu'elle ne l'est en réalité. L'intensité du rougissement dépend de la distance à laquelle se trouve l'objet. L'extinction interstellaire maximale selon une ligne de visée A_x dans une certaine bande passante x est donnée par

$$A_x = R_x E(B - V) \quad (1.3)$$

L'excès de couleur $E(B - V)$ ne dépend que de la position de l'étoile. Les valeurs de $E(B - V)$ utilisées dans la présente thèse sont celles de Schlafly & Finkbeiner (2011). R_x est le facteur de rougissement et ne dépend que de la bande-passante.

Une correction doit être appliquée à A_x pour tenir compte de la distance à laquelle se trouve l'objet. Si la distance est connue, via la parallaxe, cette correction peut être faite

directement, suivant la paramétrisation de Harris et al. (2006). Brièvement, l'extinction est supposée nulle si l'objet se trouve à moins de 100 pc, est considérée maximale si la distance par rapport au plan galactique est $|z| > 250$ pc, et varie linéairement entre ces deux régimes. Dans le cas où la distance n'est pas connue, il faut procéder par itération, comme l'ont fait Tremblay et al. (2011a) et Genest-Beaulieu & Bergeron (2014).

Une fois dérougées, les magnitudes m_ν sont converties en flux moyens f_ν^m à l'aide de l'équation suivante :

$$m_\nu = -2.5 \log f_\nu^m - 48.60 \quad (1.4)$$

où

$$f_\nu^m = \frac{\int f_\nu S_m(\nu) d\log \nu}{\int S_m(\nu) d\log \nu} \quad (1.5)$$

Dans cette dernière équation, f_ν est le flux monochromatique et $S_m(\nu)$ est la fonction de transmission de la bande-passante. Les flux synthétiques moyens H_ν^m sont ensuite calculés en remplaçant f_ν par H_ν , le flux d'Eddington monochromatique qui dépend de T_{eff} , $\log g$ et de la composition atmosphérique, dans l'équation 1.5. Il est à noter que l'équation 1.4 n'est valide que pour les magnitudes basées sur le système AB.

Les flux moyens observés et synthétiques sont reliés par l'angle solide :

$$f_\nu^m = 4\pi(R/D)^2 H_\nu^m \quad (1.6)$$

Une première minimisation du χ^2 est effectuée en supposant une gravité de surface de $\log g = 8.0$. Le χ^2 est défini comme la somme des différences entre les flux observés et théoriques, pondérés par les incertitudes. La procédure de minimisation utilisée est celle de Levenberg-Marquardt, décrite dans Press et al. (1992).

Cette première minimisation donne un estimé de la température effective T_{eff} ainsi que de l'angle solide $\pi(R/D)^2$, ou du rayon, si la parallaxe trigonométrique est connue. La relation masse-rayon (voir section 1.6.1) ainsi que les modèles évolutifs sont ensuite utilisés pour obtenir la gravité de surface, qui sera fort probablement différente de l'estimé de départ ($\log g = 8.0$). Il s'agit ensuite de procéder par itération jusqu'à ce que la valeur de $\log g$ ait convergée. Les autres paramètres d'importance, tel que la masse ou l'âge de la naine blanche, peuvent ensuite être obtenus indirectement à l'aide de modèles évolutifs et de la

relation masse-rayon. Si aucune mesure de la parallaxe n'est disponible, la relation masse-rayon et les modèles évolutifs permettent d'obtenir un estimé de la distance. Il est à noter que la supposition de $\log g = 8.0$ n'affecte pas significativement la valeur de la température effective obtenue (Genest-Beaulieu & Bergeron, 2014).

Cette technique devient plus efficace lorsqu'une combinaison de systèmes photométriques est utilisée, plutôt qu'un seul. Par exemple, la photométrie *ugriz* du Sloan Digital Sky Survey permet de bien contraindre la partie visible et infrarouge proche de la distribution d'énergie (3543 Å à 9134 Å). Si cette photométrie est combinée aux données *JHK_s* de 2MASS (*Two Micron All-Sky Survey*) par exemple, la distribution d'énergie est alors caractérisée jusqu'à 2.159 μm.

1.6.3. Technique spectroscopique

La technique la plus communément utilisée pour déterminer les paramètres atmosphériques des naines blanches est la technique spectroscopique. Contrairement à la technique photométrique, celle-ci est légèrement différente selon le type spectral de la naine blanche analysée.

1.6.3.1. Technique spectroscopique pour les DA

La technique spectroscopique pour les DA utilisée dans cette thèse est similaire à celle décrite dans Bergeron et al. (1992), Bergeron et al. (1995a) et Liebert et al. (2005). Cette méthode compare les spectres observés et synthétiques pour déterminer la température effective et la gravité de surface de la naine blanche.

Les spectres observés sont parfois sujets à des erreurs de calibration. Ce problème peut être éliminé en normalisant autant les raies spectrales observées que synthétiques (H β à H8), ce qui constitue la première étape de la technique spectroscopique. Les spectres synthétiques sont aussi convolués avec un profil instrumental gaussien approprié selon la résolution du spectre observé. Pour effectuer la normalisation, il faut d'abord déterminer correctement où se situe le continu, ce qui est la partie la plus complexe de cette technique. Pour y arriver, on utilise les modèles, multipliés par une fonction d'ordre 6 en λ , afin de s'assurer que la fonction trouvée est la plus lisse possible. Vu le grand nombre de paramètres ajustés à cette étape, les valeurs de T_{eff} et $\log g$ obtenues ne sont pas significatives.

Une particularité des raies d'absorption est qu'elles atteignent une force maximale à une certaine température et deviennent plus faibles lorsqu'on s'éloigne de ce maximum. Dans le cas des DA, ce maximum se produit autour de 14,000 K. Il faut donc «choisir» si la solution physique se trouve du côté chaud ou du côté froid de ce maximum.

Il se trouve que la procédure utilisée pour trouver le continu permet de distinguer, dans la majorité des cas, si l'objet en question est chaud ou froid, du moins dans le cas des spectres du Sloan Digital Sky Survey (voir la section 1.7.1). La minimisation du χ^2 décrite plus haut est donc effectuée deux fois : du côté chaud et du côté froid, et la solution ayant la plus petite valeur de χ^2 est conservée.

Une fois que la fonction lisse est bien ajustée, le continu est déterminé et normalisé à l'unité. Entre 9000K et 16,000 K, les raies de Balmer sont très fortes et les modèles ne les reproduisent pas adéquatement (voir la figure 3 de Bergeron et al. 1995b et la section 3.4 de Genest-Beaulieu & Bergeron 2014). C'est pourquoi si l'ajustement suggère une température entre 9000 K et 16,000 K, le spectre observé est normalisé à nouveau, cette fois en utilisant une somme de profils pseudo-gaussiens, car ceux-ci sont une bonne approximation des raies de Balmer dans cet intervalle.

T_{eff} et $\log g$ sont ensuite obtenus à partir de ces spectres normalisés. La méthode de Levenberg-Marquardt est utilisée, en prenant comme point de départ la solution de la procédure de normalisation. Une fois les valeurs de T_{eff} et $\log g$ convergées, les corrections 3D de Tremblay et al. (2013a) sont appliquées (voir la section 1.2.1).

La technique spectroscopique est très puissante pour obtenir les paramètres atmosphériques des naines blanches. Elle a cependant ses limites. À très basse température ($T_{\text{eff}} \lesssim 6500$ K), les raies d'hydrogène deviennent très faibles, tel que montré à la figure 1.8. Ces faibles raies peuvent facilement être «perdues» dans le bruit. Par conséquent, l'obtention des paramètres atmosphériques à l'aide de la technique spectroscopique dans cette région en température est plus ardue.

1.6.3.2. *Technique spectroscopique pour les DB*

La technique spectroscopique pour les DB est légèrement différente de celle utilisée pour les DA, car il y a un troisième paramètre à obtenir, soit l'abondance d'hydrogène $\log H/\text{He}$. Cette méthode est détaillée dans Bergeron et al. (2011).

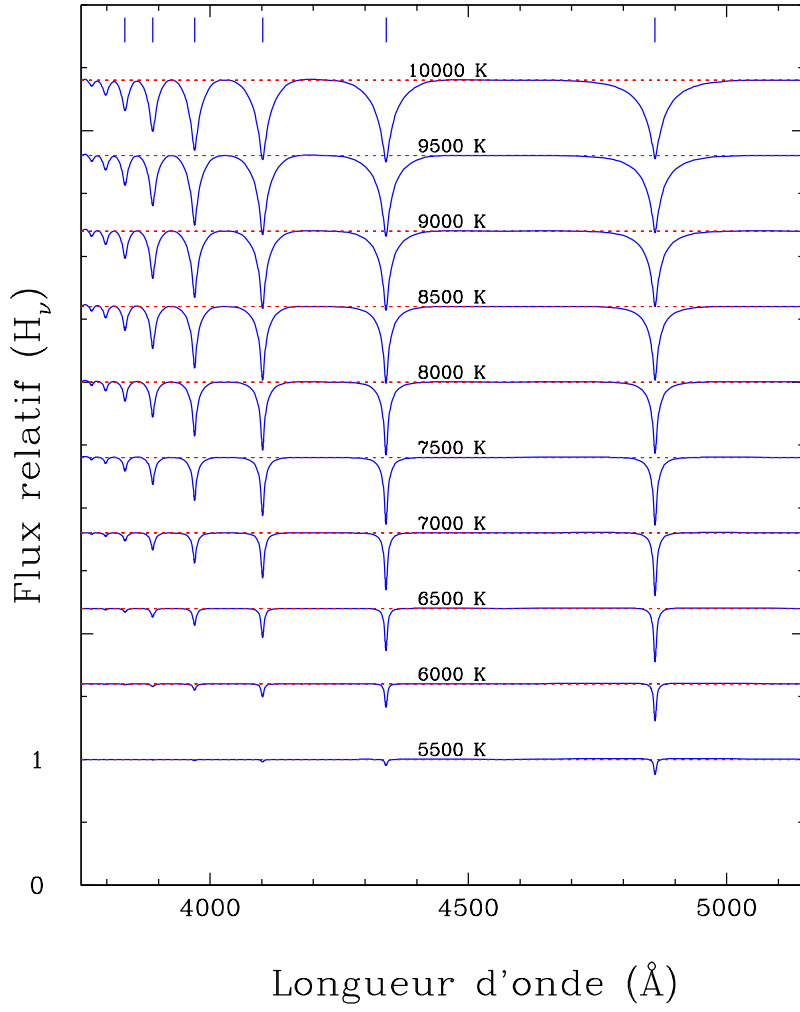


FIGURE 1.8. Spectres synthétiques normalisés de naines blanches de type DA à différentes températures effectives et $\log g = 8.0$. Les spectres ont été décalés verticalement par clarté. Les positions des différentes raies de Balmer sont identifiées.

La première étape est encore une fois la normalisation du spectre observé, ce qui est fait à l'aide de la méthode de Levenberg-Marquardt et de la grille de spectres synthétiques, multipliée par une fonction de haut degré en λ (λ^5). Les DB posent le même problème que les DA, c'est-à-dire qu'il faut «choisir» de quel côté du maximum, qui se situe à $\sim 25,000$ K, se trouve la solution physique. La même tactique est utilisée : la minimisation est faite deux fois et la solution présentant le χ^2 le plus faible est conservée.

Un premier estimé de la température effective et de la gravité de surface est d'abord obtenu en utilisant la partie bleue ($\lambda = 3750 - 5150$ Å) du spectre. Ces paramètres sont ensuite

TABLE 1.1. Limites de détection de H α et H β

S/N	H α mÅ	H β mÅ
S/N \geq 20	200	250
15 \leq S/N < 20	300	350
10 \leq S/N < 15	400	450
5 \leq S/N < 10	500	550
0 \leq S/N < 5	600	650

gardés fixes et l'abondance d'hydrogène est obtenue grâce à la raie H α ($\lambda = 6400 - 6800 \text{ \AA}$). Ces deux étapes sont répétées jusqu'à ce qu'il y ait cohérence entre tous les paramètres.

Il est à noter que l'abondance d'hydrogène peut aussi être obtenue à partir de la raie H β ($\lambda = 4800 - 5150 \text{ \AA}$) si le spectre observé ne couvre pas la région de H α . Comme H β est plus difficile à détecter, particulièrement lorsque l'abondance d'hydrogène est faible, les contraintes sur log H/He obtenues en utilisant cette raie sont moins précises (Bergeron et al., 2011).

Comme les spectres utilisés n'ont pas un signal-sur-bruit (S/N) infini, une limite de détection en termes de largeur équivalente de la raie, est appliquée lors de la détermination de log H/He. La limite appliquée dépend à la fois du S/N et de la raie utilisée (H α ou H β). Le tableau 1.1 liste ces limites.

Tout comme pour les DA, cette technique est puissante, mais comporte certaines limites. Comme il est montré à la figure 1.9, les raies d'hélium deviennent très faibles pour des températures sous $\sim 13,000 \text{ K}$ et peut rendre la technique spectroscopique moins fiable.

1.6.4. Avantages et inconvénients de chaque technique

Les techniques décrites aux sections 1.6.2 et 1.6.3 permettent toutes deux, lorsque combinée à la relation masse-rayon, d'obtenir les mêmes paramètres physiques. Il existe cependant des avantages et des inconvénients inhérents à l'utilisation de chacune d'entre elles.

Un avantage de la technique photométrique est qu'il n'y a pas de dégénérescence des solutions. Il a été mentionné dans la description de la technique spectroscopique (sections 1.6.3.1 et 1.6.3.2) que les raies atteignaient leur force maximale à une certaine température

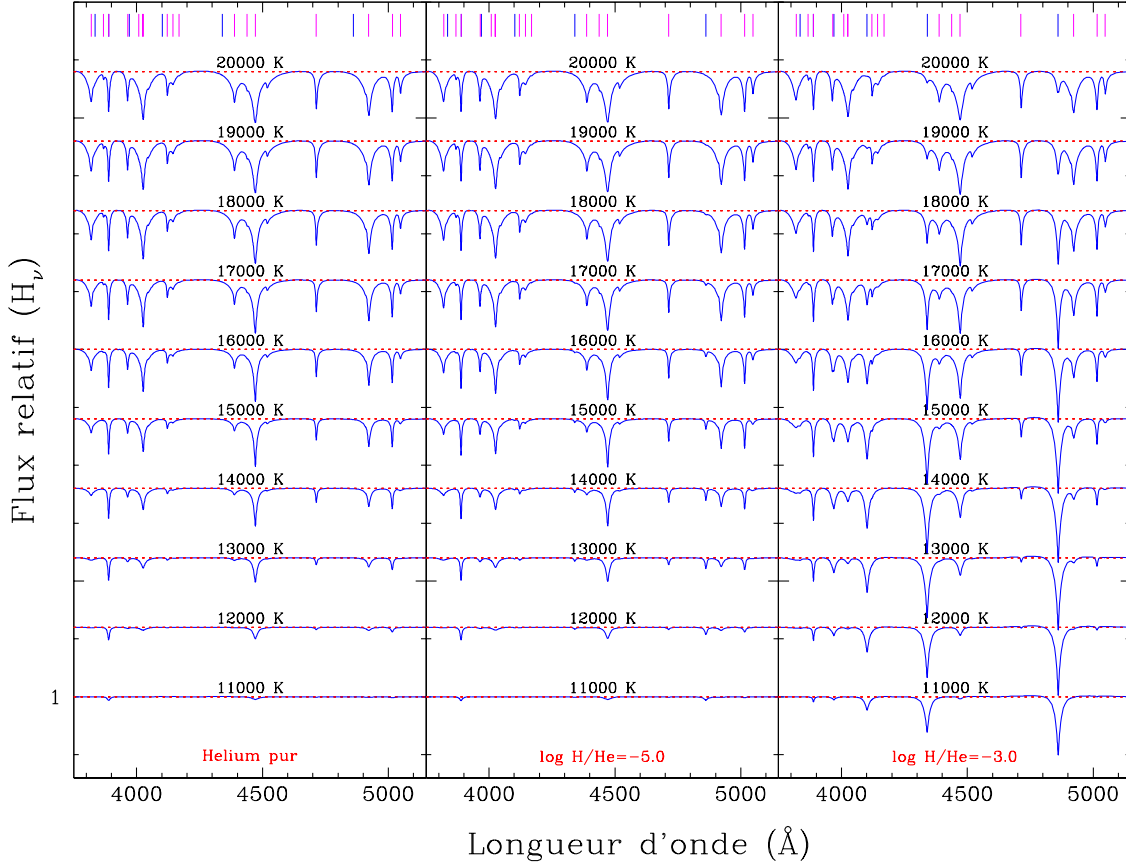


FIGURE 1.9. Spectres synthétiques normalisés de naines blanches de type DB à différentes températures effectives, $\log g = 8.0$ et différentes abondances d’hydrogène : hélium pur (gauche), $\log H/\text{He} = -5.0$ (milieu) et $\log H/\text{He} = -3.0$ (droite). Les positions des raies d’hélium (hydrogène) sont indiquées par les traits magenta (bleus).

et qu’il fallait choisir si la naine blanche en question se trouvait du côté chaud ou froid de ce maximum. Il n’existe pas de phénomène équivalent pour la photométrie. La solution photométrique pourrait donc, en principe, être utilisée pour déterminer de quel côté du maximum se situe la naine blanche. Celle-ci n’est cependant pas utilisée, car il est préférable que les paramètres provenant des deux techniques soient indépendants.

Un autre avantage évident de la technique photométrique survient lors de l’étude de naines blanches froides dont le spectre ne montre que de très faibles raies d’absorption (voir, par exemple, le spectre de DC à la figure 1.5). Dans ce cas, la technique spectroscopique est incapable de déterminer les paramètres atmosphériques. La distribution d’énergie, contrainte par la photométrie, quant à elle, reste sensible à T_{eff} même à très basse température.

À l'autre extrême, pour les naines blanches très chaudes, la photométrie devient insensible à la température, puisqu'elle se trouve dans le régime de Rayleigh-Jeans. Dans ce cas, la technique photométrique devient moins efficace et il faut se fier à la technique spectroscopique.

Finalement, les deux techniques n'ont pas le même niveau de précision et d'exactitude⁹. La technique spectroscopique est généralement plus précise que la technique photométrique (voir le chapitre 3), car les raies d'absorption sont plus sensibles aux paramètres atmosphériques. Ceci ne garantit cependant pas l'exactitude des paramètres, puisque, contrairement à la photométrie, les profils de raies sont très sensibles à la physique implémentée dans les modèles. Par conséquent, une comparaison des paramètres atmosphériques obtenus à l'aide des techniques photométrique et spectroscopique pourrait permettre de déceler certains problèmes avec la physique implémentée dans les modèles d'atmosphère.

1.7. Relevés SDSS et *Gaia*

L'étude des naines blanches a été grandement aidée par l'avènement des grands relevés. Ces relevés rendent accessibles des quantités phénoménales de données prises de façon homogène, ce qui permet l'étude d'un grand nombre d'objets. Les deux relevés les plus importants dans le cadre de cette thèse sont le *Sloan Digital Sky Survey* et *Gaia*.

1.7.1. *Sloan Digital Sky Survey*

Le *Sloan Digital Sky Survey*, ou SDSS, est un relevé photométrique et spectroscopique ayant couvert 14,555 degrés carrés du ciel en date du *Data Release 12* (DR12, 2014). Ce relevé s'effectue en deux temps. La première étape consiste à prendre des mesures photométriques dans cinq régions du spectre électromagnétique : l'ultraviolet (u , 3551 Å), le vert (g , 4686 Å), le rouge (r , 6166 Å), l'infrarouge proche (i , 7480 Å) et l'infrarouge moyen (z , 8932 Å)¹⁰.

Ensuite, selon des critères de couleurs, certaines cibles sont choisies pour un suivi spectroscopique. Les données spectroscopiques couvrent l'intervalle de longueur d'onde de 3800

9. La précision réfère à l'incertitude : plus la mesure est précise, moins l'incertitude est grande. L'exactitude réfère plutôt à la proximité de la mesure à la valeur réelle.

10. www.sdss.org/instruments/camera/

à 9200 Å. Il est possible de recueillir jusqu'à 1000 spectres simultanément¹¹, grâce à un système de plaques et de fibres optiques.

Les cibles prioritaires de ce relevé sont les quasars et les galaxies lointaines, auxquels sont automatiquement assignés des fibres optiques. Les fibres restantes sont ensuite attribuées à d'autres types de cibles, comme les naines blanches. Grâce au SDSS, le nombre de naines blanches connues a plus que décuplé, passant de 2249 (McCook & Sion, 1999) à plus de 35,000 dans le DR12 (2014).

Une classe de cibles particulièrement importante dans l'étude des naines blanches à atmosphère riche en hélium est celle des *hot standard*, qui comprend les étoiles isolées dont les couleurs sont très bleues, c'est-à-dire pour lesquelles $u - g < 0$ et $g - r < 0$. Heureusement, les naines blanches de type DB ayant une température effective supérieure à 15,000 K satisfont à ces critères de sélection, ce qui leur garantit (pratiquement) un suivi spectroscopique (Eisenstein et al., 2006a).

Bien que les données provenant du SDSS ne soient pas toujours de la meilleure qualité (voir par exemple la figure 2.1 ainsi que la figure 13 de Genest-Beaulieu & Bergeron 2014), ce point est largement compensé par la quantité d'objets présents dans les banques de données. Un autre avantage d'utiliser les données spectroscopiques provenant du SDSS est qu'elles couvrent la région H α (6400–6800 Å). Comme il a été mentionné à la section 1.6.3.2, cette région du spectre est essentielle à l'obtention de contraintes précises sur l'abondance d'hydrogène dans les atmosphères de naines blanches de type DB (Bergeron et al., 2011; Rolland et al., 2018).

1.7.2. Le relevé *Gaia*

Gaia est un satellite qui a été lancé le par l'ESA (*European Space Agency*). Le but premier de cette mission est de créer une carte tri-dimensionnelle très précise de notre Galaxie en mesurant le mouvement et la position de milliards d'étoiles. Cette carte tri-dimensionnelle permettra de mieux caractériser la formation de notre galaxie, la Voie Lactée. En date du Data Release 2 (DR2, Gaia Collaboration et al. 2018), la parallaxe trigonométrique (ou la distance) de plus de 1.3 milliards d'étoiles a été mesurée.

11. www.sdss.org/instruments/

Avant le relevé *Gaia*, la parallaxe trigonométrique de seulement ~ 350 naines blanches avait été mesurée, selon la version électronique du catalogue de naines blanches identifiées spectroscopiquement¹² (*Catalog of Spectroscopically Identified White Dwarfs*, McCook & Sion 1999). Dans le DR2 de *Gaia*, ce sont 260,000 candidates (à haut degré de confiance) naines blanches pour lesquelles la parallaxe a été mesurée (Gentile Fusillo et al., 2019).

Un avantage certain de *Gaia* par rapport aux autres relevés, tels que Hipparcos, le *Yale Parallax Catalog* (YPC) ou le *United States Naval Observatory* (USNO), outre le plus grand nombre d'objets, est la précision des données. Par exemple, pour la DA WD 0644+375, la parallaxe mesurée par Hipparcos est $\pi = 63.53 \pm 3.55$ mas (van Leeuwen, 2007), tandis que *Gaia* a obtenu $\pi = 58.5737 \pm 0.0863$ mas. Comme la parallaxe permet de contraindre certains paramètres d'une naine blanche (voir la section 1.6.2), plus la valeur de π est précise (et exacte), mieux l'étoile peut être caractérisée.

Gaia a une grande importance pour cette thèse, car, comme il a été mentionné à la section 1.6.2, la parallaxe, combinée à des mesures photométriques, permet de déterminer le rayon d'une naine blanche. Comme les données provenant de *Gaia* sont très précises, cela signifie que les valeurs de R et, par le biais de la relation masse-rayon, $\log g$ et M , obtenues par la technique photométrique le sont aussi.

1.8. Objectifs et structure de la thèse

L'étude des naines blanches repose grandement sur la détermination de leurs paramètres atmosphériques et physiques. Il y a seulement quelques années, les techniques photométrique et spectroscopique ne pouvaient être appliquées qu'à de petits échantillons, car la quantité de données accessibles était très restreinte. L'avènement des grands relevés, tels que le SDSS et *Gaia* a complètement transformé l'étude des naines blanches en rendant accessibles des données photométriques, spectroscopiques ainsi que la parallaxe trigonométrique pour des milliers de naines blanches. Le premier objectif de cette thèse est d'effectuer une analyse des naines blanches de type DA et DB contenues dans ces relevés afin de caractériser la validité des solutions photométriques et spectroscopiques.

Comme les techniques photométrique et spectroscopique ne permettent que de déterminer directement deux ou trois paramètres, il est alors impératif d'invoquer la relation masse-rayon

12. <http://www.astronomy.villanova.edu/WDCatalog/index.html>

pour obtenir les autres quantités d'intérêt. Bien qu'elle ait été testée à quelques reprises, ce ne fût qu'à l'aide de petits échantillons. Le second objectif de cette thèse est de remettre à l'épreuve la relation masse-rayon théorique en mettant à profit les résultats de l'analyse des naines blanches du SDSS et de *Gaia*. Ces deux premiers objectifs sont explorés dans l'article *A Comprehensive Spectroscopic and Photometric Analysis of DA and DB White Dwarfs from SDSS and Gaia*, publié dans *The Astrophysical Journal*, qui est reproduit au chapitre 2.

Les naines blanches de type DB sont bien moins comprises que leurs homologues riches en hydrogène, car elles sont beaucoup moins nombreuses. Comme le SDSS a permis d'identifier une quantité substantielle de nouvelles naines blanches de type DB, une analyse approfondie de ce type d'objets s'impose. Le troisième objectif de cette thèse est de caractériser les naines blanches de type DB dans leur ensemble, c'est-à-dire leur distribution en température, leur distribution de masse et la quantité d'hydrogène contenue dans leur enveloppe. Cette analyse vise aussi à une meilleure compréhension de leur évolution.

Finalement, le quatrième objectif de cette thèse est de s'attaquer à la question de l'origine de l'hydrogène dans l'atmosphère des DBA, plus particulièrement à l'hypothèse que la dilution convective ne mélange pas *tout* l'hydrogène superficiel, mais seulement une fraction de celui-ci, résultant en une atmosphère non pas homogène, mais plutôt stratifiée. La possibilité que les atmosphères de naines blanches de type DB/DBA soient stratifiées sera explorée à l'aide de modèles ayant un profil d'abondance caractérisé par l'équilibre diffusif. Les troisième et quatrième objectifs sont le point central d'un deuxième article, intitulé *A Photometric and Spectroscopic Investigation of the DB White Dwarf Population in the SDSS and Gaia*, présentement en préparation. Cet article, qui sera soumis à *The Astrophysical Journal*, est reproduit au chapitre 3.

1.9. Déclaration de l'étudiante

Pour accomplir cette thèse de doctorat, j'ai acquis et analysé toutes les données photométriques et spectroscopiques provenant du *Sloan Digital Sky Survey* mentionnées aux chapitres 2 et 3. J'ai aussi acquis les mesures de parallaxes trigonométriques du relevé *Gaia* à l'aide de la *Montreal White Dwarf Database*¹³. Toutes les figures présentes dans cette thèse ont été créées par moi, à partir de calculs que j'ai effectués, à l'exception de quelques graphiques

13. <http://www.montrealwhitedwarfdatabase.org/home.html>

présentés dans le chapitre d'introduction. La provenance des figures est alors clairement indiquée dans la légende associée, le cas échéant. J'ai aussi effectué l'essentiel de l'analyse présentée aux chapitres 2 et 3.

Le chapitre 3 présente de nouveaux modèles d'atmosphère chimiquement stratifiés. Le code de modèle d'atmosphère de base m'a été fourni par Pierre Bergeron. J'ai ensuite écrit et implémenté dans ce code une nouvelle routine permettant d'inclure un profil d'abondance en équilibre diffusif dans le calcul de la structure atmosphérique, tel que décrit dans l'annexe B.

Finalement, c'est moi qui ai rédigé l'entièreté des chapitres 1 et 4, ainsi que l'annexe B. J'ai aussi rédigé l'essentiel des chapitres 2 et 3.

Chapitre 2

A Comprehensive Spectroscopic and Photometric Analysis of DA and DB White Dwarfs from SDSS and *Gaia*

C. Genest-Beaulieu¹ & P. Bergeron¹

¹ *Département de Physique, Université de Montréal, Montréal, QC H3C 3J7, Canada; genest@astro.umontreal.ca, bergeron@astro.umontreal.ca.*

Received 10 December 2018 ; Accepted 21 December 2018

Published in *The Astrophysical Journal*

January 2019, Volume 871, page 169

DOI: 10.3847/1538-4357/aafac6

©AAS. Reproduced with permission.

2.1. Abstract

We present a detailed spectroscopic and photometric analysis of DA and DB white dwarfs drawn from the Sloan Digital Sky Survey with trigonometric parallax measurements available from the *Gaia* mission. The temperature and mass scales obtained from fits to *ugriz* photometry appear reasonable for both DA and DB stars, with almost identical mean masses of $\langle M \rangle = 0.617 M_{\odot}$ and $0.620 M_{\odot}$, respectively. The comparison with similar results obtained from spectroscopy reveals several problems with our model spectra for both pure hydrogen and pure helium compositions. In particular, we find that the spectroscopic temperatures of DA stars exceed the photometric values by $\sim 10\%$ above $T_{\text{eff}} \sim 14,000$ K, while for DB white dwarfs, we observe large differences between photometric and spectroscopic masses below $T_{\text{eff}} \sim 16,000$ K. We attribute these discrepancies to the inaccurate treatment of Stark and van der Waals broadening in our model spectra, respectively. Despite these problems, the mean masses derived from spectroscopy — $\langle M \rangle = 0.615 M_{\odot}$ and $0.625 M_{\odot}$ for the DA and DB stars, respectively — agree extremely well with those obtained from photometry. Our analysis also reveals the presence of several unresolved double degenerate binaries, including DA+DA, DB+DB, DA+DB, and even DA+DC systems. We finally take advantage of the *Gaia* parallaxes to test the theoretical mass-radius relation for white dwarfs. We find that 65% of the white dwarfs are consistent within the 1σ confidence level with the predictions of the mass-radius relation, thus providing strong support to the theory of stellar degeneracy.

Key words: stars: fundamental parameters — techniques: photometric – techniques: spectroscopic – white dwarfs

2.2. Introduction

Our understanding of white dwarf stars relies heavily on the determination of their physical parameters, such as effective temperature, surface gravity, luminosity, mass, radius, atmospheric composition, and cooling age. Several independent methods have been developed over the years to measure directly some of these parameters, while others are obtained indirectly through detailed evolutionary models.

The most widely used method, at least until now, to measure the effective temperature (T_{eff}) and the surface gravity ($\log g$) of white dwarfs involves the comparison of the observed and model spectra, known as the spectroscopic technique. First applied to a large sample

of DA stars by Bergeron et al. (1992), this technique has been used repeatedly since then in several other studies (see, e.g., Liebert et al. 2005, Koester et al. 2009a, Koester et al. 2009b, Tremblay et al. 2011a, Gianninas et al. 2011, Genest-Beaulieu & Bergeron 2014). A similar approach has also been applied in the context of DB white dwarfs (Eisenstein et al. 2006a, Voss et al. 2007, Bergeron et al. 2011, Koester & Kepler 2015, Rolland et al. 2018); in this case, the hydrogen abundance is also being measured spectroscopically.

Another method that can be applied to large ensembles of white dwarfs is the photometric technique, where the observed energy distribution, built from magnitudes in various bandpasses, is compared to the predictions from model atmospheres (see, e.g., Bergeron et al., 1997). This method yields the effective temperature and the solid angle $\pi(R/D)^2$ of the star; if the trigonometric parallax (or distance) is known, the radius can be obtained directly. Until recently, trigonometric parallaxes were available for only a few hundreds, mostly cool white dwarfs (Bergeron et al. 2001, Holberg et al. 2012, Tremblay et al. 2017, Bédard et al. 2017). In the absence of trigonometric parallax measurements, one usually assumes a value of $\log g = 8$, in which case the photometric method can be applied to large white dwarf samples, such as those identified in the Sloan Digital Sky Survey (SDSS, Genest-Beaulieu & Bergeron 2014). In some situations, the photometric technique is the only method applicable, for example for cool white dwarfs, which present no absorption features.

With either the spectroscopic or photometric techniques, the mass of the white dwarf can only be obtained from detailed evolutionary models, which provide the required temperature-dependent relation between the mass and the radius, as well as cooling ages. This theoretical mass-radius relation for white dwarfs has recently been tested, but only for relatively small samples (Tremblay et al. 2017, Parsons et al. 2017, Bédard et al. 2017), a situation that is about to change by taking advantage of the recently measured trigonometric parallaxes from *Gaia* (Gaia Collaboration et al., 2018).

One of the most important issue regarding both the spectroscopic and photometric techniques is the precision and accuracy of each method. Statistically speaking, the precision of the method describes random errors, a measure of statistical variability, repeatability, or reproducibility of the measurement, while the accuracy represents the proximity of the measurements to the true value being measured, in our case, the true T_{eff} and $\log g$ (or mass) values. It has been argued repeatedly in the literature that the spectroscopic technique yields

more precise atmospheric parameters than the photometric technique, in general because of the moderate quality of photometric and parallax measurements. However, the exquisite parallax data from *Gaia* and photometric data from SDSS or Pan-STARRS may change this picture drastically in favor of the photometric approach.

Another advantage of the photometric technique is that the synthetic photometry is less sensitive to the input physics included in the model atmospheres. Indeed, the shape and strength of the spectral lines are affected by a number of factors (line broadening, convective energy transport, etc.), which in turn affect the atmospheric parameters measured spectroscopically. One well-known example is the so-called high-log g problem in cool DA white dwarfs, which was explained by an inadequate treatment of convection in standard 1D model atmospheres (Tremblay et al., 2013a).

The question of the precision and accuracy of the spectroscopic and photometric methods using various white dwarf samples and photometric data sets has been discussed at length by Tremblay et al. (2019, see also Gentile Fusillo et al. 2019). Because of the utmost importance of this issue for the white dwarf field, and also because of our different approach to the problem, we present in this paper our own independent assessment of the internal consistency between both fitting techniques by comparing the atmospheric and physical parameters of DA and DB white dwarfs obtained from spectroscopy with those derived from the photometric technique. The white dwarf samples used in this study are presented in Section 2.3, followed by a brief description of our models in Section 2.4. Our photometric and spectroscopic analyses are presented in Sections 2.5 and 2.6, respectively. Section 2.7 is dedicated to the comparison of the atmospheric parameters obtained from photometry and spectroscopy. Using these results, the theoretical mass-radius relation is then put to the test in Section 2.8. We conclude in Section 2.9.

2.3. Sample

The primary goal of this study is to compare the atmospheric parameters of DA and DB white dwarfs obtained from different techniques and data types. Given that the Sloan Digital Sky Survey (SDSS) provides photometry and spectroscopy for over 30,000 white dwarfs, we base our analysis on this particular data set. We started by retrieving all spectroscopic and photometric data for all DA and DB white dwarfs — including all subtypes (DAH,

DB:, DBZ, etc.) — spectroscopically identified in the SDSS, up to the Data Release 12 (Kleinman et al., 2013; Kepler et al., 2015, 2016). This represents a total of 27,217 DA and 2227 DB spectra, with corresponding *ugriz* photometric data sets. We also want to take advantage of the *Gaia* DR2 catalog (Gaia Collaboration et al., 2018), which contains precise trigonometric parallax measurements for a large number of SDSS objects. In order to ensure that the atmospheric parameters we derive are reliable, we need to apply a few criteria to keep only the best SDSS and *Gaia* data sets.

We first removed every object with a spectral type indicating a magnetic object (H), a known companion (+ and/or M), emission lines (E), or an uncertain spectral type (:). For the DA sample, we also removed any spectral type indicating the presence of helium (B or O) or metals (Z). Therefore, our sample contains only the spectral types DA, DB, DBA(Z), and DBZ(A). We then applied a lower limit on the signal-to-noise ratio (S/N) of the SDSS optical spectra. Given the very large number of DA white dwarfs, we chose to keep only those with $S/N \geq 25$. For the DB white dwarfs, which are not as common as DA stars, we chose to set the limit at a lower value of $S/N \geq 10$. The S/N distribution of spectra in our sample is displayed in Figure 2.1. Finally, we kept only the objects with *Gaia* parallax measurements more precise than 10% ($\sigma_\pi/\pi \leq 0.1$).

After applying all these criteria, we are left with 2236 and 461 individual spectra and corresponding *ugriz* data sets for DA and DB white dwarfs, respectively. Since the calibration algorithm has changed between DR7 and DR8, and that the *ugriz* zeropoints have been recalibrated in DR13¹, we use the *ugriz* magnitudes from the SDSS DR14 instead of the values given in the aforementioned catalogs.

Figure 2.2 presents the distribution of the white dwarfs in our sample as a function of distance and spectral type. We note that most of the objects in our sample are located at large distances where interstellar reddening becomes important ($D \gtrsim 100$ pc). This will be discussed in section 2.5.1.

2.4. Theoretical Framework

Since our sample contains both DA and DB white dwarfs, we require two different grids of model atmospheres and synthetic spectra.

1. <https://www.sdss.org/dr14/algorithms/fluxcal/>

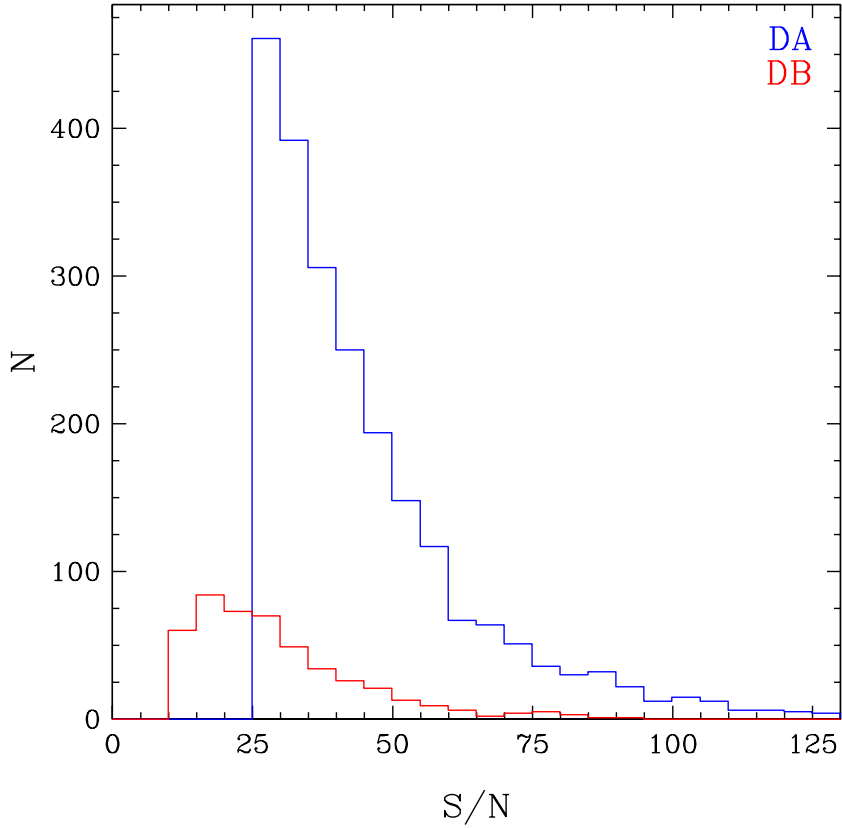


Figure 2.1. Distribution of signal-to-noise ratios of the DA (blue) and DB (red) white dwarfs in our sample.

2.4.1. DA Model Atmospheres

Our pure hydrogen grid for the DA stars is calculated with two different codes. For $T_{\text{eff}} < 30,000$ K, we use the LTE version described at length in Tremblay & Bergeron (2009). Convective energy transport, which becomes important below $T_{\text{eff}} \sim 15,000$ K, is treated with the ML2/ $\alpha = 0.7$ version of the mixing-length theory (MLT). The adopted parameterization of the MLT is important, particularly for cool DA white dwarfs, and it affects mostly the atmospheric parameters determined from spectroscopic data (see section 2.6.3). Above 30,000 K, NLTE effects are taken into account using TLUSTY (Hubeny & Lanz, 1995). Combining both grids, we obtain model spectra ranging from $T_{\text{eff}} = 1500$ K up to 120,000 K, with surface gravities between $\log g = 6.5$ and 9.0. Note that both model grids rely on the improved Stark profiles of Tremblay & Bergeron (2009).

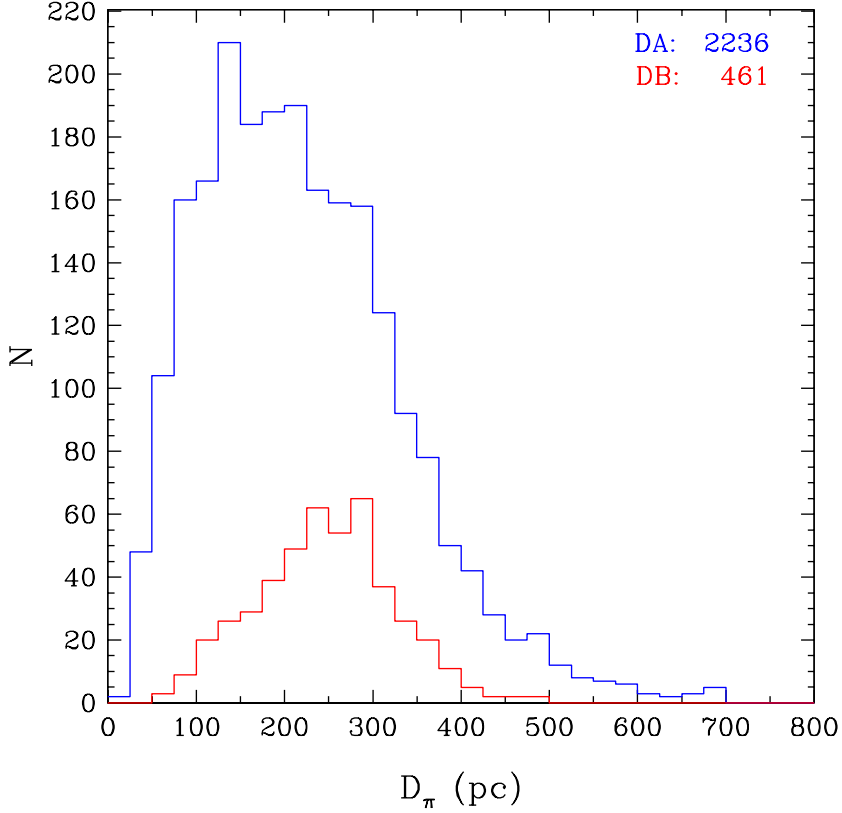


Figure 2.2. Distribution of parallactic distances for the DA (blue) and DB (red) white dwarfs in our sample.

2.4.2. DB/DBA Model Atmospheres

Our DB/DBA model grid is similar to that described in Bergeron et al. (2011) (but see section 2.6.2). These models are in LTE and calculated using the $ML2/\alpha = 1.25$ parameterization of the MLT. Our grid covers effective temperatures between 11,000 K and 50,000 K, surface gravities ranging from $\log g = 7.0$ to 9.0, and hydrogen abundances from $\log N(H)/N(He) = -6.5$ to -2.0 , and an additional pure helium grid.

Below $T_{\text{eff}} \sim 16,000$ K, He I line broadening by neutral particles becomes important. We can divide this into two parts: van der Waals and resonance broadening. In our models, these two broadening mechanisms are combined following the procedure described in detail by Beauchamp (1995), which we summarize here. Resonance broadening is treated according to the theory of Ali & Griem (1965), while van der Waals broadening requires a more elaborate approach. The width of the Lorentzian profile (ω_{vdW}) is calculated twice, once with the

theory described in Unsold (1955), and the second time by following the approach discussed in Deridder & van Rensbergen (1976). The Deridder & van Rensbergen theory systematically predicts a larger profile if the initial and final effective quantum numbers of the transition are higher than 2 or 3. Since they used the Smirnov potential, which becomes invalid below these numbers, we keep the following conservative value for the width of the Lorentzian profile:

$$\omega_{\text{vdW}} = \max(\omega_{\text{Unsold}}, \omega_{\text{Deridder}}) . \quad (2.1)$$

It was also found empirically by Beauchamp (1995) that the neutral helium lines of cool DB stars at $\lambda = 4121 \text{ \AA}$ and 4713 \AA could be better reproduced if they were strictly treated within the Unsold (1955) theory, which is the procedure we adopt here as well.

Finally, Lewis (1967) found that the combination of the resonance and van der Waals broadening led to a profile with $\omega_{\text{neutral}} \sim 0.6 - 0.8 (\omega_{\text{resonance}} + \omega_{\text{vdW}})$. However, that study was only valid for temperatures around 100 K, hardly applicable to our DB models. Therefore, the conservative value of

$$\omega_{\text{neutral}} = \max(\omega_{\text{resonance}}, \omega_{\text{vdW}}) \quad (2.2)$$

is adopted instead. For simplicity, we will refer to the above procedure as the Deridder & van Rensbergen theory.

Note that more recent self-broadening calculations of helium lines have been performed by Leo et al. (1995), but their results are only available at temperatures of $T = 80 \text{ K}$ and 300 K , hardly applicable in the context of our DB models, as before.

2.5. Photometric Analysis

The first step in our analysis is to measure the atmospheric and physical parameters derived from photometry. Before presenting the results, we first describe the technique used to determine these parameters, and we also explore the effects of the presence of atmospheric hydrogen on the photometric solutions of DB white dwarfs.

2.5.1. Photometric Technique

The photometric technique relies on the energy distribution to measure the effective temperature and stellar radius. We use here the method described at length in Bergeron et al. (1997), which is the same for both DA and DB stars. Since we are using the SDSS *ugriz* photometry, we first need to apply the corrections to the u , i , and z bands to account for the transformation from the SDSS to the AB magnitude system. These corrections, given in Eisenstein et al. (2006a), are

$$\begin{aligned} u &= u_{\text{SDSS}} - 0.040 \\ i &= i_{\text{SDSS}} + 0.015 \\ z &= z_{\text{SDSS}} + 0.030 \end{aligned} \tag{2.3}$$

For completeness, we repeated the experiment displayed in Figure 8 of Genest-Beaulieu & Bergeron (2014) where observed magnitudes are compared with those predicted by the photometric technique, and we found that the above constants are still appropriate, and lead to a better agreement between both sets of magnitudes.

One important aspect to consider while dealing with photometric observations is interstellar reddening, which becomes important for $D \gtrsim 100$ pc. As can be seen from Figure 2.2, the majority of our objects are located beyond 100 pc, implying that interstellar extinction cannot be neglected in our analysis. The procedure used here is based on the approach described by Harris et al. (2006), where the extinction is assumed to be negligible for stars with distances less than 100 pc, to be maximum for those located at $|z| > 250$ pc from the galactic plane, and to vary linearly along the line of sight between these two regimes. We also explore in Section 2.7.1 an alternative procedure proposed by Gentile Fusillo et al. (2019). Since the trigonometric parallax is known for every object in our sample, magnitudes can be dereddened directly. This procedure is accomplished using the $E(B - V)$ values from Schlafly & Finkbeiner (2011).

Every dereddened magnitude m_ν is then converted into an average flux f_ν^m using the relation

$$m_\nu = -2.5 \log f_\nu^m - 48.60 \tag{2.4}$$

where

$$f_\nu^m = \frac{\int f_\nu S_m(\nu) d\log \nu}{\int S_m(\nu) d\log \nu} , \quad (2.5)$$

and where f_ν is the monochromatic flux from the star received at Earth, and $S_m(\nu)$ is the total system response, including atmospheric transmission and mirror reflectance.

The same conversion is performed using our synthetic spectra. We obtain the average synthetic fluxes, H_ν^m , by substituting f_ν in equation 2.5 with the monochromatic Eddington flux H_ν . The average observed and model fluxes are related through the equation

$$f_\nu^m = 4\pi (R/D)^2 H_\nu^m \quad (2.6)$$

where R is the radius of the white dwarf, and D its distance from Earth. We then proceed to minimize the χ^2 value, which is defined in terms of the difference between observed and model fluxes over all bandpasses, properly weighted by the photometric uncertainties. Our minimization procedure relies on the non-linear least-squares method of Levenberg-Marquardt, described in Press et al. (1992), which is based on a steepest descent method. This first step is done by assuming a surface gravity of $\log g = 8.0$. This yields an estimate of the effective temperature, T_{eff} , and the solid angle, $\pi (R/D)^2$ — or the radius R of the star since D is known from the trigonometric parallax. Evolutionary models are then used to obtain the stellar mass M , and a new estimate of the surface gravity, which will be different from our initial assumption of $\log g = 8.0$. The entire fitting procedure is then repeated until all parameters are consistent. The uncertainties associated with the fitted parameters are obtained directly from the covariance matrix of the Levenberg-Marquardt minimization procedure (see Press et al. 1992). Here we rely on C/O-core envelope models² similar to those described in Fontaine et al. (2001) with thick hydrogen layers of $q(H) \equiv M_H/M_\star = 10^{-4}$ for DA stars, and much thinner hydrogen layers of only $q(H) = 10^{-10}$ for DB stars, given that such thin layers are representative of helium-atmosphere white dwarfs. Finally, depending on the spectral type, we use either pure hydrogen, pure helium, or mixed H/He model atmospheres (see section 2.5.2). Examples of the photometric technique for both a DA and a DBA white dwarf are illustrated in Figure 2.3.

2. See <http://www.astro.umontreal.ca/~bergeron/CoolingModels>.

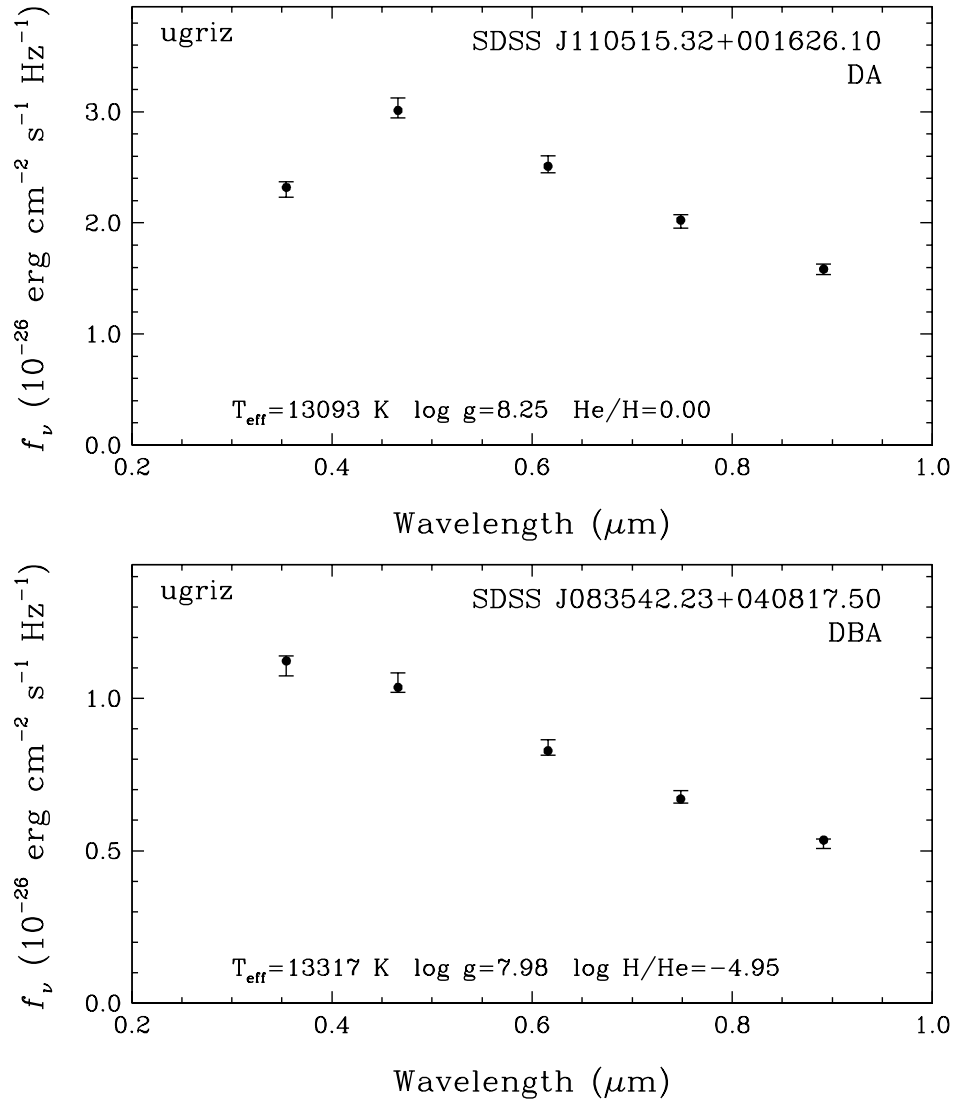


Figure 2.3. Examples of the photometric technique for the DA white dwarf SDSS J110515.32+001626.10 (top) and the DBA SDSS J083542.23+040817.50 (bottom). The error bars represent the observed data, while the best-fit model is shown by the filled circles. The resulting atmospheric parameters are given in each panel.

The precision of the photometric technique is limited by the sensitivity of the photometric measurements (here SDSS *ugriz*) to variations in effective temperature. At high T_{eff} values, the energy distribution sampled by the *ugriz* photometry is in the Rayleigh-Jeans regime. This is illustrated in Figure 2.4 where we show magnitude differences (i.e., color indices) with respect to the g magnitude for all SDSS bandpasses, as a function of effective temperature and atmospheric composition. In the case of pure hydrogen atmospheres, the energy distribution

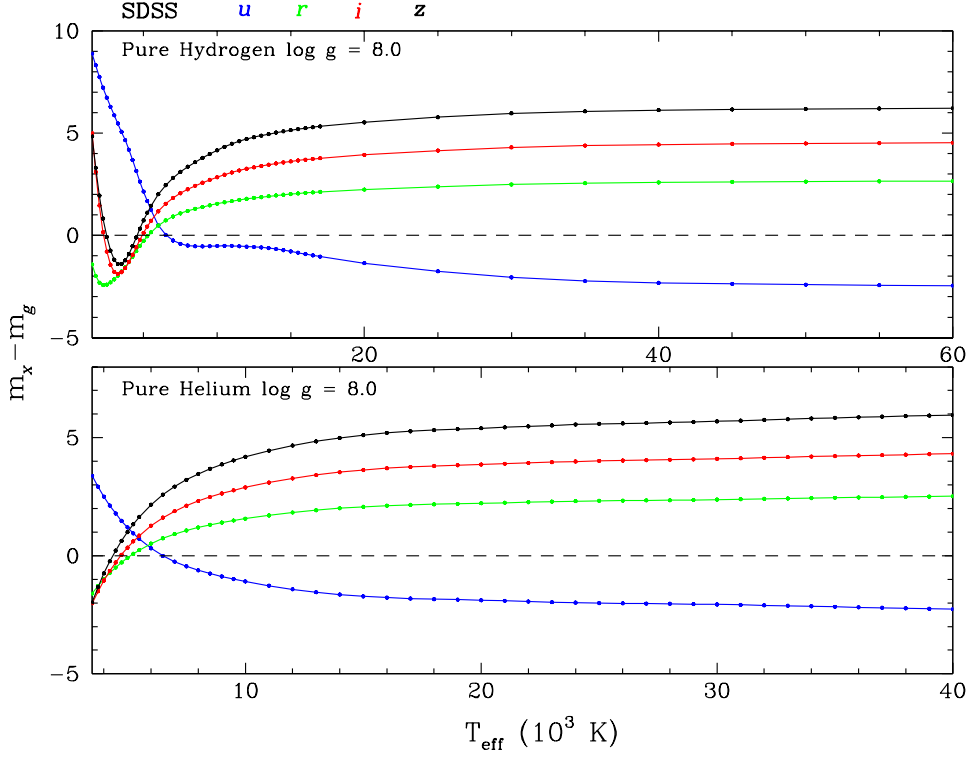


Figure 2.4. Magnitude differences between the SDSS u (blue), r (green), i (red), and z (black) bands and the SDSS g band, as a function of effective temperature, for pure hydrogen (top) and pure helium (bottom) models at $\log g = 8.0$ (note the difference in temperature scales). The dots correspond to individual model values.

varies considerably up to $T_{\text{eff}} \sim 35,000$ K, and very little above this temperature. This means that the photometric technique becomes less reliable above 35,000 K for DA white dwarfs. The situation is similar in the case of DB stars. For DA stars, the Balmer jump affects the $u - g$ color index significantly, which can be observed here as the flat plateau between ~ 8000 K and 15,000 K. Also of interest is the behavior below ~ 5000 K where collision-induced absorption by molecular hydrogen becomes important. These two features are of course not observed in pure helium atmospheres.

2.5.2. Effect of the Presence of Hydrogen on the Photometric Solutions

When using the photometric technique, one usually assumes either pure hydrogen or pure helium atmospheres to determine the stellar parameters. However, most DB stars contain a certain amount of hydrogen (Koester & Kepler, 2015; Rolland et al., 2018). We show in

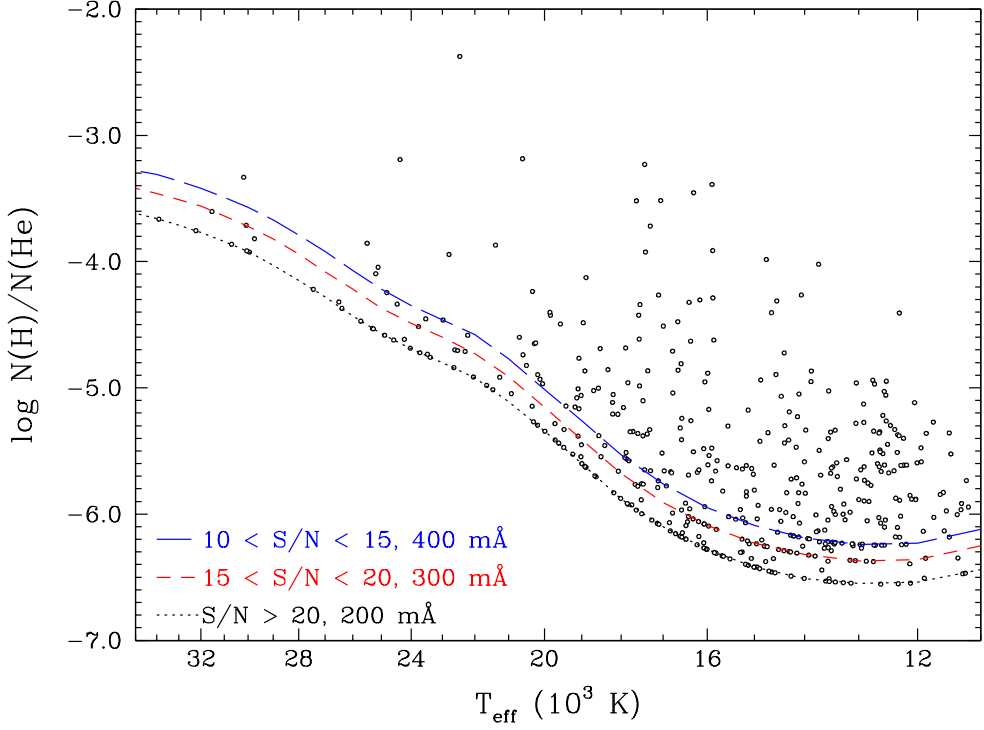


Figure 2.5. Spectroscopic hydrogen abundance as a function of effective temperature for the DB and DBA stars in our sample. Also shown are the H α detection limits for S/N > 20, 15 < S/N < 20, and 10 < S/N < 15, corresponding to equivalent widths (FWHM) of 200 mÅ (black, dotted line), 300 mÅ (red, short-dashed line), and 400 mÅ (blue, long-dashed line), respectively.

Figure 2.5 shows the hydrogen abundance (or upper limits) as a function of effective temperature for all the DB and DBA stars in our sample. In some cases the hydrogen abundance can be as large as $\log N(\text{H})/\text{N}(\text{He}) \sim -3$. Since the presence of additional free electrons in helium-rich atmospheres may affect significantly the photometric solutions — see, e.g., Figure 8 of Dufour et al. (2005) in the context of DQ white dwarfs —, we explore here the effect of the hydrogen abundance on the atmospheric parameters obtained for DBA stars using the photometric technique.

To do so, we use the same procedure as before, but instead of using pure helium models, we force the hydrogen abundance to the spectroscopic value. The effects on the effective temperature and stellar mass are displayed in Figure 2.6. The top panel shows that by using pure helium models, we tend to overestimate the effective temperature, but not significantly.

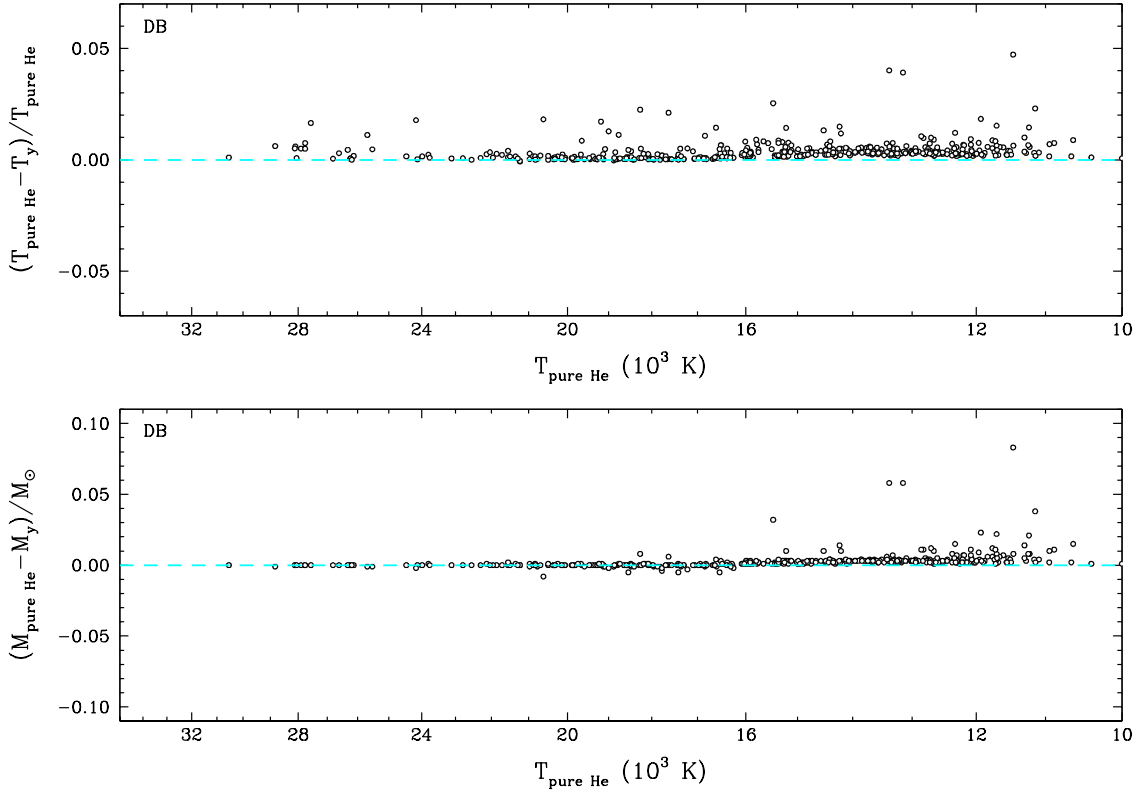


Figure 2.6. Top panel: Effect of the hydrogen abundance on the effective temperature determined photometrically, as a function of T_{eff} . $T_{\text{pure He}}$ is the effective temperature obtained from pure helium models, while T_y is that obtained by forcing the hydrogen abundance to the spectroscopic value. The dashed line corresponds to $T_{\text{pure He}} = T_y$. Bottom panel: Same as top panel, but for stellar masses. The cyan dashed line corresponds to $M_{\text{pure He}} = M_y$.

For most objects, the difference in temperature is less than 1% to 2%, which is smaller than the uncertainty associated with the photometric technique. The objects for which the difference in temperature is the largest, between ~ 2.5 and 5%, are all found below $T_{\text{eff}} \sim 14,000$ K, and these correspond to the few DBA stars in this temperature range with the largest hydrogen abundances around $\log N(\text{H})/N(\text{He}) \sim -4.0$.

The bottom panel of Figure 2.6 shows the effect on the mass determinations. Above $T_{\text{eff}} \sim 16,000$ K, the effect is completely negligible. Below this temperature, the masses obtained under the assumption of a pure helium atmosphere are slightly overestimated, by about $0.01 M_\odot$ for the bulk of our sample, but these differences can be as large as 0.05 to $0.1 M_\odot$ in some cases. These correspond also to the objects that show the largest temperature

differences in the upper panel. Since the luminosity $L \propto R^2 T_{\text{eff}}^4$, a lower temperature implies a larger radius, or a smaller mass (see also Figure 8 of Dufour et al., 2005).

Overall, we conclude that the use of mixed composition atmospheres for measuring the photometric mass and effective temperature of DBA white dwarfs yields values very similar to those obtained under the assumption of pure helium compositions. Nevertheless, to be fully consistent, we adopt in what follows the spectroscopic hydrogen abundance to measure the stellar parameters using the photometric technique.

2.5.3. Photometric Results

Using the photometric technique described in Section 2.5.1, we determined the effective temperature and stellar mass of every object in our sample. As mentioned in the previous section, for the DB/DBA stars, the hydrogen abundance (or limit) was forced to its spectroscopic value. The resulting mass distributions for the DA and DB stars in our sample are displayed as a function of effective temperature in the top panels of Figures 2.7 and 2.8, respectively.

Below $T_{\text{eff}} \sim 45,000$ K, the mass distribution for the DA white dwarfs appears well-centered around $0.6 M_{\odot}$, regardless of the effective temperature. This is expected since it is believed that white dwarfs cool with a constant mass. Above this temperature, however, the DA stars in our sample appear to have larger than average masses, around $\sim 0.7 M_{\odot}$. This is probably due to the limitations of the photometric technique using *ugriz* data in this temperature range (see Figure 2.4). The distribution of objects in the upper panel of Figure 2.7 also appears uniform as a function of T_{eff} , i.e., there are no gaps in the temperature distribution, except perhaps around 12,000 K where there seems to be a slight depletion of objects. This might be caused by selection effects in the SDSS, or it could also be due to spectral evolution mechanisms, such as the transformation of DA into non-DA white dwarfs resulting from convective mixing in this temperature range. But such considerations are outside the scope of this paper.

We can also identify a significant number of DA stars with very low photometric masses ($M \lesssim 0.45 M_{\odot}$). These objects are most likely unresolved double degenerate binaries. In these cases, the object appears overluminous because of the presence of two stars in the system, and the radius determined photometrically is thus overestimated. Because of the

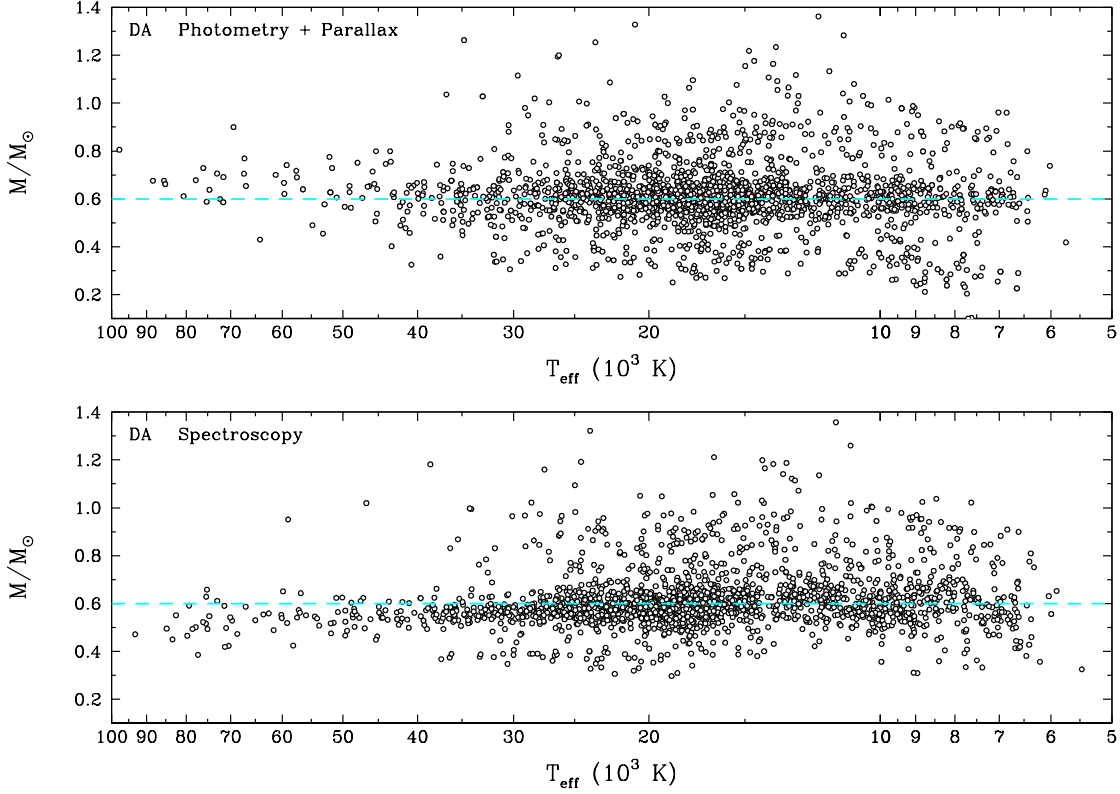


Figure 2.7. Stellar mass as a function of effective temperature obtained from photometry (top) and spectroscopy (bottom), for the DA white dwarfs in our sample. The dashed cyan line represents a constant mass of $0.6 M_{\odot}$.

mass-radius relation, the stellar mass inferred from this radius is underestimated. These objects will be discussed further in Sections 2.7.2 and 2.8. Finally, the mass distribution also reveals the existence of high-mass white dwarfs ($M \gtrsim 0.8 M_{\odot}$). These high-mass DA stars are usually thought to be the end result of stellar mergers (Iben, 1990; Kilic et al., 2018), or alternatively, they can also be explained as a result of the initial-to-final mass relation (El-Badry et al., 2018).

As for the DA white dwarfs, the mass distribution for the DB stars (top panel of Figure 2.8) shows a rather uniform distribution as a function of T_{eff} , with no obvious gaps. Unlike for the DA mass distribution, however, which was centered around $\sim 0.6 M_{\odot}$ regardless of T_{eff} , the mean mass for DB stars appears well-centered around $0.6 M_{\odot}$ for $T_{\text{eff}} \lesssim 16,000$ K, but systematically above this value at higher temperatures. Also, the most striking feature in the photometric mass distribution is that there is no significant increase in mass below

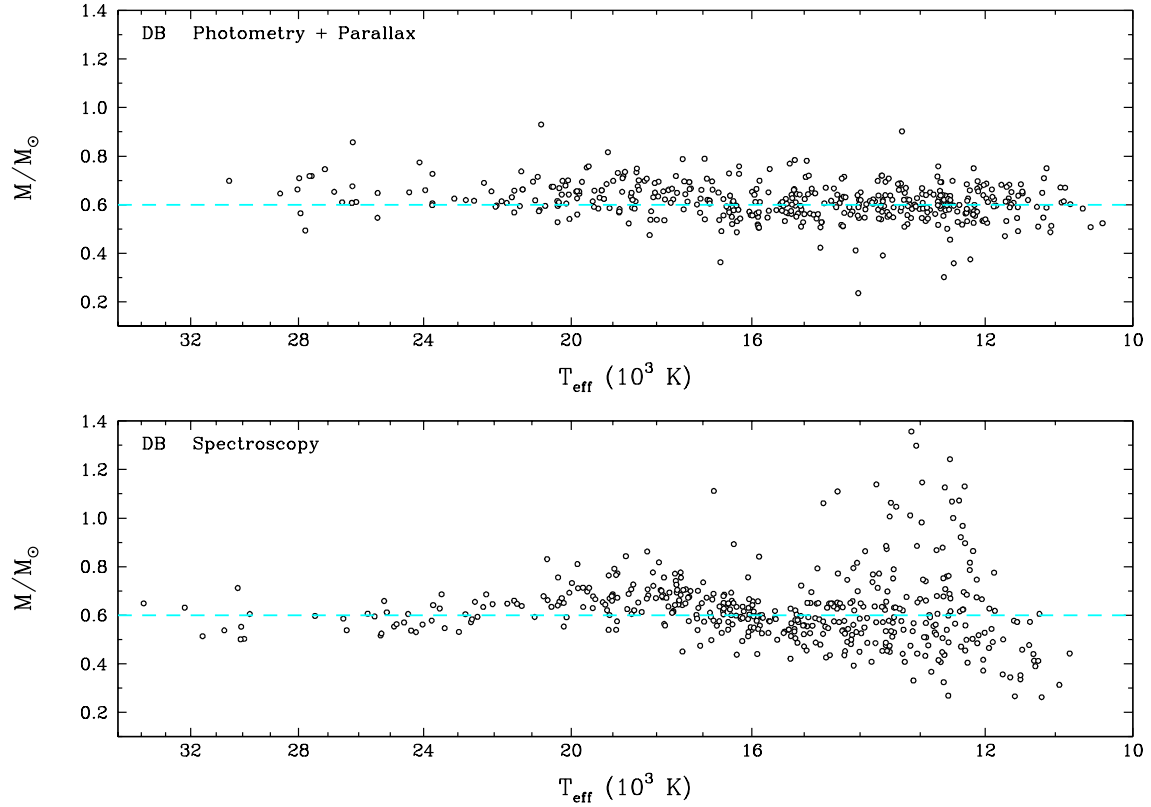


Figure 2.8. Same as Figure 2.7, but for the DB white dwarfs in our sample.

$T_{\text{eff}} \sim 16,000$ K, in sharp contrast with the spectroscopic mass distributions reported for instance by Bergeron et al. (2011) and Koester & Kepler (2015). We come back to these points further in Sections 2.6.2 and 2.7.2.

We also note the presence of a few low-mass DB white dwarfs ($M \lesssim 0.45 M_{\odot}$). Again, these are most likely unresolved double degenerate candidates, which will be discussed in more detail in Sections 2.7.2 and 2.8.

2.6. Spectroscopic Analysis

2.6.1. Spectroscopic Technique

The most widely used technique to measure the atmospheric parameters — T_{eff} , $\log g$, and atmospheric composition — of white dwarf stars is the so-called spectroscopic technique, which relies on normalized spectral line profiles. Unlike the photometric technique, which is the same regardless of the atmospheric composition, the spectroscopic technique

differs slightly depending on the spectral type of the object. We describe in turn the fitting procedures used for both DA and DB stars in our SDSS sample.

2.6.1.1. DA White Dwarfs

For DA white dwarfs, we use a technique similar to that described in Bergeron et al. (1992), Bergeron et al. (1995b), and Liebert et al. (2005). The first step is to normalize the hydrogen lines, from $H\beta$ to $H8$, for both the observed and synthetic spectra, convolved with the appropriate Gaussian instrumental profile (3 Å FHWM in the case of the SDSS spectra). The comparison is then carried out in terms of these normalized line profiles only. In order to properly define the continuum on each side of the line, we use two different procedures depending on the temperature range. For $16,000 \text{ K} < T_{\text{eff}} < 9000 \text{ K}$, we fit the entire spectrum using a sum of pseudo-Gaussian profiles, as they reproduce quite well the spectral line profiles in this temperature range, an example of which is shown in the top right panel of Figure 2.9. Outside of this temperature range, we rely on our synthetic spectra to reproduce the observed spectrum, including a wavelength shift, as well as several order terms in λ (up to λ^6), to obtain a smooth fitting function. This is achieved using the Levenberg-Marquardt method described above. Since the hydrogen lines reach their maximum strength around $T_{\text{eff}} = 14,000 \text{ K}$, both the cool and hot solutions are tested and the one with the lowest χ^2 is kept. The resulting best fit is then used to normalize the line profiles to a continuum set to unity, although the atmospheric parameters obtained at this point are meaningless because of the high number of fitting parameters used in the normalization procedure. However, these T_{eff} and $\log g$ estimates can be used as a starting point for the full χ^2 minimization procedure since they are usually quite close to the physical solution. This also helps us to determine on which side of the maximum line strength our object is located. In principle, the photometric temperature could also be used to distinguish between the cool and hot solutions, but we want our spectroscopic fitting procedure to be as independent as possible from the photometric approach.

Once the lines are properly normalized, the effective temperature and surface gravity are determined using the Levenberg-Marquardt procedure. Finally, the 3D corrections from Tremblay et al. (2013a) are applied to both T_{eff} and $\log g$. A full example of the fitting procedure for DA white dwarfs is presented in Figure 2.9.

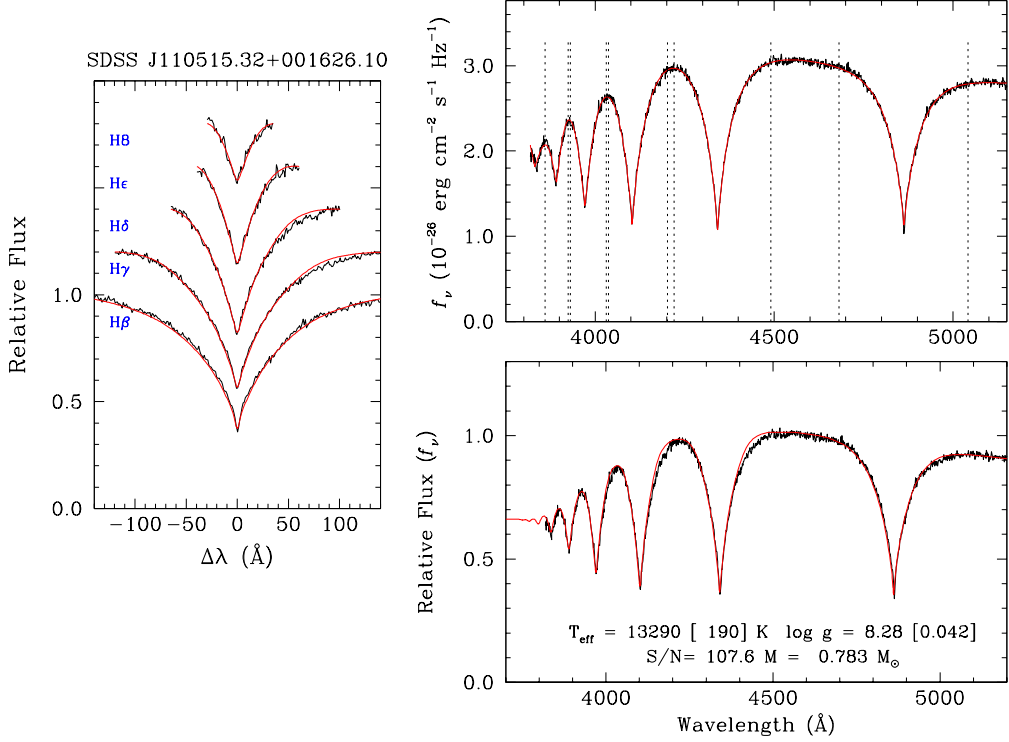


Figure 2.9. Example of the spectroscopic technique for the DA white dwarf SDSS J110515.32+001626.10. Top right panel: The smooth fitting function (red) used to define the continuum is plotted over the observed spectrum (black). Left panel: Best model fit (red) to the observed (normalized) hydrogen line profiles (black). Bottom right panel: Final solution (red) superposed on the observed spectrum (black), both normalized at 4600 Å. The derived stellar parameters are also given in the figure.

The uncertainties associated with spectroscopic T_{eff} and $\log g$ values were estimated by Liebert et al. (2005) for the DA stars in the Palomar-Green survey. Multiple measurements of the same stars were used to determine that the overall errors are 1.4% in T_{eff} and 0.042 dex in $\log g$. Note that these values were obtained using a spectroscopic sample with $S/N > 50$. In our SDSS sample, however, most of our DA spectra have $S/N \lesssim 50$ (see Figure 2.1), with very few objects at higher values. Nevertheless, we will assume here the same uncertainties as those of Liebert et al., but we keep in mind that these are most likely underestimated.

2.6.1.2. DB/DBA White Dwarfs

The spectroscopic technique used for the DB/DBA white dwarfs differs slightly from that used for DA stars since there is a third parameter to measure: the hydrogen abundance. We

use a technique similar to that described in Bergeron et al. (2011). The normalization procedure for the DB spectra relies on our synthetic spectra to obtain a smooth fitting function used to determine the continuum, as described above for the DA stars. Again, we find a solution on each side of the maximum line strength, which occurs near 25,000 K for DB white dwarfs, and the solution with the smallest χ^2 is used to define the continuum. As before, this normalization procedure uses too many fitting parameters for the values of T_{eff} , $\log g$, and $\log N(\text{H})/N(\text{He})$ to be meaningful.

Once the observed spectrum is normalized, the first step is to obtain an estimate of the effective temperature and surface gravity, using the blue part of the spectrum ($\lambda = 3750 - 5150 \text{ \AA}$). Keeping those parameters fixed, the hydrogen abundance is obtained by fitting the region near $\text{H}\alpha$ ($\lambda = 6400 - 6800 \text{ \AA}$). For some stars, this part of the spectrum is problematic, so the hydrogen abundance is determined using $\text{H}\beta$ instead. The entire procedure is then repeated in an iterative fashion, until the value of $N(\text{H})/N(\text{He})$ has converged. In several cases, only upper limits on the hydrogen abundance could be obtained based on the absence of $\text{H}\alpha$ within the detection limit (see Figure 2.5). An example of the fitting procedure for a typical DBA white dwarf is shown in Figure 2.10.

Bergeron et al. (2011) determined, in the same manner as Liebert et al. (2005), that the overall error on the effective temperature and surface gravity were 2.3% and 0.052 dex, respectively. Although we will be using those estimates, it should be noted that they determined those values with much higher signal-to-noise spectra than what is use in the present study ($S/N \gtrsim 50$ in Bergeron et al. 2011 vs $S/N > 10$ here, see Figure 2.1). Therefore, our uncertainties are most likely underestimated.

Cukanovaite et al. (2018) calculated a series of 3D hydrodynamical white dwarf atmosphere models with pure helium compositions, similar to those for DA stars by Tremblay et al. (2013a). They also published 3D corrections to be applied to 1D spectroscopic solutions, which are found to be important in the range $T_{\text{eff}} \sim 17,000 \text{ K} - 20,000 \text{ K}$. However, since it is expected that the presence of hydrogen will affect these corrections, and that such calculations are currently underway, we refrain from applying any correction to our spectroscopic solutions at this stage. We will keep this in mind, however, when we compare the photometric and spectroscopic results in Section 2.7. Note that these more realistic 3D

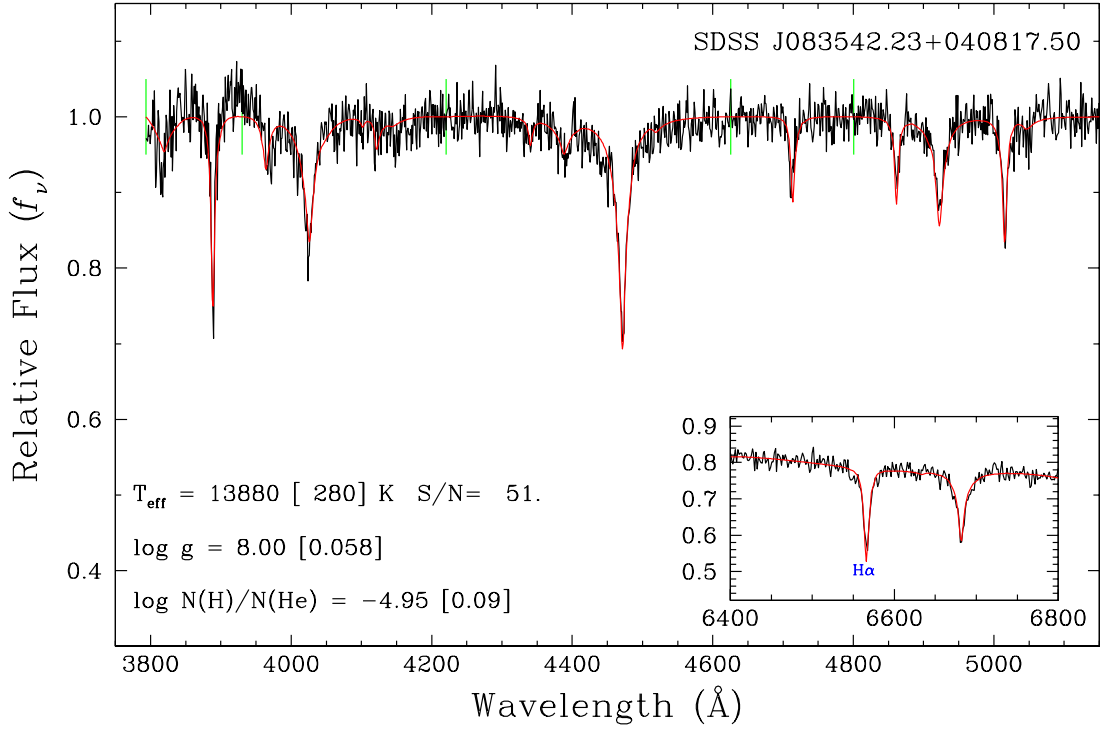


Figure 2.10. Example of the spectroscopic technique for the DBA white dwarf SDSS J083542.23+040817.50. The best fit (red) is plotted over the normalized observed spectrum (black). The inset shows the region near H α used to determine the hydrogen abundance, or upper limits. The derived atmospheric parameters are also given in the figure.

hydrodynamical models should not affect in any way the photometric analyses presented above for both DA and DB white dwarfs.

2.6.2. van der Waals Broadening in DB White Dwarfs

A well-known problem in the case of DB white dwarfs is the apparent increase in $\log g$, or mass, at low effective temperatures ($T_{\text{eff}} \lesssim 15,000$ K). This phenomenon has been reported repeatedly, for instance, in Beauchamp et al. (1996), Bergeron et al. (2011), and Koester & Kepler (2015). The photometric mass distribution displayed in the top panel of Figure 2.8 reveals that this increase in mass occurs only when the atmospheric parameters are determined using the spectroscopic technique, a conclusion also reached by Tremblay et al. (2019). A similar phenomenon was also observed in the $\log g$ distribution of cool DA stars — the so-called high- $\log g$ problem — but in this case, Tremblay et al. (2013a) showed that

the problem lies in the use of the mixing-length theory to treat convective energy transport, and that more realistic 3D hydrodynamical calculations could solve this high-log g problem.

The high-log g values inferred for cool DB white dwarfs most likely have a different origin, however, since in the temperature regime where the problem is observed, convection is almost completely adiabatic (Cukanovaite et al., 2018). Instead, it has been generally argued that van der Waals broadening was the source of the problem (Bergeron et al. 2011 and references therein). In their paper, Bergeron et al. (2011, see also Rolland et al. 2018) erroneously mention that they used the Deridder & van Rensbergen theory to treat van der Waals broadening, as defined in Section 2.4.2, while they were in fact relying on the more simple theory of Unsold (1955)³. To clarify this situation, we fitted all the DB stars in our SDSS sample using both the Unsold and the Deridder & van Rensbergen theories, the results of which are displayed in Figure 2.11.

Our results using the Unsold theory can be compared directly with those shown, for instance, in Figure 6 of Rolland et al. (2018). Although the sample analyzed by Rolland et al. is significantly smaller than our SDSS sample, both distributions are qualitatively similar. In particular, they both show a large increase in mass below $T_{\text{eff}} \sim 15,000$ K. By using instead the Deridder & van Rensbergen theory (bottom panel of Figure 2.11), we still find white dwarfs with large masses ($M \sim 1.2 - 1.3 M_{\odot}$) at low temperatures, but more importantly, the mass of the bulk of our sample has been reduced from a value above $0.6 M_{\odot}$ to a value significantly below this mark. Furthermore, the mass distribution now contains several objects with low masses ($M \lesssim 0.45 M_{\odot}$). Finally, the scatter at low temperatures remains large with both theories. Note that the stellar masses are relatively unaffected above $\sim 16,000$ K, where Stark broadening dominates.

The results displayed in Figure 2.11 indicate that the theory of van der Waals broadening still requires significant improvement before any meaningful spectroscopic analysis of cool DB/DBA white dwarfs can be achieved. For instance, our particular choice (see Section 2.4.2) — based on the results of Lewis (1967) — to use $\omega_{\text{neutral}} = \max(\omega_{\text{resonance}}, \omega_{\text{vdW}})$ instead of the sum of the two contributions, might not be appropriate. Mullamphy et al. (1991) indeed found that a simple sum, $\omega_{\text{neutral}} = \omega_{\text{resonance}} + \omega_{\text{vdW}}$, provided a better agreement between

3. In this case, the Unsold theory was used for every line, but the total width was still $\omega_{\text{neutral}} = \max(\omega_{\text{resonance}}, \omega_{\text{vdW}})$.

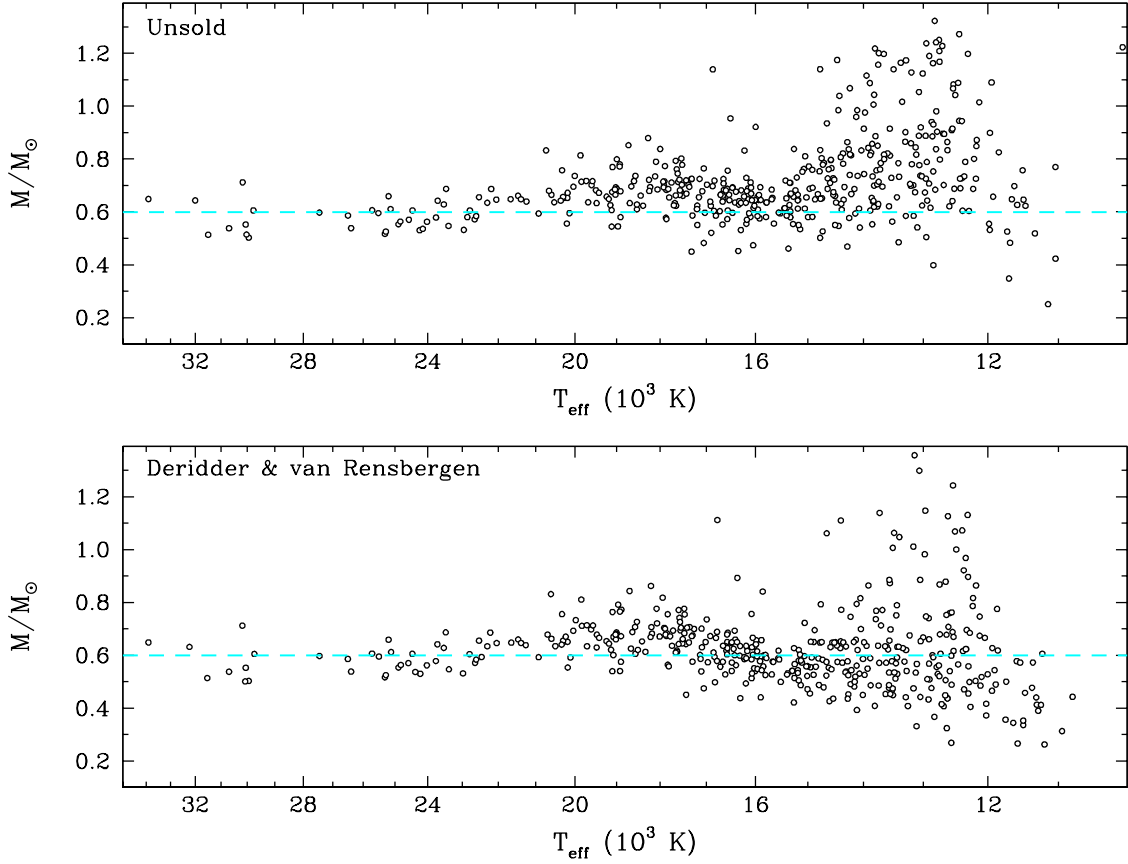


Figure 2.11. Spectroscopic mass distribution as a function of effective temperature for the DB white dwarfs in the SDSS sample, using the van der Waals broadening theory of Unsold (1955, top) and Deridder & van Rensbergen (bottom; as defined in Section 2.4.2). The dashed line in both panels corresponds to a constant mass of $0.6 M_{\odot}$.

theory and experiment. However, the inadequacy in the treatment of He I line broadening by neutral particles is outside the scope of this paper, and further improvements will be explored elsewhere. For the lack of a better theory for van der Waals broadening, we use in the remainder of our analysis the Deridder & van Rensbergen theory, as defined in Section 2.4.2.

For completeness, we show in Figure 2.12 the differences in effective temperature, mass, and hydrogen abundance obtained from models using the Deridder & van Rensbergen and Unsold theories, but only for the objects in our sample with $T_{\text{eff}} < 17,000$ K. The maximum differences occur near $T_{\text{eff}} \sim 13,000$ K, and are of the order of 2.5% in temperature, $0.2 M_{\odot}$ in mass, but only 0.2 dex in $\log N(\text{H})/N(\text{He})$.

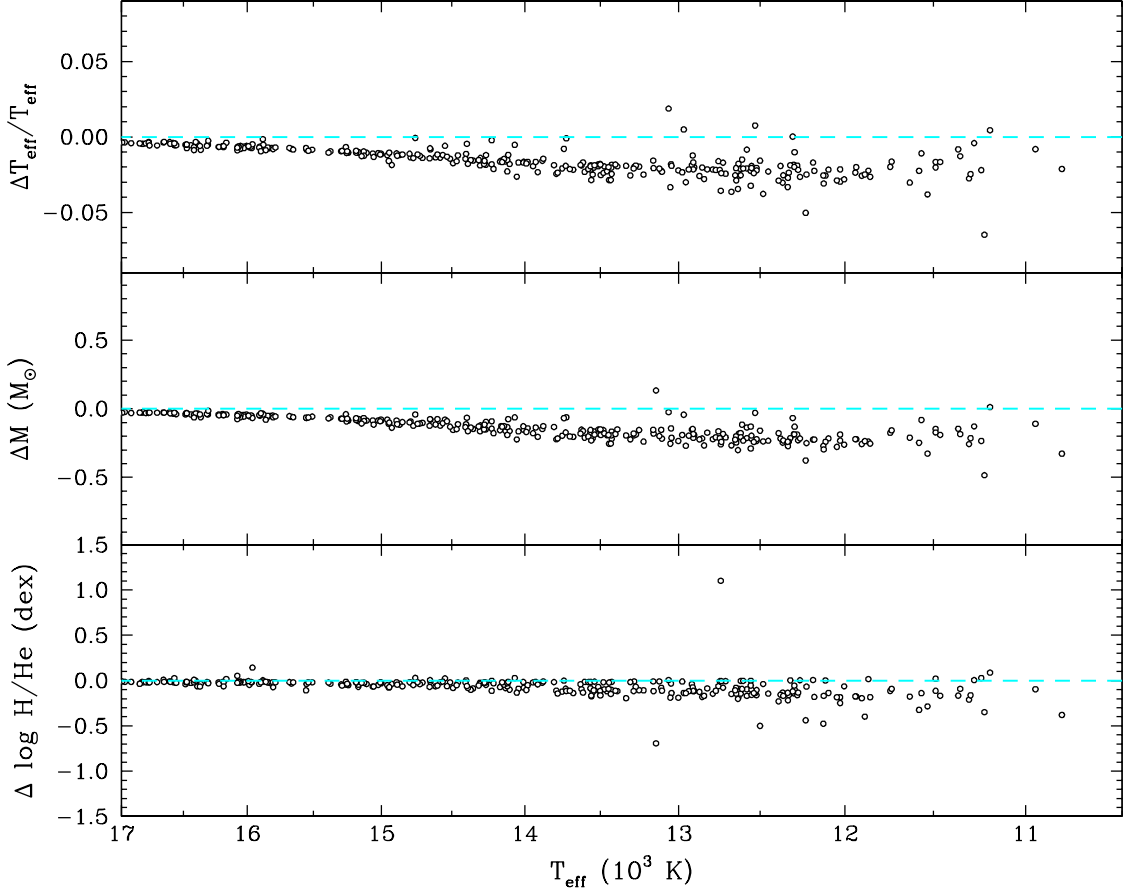


Figure 2.12. Differences in effective temperature, mass, and hydrogen abundances as a function of T_{eff} obtained between models using the van der Waals broadening theory of Deridder & van Rensbergen (as defined in Section 2.4.2) and the Unsold (1955) theory.

2.6.3. Spectroscopic Results

Using the spectroscopic techniques described in section 2.6.1, we measured the atmospheric parameters of all the DA and DB stars in our SDSS sample. Stellar masses were then obtained by converting the spectroscopic $\log g$ values into mass using the same evolutionary models as those described in Section 2.5.1. We discuss these results in turn.

The spectroscopic mass distribution for the DA white dwarfs is shown as a function of effective temperature in the bottom panel of Figure 2.7, which can be contrasted with the photometric distribution in the upper panel. Both distributions reveal several high-mass white dwarfs ($M \gtrsim 0.8 M_{\odot}$), which, as mentioned above, are believed to be the product of stellar mergers, or alternatively, the result of the initial-to-final mass relation. We also

note the presence of low-mass white dwarfs ($M \lesssim 0.4 M_{\odot}$) in both distributions, most likely unresolved double degenerate binaries (see Section 2.7.2).

The spectroscopic mass distribution of DA stars shows a rather uniform distribution as a function of T_{eff} , with the exception of an obvious gap near 14,000 K. Similar but less obvious gaps were mentioned in the photometric mass distribution as well (see Section 2.5.3), but these occur at different temperatures and are probably unrelated. The gap observed in the spectroscopic mass distribution of DA stars actually corresponds to the temperature where hydrogen lines reach their maximum strength. If our models predict lines that are stronger than what is actually observed, the spectroscopic technique will push the stars away from the maximum, either on the cool or hot side, to match the observed spectrum, as observed here. On the other hand, if the predicted lines are weaker than observed, stars would tend to accumulate near $T_{\text{eff}} \sim 14,000$ K. Both situations are illustrated in Figure 3 of Bergeron et al. (1995b) where the mass distribution of bright DA stars is shown as a function of effective temperatures for different parameterizations of the MLT, which affect significantly the predicted maximum line strength. Also of importance are the adopted Stark broadening profiles used in the synthetic spectrum calculations — those of Tremblay & Bergeron (2009) in our models. The gap observed in Figure 2.7 suggests that Stark broadening or the treatment of convection, or even both, might need to be revisited.

There is even a third alternative explanation for the presence of this gap. Indeed, Genest-Beaulieu & Bergeron (2014) reported a similar deficit of objects near 14,000 K in the spectroscopic temperature distribution of DA stars from the SDSS (see their Section 3.4 and their Figures 14 and 15), while an *accumulation* of objects was observed instead when using the DA spectra from Gianninas et al. (2011). Furthermore, they also found that while the mass distribution as a function of T_{eff} followed a constant mean value of $\sim 0.6 M_{\odot}$ when using the Gianninas sample, the spectroscopic masses at higher temperatures were lower than this canonical value when using SDSS spectra, as also observed here in the lower panel of Figure 2.7 (for $T_{\text{eff}} \gtrsim 30,000$ K). Based on these results, Genest-Beaulieu & Bergeron concluded that the SDSS spectra may still suffer from calibration issues.

The spectroscopic mass distribution for the DB stars, presented in the bottom panel of Figure 2.8, is much more complex than in the case of DA white dwarfs. The most striking detail about this distribution is the very large scatter in mass for $T_{\text{eff}} \lesssim 15,000$ K. This

was also discussed in Section 2.6.2, and the most likely cause of this scatter is the improper treatment of van der Waals broadening in our model atmospheres. Also, contributing to this scatter is the lack of sensitivity of the spectroscopic technique below $T_{\text{eff}} \sim 12,000$ K, when the helium lines become too weak (see, e.g., Figure 3 of Rolland et al. 2018).

The spectroscopic mass distribution for DB stars also shows a significant increase in mass of $\sim 0.1 M_{\odot}$ in the range $20,000 \text{ K} > T_{\text{eff}} > 16,000 \text{ K}$. As discussed above, this corresponds to the temperature range where 3D hydrodynamical effects are expected to become important in pure helium DB stars (Cukanovaite et al., 2018). Cukanovaite et al. showed that the largest differences in spectroscopic $\log g$ values inferred from both 1D and 3D models occur at $T_{\text{eff}} \sim 18,000$ K, and that 1D models tend to overestimate the surface gravities, and thus masses, as observed here. But as discussed above, the photometric masses also lie above $0.6 M_{\odot}$ in the same temperature range. We come back to this point in the next section.

2.7. Comparison of Photometric and Spectroscopic Atmospheric Parameters

In this section we compare the effective temperatures and stellar masses obtained from the photometric and spectroscopic techniques (Sections 2.5 and 2.6) for both the DA and DB white dwarfs in our SDSS sample.

2.7.1. Effective Temperatures

The differences between the spectroscopic and photometric effective temperatures — T_{spec} and T_{phot} — for the DA white dwarfs in our sample are shown as a function of T_{spec} in the top panel of Figure 2.13. Here and below, we use black (red) symbols to indicate white dwarfs whose temperature estimates are within (outside) the 1σ confidence level, where σ is defined as the combined photometric and spectroscopic uncertainties, $\sigma^2 \equiv \sigma_{T_{\text{phot}}}^2 + \sigma_{T_{\text{spec}}}^2$. Using this definition, we find that 63.3% of the DA white dwarfs in our sample have temperature estimates that agree within 1σ . This is somewhat lower than expected from Gaussian statistics (68%), but as mentioned in Sections 2.6.1.1 and 2.6.1.2, we are most likely underestimating the uncertainties associated with our *spectroscopic* parameters, for both the DA and DB white dwarfs.

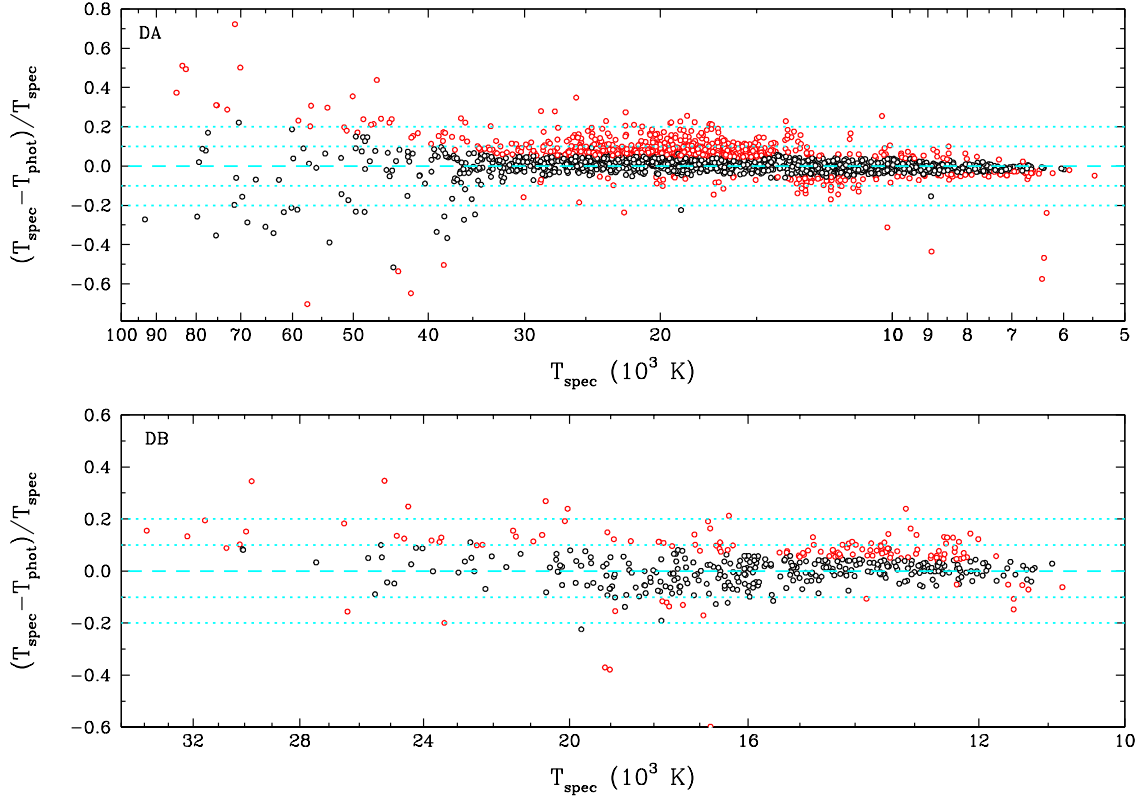


Figure 2.13. Differences between spectroscopic and photometric effective temperatures as a function of T_{spec} for the DA (top) and DB (bottom) white dwarfs in our SDSS sample. Objects with temperature differences within (outside) the 1σ confidence level are shown in black (red). The dashed line corresponds to $T_{\text{spec}} = T_{\text{phot}}$, while the dotted lines show $\pm 10\%$ and $\pm 20\%$ differences in temperature.

Despite this overall agreement between the photometric and spectroscopic temperatures, we can observe some obvious systematic effects in the top panel of Figure 2.13, which depend on the range of temperatures considered. For instance, below $T_{\text{eff}} \sim 14,000$ K, as much as 76% of the objects agree within 1σ , with no obvious systematic trend. Above this temperature, however, only 58% of the sample is within 1σ , and more importantly, spectroscopic temperatures are about 5% to 10% higher than those inferred from photometry. This systematic offset also appears to be fairly constant through the entire temperature range above 14,000 K. A similar offset has been reported before by Genest-Beaulieu & Bergeron (2014, see their Figure 20 and the discussion in their Section 4) using similar SDSS photometric and spectroscopic data. The authors note that this effect is also observed (see their Figure

22) when using the DA spectra from Gianninas et al. (2011), and is thus not related to the particular use of SDSS spectra. Tremblay et al. (2019) also observed a similar systematic offset using *Gaia* photometry, but in their case, the offset is seen for all temperatures.

Since interstellar reddening is important for the SDSS sample, in particular for the hotter and thus intrinsically more luminous and more distant objects, we explore in Figure 2.14 the exact same results as in Figure 2.13, but this time as function of the parallactic distance D_π . We can see here that the systematic offset in temperature is not a function of distance, and more importantly, it is also present below 100 pc where interstellar reddening is negligible according to the dereddening procedure described in Harris et al. (2006). Gentile Fusillo et al. (2019) proposed an alternative dereddening procedure (see their Section 4) that differs slightly from that used by Harris et al., in particular for $D < 100$ pc. We explore in Figure 2.15 the differences between these two recipes, but only for the DA stars in our sample. As can be seen, the results are virtually identical. Actually, the fraction of white dwarfs whose temperature estimates are within the 1σ confidence level decreases from a value of 63.3% with the Harris et al. procedure, to a value of 61.2% with the Gentile Fusillo et al. approach. We thus conclude that our dereddening procedure described in Section 2.5.1 is probably reliable, and that it is not the source of the systematic temperature discrepancy observed in Figure 2.13.

One possible reason for the temperature discrepancy might be related to the physics of line broadening theory, which is likely to affect more importantly the spectroscopic parameters than those obtained from photometry, a solution also proposed by Tremblay et al. (2019). For instance, Genest-Beaulieu & Bergeron (2014) compared in their Figure 23 the photometric and spectroscopic temperatures for the DA stars in the Gianninas et al. sample, but by using model spectra calculated with the Stark profiles of Lemke (1997) — with twice the value of the critical electric microfield β_{crit} in the Hummer-Mihalas occupation probability formalism (see Bergeron et al. 1992 and references therein) — instead of those of Tremblay & Bergeron (2009) used in our analysis. They obtained a much better agreement with these older profiles above $T_{\text{eff}} \sim 20,000$ K, although other systematic effects were introduced between 13,000 K and 19,000 K. Nevertheless, these results strongly suggest that Stark broadening probably needs further improvements, for instance along the lines of the promising work of Gomez et al. (2017).

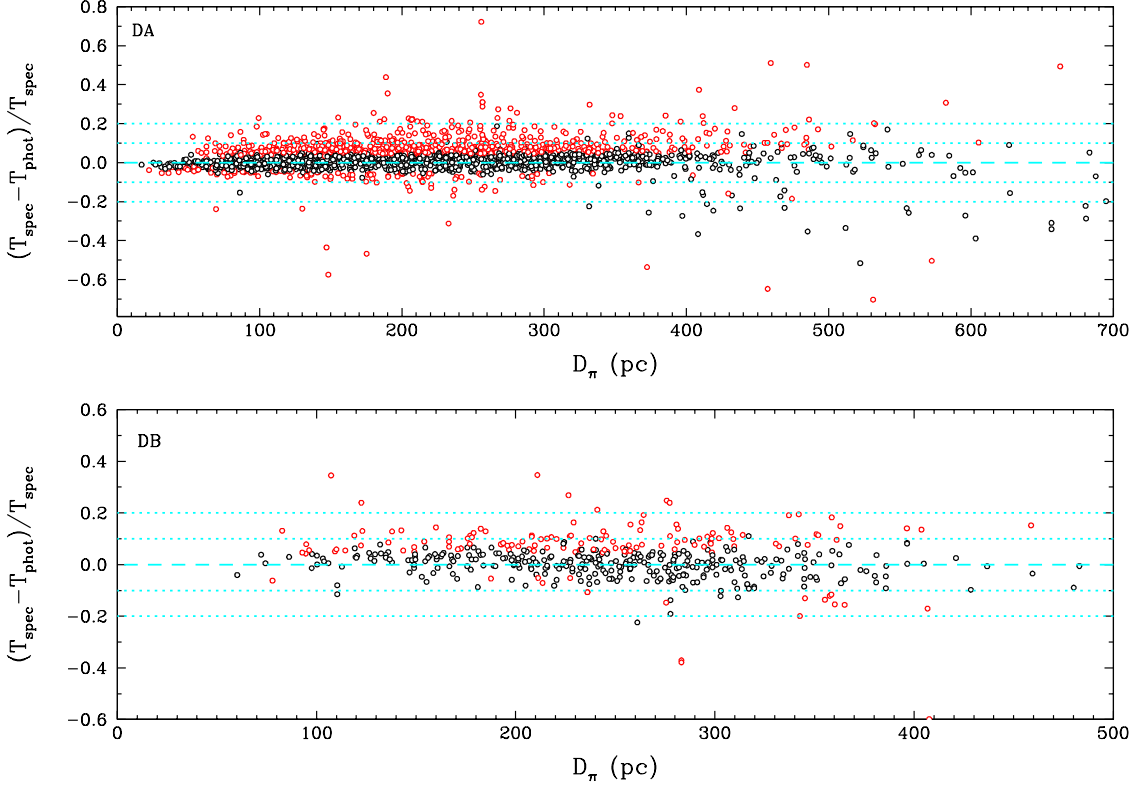


Figure 2.14. Same as Figure 2.13 but as a function of parallactic distances.

The region around $T_{\text{eff}} = 14,000$ K in Figure 2.13 also appears problematic. As mentioned above, this corresponds to the temperature at which the hydrogen lines reach their maximum strength. The spectroscopic solutions in this region are particularly sensitive to the treatment of atmospheric convection, to 3D hydrodynamical effects, to the physics of Stark broadening, and even to flux calibration issues. All these effects are responsible for moving the objects around the region where the lines reach their maximum strength, and for producing the increased scatter near 14,000 K in Figure 2.13. It is even possible that for some objects, the spectroscopic technique did not pick the correct solution, cool or hot, in particular when both are close to the photometric temperature, in which case it is virtually impossible to discriminate between both solutions.

Finally, we note in Figure 2.13 that the scatter increases significantly for $T_{\text{spec}} > 40,000$ K. This is obviously caused by the lack of sensitivity of the *ugriz* photometry in the Rayleigh-Jeans regime (see Figure 2.4). This scatter could possibly be reduced if we were to extend our set of photometric data towards shorter wavelengths, by using *Galex* photometry, for instance.

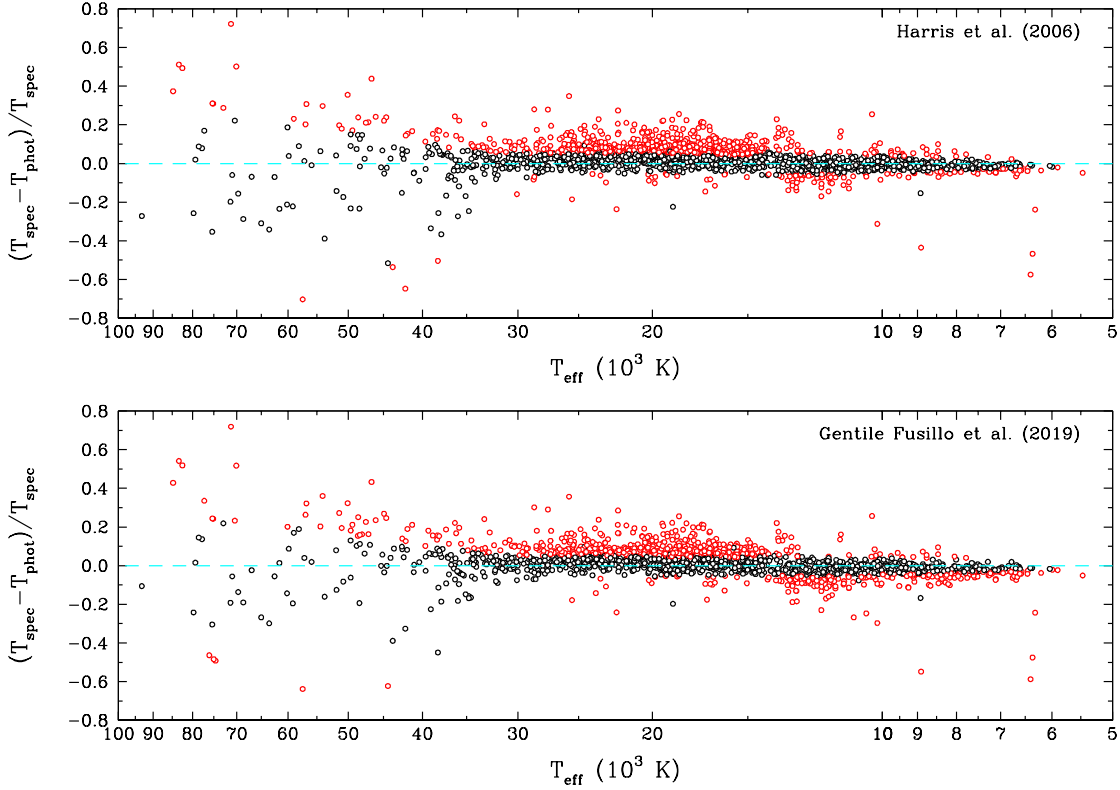


Figure 2.15. Same as the upper panel of Figure 2.13 (DA stars only), where interstellar extinction is taken into account by following the approach described by Harris et al. (2006, upper panel) and by Gentile Fusillo et al. (2019, lower panel).

In some cases, the large differences between the photometric and spectroscopic solutions may be indicative of the presence of an unresolved double degenerate binary. An example of such a candidate in our sample is SDSS J143809.25+221242.26, displayed in Figure 2.16. The best photometric fit indicates a temperature of 9329 K and a rather low value of $\log g = 7.78$. We also note that this is a particularly bad photometric fit, especially at ugr . If we drop the u bandpass, we can achieve a much better fit (not shown here) with $T_{\text{eff}} = 8700$ K and $\log g = 7.63$, in good agreement with the pure hydrogen fit from the Montreal White Dwarf Database (Dufour et al., 2017), based on Pan-STARRS *grizy* photometry ($T_{\text{eff}} = 8444$ K, $\log g = 7.56$). In the bottom panels of Figure 2.16, we show our best spectroscopic fits for the same object assuming a hot and a cool solution. The hot solution provides a much better fit to the observed hydrogen line profiles, while the cool solution predicts lines that are way too deep; both spectroscopic temperatures are significantly different from the photometric value, however. This large temperature discrepancy as well as the distortion of the photometric fit

suggest that SDSS J143809.25+221242.26 is an unresolved degenerate binary composed of a DA+DC, where the hydrogen lines of the DA component are being diluted by the DC white dwarf in the system. Note that Kepler et al. (2015) reported values of $T_{\text{eff}} = 10,049$ K and $\log g = 9.04$ for the same object. A more detailed analysis of this system, and other such binary candidates in our sample, is outside the scope of this paper.

The differences between the spectroscopic and photometric effective temperatures for the DB white dwarfs in our sample are displayed in the bottom panel of Figure 2.13. Overall, the photometric and spectroscopic temperatures are within the 1σ confidence level for 69.6% of the objects in our sample, as expected from Gaussian statistics. As discussed in section 2.6.2, neutral broadening dominates below 16,000 K, and improvement in the treatment of van der Waals broadening is required in our models. If we exclude the objects cooler than this temperature, 71.8% of our sample is now within 1σ . Since the use of the Deridder & van Rensbergen theory rather than the Unsold theory has lowered the effective temperatures obtained with the spectroscopic technique (see top panel of Figure 2.12), a more refined treatment of van der Waals broadening will most likely lower those temperatures even further, giving us a better agreement between T_{spec} and T_{phot} in this regime.

We mentioned earlier that the SDSS spectroscopic data might still have a calibration issue, and that this could be the cause of the systematic offset in temperature ($T_{\text{spec}} > T_{\text{phot}}$) observed in Figure 2.13 for the DA stars. However, residual calibration problems would also affect the DB spectroscopic data. The fact that the offset in temperature is not seen in the DB sample — except for $T_{\text{spec}} \lesssim 16,000$ K where we know our spectroscopic effective temperatures are more uncertain — suggests that the root of the problem most likely lies within our models, and not in the data.

Finally, the increased scatter at the high end of the temperature distribution for the DB white dwarfs in Figure 2.13 is again due to the lack of sensitivity of the photometric technique, and could possibly be reduced by combining multiple photometric systems.

2.7.2. Stellar Masses

The differences between the spectroscopic and photometric masses — M_{spec} and M_{phot} — for the DA white dwarfs in our sample are shown as a function of T_{spec} in the top panel of Figure 2.17. Unlike for the effective temperature, the distribution of mass differences

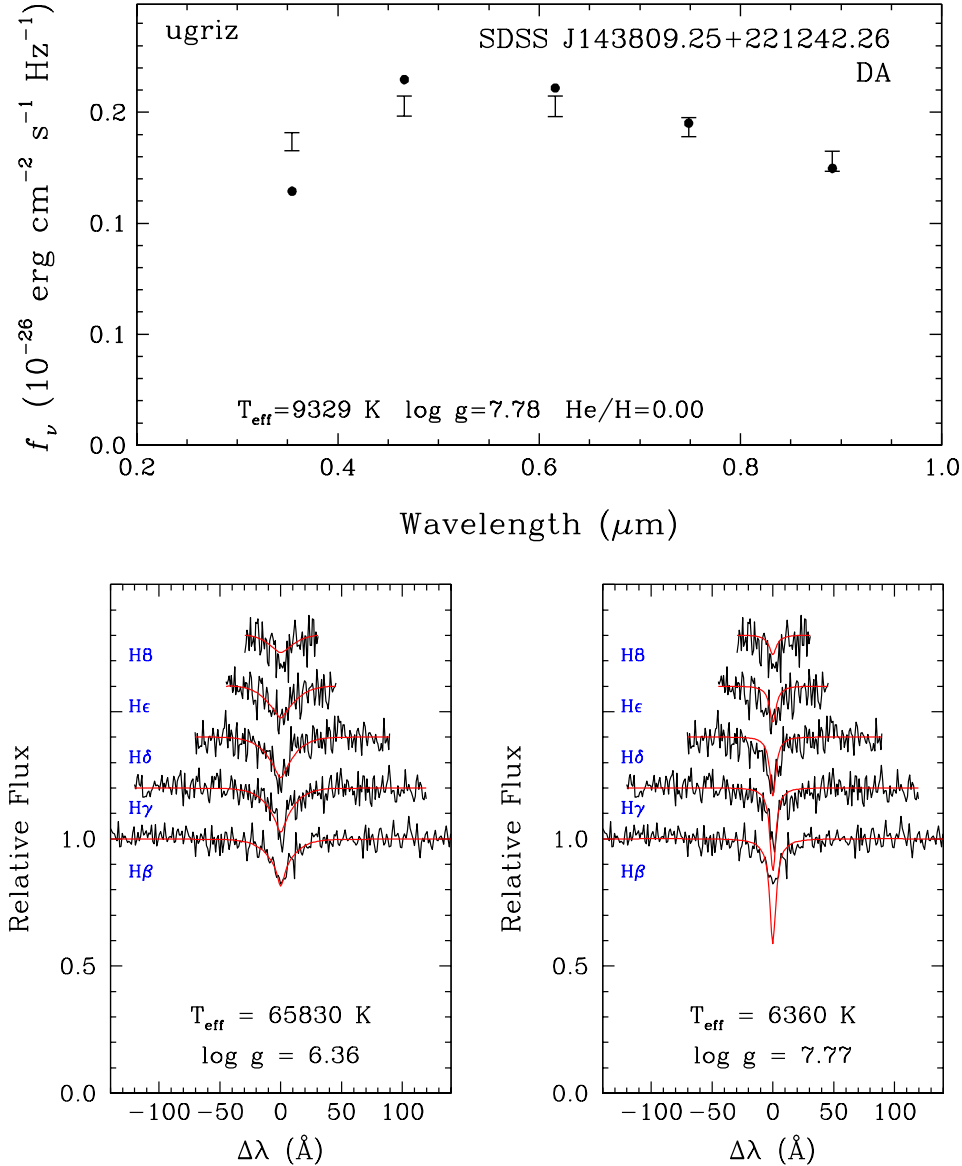


Figure 2.16. Top panel: Best photometric fit to SDSS J143809.25+221242.26 — a double degenerate DA+DC candidate — assuming a single DA star with a pure hydrogen atmosphere. Bottom panels: Best spectroscopic fits for the same object showing the hot (left) and cool (right) solutions.

shows no obvious systematic effect, which suggests that *the spectroscopic mass scale is more reliable than the corresponding temperature scale*, and less affected by the problems with Stark broadening profiles discussed above.

Overall, the photometric and spectroscopic masses agree within the 1σ confidence level for 60.9% of the objects in our sample, slightly below what is expected from Gaussian

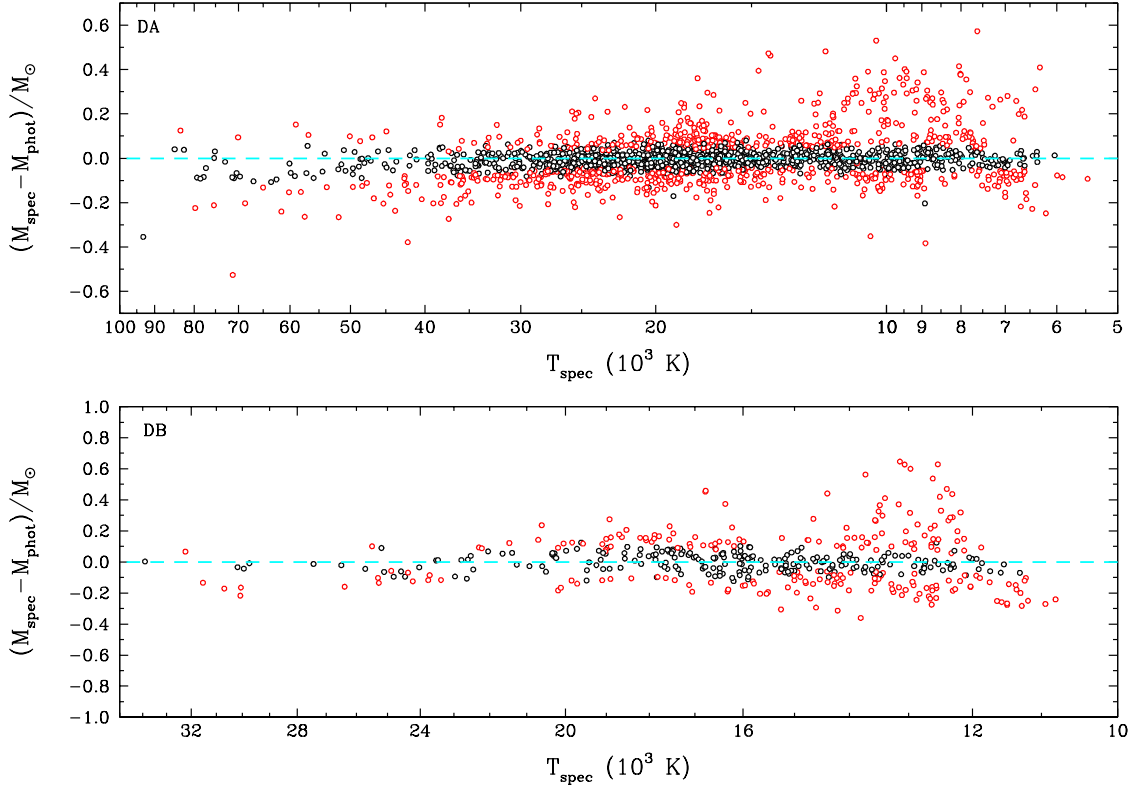


Figure 2.17. Differences between spectroscopic and photometric masses as a function of T_{spec} for the DA (top) and DB (bottom) white dwarfs in our SDSS sample. Objects with mass estimates within 1σ are shown in black, and those outside are in red. The dashed line corresponds to $M_{\text{spec}} = M_{\text{phot}}$.

statistics. However, we can see in Figure 2.17 a significant number of DA stars with $M_{\text{spec}} - M_{\text{phot}} \gtrsim 0.2 M_{\odot}$, which most likely correspond to unresolved DA+DA double degenerate binaries. As discussed in Section 2.5.3, these objects have very low inferred photometric masses, while the combined spectrum resembles that of a single DA white dwarf with intermediate effective temperature and mass (Liebert et al., 1991). An example of such a double degenerate candidate in our sample is SDSS J154130.76+032313.00, shown in Figure 2.18. The photometric fit indicates a very low surface gravity for this object, $\log g = 7.29$, while the spectroscopic solution yields a normal value of $\log g = 7.98$. Hence this system is most likely composed of two normal mass DA stars. Note that both the spectroscopic and photometric fits appear totally normal. This means that DA+DA unresolved binaries can be difficult to detect if one relies only on spectroscopic data. If we omit the binary candidates

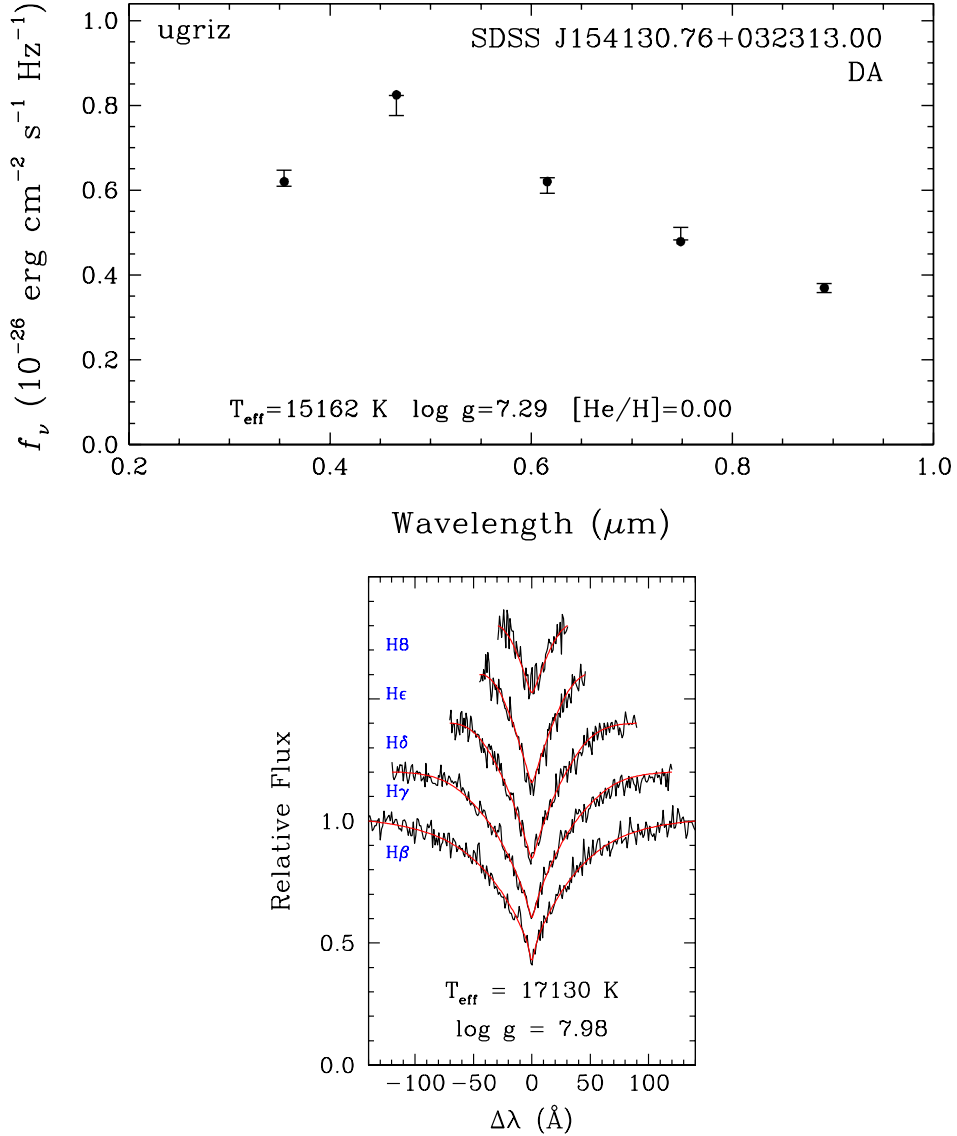


Figure 2.18. Best photometric (top) and spectroscopic (bottom) fits to SDSS J154130.76+032313.00, a DA+DA double degenerate candidate.

from our sample, we now find that 64% of the DA stars have photometric and spectroscopic masses that agree within 1σ , closer to what is expected from Gaussian statistics.

The mass comparison for the DB white dwarfs is presented in the bottom panel of Figure 2.17. For this sample, only half of the objects are within the 1σ confidence level, significantly below the Gaussian statistics. However, the number of DB stars outside 1σ is dominated by objects at low temperatures, where van der Waals broadening in our models yields uncertain spectroscopic masses. If we restrict our sample to $T_{\text{eff}} > 16,000$ K, the proportion of objects

within 1σ increases to 60.5%, much closer to the expectation from Gaussian statistics. The second factor that could improve the agreement between spectroscopic and photometric masses is the use of 3D hydrodynamical models, which are expected to affect the masses mostly between 20,000 K and 16,000 K, as discussed in Section 2.6.3. However, we note in Figure 2.17 that our mass estimates already agree fairly well in this particular range of temperature, suggesting that 3D effects must be small.

As for DA white dwarfs, our DB sample is likely to contain unresolved double degenerate binaries, an example of which is the DBA white dwarf SDSS J150506.24+383017.39, displayed in Figure 2.19. The photometric fit indicates an extremely low surface gravity of $\log g = 7.37$, or a mass of $0.302 M_{\odot}$. Also, our spectroscopic fit for the same object, under the assumption of a single star, reproduces the hydrogen lines very poorly (middle panel of Figure 2.19). However, if we attempt to fit the same spectrum as a combination of a DB and a DA white dwarf (here we assume $\log g = 8.0$ for both components for simplicity), we are able to reproduce both the hydrogen and helium lines perfectly, as shown in the bottom panel of Figure 2.19.

The DB white dwarf SDSS J064452.30+371144.30 is another example. Its photometric fit, shown in the top panel of Figure 2.20, indicates a surface gravity of $\log g = 7.66$, or a mass of $M = 0.412 M_{\odot}$. In this case, however, we are able to successfully reproduce the optical spectrum with single star models, as shown in the bottom panel of Figure 2.20. Furthermore, the spectroscopic surface gravity has a normal value of $\log g = 7.96$. This suggests that this object is an unresolved double degenerate binary composed of two DB stars with more normal masses, where the combined spectrum resembles that of a single DB white dwarf with intermediate atmospheric parameters. The deconvolution of this system will be presented elsewhere.

Bergeron et al. (2011, see also Beauchamp et al. 1996) found no evidence for the existence of low-mass ($M < 0.5 M_{\odot}$) DB white dwarfs in their sample, suggesting that common envelope scenarios, which are often invoked to explain low-mass DA white dwarfs, are not producing DB stars. If we exclude all double degenerate binary candidates from our DB sample, as well as all cool DB white dwarfs for which spectroscopic masses are unreliable due our improper treatment of van der Waals broadening, we find no evidence for low-mass DB white dwarfs, in agreement with the conclusions of previous investigations.

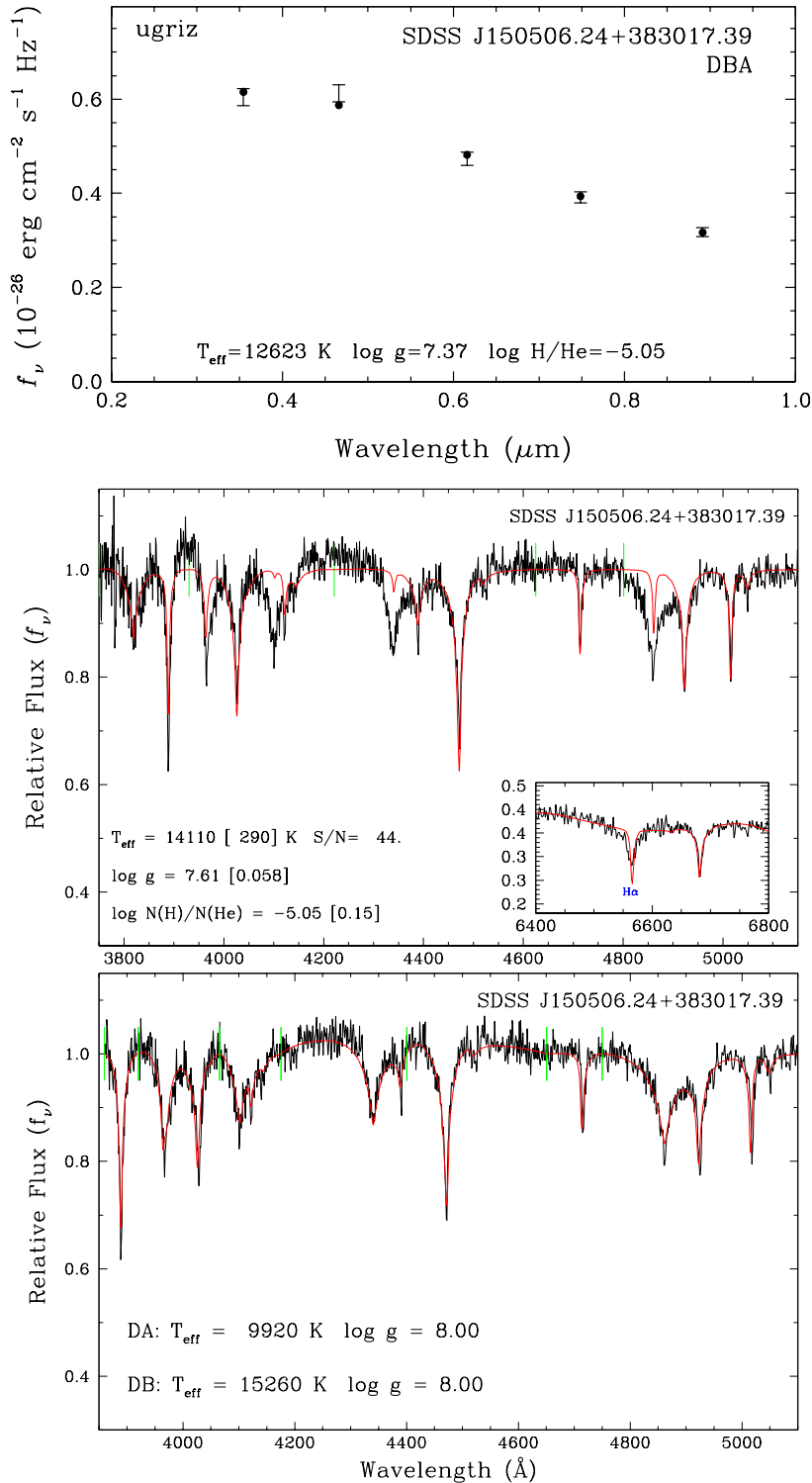


Figure 2.19. Top panel: Best photometric fit to the DBA white dwarf SDSS J150506.24+383017.39. Middle panel: Best spectroscopic fit of the same white dwarf under the assumption of a single star. Bottom panel: same as middle panel, but by assuming a DB+DA double degenerate binary.

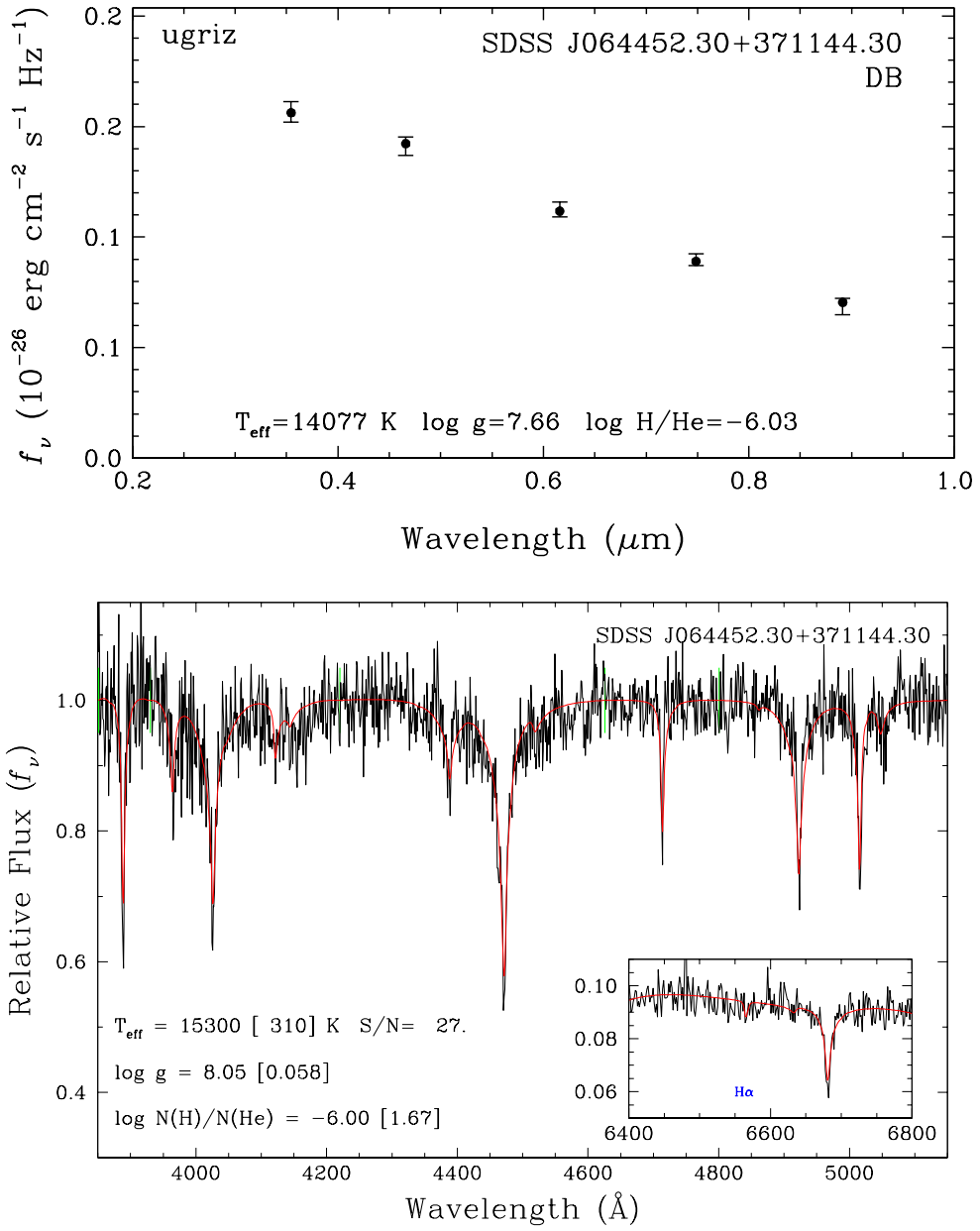


Figure 2.20. Best photometric (top) and spectroscopic (bottom) fits to SDSS J064452.30+371144.30, an unresolved DB+DB double degenerate candidate.

To end our mass comparison, we present in Figure 2.21 the cumulative photometric and spectroscopic mass distributions for both the DA and DB white dwarfs in our sample. For the DA stars, the photometric and spectroscopic distributions are in excellent agreement, in particular the mean mass values, $\langle M_{\text{phot}} \rangle = 0.617 M_\odot$ and $\langle M_{\text{spec}} \rangle = 0.615 M_\odot$. These values are entirely consistent with previous spectroscopic studies, for instance Liebert et al. (2005)

using the PG sample ($\langle M \rangle = 0.603 M_{\odot}$), Tremblay et al. (2011a) using DA white dwarfs from the SDSS DR4 ($\langle M \rangle = 0.613 M_{\odot}$), and Genest-Beaulieu & Bergeron (2014) using DA white dwarfs from the SDSS DR7 ($\langle M \rangle = 0.609 M_{\odot}$). The dispersion of the photometric distribution ($\sigma_{\text{phot}} = 0.147 M_{\odot}$) is somewhat larger than that of the spectroscopic distribution ($\sigma_{\text{spec}} = 0.125 M_{\odot}$), which is caused by the presence of unresolved double degenerates in our sample. These objects form the small bump at $\sim 0.4 M_{\odot}$, and affect the photometric masses more significantly.

In the case of DB stars, the photometric and spectroscopic mass distributions have very different shapes (right panel of Figure 2.21) despite the fact that the mean masses, $\langle M_{\text{phot}} \rangle = 0.620 M_{\odot}$ and $\langle M_{\text{spec}} \rangle = 0.625 M_{\odot}$, are in excellent agreement. In particular, the spectroscopic distribution shows both a low-mass and a high-mass tails that are not observed in the photometric distribution. An examination of Figure 2.8 (bottom panel) reveals that all spectroscopic low-mass and high-mass DB stars in our sample are at low temperatures, $T_{\text{eff}} < 16,000$ K, where the treatment of van der Waals broadening is problematic. Hence both tails are simple artifacts due to unreliable spectroscopic masses. As discussed above, we find no evidence for low-mass DB stars in the photometric mass distribution, with the exception of a small bump around $0.3 M_{\odot}$ caused by the unresolved double degenerates in our sample.

Other mean mass values for DB white dwarfs, determined from spectroscopy, are reported in the literature — $\langle M \rangle = 0.596 M_{\odot}$ (Voss et al., 2007, based on SPY spectra) and $0.671 M_{\odot}$ (Bergeron et al., 2011). Similarly, Koester & Kepler (2015) obtained a mean mass of $0.706 M_{\odot}$ for their complete sample of DB stars from the SDSS DR10 and 12, but a lower value of $\langle M \rangle = 0.606 M_{\odot}$ when their sample was restricted to $16,000 \text{ K} \leq T_{\text{eff}} \leq 22,000$ K. Note that these mean mass values cannot be compared easily because of differences in the treatment of van der Waals broadening in the models, and even in the assumed convective efficiency.

Finally, we note that the mean masses for white dwarfs in the SDSS obtained by Tremblay et al. (2019, see their Figure 13, right panel) based on *Gaia* photometry — $\langle M \rangle = 0.586 M_{\odot}$ and $0.580 M_{\odot}$ for DA and DB stars, respectively — are 0.03 to $0.04 M_{\odot}$ smaller than our own photometric masses based on *ugriz* photometry. We will explore these differences in a future publication.

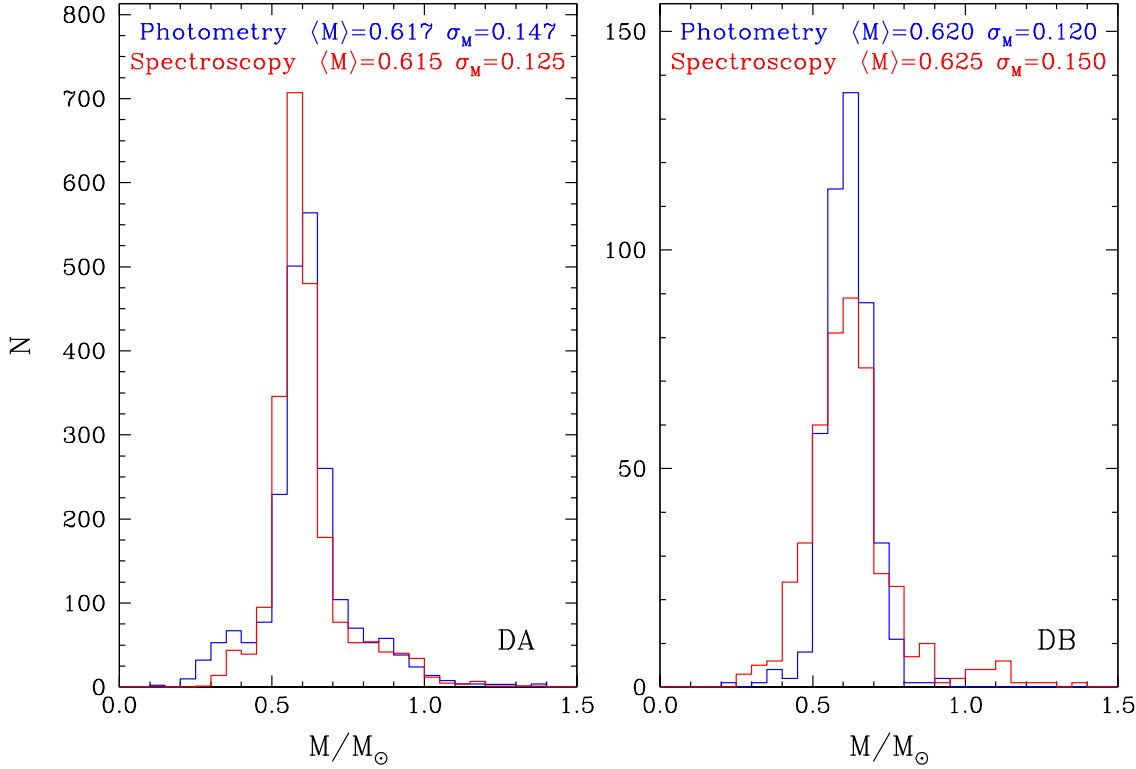


Figure 2.21. Photometric (blue) and spectroscopic (red) cumulative mass distributions for the DA (left) and DB (right) white dwarfs in our sample. The corresponding mean masses and dispersions are given in each panel.

2.8. The Mass-Radius Relation for White Dwarfs

The photometric technique allows us to measure the effective temperature T_{eff} and the solid angle $\pi(R/D)^2$, and thus the stellar radius R if the distance D is known from trigonometric parallax measurements. The spectroscopic technique, on the other hand, yields T_{eff} , $\log g$, and the hydrogen abundance (or limits) in the case of DB white dwarfs. In both cases, however, the mass of the object can only be obtained from the theoretical mass-radius relation for white dwarfs, which we put to the test in this section using the results obtained so far.

Since we have trigonometric parallax measurements, we know the precise distance to every white dwarf in our sample. We can thus compare this parallactic distance D_{π} to the distance obtained from the mass-radius relation, D_{MR} , calculated using the procedure outlined in Bédard et al. (2017). First, the spectroscopic $\log g$ value is converted into radius R

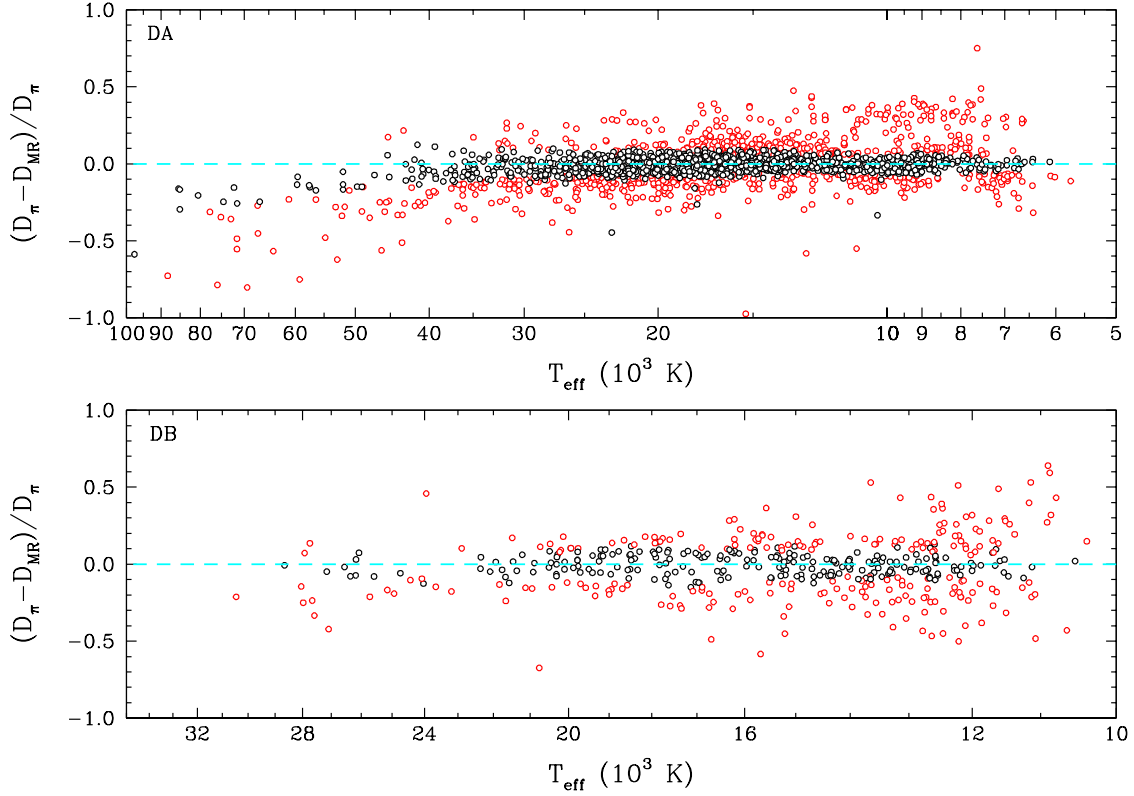


Figure 2.22. Comparison between the parallactic distance D_π and the distance obtained from the mass-radius relation D_{MR} , as a function of effective temperature, for both the DA (top) and DB (bottom) white dwarfs in our sample. The objects for which the distance estimates are within the 1σ confidence level are shown in black.

using evolutionary models, which is then combined with the photometric solid angle $\pi(R/D)^2$ to obtain the desired distance D_{MR} . When using this approach, the solid angle $\pi(R/D)^2$ can be measured in two different ways. The first one is to consider both the effective temperature and the solid angle free parameters in the minimization procedure; the second is to force the effective temperature to the spectroscopic value and to fit only the solid angle. Given the uncertainties with the spectroscopic temperature scales discussed in Section 2.7, we adopt the former approach. Also, it is justified to rely on spectroscopic $\log g$ values for this exercise since the surface gravity (or mass) scale appears reasonably accurate according to the results shown in Figure 2.17.

Figure 2.22 shows the difference between D_π and D_{MR} as a function of effective temperature, for both the DA and DB white dwarfs in our sample. For the DA stars, these distance

estimates are within the 1σ confidence level for 61.4% of the objects in our sample, a value somewhat lower than what is expected from Gaussian statistics. However, we can see from this figure that most of the outliers are found (1) at high temperatures ($T_{\text{eff}} \gtrsim 40,000$ K) where the energy distribution sampled by the *ugriz* photometry is in the Rayleigh-Jeans regime, and (2) at the top of the figure where unresolved double degenerate binaries are expected. If we drop all the objects above 40,000 K, as well as all the binary candidates, the fraction of objects within 1σ increases to 64.6%, again much closer to the expected value of 68%.

For the DB stars in Figure 2.22, we find only 49.2% of the objects in our sample with distance estimates that are within the 1σ confidence level, a value significantly lower than the expected 68%. Here we see, however, that most of the outliers are located at low effective temperatures where van der Waals broadening becomes important. If we restrict our sample to $T_{\text{eff}} > 16,000$ K, and also omit the double degenerate binary candidates, the fraction of objects within 1σ increases to 58.5%. This is still short of the expected fraction, but the number of objects left in our sample if we exclude the cool DB stars is admittedly small.

Another way to test the mass-radius relation is to plot the stellar radius R , obtained *directly* from the photometric technique, against the mass obtained by combining this photometric radius with the spectroscopic $\log g$ ($g = GM/R^2$). This procedure allows us to measure the radius and the mass of an object without the use of any theoretical mass-radius relation. Our results for all the DA and DB white dwarfs in our sample are displayed in Figure 2.23, together with theoretical mass-radius relations (see Section 2.5.1) for C/O-core, thick hydrogen envelope models at various representative T_{eff} values. Note that in such a diagram, thin layer models would be almost impossible to distinguish from thick layer models (see Bédard et al. 2017). As in Bédard et al., we use different color symbols to indicate objects that exhibit differences larger than the 1σ confidence level between the two distance estimates D_π and D_{MR} introduced above.

While most of the data points (the black symbols) align well on the expected mass-radius relation, we see a very large scatter, especially towards higher masses. As discussed in Bédard et al. (2017), the upper right corner of this diagram is populated by unresolved double degenerate binaries. For such overluminous systems, the stellar radius is overestimated, while

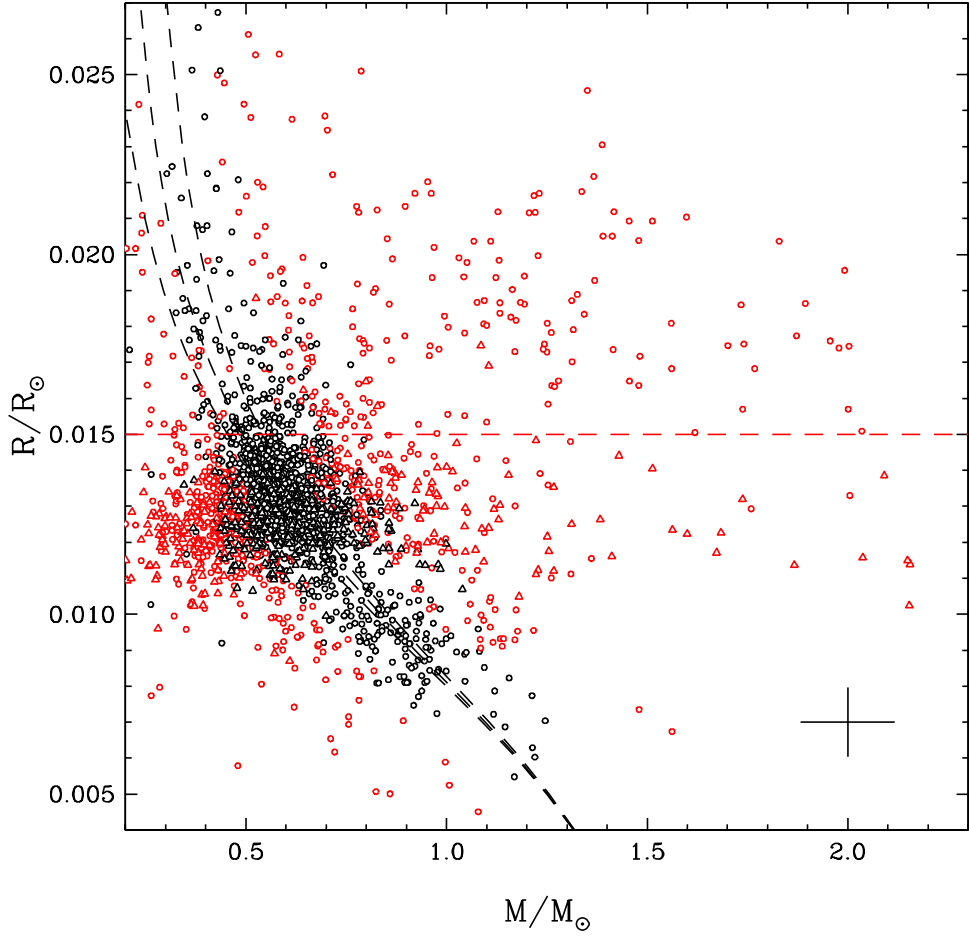


Figure 2.23. Radius as a function of mass for all the DA (circles) and DB (triangles) white dwarfs in our sample. The cross in the lower right corner represents the average uncertainties. Objects for which the difference between D_π and D_{MR} exceeds the 1σ confidence level are shown in red. Also shown are the theoretical mass-radius relations for C/O-core, thick hydrogen envelope models at $T_{\text{eff}} = 8000, 15,000$, and $25,000$ K (black dashed lines, from left to right). The dashed red horizontal line is located at $R = 0.015 R_\odot$ (see text).

the spectroscopic $\log g$ value appears normal, resulting into a large inferred mass in the mass-radius diagram. For example, for the DA+DA binary candidate SDSS J154130.76+032313.00 displayed in Figure 2.18, we obtain from the photometric technique $R = 0.02093 R_\odot$ and a spectroscopic value of $\log g_{\text{spec}} = 7.98$, resulting in a large mass of $M = 1.513 M_\odot$, well above the Chandrasekhar limit.

Single star evolution predicts that white dwarfs with masses below $M \sim 0.45 M_\odot$ should not have formed within the lifetime of the Galaxy. This corresponds to a stellar radius of

$\sim 0.015 R_\odot$ at 10,000 K, represented by the horizontal dashed line in Figure 2.23. We see that the most massive objects below this line — with normal photometric radii around $0.012 R_\odot$ — are DB white dwarfs. More specifically, these correspond to the cool DB stars in our sample with $T_{\text{eff}} < 16,000$ K, and with uncertain high $\log g$ values (see bottom panel of Figure 2.11). Similarly, we see a large concentration of low-mass DB white dwarfs (red triangles) on the extreme left around $0.012 R_\odot$. These correspond to DB stars in the same temperature range, but this time with low spectroscopic $\log g$ values (see again bottom panel of Figure 2.11). All of these cool DB white dwarfs are expected to align on the mass-radius relation once a proper treatment of van der Waals broadening becomes available.

If we remove the DB stars from our sample, we are still left with a fairly large number of DA stars to the left of the theoretical curves with discrepant ($> 1\sigma$) distance estimates (red circles). Provencal et al. (1998) proposed that these white dwarfs might not have a C/O core, but rather an iron core. Bédard et al. (2017) tested this hypothesis and found that Fe-core models could indeed explain the location of these objects in the mass-radius diagram, but they could not completely rule out that these were not normal C/O-core white dwarfs, within the uncertainties. The most compelling case of an Fe-core white dwarf was G87-7, with a parallactic distance of $D_\pi = 15.7$ pc based on *Hipparcos*. The distance obtained from C/O-core models, $D_{\text{MR}} = 17.5$ pc, was found to be significantly different from the parallactic distance, while the distance inferred from Fe-core models, $D_{\text{MR}} = 15.9$ pc, was in much better agreement. This discrepancy has now been resolved with the *Gaia* parallax, which yields $D_\pi = 17.07$ pc, in excellent agreement with the distance inferred from C/O-core models.

To summarize, if we restrict our analysis to single white dwarfs ($M_{\text{spec}} - M_{\text{phot}} < 0.2 M_\odot$), and to the temperature range where the physics of our model atmospheres is better understood ($T_{\text{eff}} < 40,000$ K for DA stars, and $T_{\text{eff}} > 16,000$ K for DB stars), we find that about 65% are within the 1σ confidence level of the mass-radius relation (based on the distance comparison), and about 92% are within 2σ . We stress again the fact that we are probably underestimating in our analysis the uncertainties associated with the *spectroscopic* atmospheric parameters, thus these numbers represent only lower limits. With these caveats in mind, we conclude that the theoretical mass-radius relation for white dwarfs rests on solid

empirical grounds, a conclusion also reached by Holberg et al. (2012), Tremblay et al. (2017), Parsons et al. (2017), and Bédard et al. (2017), but for significantly smaller samples.

2.9. Conclusion

We performed a detailed spectroscopic and photometric analysis of 2236 DA and 461 DB white dwarfs from the Sloan Digital Sky Survey with trigonometric parallax measurements available from the *Gaia* mission. The temperature and mass scales obtained from fits to *ugriz* photometry appear reasonable for both DA and DB stars. The photometric mass distributions for DA and DB stars are comparable, with almost identical mean masses of $\langle M \rangle = 0.617 M_{\odot}$ and $0.620 M_{\odot}$, respectively. However, the DA mass distribution shows well-defined low-mass and high-mass tails, which are not observed in the DB photometric mass distribution. In particular, we find no evidence in our sample for single, low-mass DB white dwarfs.

The comparison of the effective temperatures and stellar masses obtained from the photometric and spectroscopic techniques reveals several problems with the model spectra for both pure hydrogen and pure helium compositions. For DA stars, we found a systematic offset in temperature, with the spectroscopic temperatures exceeding the photometric values by $\sim 10\%$ above 14,000 K. Since this offset is not observed for DB stars in the same temperature range, we believe that some inaccuracy in the theory of Stark broadening for hydrogen lines is at the origin of the observed temperature discrepancies. Despite these problems, the $\log g$ and mass scales derived from spectroscopy appear unaffected since the spectroscopic mass distribution agrees extremely well with that obtained from photometry. For instance, the spectroscopic mean mass for the DA stars, $\langle M \rangle = 0.615 M_{\odot}$, differs from the photometric mean value by only $0.002 M_{\odot}$.

For the DB white dwarfs, both the temperature and mass scales agree well above 16,000 K, but abnormally low and high spectroscopic masses are found at lower temperatures that are significantly different from the corresponding photometric masses. We attribute these discrepancies to the inaccurate treatment of van der Waals broadening in our model spectra for DB white dwarfs, as well as to the limitations of the spectroscopic technique at low effective temperatures, when the neutral helium lines become too weak. Despite these problems, the

spectroscopic mean mass for the DB stars, $\langle M \rangle = 0.625 M_{\odot}$, differs by only $0.005 M_{\odot}$ from the photometric mean value.

By comparing the physical parameters using both the photometric and spectroscopic techniques, we were able to identify very easily several unresolved double degenerate binaries in our sample with various spectral types, including DA+DA, DB+DB, DA+DB, and even DA+DC systems. All of these appear overluminous, and thus have extremely low photometric masses. Double degenerates composed of identical spectral types may have normal spectroscopic $\log g$ values, however.

We finally took advantage of the *Gaia* parallaxes to test the theoretical mass-radius relation for white dwarfs. If we exclude the double degenerate binary candidates from our sample, and restrict our analysis to the temperature range where the spectroscopic $\log g$ values are reasonably accurate, we find that the parallactic distance and the distance obtained from the mass-radius relation are within the 1σ confidence level for about 65% of the white dwarfs in our sample, which confirms the validity of the theoretical mass-radius relation for white dwarfs.

We are grateful to A. Bédard for a careful reading of our manuscript, and to the referee, D. Koester, for his constructive comments and suggestions. We would also like to thank P.-E. Tremblay and E. Cukanovaite for useful discussions, and in particular for mentioning to us the problem with our former use of van der Waals broadening. This work is supported in part by the NSERC Canada and by the Fund FRQ-NT (Québec). This work has made use of data from the European Space Agency (ESA) mission *Gaia* (<https://www.cosmos.esa.int/gaia>), processed by the *Gaia* Data Processing and Analysis Consortium (DPAC, <https://www.cosmos.esa.int/web/gaia/dpac/consortium>). Funding for the DPAC has been provided by national institutions, in particular the institutions participating in the *Gaia* Multilateral Agreement. This research has made use of the NASA/ IPAC Infrared Science Archive, which is operated by the Jet Propulsion Laboratory, California Institute of Technology, under contract with the National Aeronautics and Space Administration.

Chapitre 3

A Photometric and Spectroscopic Investigation of the DB White Dwarf Population in the SDSS and *Gaia*

C. Genest-Beaulieu¹ & P. Bergeron¹

¹ *Département de Physique, Université de Montréal, Montréal, QC H3C 3J7, Canada; genest@astro.umontreal.ca, bergeron@astro.umontreal.ca.*

À soumettre à *The Astrophysical Journal*

3.1. Abstract

We present a comprehensive analysis of DB white dwarfs drawn from the Sloan Digital Sky Survey, based on model fits to *ugriz* photometry and medium resolution spectroscopy from the SDSS. We also take advantage of the exquisite trigonometric parallax measurements recently obtained by the *Gaia* mission. Using the so-called photometric and spectroscopic techniques, we measure the atmospheric and physical parameters of each object in our sample (T_{eff} , $\log g$, H/He, Ca/He, R , M), and compare the values obtained from both techniques in order to assess the precision and accuracy of each method. We then explore in great detail the surface gravity, stellar mass, and hydrogen abundance distributions of DB white dwarfs as a function of effective temperature. We present some clear evidence for a large population of unresolved double degenerate binaries composed of DB+DB and even DB+DA white dwarfs. In the light of our results, we finally discuss the spectral evolution of DB white dwarfs, in particular the evolution of the DB-to-DA ratio as a function of T_{eff} , and we revisit the question of the origin of hydrogen in DBA white dwarfs.

Key words: stars: evolution — stars: fundamental parameters — techniques: photometric — techniques: spectroscopic — white dwarfs

3.2. Introduction

The Sloan Digital Sky Survey (SDSS) has dramatically changed our view of white dwarf stars by not only increasing the number of known degenerates by a factor of more than 10, but also by providing a set of homogeneous spectroscopic and photometric observations (Abazajian et al., 2003). More recently, another major milestone has been achieved by the *Gaia* mission (Gaia Collaboration et al., 2018), which provided accurate trigonometric parallax measurements for 260,000 white dwarfs, and white dwarf candidates (Gentile Fusillo et al., 2019). These accurate distances, coupled with large photometric surveys such as SDSS, *Gaia*, or Pan-STARRS, open an all new window on the measurement of white dwarf parameters (Gentile Fusillo et al., 2019; Tremblay et al., 2019; Genest-Beaulieu & Bergeron, 2019; Bergeron et al., 2019). In Genest-Beaulieu & Bergeron (2019), we presented a detailed comparison of white dwarf parameters obtained with the so-called spectroscopic and photometric techniques for both DA and DB stars (see also Genest-Beaulieu & Bergeron 2014 and

Tremblay et al. 2019). In this paper, we want to focus more specifically on the origin and formation of DB white dwarfs.

While a countless number of spectroscopic analyses of DA white dwarfs has been published in the literature (Bergeron et al. 1992, Liebert et al. 2005, Koester et al. 2009b, and Gianninas et al. 2011, just to name a few), only a few are available for DB stars (Eisenstein et al., 2006a; Voss et al., 2007; Bergeron et al., 2011; Koester & Kepler, 2015; Rolland et al., 2018). More importantly, while the atmospheric parameters for DA white dwarfs agree generally well between these various analyses, those of DB stars show larger discrepancies, which can probably be traced back to differences in model atmospheres and fitting techniques. For instance, the treatment of van der Waals broadening remains one of the largest source of uncertainty at low effective temperatures ($T_{\text{eff}} \lesssim 16,000$ K; Genest-Beaulieu & Bergeron 2019 and references therein). Also of importance is the assumed convective efficiency at high temperatures ($T_{\text{eff}} \sim 25,000$ K), or even the validity of the mixing-length theory used so far in all model atmosphere calculations for DB stars. Cukanovaite et al. (2018) indeed showed that 3D hydrodynamical effects, similar to those found in the context of DA stars (Tremblay et al., 2013a,b), should be equally important for DB white dwarfs. Hence, despite all these efforts, our understanding of the effective temperature, stellar mass, and hydrogen abundance distributions of DB white dwarfs remains sketchy at best. For instance, there are still unanswered questions regarding the mass distribution of DB versus DBA white dwarfs, or the reality of low- and high-mass DB white dwarfs, or even the existence of unresolved double degenerate binaries among the DB population.

Many open questions also remain concerning the origin of DB white dwarfs. There is now little doubt that most DB white dwarfs have evolved from the transformation of DA stars through a process referred to as convective dilution, where the thin hydrogen surface layer ($M_{\text{H}} \sim 10^{-16} - 10^{-14} M_{\odot}$) of the DA progenitor is gradually eroded and thoroughly mixed with the underlying helium convection zone. However, the details of this mixing process, and in particular the temperature at which it takes place, remain poorly understood (MacDonald & Vennes, 1991; Rolland et al., 2018). There is also the question of the existence of the DB-gap, a region between $T_{\text{eff}} \sim 45,000$ K and 30,000 K originally believed to be devoid of helium-atmosphere white dwarfs (Liebert et al., 1986; Fontaine & Wesemael, 1987). It is this particular feature that actually led to the interpretation of the DA-to-DB transition at

the red edge of the gap. Now thanks to the SDSS, this gap has been partially filled by hot DB stars (Eisenstein et al., 2006a; Koester & Kepler, 2015), but a strong deficiency of helium-atmosphere white dwarfs still remain in this temperature range, and the exact fraction is uncertain due, once again, to inaccuracies in the temperature scale of hot DB stars.

Important insight can also be gained from a careful determination of the ratio of DB to DA stars as a function of effective temperature, ideally in a volume-limited sample to avoid all possible selection biases. Since the convective dilution process is a strongly-dependent function of the thickness of the hydrogen layer, one could in principle map the hydrogen layer mass (M_H) in DA stars that turned into DB white dwarfs, by carefully comparing their respective luminosity functions. For instance, Bergeron et al. (2011, see their Figure 24) used the DA and DB white dwarfs identified in the Palomar-Green (PG) survey to show that the DA-to-DB transition occurred for most objects around $T_{\text{eff}} \sim 20,000$ K, instead of the canonical value of 30,000 K, an estimate originally based of the location of the red edge of the DB gap. This result led the authors to suggest that a fraction of DB stars may have preserved a helium-rich atmosphere throughout their lifetime, an interpretation certainly supported by the existence of hot, helium-atmosphere white dwarfs in the DB gap.

Another topic of importance is related to the presence of hydrogen in DB white dwarfs — the DBA stars. Hydrogen is detected at the photosphere of a significant fraction of DB stars — mostly through spectroscopic observations at H α —, although the exact fraction varies from study to study depending on the quality of the observations, and most importantly the signal-to-noise ratio (S/N). For instance, Bergeron et al. (2011) found that 44% of their sample of 108 objects showed hydrogen, but further spectroscopic observations at H α of the same sample by Rolland et al. (2018) increased this ratio to 63%. On the other hand, Koester & Kepler (2015) estimated that this fraction could be as high as 75% based on the best spectroscopic data in the SDSS.

An important controversy in the literature also has to do with the origin of hydrogen in these DBA white dwarfs. One possible explanation is that hydrogen has a residual origin, resulting from the convective dilution of the thin hydrogen layer with the more massive helium convection zone. However, the total mass of hydrogen within the mixed H/He convection zone, inferred from the observed hydrogen abundance at the photosphere, is so large — of the order of $M_H = 10^{-12} M_\odot$ — that a DA progenitor with such a massive hydrogen layer

would have never mixed in the first place. Or put differently, the thickness of the hydrogen layer required for the convective dilution process to occur would yield photospheric hydrogen abundances that are orders of magnitudes smaller than those observed in DBA white dwarfs.

One possible solution to this problem is to have an external source of hydrogen that would increase its photospheric abundance significantly, *assuming mixing has already occurred*. Many external sources have been proposed in the literature, including accretion from the interstellar medium (MacDonald & Vennes, 1991), from comets (Veras et al., 2014), or even from disrupted planets (Raddi et al., 2015; Gentile Fusillo et al., 2017). One problem with this interpretation, however, is that the average hydrogen accretion rate required to account for the observed abundances in DBA white dwarfs, would build over time a hydrogen layer at the surface of the DA progenitor thick enough, that such a DA star would never undergo the DA-to-DB transition (Rolland et al., 2018). Also, one would have to explain the existence of DB stars with no detectable traces of hydrogen, in particular at low temperatures where small traces of hydrogen ($\log H/\text{He} \sim -6$) can be easily detected. Nevertheless, there are obvious cases of DBA stars with extremely large abundances of hydrogen and metals (SDSS J124231.07+522626.6, GD 16, GD 17, GD 61, and GD 362; see Gentile Fusillo et al. 2017 and references therein), for which the interpretation in terms of accretion of water-rich asteroid debris cannot be questioned. Gentile Fusillo et al. (2017) even discuss a possible correlation between the presence of hydrogen and metals in DBA white dwarfs, suggesting that some fraction of the hydrogen detected in many, perhaps most, helium-atmosphere white dwarfs is accreted alongside metal pollutants.

In order to shed some light on several of the issues discussed above, we present in this paper a thorough photometric and spectroscopic analysis of the DB white dwarfs identified in the SDSS. We first describe in Section 3.3 the DB white dwarf sample drawn from the SDSS database, including the spectroscopic, photometric, and astrometric observations, which will be analyzed using the theoretical framework outlined in Section 3.4. We also explore at length in Section 3.5 the error budget of our analysis. We then present in Section 3.6 the results of the atmospheric and physical parameters of all DB white dwarfs in our sample, while objects of particular astrophysical interest are discussed on Section 3.7. Finally, in the light of our results, we discuss in detail the spectral evolution of DB white dwarfs in Section

3.8, and we also explore the case of stratified atmospheres in Section 3.9. Some concluding remarks follow in Section 3.10.

3.3. DB White Dwarf Sample

The first step of our investigation is to perform a full model atmosphere analysis of DB white dwarfs using the photometric and spectroscopic data from the SDSS database, as well as the trigonometric parallaxes from the *Gaia* survey. We describe these spectroscopic, photometric, and astrometric samples in turn.

3.3.1. Spectroscopic Sample

We retrieved the observed spectra of all the spectroscopically identified DB white dwarfs in the SDSS, up to the DR12 (Kleinman et al., 2013; Kepler et al., 2015, 2016). Since we want to characterize the entire population of DB white dwarfs, we kept every subtype in our sample and did not apply any criterion on the S/N value, but a visual inspection of the spectroscopic fits allowed us to remove any problematic data. We did however remove all objects with a spectral type indicating a companion (M or +). Our final spectroscopic sample is composed of 2058 spectra, representing 1916 individual white dwarfs, since 128 of these have multiple spectroscopic observations. Except in Section 3.5.2, where each spectrum will be treated as an independent object, we will retain only the best S/N spectrum of each object for our model atmosphere analysis.

Of the 1916 individual white dwarfs, 1522 (or 79.4%) are classified as DB, including the DB stars showing traces of hydrogen (DBA) and/or metals (DBZ), while the other 20.6% (394 objects) is composed of all other subtypes, including magnetic objects (H), spectra with carbon features (Q), and uncertain spectral types (:). Even though our spectroscopic solution for these other subtypes might be uncertain, it should not impact our conclusion significantly since they represent only a small fraction of the entire sample. The S/N distribution of our spectroscopic sample is presented in Figure 3.1.

3.3.2. Photometric and Astrometric Sample

Since an independent determination of the physical parameters can be obtained from photometry, we also retrieved the *ugriz* magnitudes for all objects in our spectroscopic sample. We rely on the *ugriz* photometric data from the SDSS 14th data release (DR14),

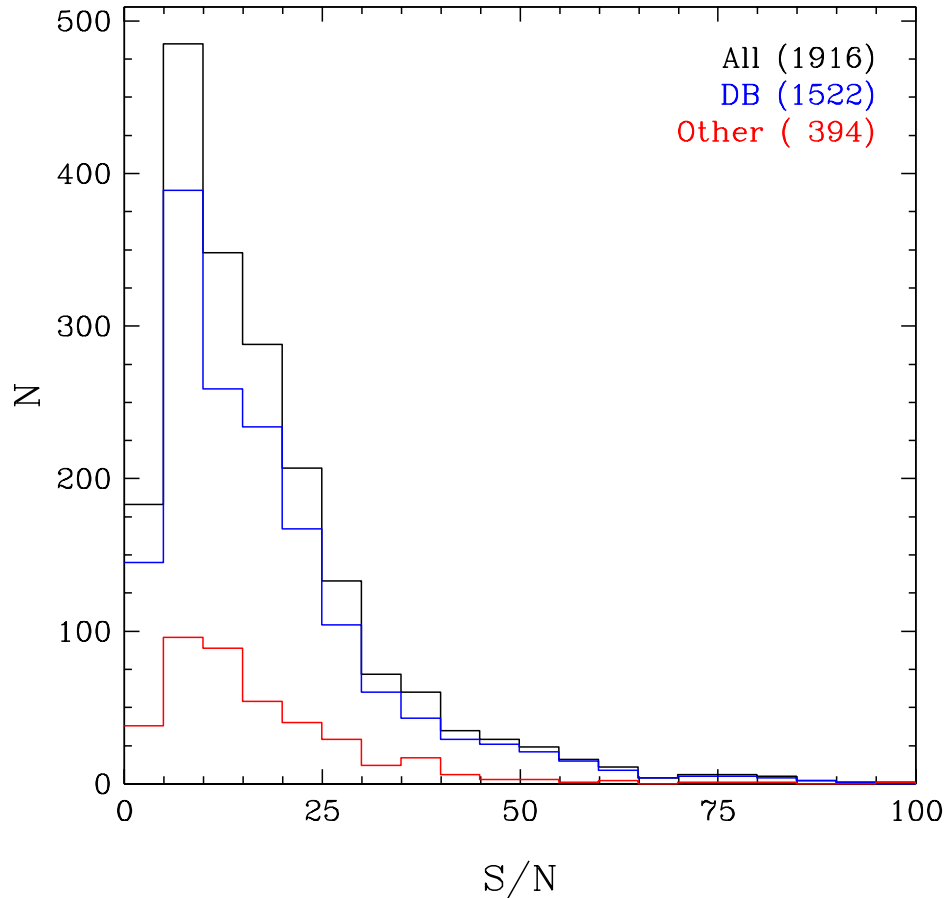


Figure 3.1. Distribution of S/N of the complete spectroscopic sample (black), the DB subsample (blue), including the DB white dwarfs showing traces of hydrogen (DBA) and/or metals (DBZ), and other subtypes (red).

since the calibration algorithm has been improved between DR7 and DR8, and the *ugriz* zero-points have been recalibrated in DR13¹ as well. We also want to take advantage of the *Gaia* DR2 catalog (Gaia Collaboration et al., 2018), which provides precise trigonometric parallax measurements for around 260,000 high confidence white dwarf candidates (Gentile Fusillo et al., 2019), and we thus retrieved the parallaxes for all DB stars in our SDSS sample, if available (about 90% of the objects in our spectroscopic sample). Again here, we applied no specific selection criteria on the quality of the *ugriz* photometry or on the trigonometric parallaxes, but we visually inspected all photometric fits, and removed any obvious bad photometric or parallax data. As before, we also removed all spectral types containing an M

1. <https://www.sdss.org/dr14/algorithms/fluxcal/>

or a +. Our final photometric sample is composed of 1669 photometric data sets, of which 1350 (or 80.9%) are DB stars, including spectral types indicating the presence of hydrogen (DBA) and/or metals (DBZ); the other 19.1% (319 photometric sets) is composed of all other subtypes already mentioned above.

The distribution of white dwarfs in our sample as a function of distance and spectral type is presented in Figure 3.2. As can be seen, most objects are located at very large distances ($D > 100$ pc), which implies that their observed $ugriz$ magnitudes will be significantly affected by interstellar reddening. Interstellar extinction will be treated here (see also Genest-Beaulieu & Bergeron 2019 and Bergeron et al. 2019) following the procedure outlined in Harris et al. (2006), where the extinction is considered negligible if $D \leq 100$ pc, to be maximum for the objects located at $|z| > 250$ pc from the galactic plane, and to vary linearly between these two regimes.

3.4. Theoretical Framework

The grid of model atmospheres used in the following photometric and spectroscopic analyses is similar to that described in Bergeron et al. (2011), except for the treatment of van der Waals broadening. We use here a treatment based on Deridder & van Rensbergen (1976) instead of Unsold (1955); see Sections 3.2 and 5.2 of Genest-Beaulieu & Bergeron (2019, hereafter GBB19) for details. These models are in LTE and convection is treated with the ML2/ $\alpha=1.25$ version of the mixing-length theory (MLT). Our grid covers a range of effective temperatures from 11,000 K to 50,000 K, surface gravities from $\log g = 7.0$ to 9.0, and hydrogen abundances (in number) from $\log H/He = -6.5$ to -2.0 , as well as a pure helium grid. Additional models have also been calculated that include the Ca II H and K doublet, in order to properly fit the white dwarfs in our sample showing strong calcium lines. This smaller grid is similar to that described in Bergeron et al. (2011) — except again for the treatment of van der Waals broadening — and covers a range of $T_{\text{eff}} = 12,000$ K to 19,000 K, calcium abundances of $\log Ca/He = -7.5, -7.0, -6.5$, and -6.0 , and the same range of $\log g$ and H/He values as before.

To determine the atmospheric and physical parameters of the DB white dwarfs in our sample, we rely on the photometric and spectroscopic techniques described at length in GBB19 and references therein. Briefly, with the photometric approach, the effective temperature

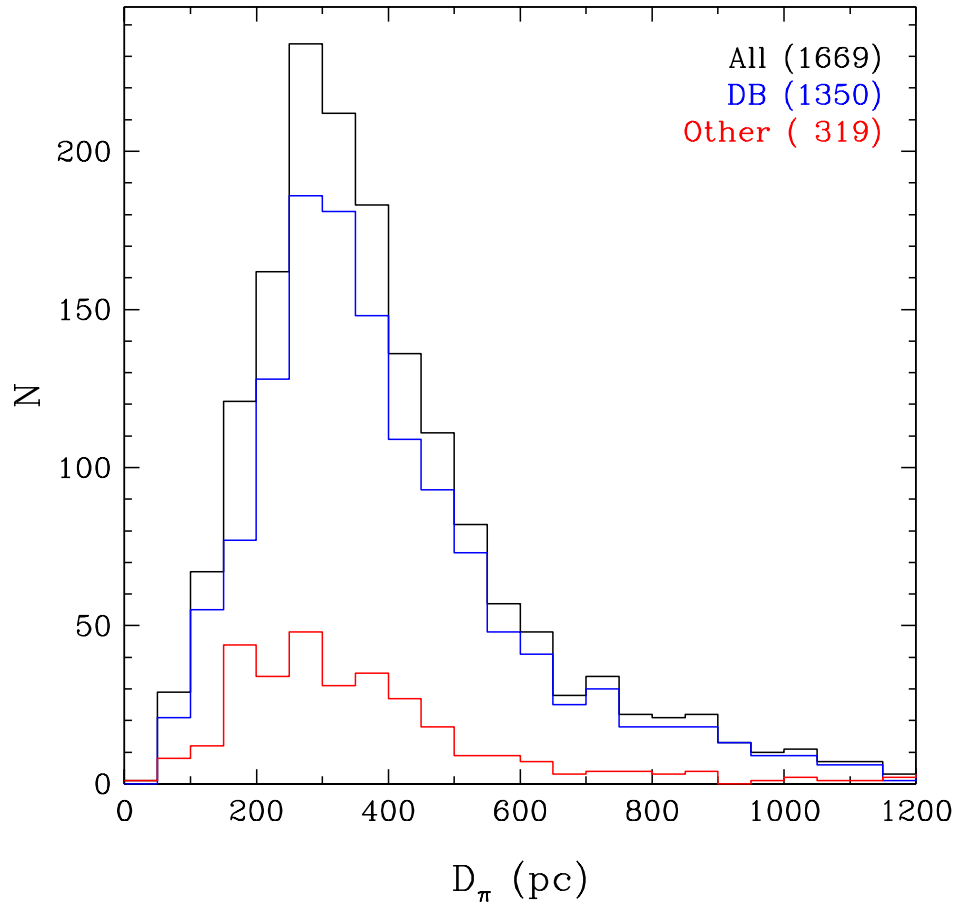


Figure 3.2. Distribution of parallactic distances for the complete photometric sample (black), the DB and DBA subsample (blue), and the other subtypes (red).

T_{eff} and solid angle $\pi(R/D)^2$ are obtained by comparing the observed energy distribution — built from the *ugriz* photometry — with the predictions of model atmospheres, while with the spectroscopic method, T_{eff} , the surface gravity $\log g$, and the hydrogen abundance H/He are obtained by comparing the observed and synthetic spectra, both normalized to a continuum set to unity. Stellar masses can then be derived from evolutionary models. We rely here on C/O-core envelope models² similar to those described in Fontaine et al. (2001) with thin hydrogen layers of $q(\text{H}) \equiv M_{\text{H}}/M_\star = 10^{-10}$, which are representative of helium-atmosphere white dwarfs. For the DB stars in our sample showing calcium lines, we explore the spectroscopic fits obtained for each calcium abundance in our grid, and adopt the solution with the lowest χ^2 value.

2. See <http://www.astro.umontreal.ca/~bergeron/CoolingModels>.

3.5. Error Estimation

As discussed in the Introduction, our understanding of the nature and evolution of DB white dwarfs rests heavily on our ability to measure their atmospheric and physical parameters with great accuracy and precision. We thus present in this section a thorough analysis of the photometric and spectroscopic errors associated with the determinations of white dwarf parameters.

3.5.1. Photometric Errors

The errors associated with our photometric solutions can be obtained directly from the covariance matrix of the Levenberg-Marquadt minimization procedure used in the photometric technique. These depend mostly on the uncertainty associated with the observed magnitudes and the sensitivity of the *ugriz* photometry to the atmospheric parameters. We apply here a lower limit of 0.03 mag on each bandpass so that the photometric solution is not driven by a single magnitude with an extremely small uncertainty (see also Bergeron et al. 2019). As also discussed in Bergeron et al. (2019), the SDSS magnitude system is not exactly on the AB magnitude system, and corrections of the order of 0.03 mag must be added to some bandpasses, all of which remain uncertain. Since we use the trigonometric parallax in the fitting procedure, the errors on the atmospheric parameters will depend on σ_π as well. Note that all values reported in this section are for the DB stars only, and we expect our errors for other subtypes (e.g. magnetic DB stars or uncertain spectral types) to be even larger.

The errors associated with our photometric effective temperatures are presented in the top panel of Figure 3.3. The mean error for the overall sample is $\sim 10\%$ in T_{eff} , but the individual errors vary significantly as a function of temperature since they widely depend on the sensitivity of the *ugriz* photometry to variations in T_{eff} (see Figure 4 of GBB19). For instance, the errors drop significantly below $\sim 16,000$ K, where the *ugriz* photometry is very sensitive to T_{eff} , reaching values as small as 2% near 10,000 K. More puzzling is the significant increase in $\sigma_{T_{\text{eff}}}$ in the range $26,000 \text{ K} > T_{\text{eff}} > 22,000 \text{ K}$. We traced back this feature — never discussed in the literature, to our knowledge — to the particular behavior of the Eddington fluxes in the optical regions, which increase very slowly in this temperature

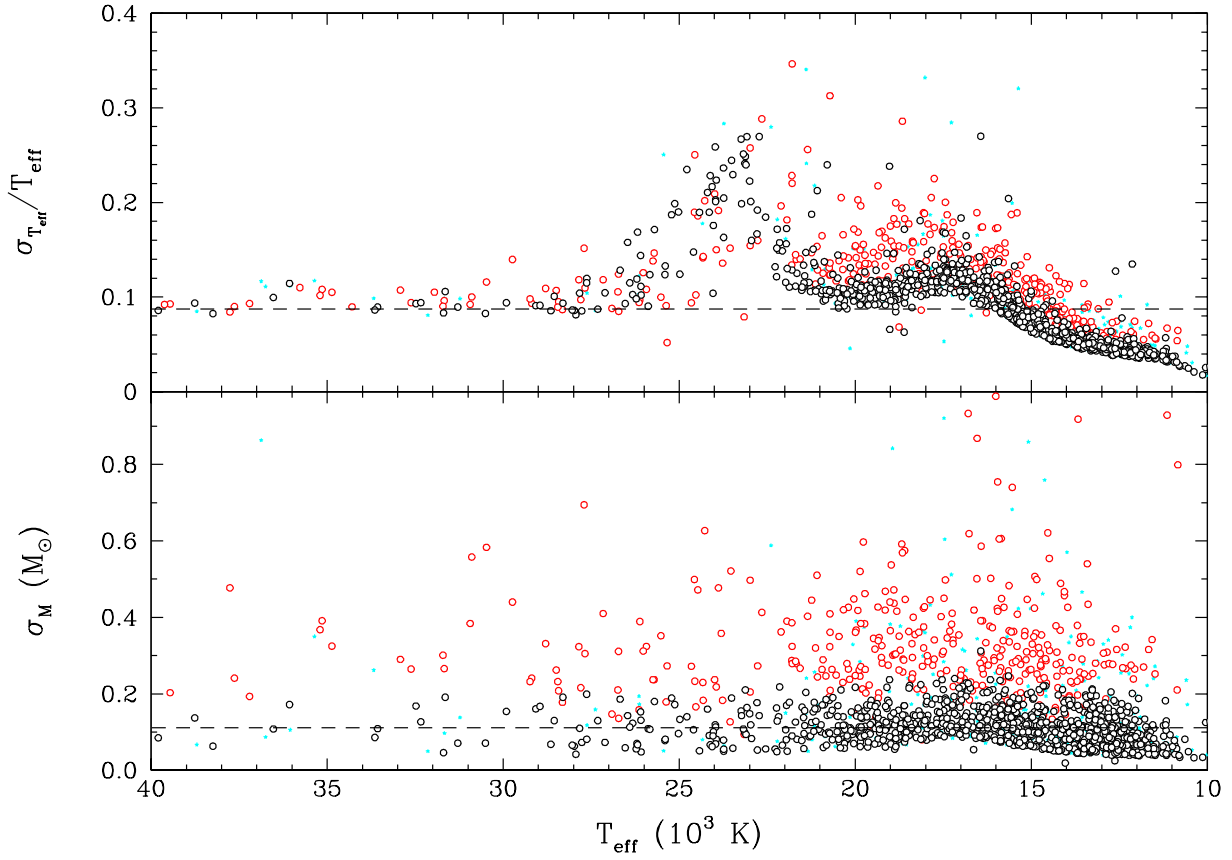


Figure 3.3. Distribution of errors on T_{eff} (top panel) and stellar mass (bottom panel) obtained from the photometric technique, as a function of effective temperature. The open circles represent the DB and DBA stars in our sample with $\sigma_{\pi}/\pi < 0.25$ (black) and $\sigma_{\pi}/\pi > 0.25$ (red). The dashed lines indicate the mean errors of the DB/DBA photometric subsample with $\sigma_{\pi}/\pi < 0.25$. All other spectral types are represented by cyan dots.

range³, when the main opacity source switches from the He I bound-free opacity to the He II free-free opacity, as illustrated in Figure 3.4. Finally, $\sigma_{T_{\text{eff}}}$ does not appear to be significantly affected by the parallax uncertainties σ_{π} . If we restrict our sample to the objects for which $\sigma_{\pi}/\pi < 0.25$, we obtain $\langle \sigma_{T_{\text{eff}}} \rangle = 8.7\%$, a value only slightly lower than that obtained above. This is an expected result since T_{eff} is determined mainly from the shape of the energy distribution, which does not depend on the parallactic distance (after dereddening).

The errors associated with photometric masses are presented in the bottom panel of Figure 3.3. The mean error for the overall sample is somewhat high, $\langle \sigma_M \rangle = 0.341 M_{\odot}$, but

3. The range of temperature at which this behavior is observed is actually a function of $\log g$.

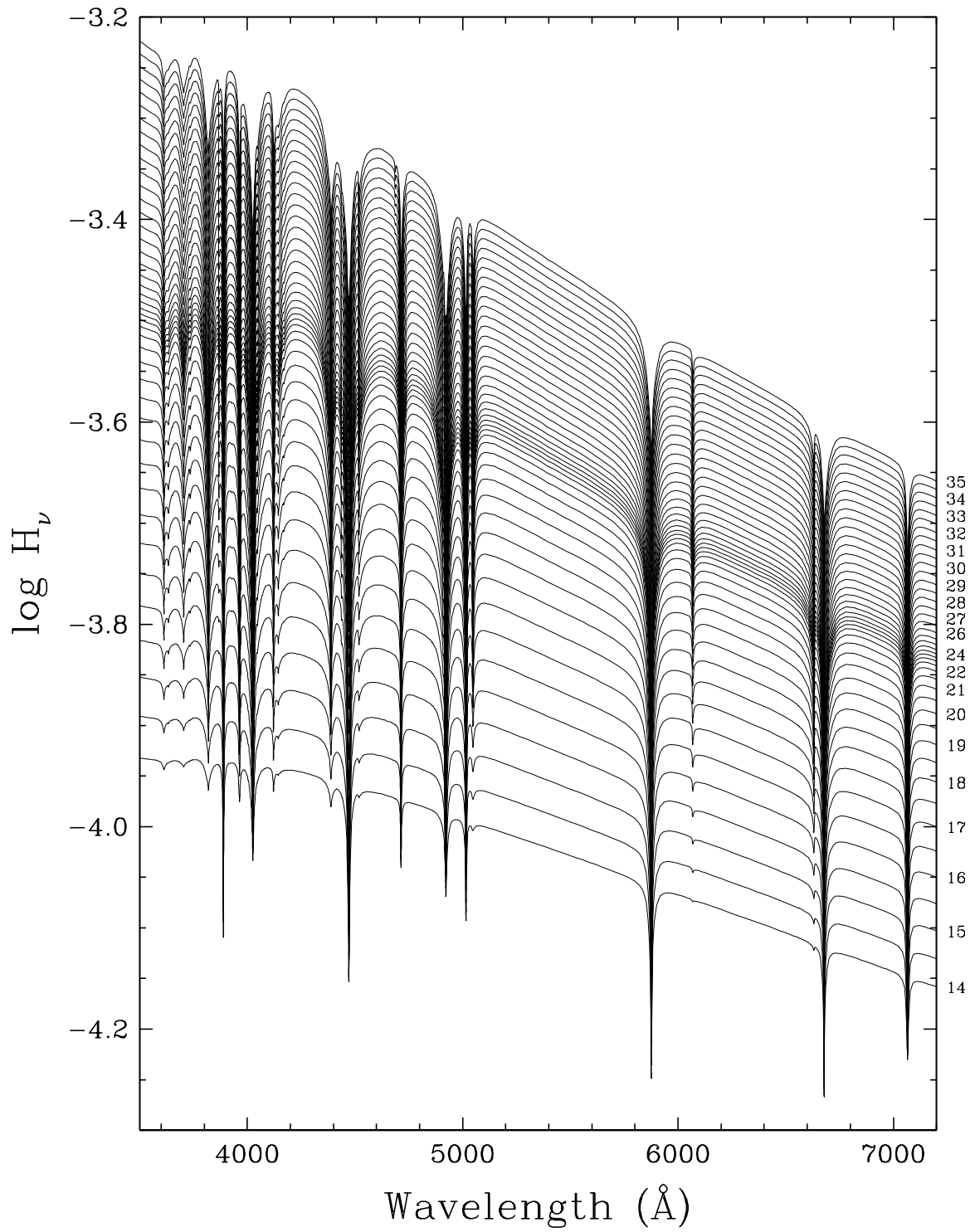


Figure 3.4. Eddington fluxes (in units of $\text{ergs cm}^{-2} \text{s}^{-1} \text{Hz}^{-1}$) as a function of wavelength for pure helium DB models at $\log g = 8$, and for various effective temperatures (in units of 10^3 K) indicated in the figure.

this is mostly caused by the objects in our sample with very large parallax uncertainties. Unlike for the effective temperature, the precision on the mass relies heavily on σ_π since the parallactic distance is used to obtain the radius from the solid angle, which is then converted into mass using the mass-radius relation (see section 4.1 of GBB19). If we restrict our sample to objects with $\sigma_\pi/\pi < 0.25$, we obtain a much lower mean value for the error of $\langle \sigma_M \rangle = 0.112 M_\odot$. We also note that the σ_M distribution in Figure 3.3 is fairly constant with effective temperature, unlike what is observed for $\sigma_{T_{\text{eff}}}$.

Finally, if we do not apply the 0.03 mag lower limit uncertainty on the *ugriz* magnitudes, the mean uncertainties are only slightly lower: $\langle \sigma_{T_{\text{eff}}} \rangle = 6.85\%$ and $\langle \sigma_M \rangle = 0.102 M_\odot$ (for $\sigma_\pi/\pi < 0.25$).

3.5.2. Spectroscopic Errors

The spectroscopic errors associated with the atmospheric parameters — T_{eff} , $\log g$, and H/He — can be estimated from the covariance matrix of the Levenberg-Marquadt procedure used in our fitting technique. These so-called *internal errors* represent the ability of our models to reproduce the data, and can be made arbitrarily small if the S/N of the spectra is high enough (see Liebert et al. 2005 for a full discussion). The internal errors on T_{eff} , $\log g$, and H/He are displayed in Figure 3.5 as a function of effective temperature, together with the errors on the spectroscopic mass, obtained by combining the effects of $\sigma_{T_{\text{eff}}}$ and $\sigma_{\log g}$ on the mass determination (note that σ_M is completely dominated by the contribution of $\sigma_{\log g}$, however).

The mean error on T_{eff} for the overall sample is $\langle \sigma_{T_{\text{eff}}} \rangle = 4.43\%$, or 2.59% if we restrict our sample to $S/N > 10$. The individual errors $\sigma_{T_{\text{eff}}}$ (in percentage) are fairly constant with effective temperature, except between $\sim 20,000$ K and $30,000$ K where the helium lines become less sensitive to T_{eff} (see Figure 1 of Bergeron et al. 2011). The mean error on $\log g$ is $\langle \sigma_{\log g} \rangle = 0.263$, and on the mass $\langle \sigma_M \rangle = 0.156 M_\odot$; these values drop to 0.163 and $0.088 M_\odot$, respectively, if we restrict our sample to $S/N > 10$. Unlike for $\sigma_{T_{\text{eff}}}$, there is no increased scatter in the distributions between $20,000$ K and $30,000$ K, indicating that the helium lines remain sensitive to $\log g$ and mass in this temperature range. However, we can see that the individual errors become more important below $T_{\text{eff}} \sim 16,000$ K, where neutral broadening remains a large source of uncertainty in our models (see GBB19 and references therein). If

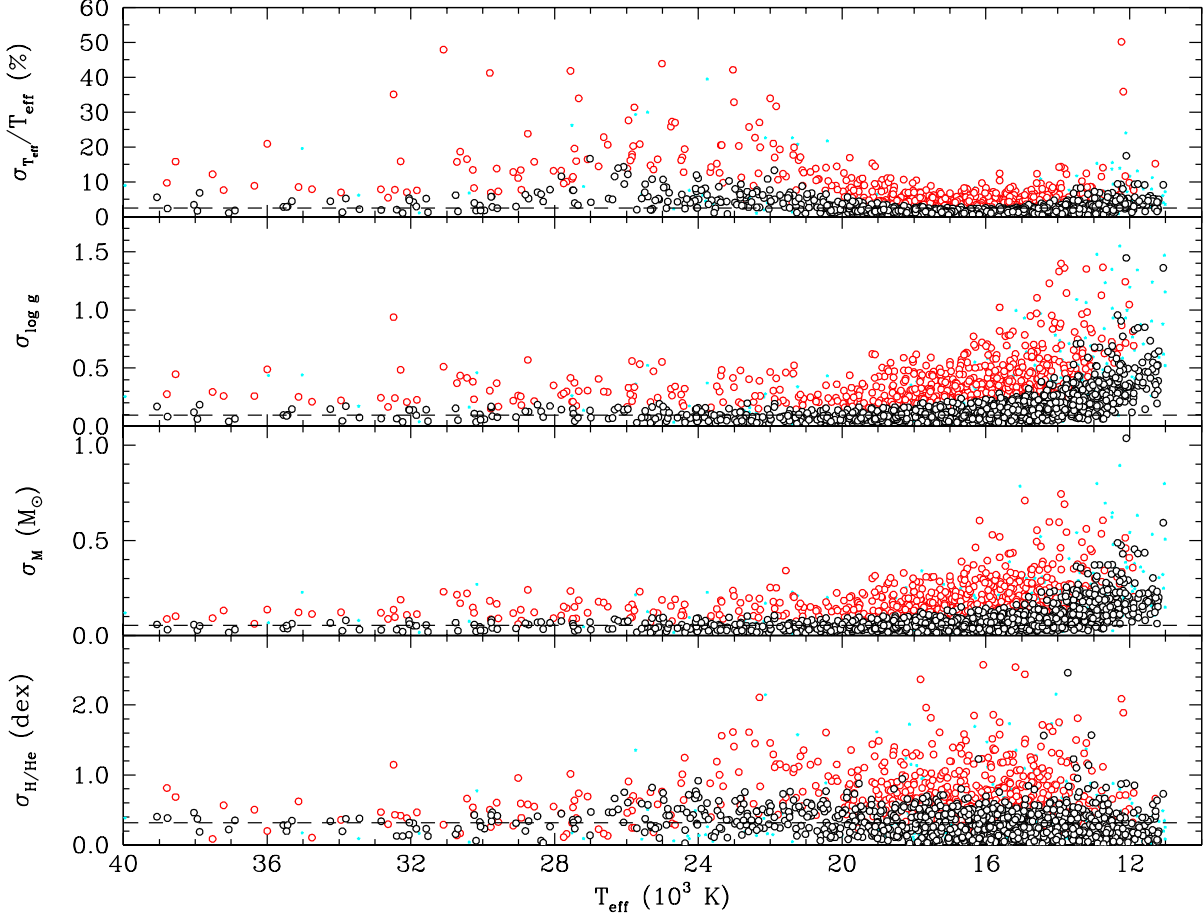


Figure 3.5. Internal errors on T_{eff} , $\log g$, M , and H/He obtained from the spectroscopic technique, as a function of effective temperature. The open circles represent the DB(Z) and DBA(Z) white dwarfs with $S/N > 10$ (black) and $S/N < 10$ (red); all other subtypes are represented by cyan dots. The dashed lines indicate the corresponding mean errors for the objects with $S/N > 10$, and $T_{\text{eff}} > 16,000$ K for $\sigma_{\log g}$ and σ_M .

we exclude the objects below 16,000 K, the mean errors drop even further to $\langle \sigma_{\log g} \rangle = 0.094$ and $\langle \sigma_M \rangle = 0.053 M_{\odot}$ (for $S/N > 10$). Finally, the mean error on the hydrogen abundance is $\langle \sigma_{\text{H/He}} \rangle = 0.486$ dex (or 0.314 dex for the sample with $S/N > 10$), but this somewhat large mean value is dominated by the objects for which we could only determine an upper limit on the hydrogen abundance. If we restrict our estimation to the DBA stars in our sample, the mean error drop to 0.298 dex (or 0.213 dex for the sample with $S/N > 10$).

Another way to estimate the errors using the spectroscopic technique is from multiple observations of the same star, as described for instance in Liebert et al. (2005) and Bergeron

et al. (2011). To get a good estimate of the external errors, we excluded all spectra with $S/N < 10$ as well as uncertain spectral types, which left us with 49 objects with multiple spectra. For those with more than two observations, we kept only the two highest S/N spectra. These so-called *external errors* are displayed in Figure 3.6. The mean external errors are $\langle \Delta T_{\text{eff}}/T_{\text{eff}} \rangle = 2.40\%$, $\langle \Delta \log g \rangle = 0.152$, $\langle \Delta M \rangle = 0.086 M_{\odot}$, and $\langle \Delta \text{H/He} \rangle = 0.199$ dex. These values compare favorably well with the internal errors discussed above. Bergeron et al. (2011) obtained smaller values of $\langle \Delta T_{\text{eff}}/T_{\text{eff}} \rangle = 2.3\%$ and $\langle \log g \rangle = 0.052$, which can be explained by the fact that the spectra used in their analysis had $S/N > 50$, while in our restricted sample $\langle S/N \rangle \sim 25$ (see Figure 3.1). Perhaps a more useful comparison is with the values obtained by Koester & Kepler (2015) based on multiple spectra from the SDSS. They obtained similar mean errors of 3.1% in T_{eff} , 0.12 in $\log g$, and 0.18 dex in H/He.

We reevaluate again in Section 3.6.5 the precision and accuracy of the photometric and spectroscopic techniques, but only after we compare the atmospheric and physical parameters determined using both fitting methods.

3.6. Atmospheric and Physical Parameters of DB White Dwarfs

Our main goal is to characterize the entire DB white dwarf population in the SDSS. To do so, we take advantage of the photometric and spectroscopic techniques to obtain independent determinations of the atmospheric and physical parameters of each star, such as the effective temperature T_{eff} , the surface gravity $\log g$, the stellar mass M , and the hydrogen abundance ratio H/He. Note that the latter can only be determined spectroscopically. The derived parameters are provided in Appendix C. Even though our sample contains several subtypes, particular attention will be given to the DB and DBA white dwarfs (with or without metals) as these represent about 80% of our sample (see Section 3.3). In this section, we discuss in turn the surface gravity, stellar mass, and photospheric hydrogen abundance distributions.

3.6.1. Surface Gravity Distributions

We present in Figure 3.7 the photometric and spectroscopic surface gravities as a function of effective temperature for all DB white dwarfs in our sample. The photometric $\log g$ distribution (upper panel) is well centered on the $0.6 M_{\odot}$ evolutionary sequence at all temperatures, as expected. Moreover, the dispersion in $\log g$ values appears fairly constant with

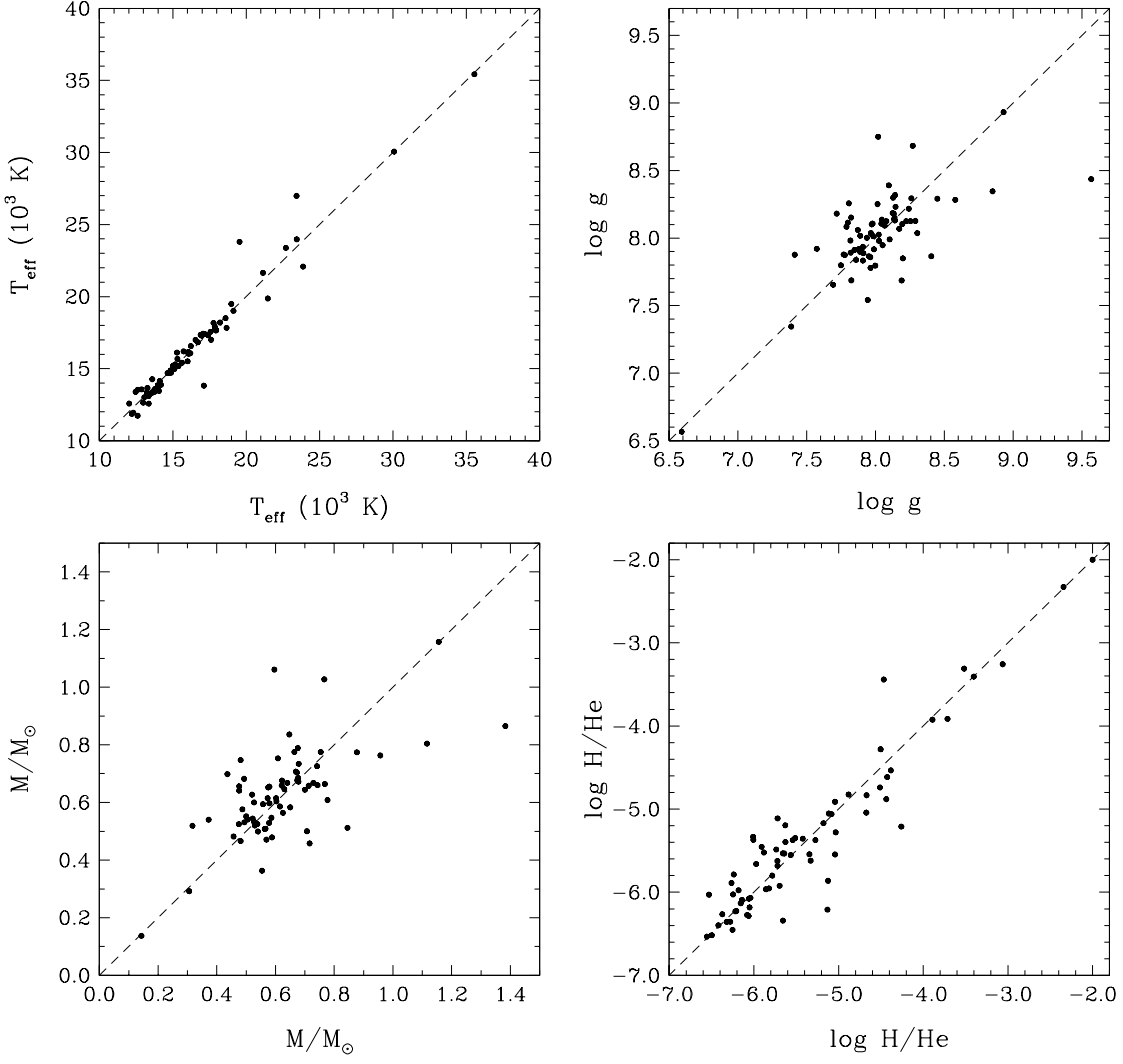


Figure 3.6. Comparison of T_{eff} , $\log g$, M , and $\log \text{H}/\text{He}$ for the 49 objects in our sample with multiple spectroscopic observations and with $S/N > 10$.

T_{eff} , and the distribution in temperature is also uniform, in the sense that there are no regions with an obvious accumulation or depletion of objects. The spectroscopic $\log g$ distribution (middle panel) is also uniform in temperature, but contrary to the photometric distribution, it deviates significantly from the $0.6 M_\odot$ sequence in several temperature ranges. First, at the very cool end of the distribution ($T_{\text{eff}} \lesssim 13,000 \text{ K}$), the $\log g$ values are much lower than the canonical $\log g = 8$ value. This behavior can be partially explained by the weakness of the helium lines in this temperature range (see Figure 3 of Rolland et al. 2018), and the spectroscopic technique has most likely reached its limits below which the atmospheric parameters become unreliable. We estimated this limit at the temperature where the equivalent width

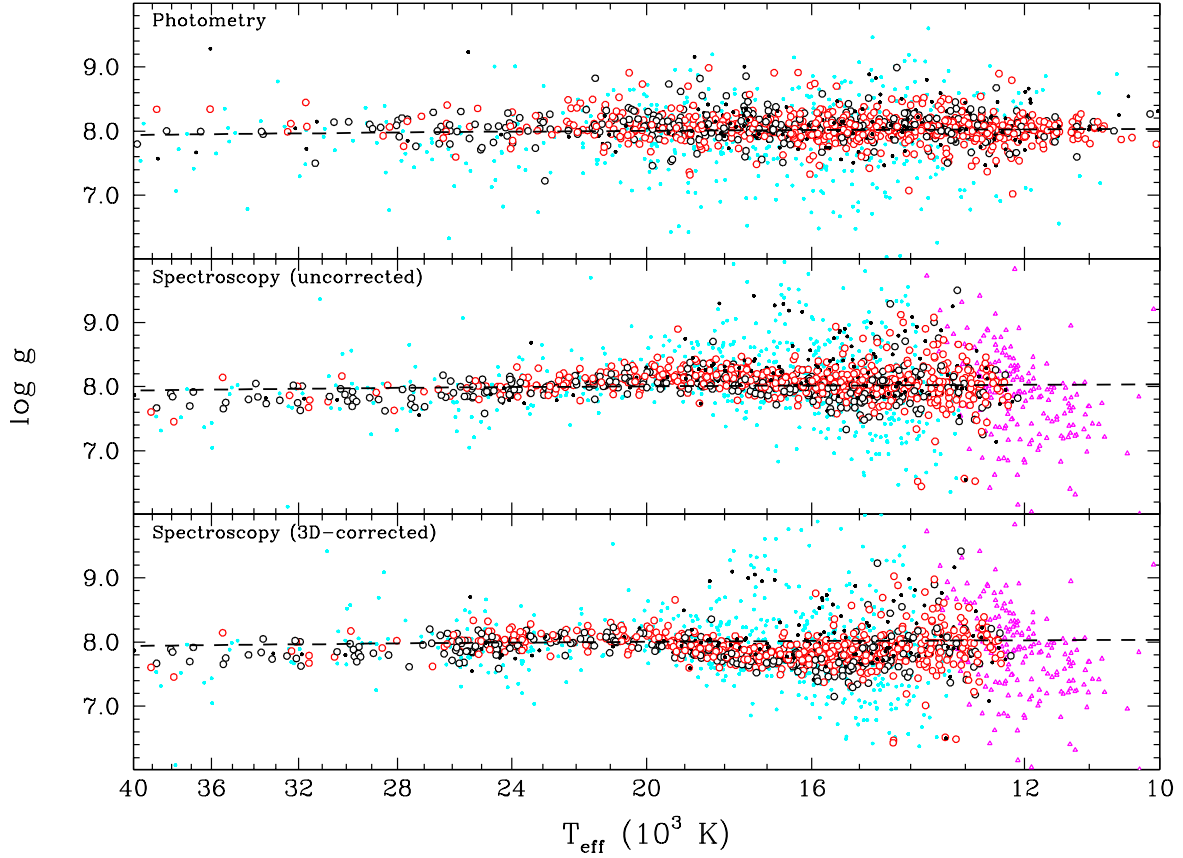


Figure 3.7. Photometric (upper panel) and spectroscopic (middle panel) $\log g$ distributions as a function of T_{eff} . The open circles represent the DB (black) and DBA (red), with or without metals, while the black dots correspond to other spectral types with $\sigma_{\pi}/\pi < 0.25$ (photometry) or $S/N > 10$ (spectroscopy). Spectra with marginal helium lines are shown as magenta triangles, and any object with $\sigma_{\pi}/\pi > 0.25$ or $S/N < 10$, regardless of the spectral type, is represented by a cyan dot. Bottom panel: Same as middle panel, but with the 3D hydrodynamical corrections taken into account. In all panels, the dashed line represents a $0.6 M_{\odot}$ evolutionary sequence.

of the He I $\lambda 4471$ line becomes smaller than 3 Å (4 Å, 5 Å) for $S/N > 20$ ($10 < S/N < 20$, $S/N < 10$). These objects are shown as magenta triangles in Figure 3.7 and will not be considered any further in our analysis.

However, even by removing from the sample these spectra with marginally detectable helium lines, we still see a larger scatter around $T_{\text{eff}} \sim 13,000 - 16,000$ K, in contrast to what is observed in photometry. The main line broadening mechanism in this particular

temperature range is the broadening by neutral particles, or more specifically van der Waals broadening. As mentioned in several studies, the large scatter at the cool end of the spectroscopic $\log g$ distribution ($T_{\text{eff}} < 16,000$ K) is mostly caused by the improper treatment of van der Waals broadening (Beauchamp et al. 1996; Bergeron et al. 2011; Koester & Kepler 2015; GBB19), and the theory currently used in our model atmospheres probably still requires some improvement in order to determine more accurate $\log g$ values below $T_{\text{eff}} = 16,000$ K. Nevertheless, we do find convincing cases of white dwarfs in this temperature range with a broad range of spectroscopic $\log g$ values. This is illustrated in Figure 3.8, where we show 3 DB(A) white dwarfs with similar spectroscopic temperatures ($T_{\text{eff}} \sim 14,700$ K), but with different surface gravities, ranging from $\log g = 7.7$ to 8.3 (see also Figure 7 of Limoges & Bergeron 2010 and the related discussion). For these 3 objects, the shape and strength of the He I $\lambda 3820$ and $\lambda 4388$ lines, which are particularly $\log g$ -sensitive in this temperature regime, vary significantly. We would like to stress that this is independent of any theoretical modeling, since it is observed directly in the spectrum. This suggests that, despite the unsatisfactory treatment of van der Waals broadening, at least part of the scatter in $\log g$ observed below $T_{\text{eff}} = 16,000$ K might be real after all. This is supported by the fact that the photometric distribution also shows several high- $\log g$ objects. We come back to this point further in Section 3.6.2.

At the hot end ($T_{\text{eff}} > 27,000$ K) of the spectroscopic $\log g$ distribution in Figure 3.7, we see also a trend towards lower $\log g$ values, with inferred masses below $0.6 M_{\odot}$, again in sharp contrast with what is observed in photometry⁴. Tremblay et al. (2011a) and Genest-Beaulieu & Bergeron (2014) observed a similar phenomenon when analyzing the spectroscopic $\log g$ distribution of DA white dwarfs from the SDSS. In this case, a comparison with the DA spectra taken from Gianninas et al. (2011, see for instance Figures 14 and 15 of Genest-Beaulieu & Bergeron), *where this effect was not observed*, indicated that the apparent decrease in $\log g$ when using the SDSS spectra could be attributed to residual flux calibration issues.

4. Note that these hot objects in spectroscopy appear at lower photometric temperatures when the energy distribution sampled by the *ugriz* photometry is in the Rayleigh-Jeans regime (see Figure 13 of GBB19), but this barely affects the photometric masses, as shown in Figure 17 of GBB19 (see also Figure 7 of Bergeron et al. 2019).

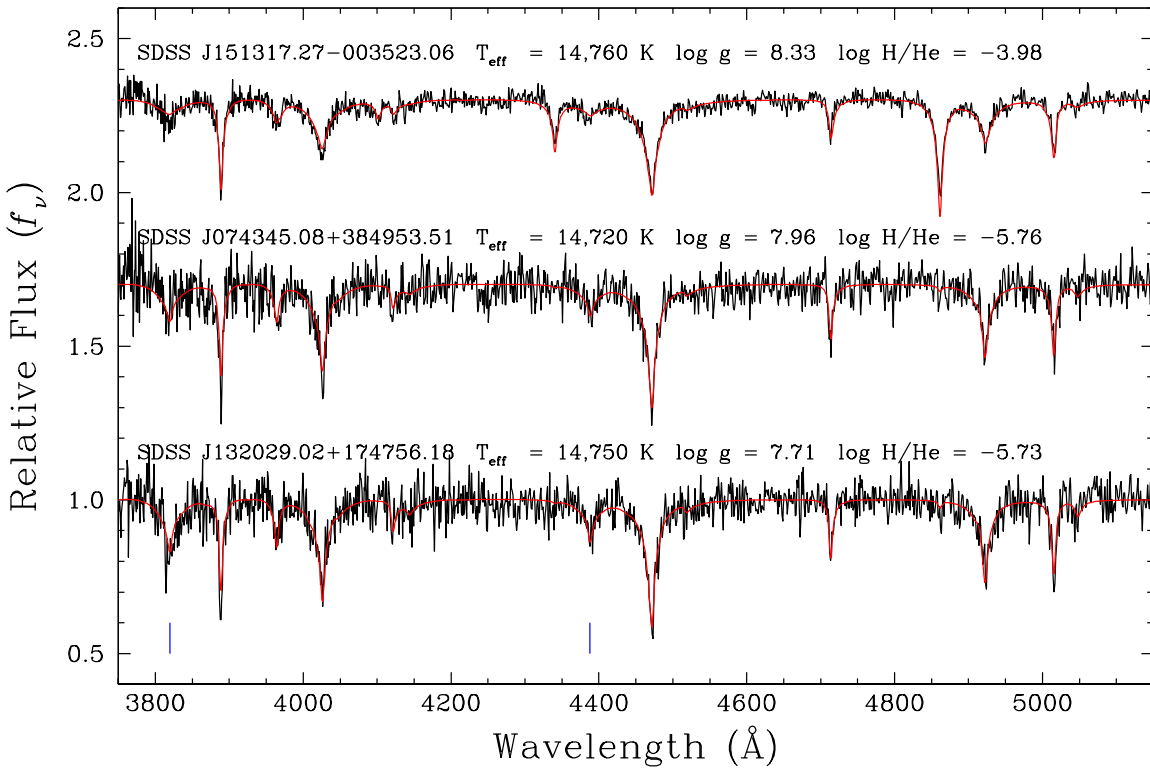


Figure 3.8. Our best spectroscopic fits to 3 DB(A) white dwarfs near $T_{\text{eff}} = 14,700 \text{ K}$, but with significantly different surface gravities. The spectra have been normalized to a continuum set to unity and the best-fit solutions are shown by the red lines. The atmospheric parameters for each object are indicated as well. The location of He I $\lambda 3820$ and $\lambda 4388$, which are the most $\log g$ -sensitive in this temperature regime, is shown by the blue tick marks.

Since this calibration problem must also affect the spectra of DB white dwarfs, we conclude that the apparent decrease in spectroscopic $\log g$ values observed in Figure 3.7 above $T_{\text{eff}} \sim 27,000 \text{ K}$ is most likely an artifact caused by calibration issues with the SDSS spectra.

Another possibility, mentioned by Koester & Kepler (2015), is that the cooler white dwarfs might originate from more massive progenitors, since DB stars at $T_{\text{eff}} \sim 10,000 \text{ K}$ are about 5×10^8 years older than those at $T_{\text{eff}} \sim 30,000 \text{ K}$. They estimated that the hotter stars could be less massive than the cooler ones by about $0.05 M_\odot$, thus explaining the slight decrease in $\log g$. However, even though this would be a valid explanation in a stellar cluster where there is a single burst of star formation, it certainly does not apply in the case of field

white dwarfs where continuous star formation occurs. And indeed, such an effect in $\log g$ (or mass) is not detected in the DA population (see Figure 30 of Gianninas et al. 2011 for instance).

Finally, the spectroscopic $\log g$ distribution in Figure 3.7 also shows a small but significant increase in the range $22,000 \text{ K} > T_{\text{eff}} > 16,000 \text{ K}$, also noted by GBB19. In this region, we obtain from spectroscopy $\langle \log g \rangle = 8.15$ (for $S/N > 10$), a value slightly larger than that obtained from photometry, $\langle \log g \rangle = 8.08$ (for $\sigma_{\pi}/\pi < 0.25$). This corresponds to the temperature range where the 3D hydrodynamical effects become important according to Cukanovaite et al. (2018), who recently calculated 3D model atmospheres for pure helium-atmosphere white dwarfs. Cukanovaite et al. also published 3D corrections (see their Table 2) to be applied to the 1D spectroscopic solutions (assuming $ML2/\alpha = 1.25$), which are reproduced here in Figure 3.9, for completeness. The largest corrections in $\log g$ occur near 17,000 K — which incidentally coincides with the maximum increase in $\log g$ observed in the middle panel of Figure 3.7 —, while the largest corrections in T_{eff} occur at much higher temperatures, near $T_{\text{eff}} = 25,000 \text{ K}$.

The 3D-corrected spectroscopic $\log g$ distribution for our sample is displayed in the bottom panel of Figure 3.7. While the mean $\log g$ value between 20,000 K and 22,000 K is now 8.05 — in excellent agreement with the photometric mean — the surface gravities below this temperature range are over-corrected when compared to the photometric results. For instance, between $T_{\text{eff}} \sim 15,000 \text{ K}$ and 20,000 K, the spectroscopic distribution has a mean value of $\log g = 7.87$ (for $S/N > 10$), which is 0.18 dex below the corresponding photometric value, suggesting that the $\log g$ corrections in this temperature range are probably overestimated. The 3D corrections in T_{eff} appear problematic as well. Indeed, while the photometric and uncorrected $\log g$ distributions are uniform as a function of effective temperature, the corrected spectroscopic distribution now shows an accumulation of objects around 25,000 K, as well as a depletion of objects near 28,000 K.

However, it is important to stress at this point that these 3D corrections are available for pure helium atmospheres only, and it is expected that calculations currently underway, which include the presence of hydrogen, will improve the results. We defer the rest of our discussion of these 3D corrections to the end of the next section.

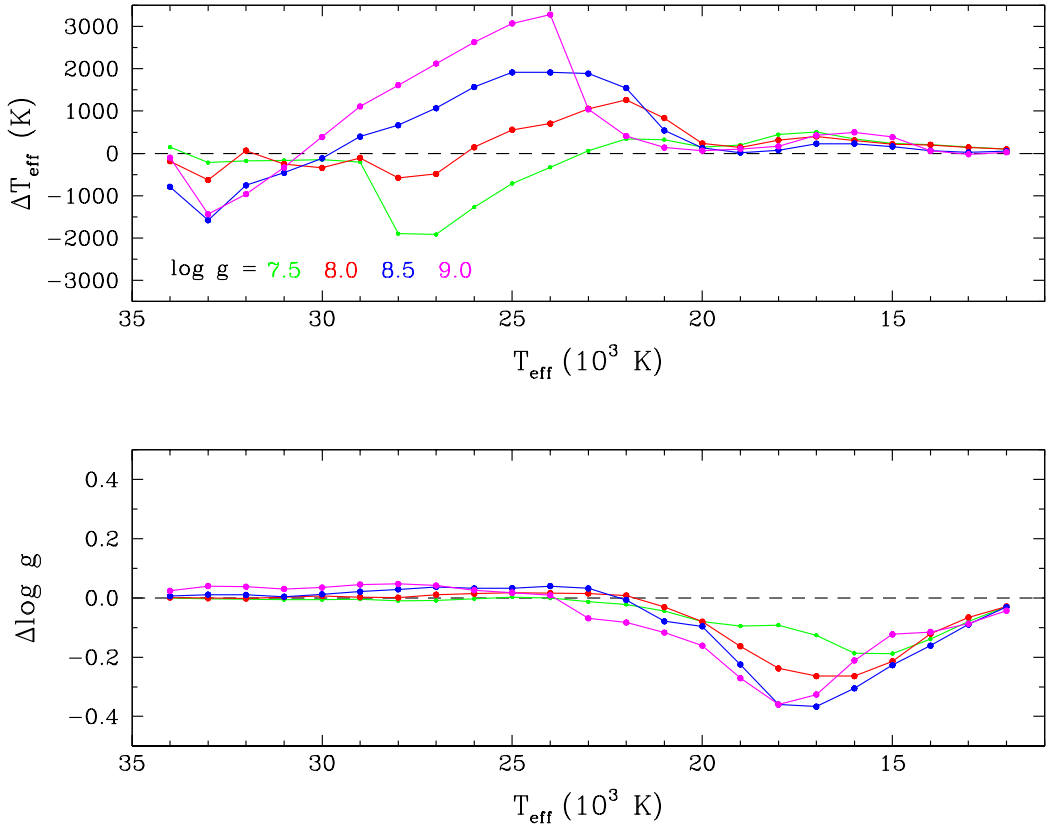


Figure 3.9. Theoretical 3D hydrodynamical corrections in T_{eff} (top panel) and $\log g$ (bottom panel) to be applied to 1D spectroscopic solutions, as a function of effective temperature and for various $\log g$ values, as described in Table 2 of Cukanovaite et al. (2018).

3.6.2. Mass Distributions

The stellar radii and $\log g$ values obtained from the photometric and spectroscopic techniques, respectively, can be converted into stellar mass using the evolutionary models described in Section 3.4. These photometric and spectroscopic masses for all the DB white dwarfs in our sample are displayed in Figure 3.10 as a function of effective temperature. We focus here on the results from our best data sets, represented by black and red circles for the DB and DBA white dwarfs, respectively. Not unexpectedly, we observe here the same behavior as with the $\log g$ distribution. In particular, the photometric mass distribution is well centered at $0.6 M_{\odot}$, while the spectroscopic distribution exhibits all the pitfalls previously described. Most noteworthy are the spectroscopic masses in the $16,000 - 22,000$ K temperature range, which are systematically larger than the canonical $0.6 M_{\odot}$ value, while

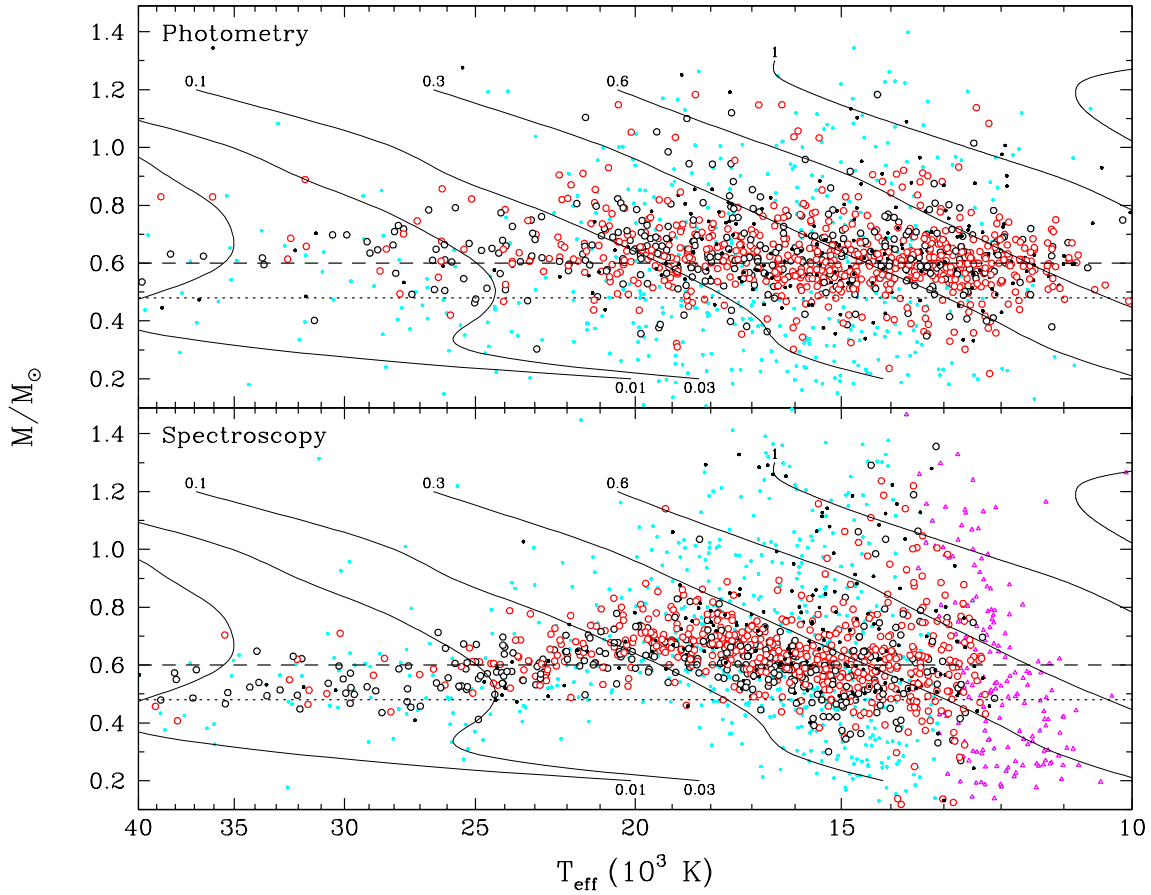


Figure 3.10. Photometric and spectroscopic masses as a function of effective temperature. The description of symbols is identical to that of Figure 3.7. Also shown as solid lines are theoretical isochrones obtained from models with C/O cores, $q(\text{He}) = 10^{-2}$, and $q(\text{H}) = 10^{-10}$, labeled in units of 10^9 years. The horizontal dotted and dashed lines are located at $M = 0.48 M_\odot$ and $M = 0.6 M_\odot$, respectively (see text).

they appear systematically lower than this value outside this temperature range. As discussed above, these features can be explained as a combination of residual flux calibration problems with the SDSS spectra, 3D hydrodynamical effects, and inadequate van der Waals broadening, which all affect our spectroscopic solutions.

Another way to investigate the white dwarf masses is to look at the cumulative mass distributions. To ensure the best possible mass values, we restricted our spectroscopic sample to the objects with $\text{S/N} > 10$, and discarded the spectra showing only marginal helium lines (see Section 3.6.1). Similarly, for the photometric mass distribution, we restricted our

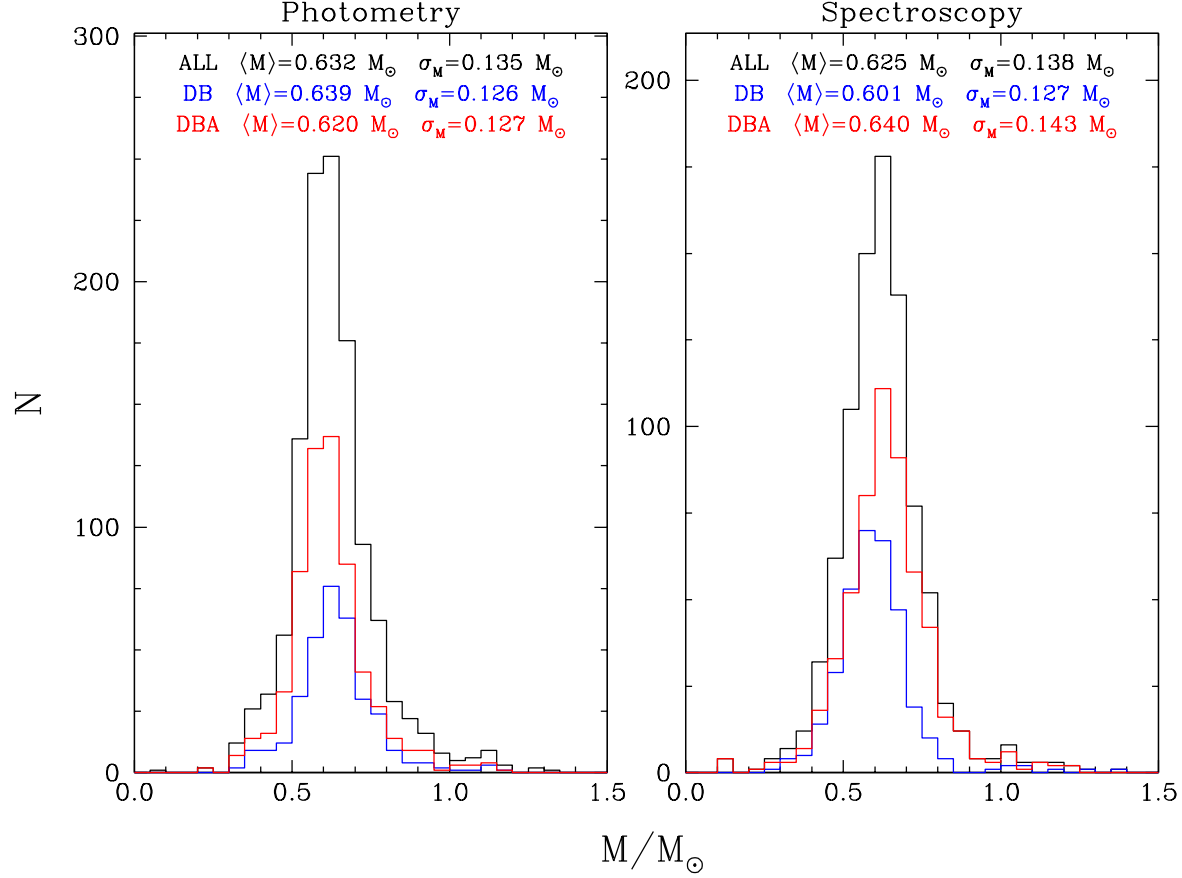


Figure 3.11. Left: Photometric mass distribution for the objects with $\sigma_{\pi}/\pi < 0.25$. Right: Spectroscopic mass distribution for the DB spectra with $S/N > 10$. The objects with very marginal helium lines and the few DBZ that did not converge within our grid have been excluded. Also shown are the corresponding mass distributions for the DB (blue) and DBA (red) subsamples. The mean masses and standard deviations are also given.

sample to $\sigma_{\pi}/\pi < 0.25$. The resulting cumulative mass distributions, both photometric and spectroscopic, are displayed in Figure 3.11. Despite the problems mentioned in the previous paragraph, the cumulative mass distributions obtained from photometry and spectroscopy are remarkably similar. They both have a mean mass of $\sim 0.63 M_{\odot}$, and very similar dispersions ($\sigma_{M,\text{phot}} = 0.135 M_{\odot}$ and $\sigma_{M,\text{spec}} = 0.138 M_{\odot}$). These mean masses are much lower than the value of $0.706 M_{\odot}$ reported by Koester & Kepler (2015) for their complete sample, which can probably be attributed to differences in model atmospheres and fitting techniques (see Section 3.6.4). Note, however, that their favored mean mass for DB white dwarfs is $0.606 M_{\odot}$, based exclusively on the objects between $T_{\text{eff}} = 16,000$ K and $22,000$ K.

One particular feature often reported regarding the mass distribution of DB white dwarfs is the complete absence of a low-mass tail (Beauchamp et al. 1996; Bergeron et al. 2011; GBB19), suggesting that common envelope evolution scenarios, which are often invoked to explain low-mass ($\lesssim 0.48 M_{\odot}$) DA stars (Bergeron et al., 1992), do not produce DB white dwarfs. Our spectroscopic mass distribution displayed in Figure 3.11 shows a few DB white dwarfs with such low masses, but an examination of Figure 3.10 (where this low-mass limit is indicated by the dotted line) reveals that these objects are located either below $T_{\text{eff}} = 16,000$ K, where our solutions are more uncertain due to the improper treatment of van der Waals broadening, or above $T_{\text{eff}} \sim 25,000$ K, where the calibration issues with the SDSS spectra affect the spectroscopic solutions. The photometric mass distributions in both Figures 3.10 and 3.11, which are not affected by these problems, also show several low-mass objects, but these are most likely unresolved double degenerates, as discussed in Section 3.7.1. Therefore, we find no evidence in our analysis for the existence of low-mass DB white dwarfs, a conclusion also reached by Beauchamp et al. (1996), Bergeron et al. (2011), and GBB19.

The high-mass tail of the spectroscopic mass distribution observed in Figure 3.11 is often attributed to the improper treatment of van der Waals broadening in model atmospheres (Bergeron et al. 2011; Koester & Kepler 2015; GBB19). This is supported by the fact that most objects with large spectroscopic masses are located below 16,000 K where this type of line broadening dominates (see Figure 3.10). This might not be the whole story, however, since the photometric mass distribution also shows a similar high-mass tail (see also Figure 3.10). We present in Figure 3.12 our best photometric and spectroscopic fits for four massive DB white dwarfs in our sample. In all cases, the photometric and spectroscopic solutions are in good agreement, within the uncertainties. Note also that they are not in the temperature regime where van der Waals broadening dominates. Consequently, their large inferred masses appear real. The existence of massive DA white dwarfs is usually explained by stellar mergers (Iben, 1990; Kilic et al., 2018), or as a result of the initial-to-final mass relation (El-Badry et al., 2018). The same mechanisms can possibly be invoked as well to explain the presence of such massive DB white dwarfs in our sample.

Another possible explanation for the origin of massive DB white dwarfs involves the so-called Hot DQ stars, whose atmospheres are dominated by carbon (Dufour et al., 2007, 2008).

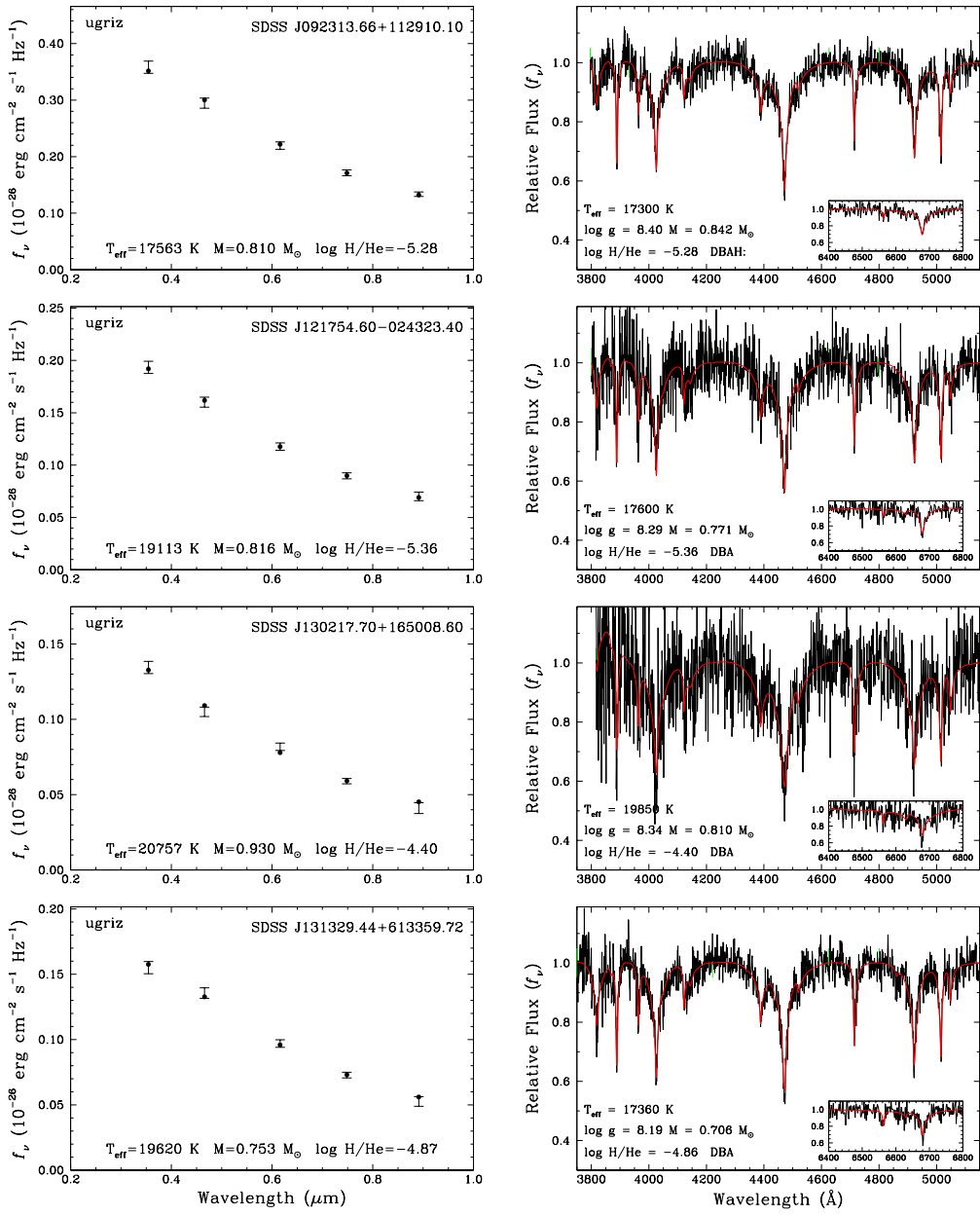


Figure 3.12. Left: Best photometric fits to four massive DB white dwarfs. The error bars represent the observed *ugriz* magnitudes and associated uncertainties, while the filled circles represent the best-fit model. Right: Corresponding best spectroscopic fits. The best-fit model (red) is plotted over the normalized observed spectrum (black). The inset shows the region near H α used to determine the hydrogen abundance, or upper limits. The derived atmospheric and physical parameters are also given.

Since Hot DQ white dwarfs are only found above $T_{\text{eff}} \sim 18,000$ K, Bergeron et al. (2011) proposed that they somehow transform into DB stars around that temperature, through a currently unknown physical mechanism. An examination of the upper panel of Figure 3.10 actually reveals that massive DB white dwarfs start to appear below $T_{\text{eff}} \sim 22,000$ K, coinciding with the coolest Hot DQ stars known today. The hot DQs also tend to be massive, since they are most likely the end result of white dwarf mergers (Dunlap & Clemens, 2015). Therefore, we suggest that some of the massive DB white dwarfs observed in our sample could be former Hot DQ stars.

Another particularly important issue is whether the mass distributions of DB and DBA white dwarfs differ or not. In our analysis, we considered an object to be a DB star if the spectroscopic technique could only determine an upper limit on the hydrogen abundance. The cumulative photometric mass distributions for DB and DBA white dwarfs are presented in the left panel of Figure 3.11. The comparison indicates that the average masses differ by less than $0.02 M_{\odot}$, and that their dispersions are identical, a result that is readily apparent when looking at the upper panel of Figure 3.10. A similar comparison with the spectroscopic mass distributions displayed in the right panel of Figure 3.11 suggest that DB white dwarfs are slightly less massive than DBA stars, by about $0.04 M_{\odot}$. However, it is also obvious from the results shown in the lower panel of Figure 3.10 that these mass differences stem from all the problems related with the spectroscopic technique across the entire temperature range, both observational and theoretical, as already discussed extensively above. We thus conclude that there is no significant mass difference between the DB and DBA white dwarfs, and that the explanation for the origin of hydrogen in DBA stars is not mass related.

Finally, we go back to our discussion of the 3D hydrodynamical corrections by looking at the cumulative mass distributions. In Figure 3.13, we compare the photometric masses — which are unaffected by 3D effects — with those obtained spectroscopically, both uncorrected and 3D-corrected. Note that the mass distributions displayed here include only the DB white dwarfs in common with both the photometric and spectroscopic samples. Although the photometric and uncorrected spectroscopic mass distributions overlap almost perfectly, the 3D-corrected distribution is significantly shifted towards lower masses. Its mean mass is $\langle M \rangle = 0.55 M_{\odot}$, which is $0.06 M_{\odot}$ lower than the value inferred from photometry, $\langle M \rangle = 0.61 M_{\odot}$. This again suggests that the proposed 3D corrections in $\log g$ are too strong. As

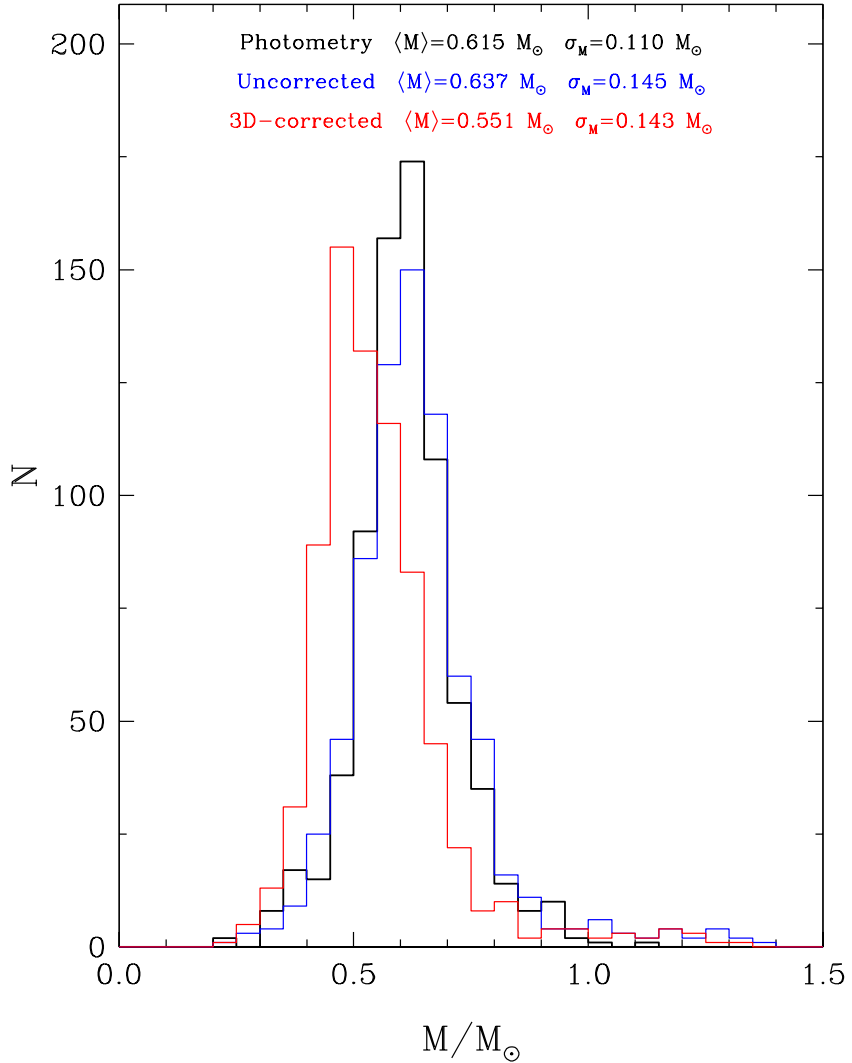


Figure 3.13. Cumulative mass distributions obtained from photometry (black) and spectroscopy (blue: uncorrected; red: 3D-corrected), for the DB white dwarfs in common between the photometric and spectroscopic samples. The objects with $S/N < 10$, $\sigma_\pi/\pi > 0.25$, or marginal helium lines have been excluded. The mean masses and standard deviations are also given in the figure.

previously mentioned, however, the corrections applied here are appropriate for pure helium models only, and it is possible that 3D hydrodynamical models including traces of hydrogen will yield a more satisfactory agreement. For the time being, since most objects in our sample show traces of hydrogen, we will refrain from applying the 3D corrections to our spectroscopic parameters in the remainder of this study.

3.6.3. Hydrogen Abundance Distribution

The final parameter we need to discuss is the hydrogen abundance ratio, H/He , which is displayed in Figure 3.14 as a function of effective temperature for all the objects in our spectroscopic sample. Since the limit of detectability of $H\alpha$ depends on the quality of the spectroscopic observations, we only kept the spectrum with the highest S/N for the objects with multiple observations. Also, as mentioned above, we considered an object to be a DB star if only an upper limit on the hydrogen abundance could be determined by our fitting technique. With this definition, we find that 61% of the objects in our sample are DBA white dwarfs, a ratio which is similar to the 63% obtained by Rolland et al. (2018), but somewhat lower than the 75% reported by Koester & Kepler (2015), although their higher value was obtained by restricting their spectroscopic sample to $S/N > 40$ (their Table 3 actually reveals a much broader range of values).

The general abundance pattern observed in Figure 3.14 is consistent with the deepening of the helium convection zone as the star cools off (see, e.g., Figure 9 of Rolland et al. 2018), in which hydrogen is gradually being diluted into a larger and more massive convective envelope. It is thus not surprising to find some of the largest hydrogen abundances at high temperatures, where the helium convection zone is the shallowest. Note that in all cases, hydrogen always remains a trace element in the stellar envelope, and its presence does not affect the structure of the convection zone in any way (Rolland et al., 2018).

Despite the poor quality of some of the SDSS spectra with $S/N < 10$ (shown by cyan dots in Figure 3.14), we can see that the derived hydrogen abundances overlap perfectly with the bulk of our other determinations, except at the hot end of the sequence where $H\alpha$ becomes increasingly more difficult to detect, especially in low S/N spectra. In such cases our fitting algorithm may yield unreliable hydrogen abundance measurements. At the cool end of the sequence, however, we are able to obtain reasonable hydrogen abundances, even from white dwarf spectra where helium lines are barely detected.

Perhaps the most striking feature in Figure 3.14 is the range of H/He values at a given effective temperature, which can reach as much as 3 orders of magnitude near $T_{\text{eff}} \sim 17,000$ K. Note that at these temperatures, $H\alpha$ can be easily detected spectroscopically, and hydrogen abundances as low as $H/He \sim 10^{-6}$ can be effectively measured, even with a relatively low S/N spectrum (see the detection limits in Figure 3.14). Even so, there is a significant fraction

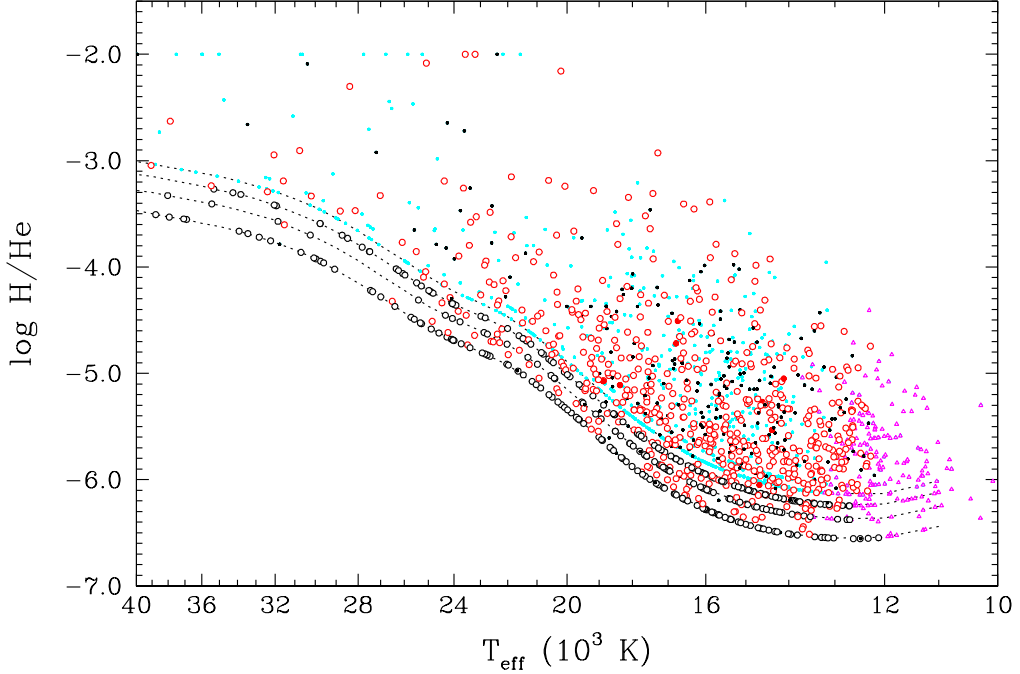


Figure 3.14. Hydrogen abundances as a function of effective temperature. The description of symbols is identical to that of Figure 3.7, with the exception that unresolved DB+DA candidates (see Section 3.7.1) are shown by red filled circles. Limits on the hydrogen abundance set by our spectroscopic observations at $\text{H}\alpha$ are shown as dotted lines for (from bottom to top) $S/N > 20$ ($200 \text{ m}\text{\AA}$ equivalent width), $15 < S/N < 20$ ($300 \text{ m}\text{\AA}$), $10 < S/N < 15$ ($400 \text{ m}\text{\AA}$), and $S/N < 10$ ($500 \text{ m}\text{\AA}$).

of DB white dwarfs in our sample, *found at all temperatures*, showing no $\text{H}\alpha$ absorption feature. Four of these, selected in a temperature range where $\text{H}\alpha$ can be most easily detected, are displayed in Figure 3.15. These cool DB stars have so little hydrogen that they must have maintained hydrogen-poor envelopes throughout their evolution. Hence, whatever scenario is invoked to explain the presence of hydrogen in DBA white dwarfs, it must be able to account for the large spread in hydrogen abundances observed here. We discuss this issue at length in Section 3.8.2.

3.6.4. Comparison with Koester & Kepler (2015)

Koester & Kepler (2015) performed a similar analysis of the DB white dwarfs in the SDSS, also drawn from the SDSS DR10 and DR12. The comparison of their effective temperatures, surface gravities, and hydrogen abundances for the 996 objects in common with

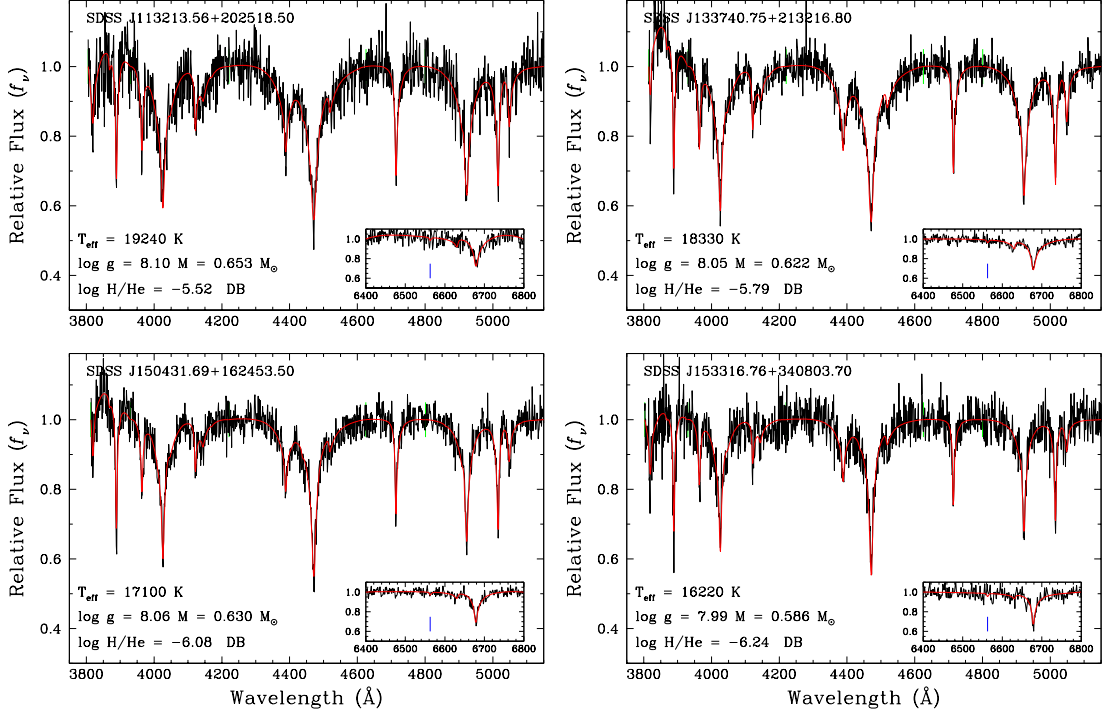


Figure 3.15. Best spectroscopic fit to four cool DB white dwarfs with no detectable H α feature. The best-fit model (red) is plotted over the normalized observed spectrum (black). The inset shows the region near H α (indicated by the tick mark) used to determine the hydrogen abundance, or upper limits. The derived atmospheric parameters are also given in each panel.

our analysis is presented in Figure 3.16. If we exclude the objects below $T_{\text{eff}} = 16,000$ K, for which Koester & Kepler assumed $\log g = 8.0$, we find a good overall agreement between our atmospheric parameters and theirs. There are however some slight discrepancies between the two sets of values, in particular around $T_{\text{eff}} \sim 24,000$ K where the helium lines reach their maximum strength. Around this region, our effective temperatures, surface gravities, and hydrogen abundances are in general higher than their values, but there is also a lot more scatter. Koester & Kepler also mention a deficiency of objects in the interval $T_{\text{eff}} = 24,000 - 26,000$ K (see their Figure 1 and Table 2), which they attribute to either the assumed convective efficiency, or to flux calibration issues with the SDSS spectra. While we use the same convective efficiency ($\text{ML2}/\alpha=1.25$) and the same SDSS spectra, we do not see such a depletion of objects in this temperature range (see, e.g., Figure 3.10). All these small

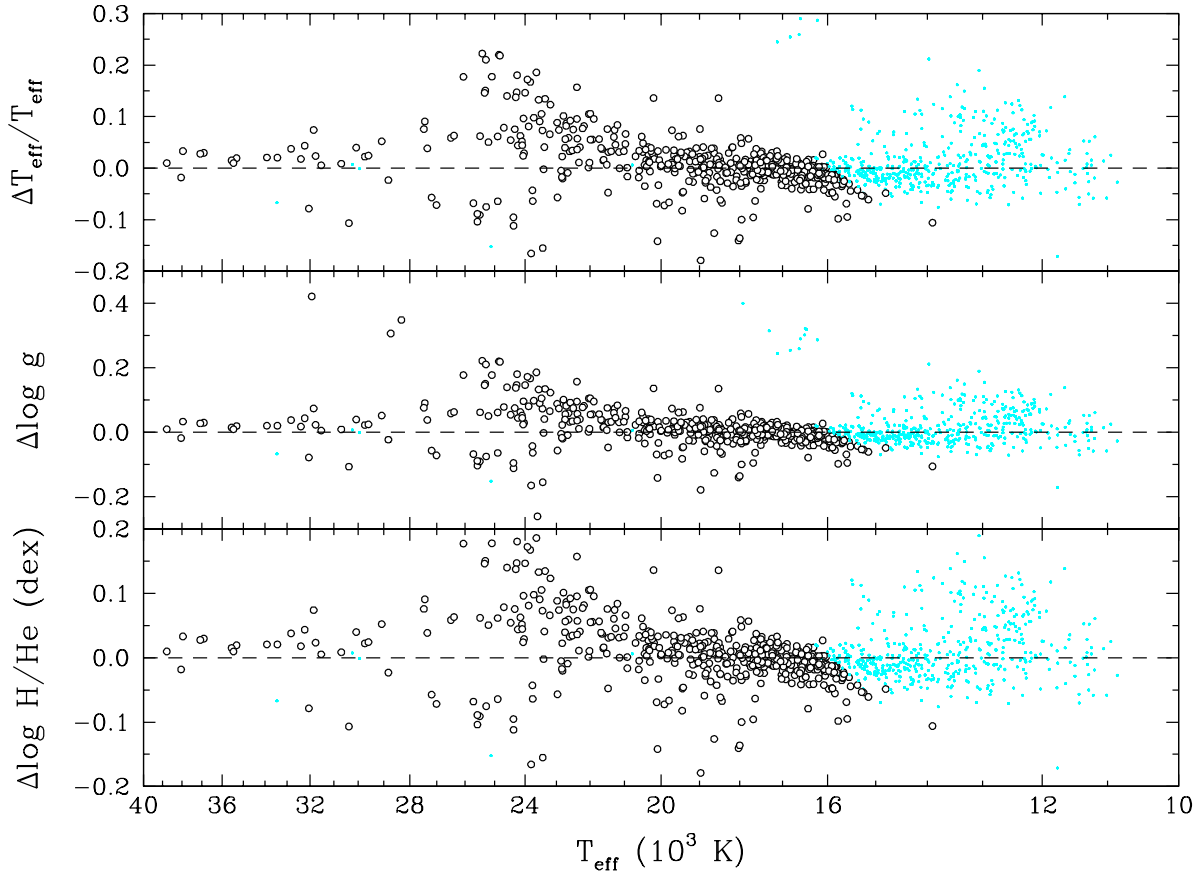


Figure 3.16. Differences in effective temperatures, surface gravities, and hydrogen abundances as a function of effective temperature between our analysis and that of Koester & Kepler (2015). The cyan dots represent the objects for which Koester & Kepler assumed $\log g = 8.0$.

discrepancies between their analysis and ours can probably be attributed to differences in model atmospheres and/or fitting techniques.

Koester & Kepler (2015) also find that, below $T_{\text{eff}} \sim 16,000$ K, their spectroscopic $\log g$ values (or masses) increase steadily, forming an almost continuous distribution (see their Figure 1). In particular, they find almost no cool DB white dwarfs with $\log g \sim 8.0$ in this temperature range, in contrast with our surface gravity distribution displayed in Figure 3.7, which shows a spread rather than a continuous increase in $\log g$ below $T_{\text{eff}} \sim 16,000$ K (see also Figure 6 of Rolland et al. 2018). Moreover, we find a significant number of white dwarfs with normal masses (see Figure 3.8), or even lower than average. These discrepant results are most likely due to differences in the treatment of van der Waals broadening between both

sets of model atmospheres. This may also explain the mean mass of $0.706 M_{\odot}$ obtained by Koester & Kepler for their complete sample, while we find a much lower value of $0.63 M_{\odot}$.

3.6.5. Accuracy and Precision of the Fitting Techniques

At this point in our analysis, it is worth reevaluating the accuracy and the precision of both the photometric and spectroscopic techniques for determining the physical parameters of DB white dwarfs using the *ugriz* photometry and optical spectra from the SDSS. In this context, the precision refers to the level of agreement of a measurement with itself when it is repeated several times, while the accuracy refers to the proximity of the measurement to the true physical value.

On the basis of our best data sets — i.e. the spectroscopic sample with $S/N > 10$ and the photometric sample with $\sigma_{\pi}/\pi < 0.25$ — we conclude that, on average, the spectroscopic technique is more *precise* than the photometric technique for determining the effective temperatures of DB white dwarfs — $\langle \sigma_{T_{\text{eff}}} \rangle = 2.59\%$ from spectroscopy versus 8.72% from photometry — *when using the SDSS photometric and spectroscopic data*. At low effective temperatures, however, the photometric technique becomes as precise as the spectroscopic technique, if not more ($\langle \sigma_{T_{\text{eff}}} \rangle \sim 2\%$ from photometry at 10,000 K). For the determination of stellar masses, the errors are also smaller from spectroscopy ($\langle \sigma_M \rangle = 0.053 M_{\odot}$ ⁵ from spectroscopy versus $0.112 M_{\odot}$ from photometry). Of course, the photometric technique may potentially yield more precise mass measurements than the spectroscopic technique, regardless of the temperature range, provided that σ_{π}/π is small enough (see section 3.5.1).

As mentioned in GBB19, the synthetic photometry is less affected by the input physics of the model atmospheres than the model spectra. For the DB white dwarfs analyzed here, the photometric mass distribution was found to be well centered on $M = 0.6 M_{\odot}$, at all temperatures, while the spectroscopic distribution deviated from this value between 21,000 K and 17,000 K, as well as below 16,000 K (see Section 3.6.2). However, GBB19 found a good agreement between the photometric and spectroscopic temperatures, except at the hot end of the distribution, where the *ugriz* photometry is in the Rayleigh-Jeans regime. We thus conclude that, for DB stars, both fitting techniques have a similar accuracy for the

5. We exclude here the temperature range where van der Waals broadening becomes a problem in our model spectra.

determination of effective temperatures, but the photometric technique is more accurate for measuring stellar masses.

Since we will compare in Section 3.8.1 the distribution of DB and DA white dwarfs, we briefly summarize some of the results from GBB19 regarding the DA stars. GBB19 found that the spectroscopic temperatures of DA stars were \sim 10% higher than the photometric values for $T_{\text{eff}} > 14,000$ K, which they attributed to some inaccuracy in the theory of Stark broadening for hydrogen lines. The spectroscopic and photometric masses, however, were in very good agreement. We thus conclude that, for the DA stars, the photometric technique is more accurate than the spectroscopic technique for the determination of effective temperatures, but both techniques have a similar accuracy when it comes to mass determinations. As for the DB white dwarfs, GBB19 also found that the spectroscopic technique yields more precise temperature and mass measurements than the photometric technique.

3.7. Objects of Particular Astrophysical Interest

Our analysis of the atmospheric and physical parameters of DB white dwarfs, described in the previous section, has revealed the existence of several objects of particular astrophysical interest. We discuss these objects in turn.

3.7.1. Double Degenerate Candidates

Unresolved double degenerate binaries can be identified by their extremely low spectroscopic masses (see, e.g., Bergeron et al. 1992), or alternatively, by their overluminosities in Hertzsprung-Russel diagrams (see Figure 10 of Bergeron et al. 1997). In the last case, due to the presence of two stars in the system, the radius is overestimated, and thus the photometric mass is underestimated. GBB19 have already identified several such degenerate binaries in the SDSS data, both spectroscopically and photometrically.

One type of double degenerate system that can be easily recognized is those composed of a DA and a DB white dwarf, an excellent example of which is KUV 02196+2816, analyzed in detail by Limoges et al. (2009). The observed spectrum of such systems resembles that of a DBA white dwarf, but the hydrogen lines are usually extremely strong and poorly reproduced by single star, homogeneous models (see Figure 19 of GBB19). We identified a total of 10 DA+DB unresolved double degenerates in our sample, listed in Table 3.1. It is

possible to obtain the effective temperatures of both components of the system by fitting the spectrum with a combination of pure hydrogen and helium-rich synthetic spectra. For simplicity, we assume here $\log g = 8.0$ for both components of the system, and a pure helium atmosphere for the DB white dwarf. The photometric⁶ and spectroscopic solutions obtained for these systems under the assumption of a single star are reported in Table 3.1, together with the effective temperatures obtained for the individual DA and DB components; our best fits are also presented in Appendix A. Note that in all cases where a parallax measurement is available, the photometric $\log g$ values are significantly lower than those inferred from spectroscopy.

Of these 10 double degenerate systems, SDSS J150506.24+383017.39 has already been reported by GBB19, while SDSS J011356.38+301514.62 has been interpreted by Manseau et al. (2016) as a hot, chemically homogeneous DBA white dwarf with $T_{\text{eff}} = 29,200$ K, $\log g = 7.91$, and $\log H/\text{He} = -1.05$. Our photometric solution for this last object, displayed in the top panel of Figure 3.17 and obtained under the assumption of a single star, implies a much lower temperature. Also, the low inferred photometric mass of only $0.236 M_{\odot}$ clearly indicates the presence of a double degenerate system. In the lower panel, we compare the spectroscopic fit obtained by Manseau et al. (2016), our own spectroscopic solution at lower effective temperature, and our spectroscopic solution assuming a DA+DB system. Clearly, this last solution provides not only the best fit to the observed spectrum, but the average temperature of the system also agrees perfectly with the photometric temperature. Finally, SDSS J091016.43+210554.20 is classified as magnetic (Kleinman et al., 2013), but our fit displayed in Appendix A indicates that this is undoubtedly a DA+DB degenerate binary, and interestingly enough, both components appear to be magnetic! Indeed, Zeeman splitting can be easily detected in both hydrogen ($H\alpha$ in particular) and helium lines.

Another type of double degenerate system we found in our sample, also discussed in GBB19, is composed of two DB white dwarfs. Unlike the DA+DB systems, these DB+DB binaries cannot be easily recognized from spectroscopy alone, since the combination of two DB spectra resembles that of a single DB white dwarf with intermediate atmospheric parameters (see Figure 20 of GBB19). However, they can still be identified by comparing

6. We simply assume $\log g = 8$ if no trigonometric parallax measurement is available.

Table 3.1. List of DA+DB double degenerate candidates

SDSS name	Photometry		Spectroscopy			Deconvolution	
	T_{eff}	M	T_{eff}	M	$\log \text{H/He}$	T_{DA}	T_{DB}
	(K)	(M_{\odot})	(K)	(M_{\odot})		(K)	(K)
011356.38 + 301514.62	14,030	0.24	16,780	0.69	-4.719	10,110	18,260
074419.82 + 302203.40 ¹	12,670	0.59	14,610	0.62	-5.270	11,330	15,770
084716.21 + 484220.40	15,280	0.62	14,680	0.88	-6.050	10,080	15,470
091016.43 + 210554.20 ²	14,900	0.67	15,390	0.72	-5.745	9,580	15,610
101316.02 + 075915.20	18,880	0.32	18,870	0.73	-5.075	12,210	30,360
103609.48 + 193841.14 ¹	15,910	0.59	16,740	0.73	-4.509	9980	16,880
112711.72 + 325229.70	13,070	0.21	14,380	0.57	-5.532	10,410	15,260
113623.54 + 320403.80 ¹	15,590	0.59	18,370	0.82	-5.111	14,120	25,800
140615.80 + 562725.90	38,700	0.45	14,340	0.91	-5.512	13,360	48,810
150506.24 + 383017.39	12,620	0.30	14,110	0.39	-5.049	10,180	15,490

¹ Photometric solution obtained by assuming $\log g = 8.0$.

² The DB and the DA components are both magnetic.

the spectroscopic and photometric masses since, as discussed above, unresolved double degenerate binaries will have low inferred photometric masses, but more normal spectroscopic masses. Because our mass estimates depend on the quality of the data, we restricted our photometric sample to objects with $\sigma_{\pi}/\pi < 25\%$, and our spectroscopic sample to objects with $S/N > 10$; we also excluded spectra showing only marginal helium lines. We then flagged the objects for which $M_{\text{spec}} - M_{\text{phot}} \geq 0.2 M_{\odot}$. Similarly, we also flagged all objects with $M_{\text{phot}} \leq 0.45 M_{\odot}$, because single star evolution predicts that such low-mass white dwarfs could not have formed within the lifetime of the Galaxy. After removing the previously identified DA+DB systems, we were left with 55 DB+DB unresolved double degenerate candidates. These systems, as well as the best photometric and spectroscopic solutions, are listed in Table 3.2. For the DA+DB systems, we were able to separate the contributions of each white dwarf. In the case of DB+DB binaries, it is possible, in principle, to deconvolve the parameters of both systems using the photometry and parallax information (Bédard et al., 2017), but this is clearly outside the scope of this paper. We would like to note that,

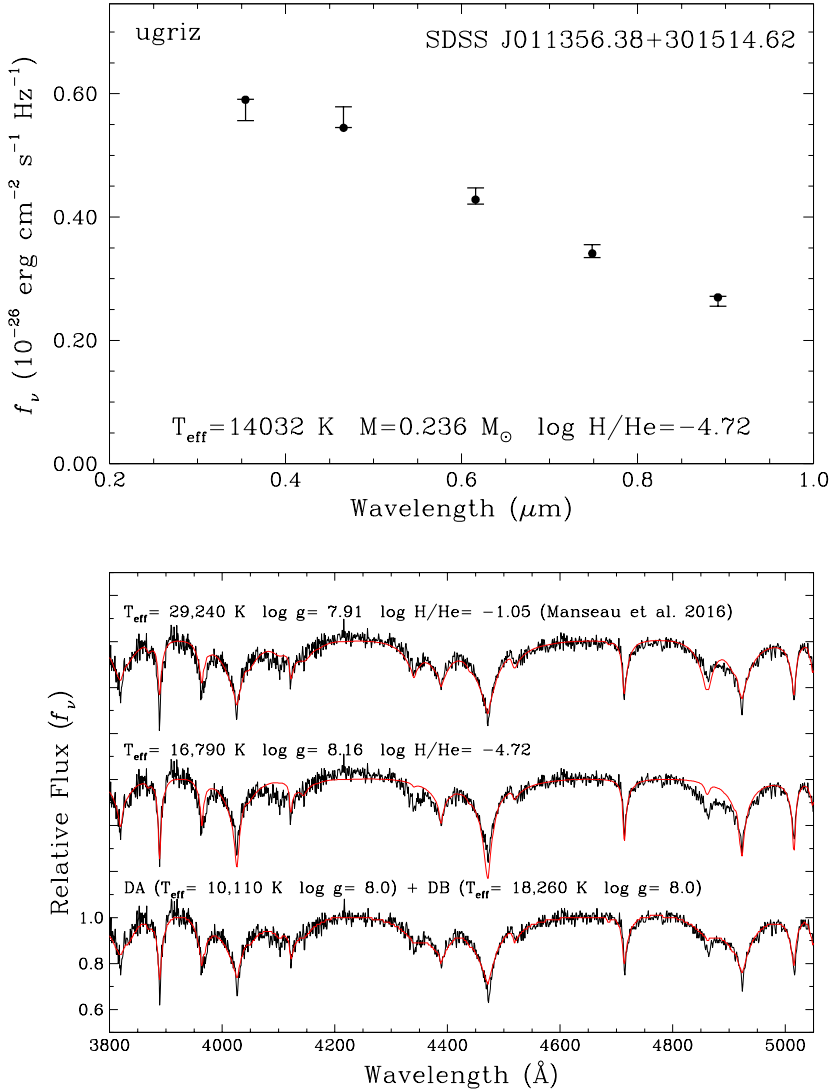


Figure 3.17. Top panel: Best photometric fit to SDSS J011356.38+301514.62 under the assumption of a single DBA white dwarf. Bottom panel: (top) best spectroscopic fit obtained by Manseau et al. (2016); (middle) our best spectroscopic fit at lower temperature; (bottom) our best fit obtained under the assumption of an unresolved DA+DB system. The atmospheric parameters of each fit are also given.

since we applied a restriction on the quality of the trigonometric parallax as well as on S/N, the list of DB+DB double degenerate systems given in Table 3.2 is by no means complete.

We summarize the results of this section by showing in Figure 3.18 the location of both DA+DB and DB+DB double degenerate candidates in a mass versus T_{eff} diagram. Remember that the photometric and spectroscopic temperatures generally differ for these systems.

Table 3.2. List of DB+DB double degenerate candidates

SDSS name	Photometry		Spectroscopy			SDSS name	Photometry		Spectroscopy		
	T_{eff} (K)	M (M_{\odot})	T_{eff} (K)	M (M_{\odot})	$\log \text{H/He}$		T_{eff} (K)	M (M_{\odot})	T_{eff} (K)	M (M_{\odot})	$\log \text{H/He}$
000730.75+275111.90	13,932	0.41	16,305	0.63	-5.880	120203.13+285647.07	16,043	0.38	17179	0.69	-5.231
002153.33+083141.82	27,313	0.49	17,789	0.81	-5.733	120735.19+225905.70	25,020	0.46	20,592	0.68	-5.201
004900.48-094203.00	18,466	0.46	19,419	0.78	-4.434	122444.73+174145.85 ¹	15967	0.40	14,527	0.61	-5.613
010532.40+064234.18 ¹	13,368	0.36	13,404	0.41	-5.694	123230.41+035036.70 ¹	19349	0.38	18,295	0.57	-5.801
011023.82+223716.25 ¹	12,275	0.42	12,771	0.59	-5.714	123735.52+602833.00 ¹	12195	0.22	15,863	0.48	-5.649
011409.86+272739.42	15,833	0.34	17,540	0.68	-4.887	124058.65+532623.60	16,327	0.57	17,591	0.89	-5.271
020409.84+212948.58	15,071	0.59	20,605	0.83	-3.186	125030.21+594932.90 ¹	14844	0.42	15,831	0.59	-5.963
024232.63-050954.75 ¹	12,181	0.40	14,438	0.56	-5.871	130106.26+023455.30	17,660	0.45	17,706	0.77	-5.570
034741.96+010823.80	26,320	0.55	17,809	0.78	-4.844	130830.53+470017.90 ¹	14705	0.42	17,109	0.54	-5.737
052941.58+603806.80 ¹	13,612	0.39	16,823	0.50	-5.665	131658.16+305148.00	18,987	0.52	19,635	0.76	-4.448
064452.30+371144.30 ¹	14,077	0.41	15,241	0.57	-6.030	141337.74+450431.60	19,841	0.36	24,983	0.61	-4.222
075224.32+150352.34 ¹	12,219	0.38	13,562	0.54	-6.373	141621.79+322638.60 ¹	31289	0.40	35,428	0.47	-3.407
082323.20+360834.79 ¹	14,876	0.39	15,180	0.65	-6.208	144650.87+285142.30	22,944	0.30	22,817	0.57	-4.479
083024.17+455206.02 ¹	15,272	0.45	14,546	0.57	-5.296	150301.95+053414.05 ¹	13681	0.45	13,120	0.75	-5.705
093512.70+003857.12 ¹	12,472	0.36	12,853	0.60	-6.053	150647.60+310313.30 ¹	18682	0.42	18,530	0.59	-5.388
093806.30+032242.53	20,190	0.49	18,864	0.74	-5.068	152320.96+005525.10 ¹	13317	0.35	13,758	0.78	-6.207
094023.58+185837.24 ¹	12,891	0.33	13,449	0.53	-6.219	153024.23+331549.72	18,154	0.47	17,544	0.70	-4.340
094638.77+621759.50 ¹	12,248	0.40	12,840	0.34	-6.244	153316.76+340803.70	16,636	0.36	16,223	0.58	-6.243
095455.12+440330.30	18,398	0.59	23,829	0.79	-4.416	153735.17+063848.07	20,498	0.49	19,785	0.79	-3.663
100140.17+025853.19	16,397	0.52	18,526	0.73	-4.689	154811.34+083613.21	21,175	0.47	19,480	0.70	-4.802
100904.42+060817.50	18,565	0.45	18,325	0.83	-5.384	161735.37+311645.41	18,860	0.31	18,470	0.60	-3.593
101022.37+272239.30	17,118	0.38	16,028	0.59	-6.085	165339.17+174838.84	16,633	0.41	18,714	0.70	-4.916
101249.63+412311.04	15,888	0.52	16,363	0.89	-5.260	165946.51+393418.30 ¹	19311	0.39	24,325	0.50	-4.454
102953.32+020812.45 ¹	14,963	0.39	14,201	0.70	-4.853	172243.19+603059.70	16,614	0.49	18,921	0.77	-5.622
103033.20+385447.59	21,194	0.44	20,387	0.80	-4.810	231041.15+141600.80 ¹	15,781	0.42	14,938	0.49	-6.097
104117.42+231036.40	25,880	0.42	21,596	0.63	-4.784	232344.88+150858.80	14,800	0.33	19,707	0.88	-4.321
105829.24+655227.20 ¹	13,665	0.43	15,381	0.42	-6.182	233305.10+005155.90	17,239	0.35	21,506	0.68	-4.405
111946.75+673631.10 ¹	13,284	0.39	15,207	0.60	-5.625						

¹ Based on photometry only

One can see that both types of binary systems are impossible to detect in spectroscopy alone, in contrast with the case of DA stars (see, e.g., Bergeron et al., 1992). However, most binary systems — but not all of them — appear as low-mass white dwarfs in the photometric mass distribution, even the DA+DB binaries.

3.7.2. DBA White Dwarfs with Large Hydrogen Abundances

There are several DBA white dwarfs in our sample with extremely large hydrogen abundances, defined arbitrarily here as $\log \text{H/He} > -3$. While we can find 9 such objects in Figure

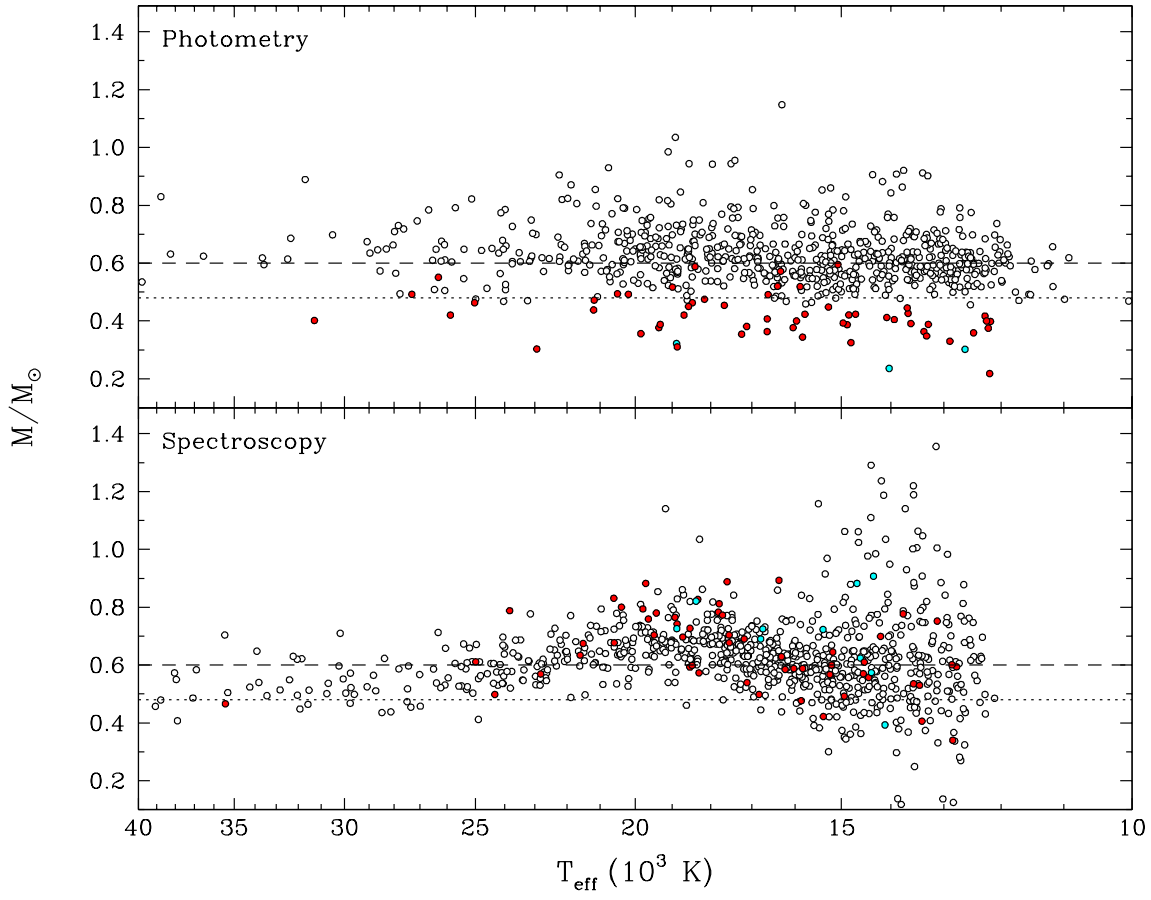


Figure 3.18. Photometric (top) and spectroscopic (bottom) masses as a function of effective temperature. DB+DB and DA+DB double degenerate candidates are shown as red and cyan circles, respectively. The horizontal dotted and dashed lines are located at $M = 0.48 M_{\odot}$ and $M = 0.6 M_{\odot}$, respectively.

3.14, only a single white dwarf with a very large hydrogen abundance ($\log H/He \sim -2$) has been identified by Rolland et al. (2018, see their Figure 5), namely PG 1311+129, also discussed at length by Bergeron et al. (2011). Among these 9 DBA stars in our sample, the five hottest objects above $T_{\text{eff}} = 24,000$ K have spectra with $S/N \sim 10$ and the presence of $H\alpha$ cannot be confirmed with certainty. However, the four cooler DBA white dwarfs, displayed in Figure 3.19, have strong, and well-defined $H\alpha$ features. One of these objects is SDSS J153725.72+51526.90 (WD 1536+520), also analyzed in detail by Farihi et al. (2016). Our best spectroscopic fit yields a hydrogen abundance of $\log H/He = -2.16$, while Farihi et al. reported an even larger hydrogen abundance of $\log H/He = -1.70$, as well as large

abundances of various heavy elements (O, Mg, Al, Si, Ca, Ti, Cr, Fe). Farihi et al. concluded that WD 1536+520 was currently accreting debris from a rocky and H₂O-rich parent body. The accretion of hydrogen in this process would also be responsible for the abnormally large hydrogen abundances observed in this DBA(Z) white dwarf. We discuss these objects further in Section 3.8.2.

3.7.3. DBZ White Dwarfs

We found a total of 118 white dwarfs in our sample with a published spectral type indicating the presence of metals (DBZ/DBAZ) in their spectrum. This is obviously a lower limit to the true number of DBZ stars, because the detection of metals — mostly the Ca II H and K doublet — depends strongly on the spectral resolution and S/N. For instance, SDSS J153725.72+51526.90 (WD 1536+520), already displayed in Figure 3.19, shows large abundances of various heavy elements (O, Mg, Al, Si, Ca, Ti, Cr, Fe; Farihi et al. 2016), but it is classified as a DBA star in the SDSS. As discussed in Section 3.4, the DBZ white dwarfs in our sample have been fitted with a specific grid of model atmospheres that includes only calcium in the equation of state and opacity calculations. This is a simplistic approach, but at least it has the benefits of including the most important (probably only) metallic features detected in the SDSS spectra of DBZ white dwarfs.

We present in Figure 3.20 our best spectroscopic fits to four DBZ white dwarfs in our sample with strong Ca II H and K lines, two of which also show a detectable H α absorption feature. In the other two cases, we detect no hydrogen, and its abundance is thus set to our limit of detectability ($\log \text{H}/\text{He} \lesssim -6$). Hence, even though the accretion of metals is often associated with the probable accretion of water-rich material (see Farihi et al. 2016, Gentile Fusillo et al. 2017, and references therein), giving rise to large photospheric hydrogen abundances such as in WD 1536+520, we do find in our sample some objects with large metal abundances, *but with no detectable hydrogen in their atmospheres*. This conclusion is based on DBZ white dwarfs found in a temperature range ($T_{\text{eff}} \sim 14,000 - 17,000$ K) where our limit of detectability is extremely low (see Figure 3.14). We come back to this point below.

3.7.4. Magnetic White Dwarfs

In section 3.6.2, we discussed the presence of massive DB white dwarfs in our photometric sample. While most of these were found below $T_{\text{eff}} \sim 22,000$ K, there are two very

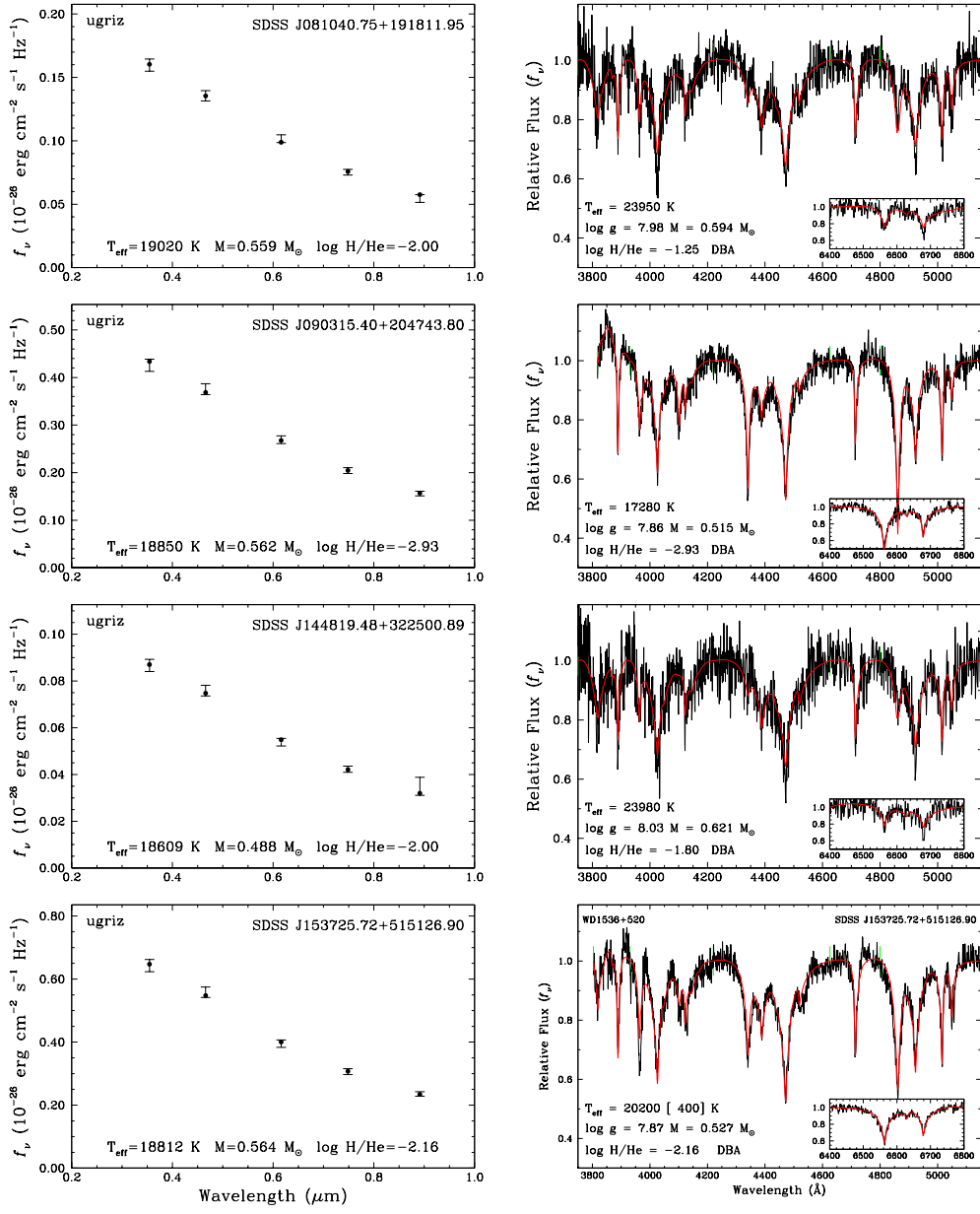


Figure 3.19. Best photometric (left) and spectroscopic (right) fits to four DBA white dwarfs in our sample with extremely large hydrogen abundances. The display is similar to that described in Figure 3.12.

massive objects located around $T_{\text{eff}} \sim 25,500$ K and 36,000 K (small black dots in the upper panel of Figure 3.10). These correspond to SDSS J094209.49+540157.50 and SDSS J143739.13+315248.80, which are classified as magnetic DB white dwarfs (DBH), with no clear absorption lines in their spectra, most likely due to the presence of a strong magnetic

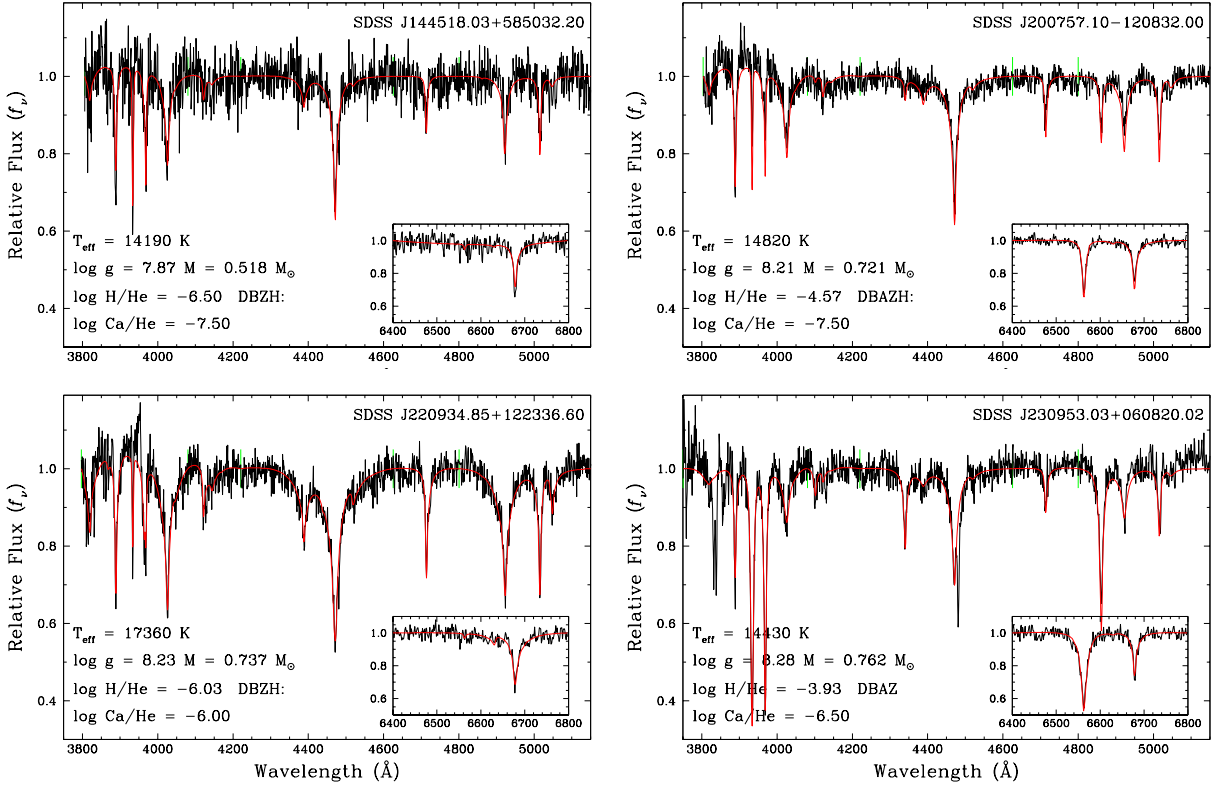


Figure 3.20. Best spectroscopic fits to four DBZ white dwarfs in our sample with strong Ca II H & K lines, without (left) and with (right) detectable hydrogen features (H α region shown in the inset).

field. For both of these objects, the photometric fit yields a very large mass of $M \sim 1.3 M_\odot$. Even though our solutions for these objects are uncertain at best, magnetic white dwarfs do tend to be more massive than the non-magnetic population (Liebert, 1988; Ferrario et al., 2015), in agreement with our results.

In some other magnetic DB stars, the magnetic field is strong enough that Zeeman splitting of the helium lines becomes clearly visible. Three examples are presented in Figure 3.21, together with our fits to SDSS J094209.49+540157.50, mentioned in the previous paragraph. In the last case, our spectroscopic fit is meaningless because the spectrum is featureless, but the photometric fit appears reasonable. Note that most objects displayed here have large inferred photometric masses (including the featureless white dwarf at $1.344 M_\odot$), but not all of them. Moreover, we also note in the case of the magnetic DA+DB double degenerate candidate SDSS J091016.43+210554.20, discussed above and displayed in Appendix A, that

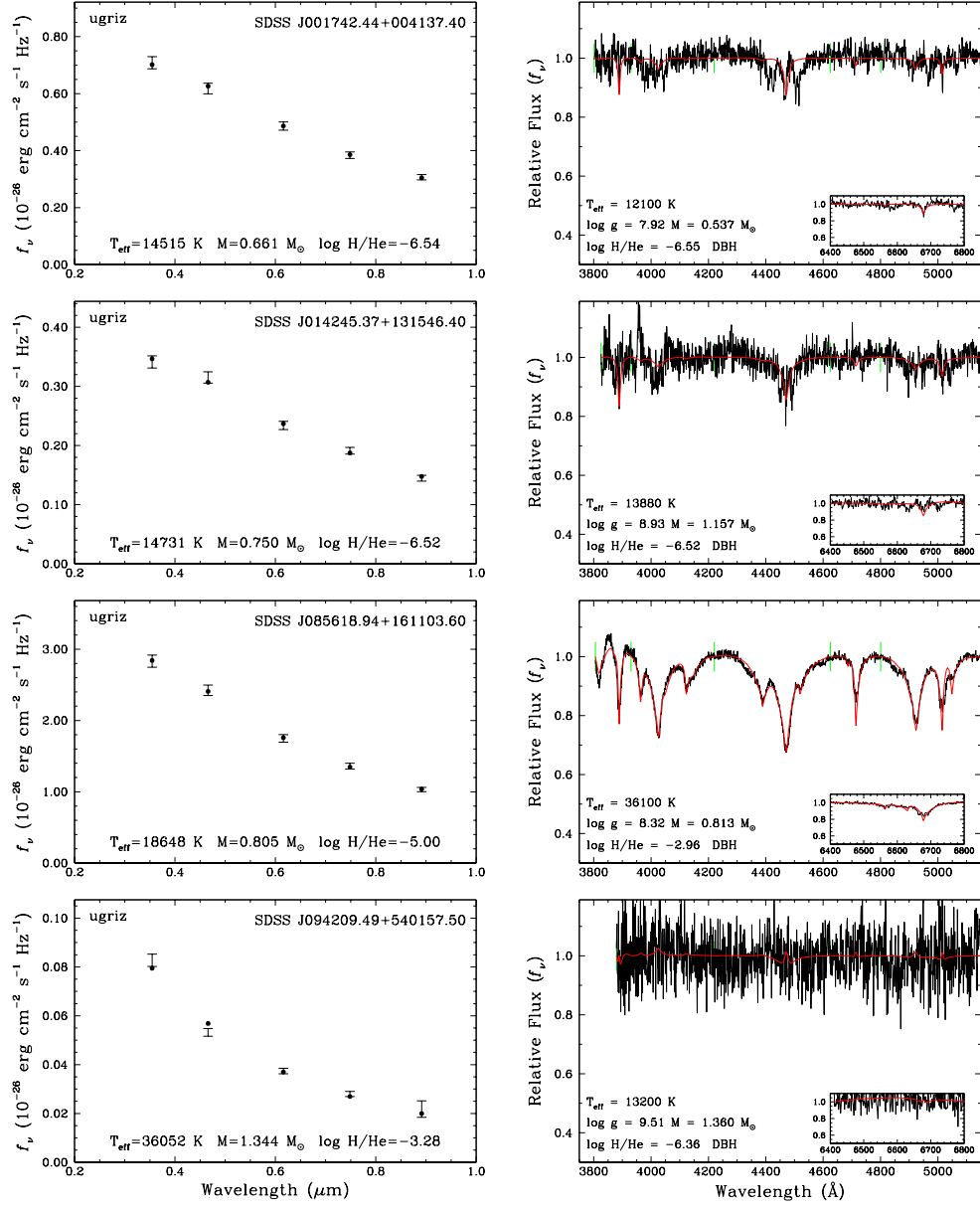


Figure 3.21. Best photometric (left) and spectroscopic (right) fits to four magnetic DB white dwarfs in our sample. The display is similar to that described in Figure 3.12.

it has the highest inferred photometric mass in Table 3.1, which implies that both magnetic components of the system are also fairly massive.

3.8. Spectral Evolution of DB White Dwarfs

In the light of our results, we now focus our attention on the spectral evolution of DB white dwarfs. In particular, we discuss in turn the evolution of the DB-to-DA ratio as a

function of effective temperature, and we revisit the question of the origin of hydrogen in DBA white dwarfs.

3.8.1. Evolution of the DB-to-DA Ratio

In order to determine the DB-to-DA ratio as a function of effective temperature, we retrieved the 27,216 spectra of DA white dwarfs identified in the SDSS DR7, DR10, and DR12 (Kleinman et al., 2013; Kepler et al., 2015, 2016). Since we want to characterize the entire population of DB and DA white dwarfs, we applied no criterion on the spectral type. Furthermore, to ensure the best possible determination of the atmospheric parameters for both DB and DA stars, we only kept the spectra with $S/N > 10$, and the best S/N spectrum for the objects with multiple observations. The model atmospheres and fitting technique used to obtain the atmospheric parameters for the DA stars are described at length in GBB19 and references therein.

Because the SDSS survey is magnitude limited, we need to take into account that DA and DB white dwarfs with similar T_{eff} and $\log g$ values have different absolute magnitudes (see, e.g., Figure 1 of Bergeron et al. 2019). Therefore, the volume sampled by each white dwarf type is different. To deal with this issue, we took advantage of the Gaia trigonometric parallaxes and retained only white dwarfs within 1 kpc. This left us with a sample of 9863 DA and 1145 DB white dwarfs. The composition of our sample, subdivided by spectral type, is presented in Table 3.3. We should note that the atmospheric parameters obtained for the irregular spectral types (magnetic, composite, etc.) are more uncertain, but this should not affect significantly our conclusions, since these subtypes represent only a small fraction of our total sample (see Table 3.3).

One important issue that also needs to be addressed is the completeness of the SDSS. One class of objects that was observed in this survey with a high priority is the so-called "hot standard" target class, which selects all isolated stars with clean photometry flags with very blue colors, $u - g < 0$ and $g - r < 0$, down to a flux limit of $g < 19$ (Eisenstein et al., 2006b). Most DB white dwarfs satisfy this condition, as they only become redder below $T_{\text{eff}} \sim 13,000$ K or so (see Figure 2 of Bergeron et al. 2019). However, in the case of DA white dwarfs, the $u - g < 0$ criterion is only satisfied for $T_{\text{eff}} \gtrsim 22,000$ K. Eisenstein et al. (2006b) estimated that the completeness of the SDSS at $u - g > 0$ is about 66% of that at

Table 3.3. Distribution of the different spectral subtypes in the DA and DB samples

DA sample			DB sample		
Spectral Type	Number	Percentage	Spectral type	Number	Percentage
DA	8440	85.57%	DB ²	859	75.02%
DAH	236	2.39%	DBH ³	12	1.05%
DAM/DA+M	725	7.35%	DBM/DB+M	41	3.58%
Other	99	1.00%	Other	2	0.17%
Uncertain ¹	363	3.68%	Uncertain ¹	231	20.47%
Total	9863	100%	Total	1145	100%

¹ Includes any spectral type containing ":".

² Also includes the DB white dwarfs with traces of hydrogen (DBA) and/or metals (DBZ).

³ Also includes the DBAH.

$u - g < 0$. Therefore, in the calculations presented below, we follow the same procedure as that described in Eisenstein et al. (2006a, see their Section 4), and increase the weight of the stars redder than $u - g = 0$ by a factor of 1.5.

The distribution of DA and DB white dwarfs as a function of effective temperature is shown in Figure 3.22, using both spectroscopic and photometric temperatures. While there are small differences between the results obtained using these two temperature scales⁷, the distributions show similar behaviors. In particular, the number of DB white dwarfs increases monotonously with decreasing effective temperature, before dropping again at lower temperatures when DB white dwarfs turn into DC stars, i.e. when neutral helium lines become barely detectable ($T_{\text{eff}} \lesssim 12,000$ K).

More puzzling is the DA distribution, which shows a sudden drop around $T_{\text{eff}} \sim 14,000$ K in spectroscopy, and around $T_{\text{eff}} \sim 12,000$ K in photometry. The difference in the location of this local minimum can probably be explained in terms of small inaccuracies in our

7. The shift between the photometric and spectroscopic distributions of DA stars at high temperatures results from the spectroscopic temperatures of DA stars being 10% higher than the photometric values, as discussed in Section 3.6.5 and in GBB19.

spectroscopic temperature scale. Indeed, this corresponds to the region where the Balmer lines reach their maximum strength, and our model spectra most likely predict stronger lines than what is actually observed, causing the spectroscopic solutions to be “pushed” on each side of the maximum (see also Figure 14 of Genest-Beaulieu & Bergeron 2014). Note that this may also be caused, in part, by residual calibration issues with the SDSS spectra, since the same experiment with the DA white dwarfs from the sample of Gianninas et al. (2011) showed an accumulation of objects instead of a depletion (see Figure 15 of Genest-Beaulieu & Bergeron 2014). But the fact remains that there is a sudden decrease of DA stars in this temperature range, regardless of the temperature scale. It is of course tempting to associate this drop with the onset of convective mixing⁸ at low effective temperature ($T_{\text{eff}} \lesssim 12,000$ K; see Figure 16 of Rolland et al. 2018), which can transform DA white dwarfs into DC stars (or helium-rich DA stars with very a weak H α feature). But to confirm this hypothesis, one would have to include all non-DA white dwarfs in this particular range of temperature. Such a major endeavor is clearly outside the scope of this paper.

Of greater interest in the present context is the fraction of DB white dwarfs as a function of effective temperature, which we present in Figure 3.23. While we show here the results using spectroscopic temperatures, the results obtained from photometry are qualitatively similar. Below $T_{\text{eff}} = 40,000$ K, down to $\sim 27,000$ K, the DB/(DA+DB) ratio remains fairly constant at $\sim 5\%$, within the uncertainties, and increases slowly to $\sim 7\%$ near 20,000 K. Below this temperature, however, the DB/(DA+DB) ratio rapidly increases to a value of 25% near 15,000 K⁹, until it drops again at lower temperatures when DB white dwarfs turn into DC stars. The picture depicted in Figure 3.23 is consistent with the results obtained by Bergeron et al. (2011), who determined the luminosity functions of DA and DB stars identified in the PG survey, and found that 20% of all white dwarfs below $T_{\text{eff}} \sim 17,000$ K are DB stars (i.e. $M_{\text{bol}} > 9.5$ in their Figure 24), while at higher temperatures, only $\sim 9\%$ of all white dwarfs are DB stars.

The variation of the DB/(DA+DB) ratio observed in Figure 3.23 is also entirely consistent with the convective dilution scenario, where the thin, radiative hydrogen layer present at the

8. We remind the reader that this process occurs when the bottom of the hydrogen convection zone in a DA white dwarf eventually reaches the underlying and more massive convective helium envelope, resulting in the *convective mixing* of the hydrogen and helium layers.

9. We note that this fraction is only slightly lower when using the photometric temperature scale.

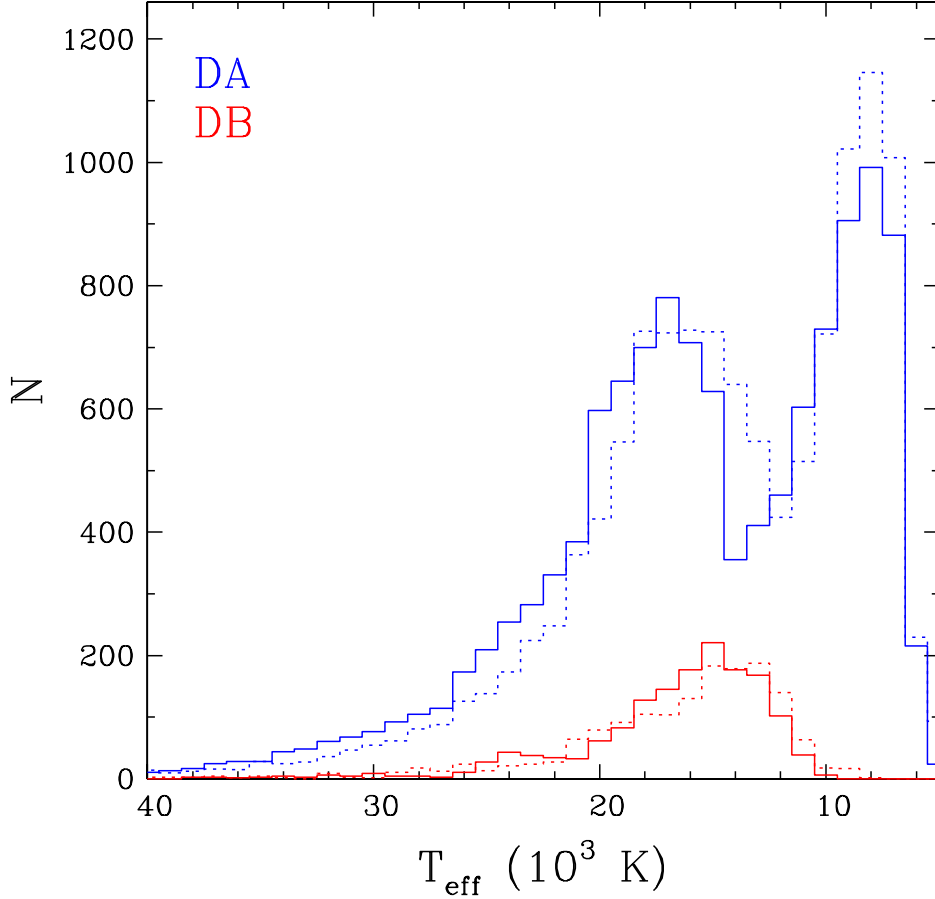


Figure 3.22. Number of DA and DB white dwarfs in our SDSS sample as a function of effective temperature. The solid and dotted distributions are based on spectroscopic and photometric temperatures, respectively. The objects with $S/N < 10$ and $D > 1$ kpc have been excluded, and a weight factor of 1.5 has also been applied to the objects with $u-g > 0$ (see text).

surface of hot DA white dwarfs is being convectively eroded by the deeper and more massive convective helium envelope, resulting in the conversion of a DA white dwarf into a DB star. Although detailed numerical simulations of this convective dilution process are still unavailable, an examination of the results displayed in Figures 9 and 10 of Rolland et al. (2018) reveals that objects with hydrogen layer masses in the range $\log M_H/M_\odot = -15.5$ up to -14 would undergo a hydrogen- to helium-atmosphere transition between $T_{\text{eff}} = 30,000$ K and 18,000 K, respectively, in perfect agreement with the results obtained here (see also MacDonald & Vennes 1991). The fact that the DB/(DA+DB) ratio increases rather abruptly

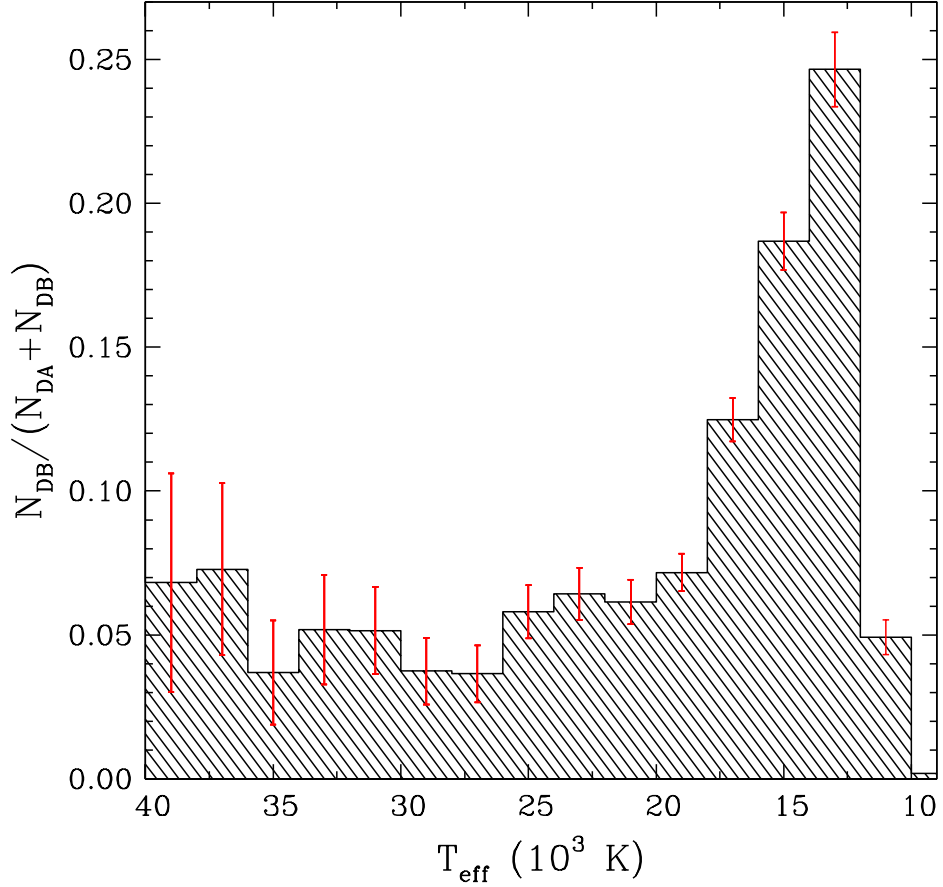


Figure 3.23. Ratio of the number of DB stars to the total number of DA+DB white dwarfs, as a function of (spectroscopic) effective temperature. The error bars represent the Poisson statistics of each bin. The objects with $S/N < 10$ and $D > 1$ kpc have been excluded.

below 20,000 K also suggests a narrow range of hydrogen layer masses for the population of DA stars that undergo the DA-to-DB transition, somewhere in the order of $\log M_{\text{H}}/M_{\odot} \sim -14$.

3.8.2. Origin of Hydrogen in DBA white dwarfs

Our hydrogen abundance determinations (or limits) from Figure 3.14 are reproduced in Figure 3.24 together with the detailed simulations from Rolland et al. (2018), which show the predictions of the convective dilution process, where a thin, superficial hydrogen layer of a given mass has been convectively diluted within the helium envelope, resulting in a homogeneously mixed H/He convection zone. More specifically, it is *assumed* in these calculations that the hydrogen layer has been convectively diluted, without paying attention

to dilution process per say. These should thus not be interpreted as evolutionary sequences in any way. Each curve in Figure 3.24 represents the location of white dwarf stars with a constant value of $\log M_{\text{H}}/M_{\odot}$, labeled in the figure. As discussed in Rolland et al., the sudden change of slope near $T_{\text{eff}} \sim 20,000$ K corresponds to the temperature where the bottom of the helium convection zone sinks deep into the white dwarf, resulting in a further dilution of the photospheric hydrogen within the deeper helium reservoir as the star cools off.

Also represented as red hatched areas in Figure 3.24 are regions in the $T_{\text{eff}} - \text{H}/\text{He}$ parameter space through which white dwarfs cannot evolve continuously with a constant hydrogen mass (see Rolland et al. 2018 for a full discussion). Hence, in order for a white dwarf to cool off with a constant total mass of hydrogen already homogeneously mixed within the convective layer, it must be able to evolve *continuously* from the left to the right in this diagram along a single sequence with a given value of $\log M_{\text{H}}/M_{\odot}$, without crossing this forbidden region. An examination of the results displayed in Figure 3.24 indicates that the hottest DBA white dwarfs in our sample ($T_{\text{eff}} \gtrsim 20,000$ K) can be accounted for by this scenario if the total hydrogen mass is less than $\log M_{\text{H}}/M_{\odot} \sim -15$, assuming the $\text{ML2}/\alpha = 0.6$ parameterization of the mixing-length theory (or even less if convection is more efficient). Note also that in the smallest hydrogen mass models ($\log M_{\text{H}}/M_{\odot} \lesssim -16$) at high temperatures, there is not enough hydrogen accumulated at the surface of the star to appear as a DA white dwarf (see Figures 3 and 4 of Manseau et al. 2016). In other words, the progenitors of some of the hottest DBA white dwarfs in our sample have never been genuine DA stars, and probably appeared as stratified DAB stars, with an extremely thin hydrogen layer floating in diffusive equilibrium at their surface. The hot ($T_{\text{eff}} \sim 30,000$ K) DAB white dwarf SDSS J1509–0108, displayed in Figure 14 of Manseau et al. (2016), represents an excellent example of such a stratified white dwarf, with only $\log M_{\text{H}}/M_{\star} = -16.78$ ($\log M_{\text{H}}/M_{\odot} = \log M_{\text{H}}/M_{\star} + 0.22$ for a $M_{\star} \sim 0.6 M_{\odot}$ white dwarf).

The other hot ($T_{\text{eff}} > 20,000$ K) DB white dwarfs in Figure 3.24 with no detectable traces of hydrogen have so little inferred total hydrogen mass in their stellar envelope that these stars always appeared as DB white dwarfs, and their immediate progenitors are most certainly the hot DB stars in the DB-gap analyzed by Eisenstein et al. (2006a). These obviously will remain DB stars, with no detectable traces of hydrogen, throughout their evolution. More importantly, even the hot DBA stars in our sample above $T_{\text{eff}} \sim 20,000$ K

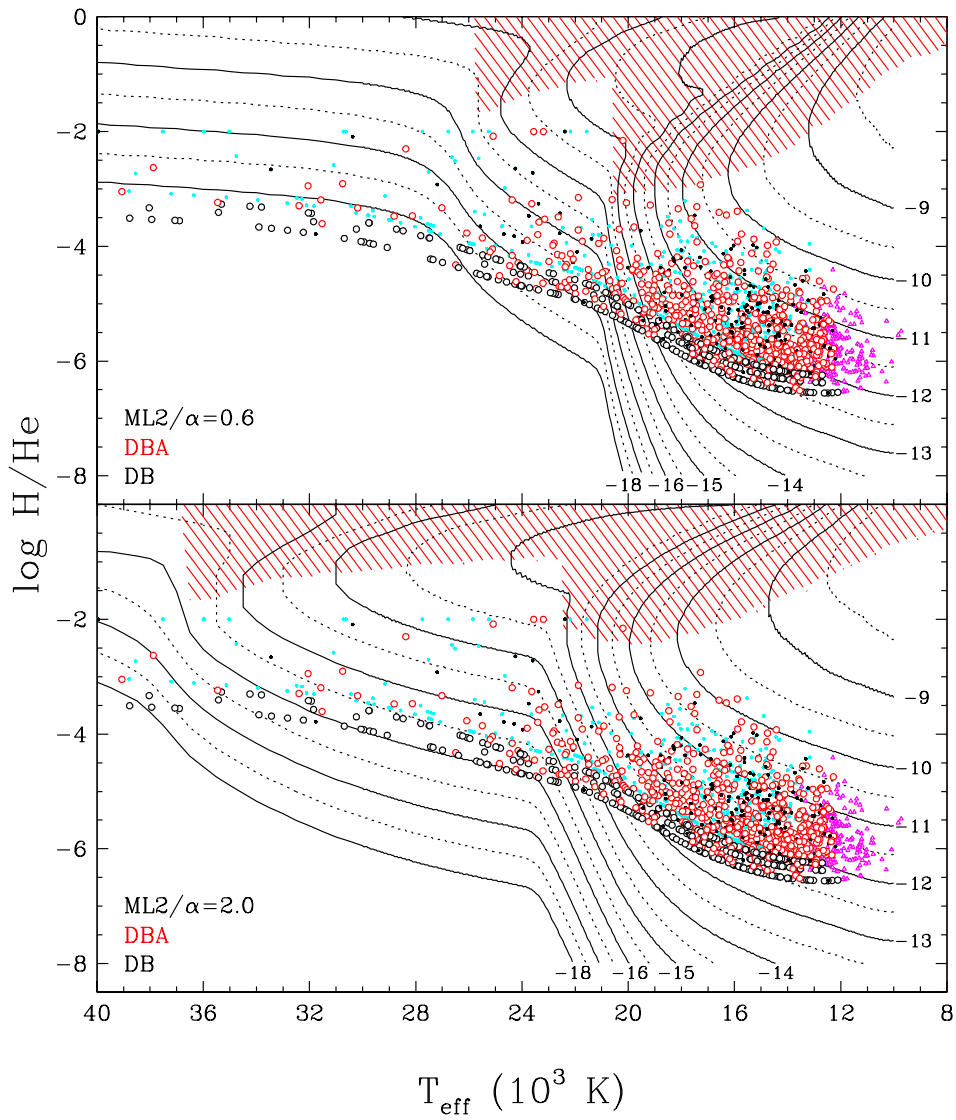


Figure 3.24. Predicted hydrogen abundances as a function of effective temperature (solid and dotted lines) from the simulations of Rolland et al. (2018) for homogeneously mixed models at $0.6 M_{\odot}$ and for both the $ML2/\alpha = 0.6$ (upper panel) and $\alpha = 2$ (lower panel) versions of the mixing-length theory. Each curve is labeled with the corresponding value of $\log M_H/M_{\odot}$. Results from Figure 3.14 are also reproduced. The red hatched areas represent the regions through which white dwarfs cannot evolve with a constant $\log M_H/M_{\odot}$.

await a similar fate, given that the deepening of the mixed H/He convection zone at lower temperatures will completely dilute any residual hydrogen left in the stellar envelope, well below the limit of visibility of hydrogen, H α in this case. In this respect, we disagree with the conclusions of Koester & Kepler (2015) who suggested that practically all DB white

dwarfs probably show some trace of hydrogen if the spectroscopic resolution and S/N are high enough. Regardless of the observational limit, there is obviously also a *theoretical limit* on H/He, predicted by model atmospheres, below which hydrogen becomes invisible (see in particular Figure 3 of Rolland et al. 2018). Such threshold limits are certainly achieved according to the results displayed in Figure 3.24. Hence we conclude that, *according to the convective dilution scenario alone*, all hot ($T_{\text{eff}} > 20,000$ K) DB and DBA white dwarfs will most likely evolve into nearly pure helium-atmosphere white dwarfs at lower temperatures, with no detectable traces of hydrogen. In contrast, DBA stars at lower temperatures should retain a trace of hydrogen much longer since the depth of the mixed H/He convection zone remains almost constant below 20,000 K (see Figure 9 of Rolland et al. 2018), thus reducing any further dilution of hydrogen.

We now turn our attention to the bulk of DBA white dwarfs in our sample, found below $T_{\text{eff}} \sim 20,000$ K in Figure 3.24. In order to account for the observed photospheric hydrogen abundances in these stars, the total hydrogen mass present in the stellar envelope must be in the range $-14 < \log M_{\text{H}}/M_{\odot} < -10$, regardless of the convective efficiency. The problem here is that hotter DA progenitors with such thick hydrogen layers in diffusive equilibrium at their surface — i.e. with chemically stratified envelopes — would inhibit convection in the deeper helium envelope (see Figure 11 of Rolland et al. 2018), preventing any DA-to-DB conversion in this temperature range. In DA white dwarfs with such thick hydrogen layers, mixing between the *convective hydrogen layer* and the deeper, and more massive helium envelope would eventually occur, but at much lower effective temperatures ($T_{\text{eff}} \lesssim 12,000$ K) according to the calculations of Rolland et al. (2018, see their Figure 16). Hence we must conclude that the total amount of hydrogen present in the bulk of DBA white dwarfs below $T_{\text{eff}} \sim 20,000$ K is too large to have a residual origin resulting from the convective dilution scenario, and that other sources of hydrogen must be invoked, such as accretion from the interstellar medium, comets, or disrupted asteroids, etc., a conclusion also reached in several previous investigations (e.g., MacDonald & Vennes 1991, Bergeron et al. 2011, Koester & Kepler 2015, Rolland et al. 2018). Despite these discrepancies, the convective dilution scenario remains the only viable explanation for the transformation of DA into DB white dwarfs below 20,000 K.

Finally, we note that all the DBA white dwarfs in our sample completely avoid the so-called forbidden region in Figure 3.24 (defined by the red hatched areas), especially with the $ML2/\alpha = 0.6$ models. Note, in particular, how the most hydrogen-rich DBA stars in our sample (including PG 1311+129), already discussed in Section 3.7.2, follow nicely the bottom limit of the forbidden region. Because the convective dilution process, which transforms a chemically stratified DA star into a homogeneous DB white dwarf, makes somehow the object “jump” over this forbidden region, the extreme DBA stars in our sample are probably in the process of being convectively mixed, with hydrogen constantly trying to float back to the surface, as suggested by Bergeron et al. (2011) in the case of PG 1311+129, which incidentally, shows small spectroscopic variations as a function of time (see their Figure 28).

3.9. Chemically Stratified Atmospheres

MacDonald & Vennes (1991) published an exhaustive set of calculations of stratified hydrogen/helium envelope models in diffusive equilibrium, for effective temperatures between $T_{\text{eff}} = 10,000$ K and 80,000 K, and for various values of the total hydrogen mass (M_H). While the chemical composition was assumed to be homogeneous within the mixed H/He convection zone, if present, the abundance profile below and above the convection zone was calculated under the assumption of radiative diffusive equilibrium. In their Figure 6, for instance, one can see in their model E that the hydrogen abundance ratio within the convection is constant at a value around $\log H/\text{He} \sim -6$ (their plot actually shows the inverse ratio), but that above the convection zone, the hydrogen abundance gradually increases, and reaches a value as high as $\log H/\text{He} \sim 2$ at the surface of their model. This is in sharp contrast to standard model atmospheres where the chemical abundance is assumed to be homogeneous throughout. MacDonald & Vennes further explored the effect of these stratified atmospheres on the emergent flux, with and without convective overshooting taken into account (see their Figure 15). Note that in their calculations, the radiative transfer equations have been solved, but using gray envelope models rather than detail model atmospheres. Furthermore, no detailed comparison with observations has been presented.

Given the problems with total amount of hydrogen present in the envelope of DBA white dwarfs, as inferred for instance from the results displayed in Figure 3.24, Bergeron et al. (2011, see their Section 5.4) suggested that perhaps the assumption of *complete mixing* of

the hydrogen layer should be questioned. It is indeed conceivable that the total amount of hydrogen present is in fact of the order of $\sim 10^{-14} M_{\odot}$, but with some of this hydrogen floating on top of the photosphere — as depicted in the envelope calculations of MacDonald & Vennes — rather than being forcefully mixed by the helium convection zone.

To test this hypothesis further, we calculated a new set of model atmospheres by allowing H/He to vary as a function of depth in the superficial radiative zone. The complete procedure is described in detail in Appendix B. Briefly, we assume a homogeneous composition in the convection zone, and the abundance profile in the radiative zone is calculated assuming diffusive equilibrium (see Pelletier et al. 1986 and Vennes et al. 1988). Thermal diffusion and radiative acceleration have been neglected since both effects are negligible in the atmosphere of DB white dwarfs. An example of the resulting abundance profiles for models at $T_{\text{eff}} = 12,000 \text{ K}, 16,000 \text{ K}, 20,000 \text{ K}$, at $\log g = 8.0$ and $\log \text{H/He} = -4.0^{10}$, is presented in Figure 3.25. Our results are qualitatively similar to those shown in Figure 6 of MacDonald & Vennes (1991), where the hydrogen abundance gradually increases towards the surface. Also shown are calculations obtained by extending the homogeneous profile in the convection zone over two pressure scale heights, thus simulating the effect of convective overshooting, at least in terms of the abundance profile.

We compare in Figure 3.26 the temperature and pressure structures, $T(\tau_R)$ and $P(\tau_R)$, of chemically homogeneous and stratified models. While the effect on the stratification of the atmosphere is negligible in the convection zone ($\log \tau_R \gtrsim -1.0$), the situation in the upper atmosphere is quite different. The main effect on the temperature structure is to create temperature inversions, which generally occur deeper in the atmosphere than those present in homogeneous models. But the most significant effect is on the pressure structure, where the presence of larger amounts of hydrogen in the upper layers of the stratified models has greatly reduced the atmospheric pressure, as a result of the increased opacity of hydrogen in these regions.

The effect of chemically stratified atmospheres on the synthetic spectrum calculations is shown in Figure 3.27 for the same models as before. In the two cooler models displayed here, the effect of chemical stratification on the helium lines is negligible, but in the hotter

10. Note that when referring to chemically stratified atmospheres, the hydrogen abundance corresponds to the H/He ratio in the convection zone.

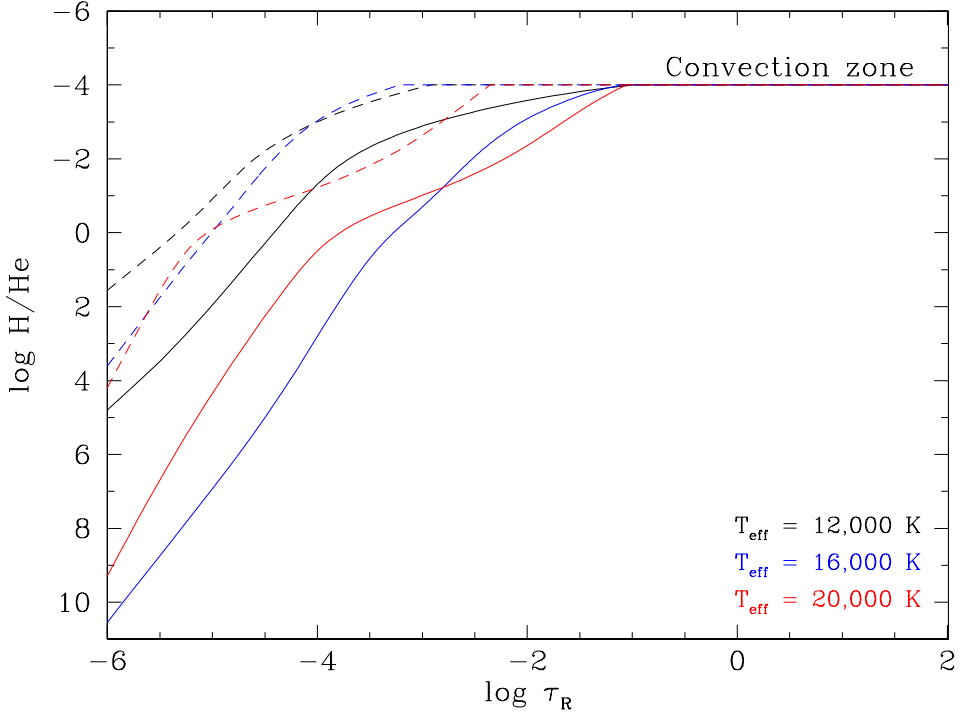


Figure 3.25. Hydrogen abundance profile as a function of Rosseland optical depth in chemically stratified atmospheres at $T_{\text{eff}} = 12,000$ K, 16,000 K, and 20,000 K, and $\log g = 8.0$, with (dashed line) and without (solid line) convective overshooting (two pressure scale heights) taken into account. The hydrogen abundance ratio is kept fixed at $\log H/\text{He} = -4.0$ in the convection zone.

model, we can observe emission in the line cores, resulting from the strong temperature inversions noticed in Figure 3.26. This effect can be reduced by allowing some convective overshooting in our calculations, more specifically, by extending the homogeneous abundance profile over a few pressure scale heights (see Figure 3.25). A synthetic spectrum calculated at $T_{\text{eff}} = 20,000$ K, which includes convective overshooting over two pressure scale heights, is displayed in Figure 3.27 for comparison.

More interesting in the present context is the effect on the hydrogen lines, in particular in the two cooler models illustrated in Figure 3.27, where the hydrogen lines in the blue region of the spectrum are predicted significantly deeper in the stratified models. For an observed DBA white dwarf, stratified model spectra would thus yield a *lower hydrogen abundance* than homogeneous models. Again we remind the reader that this abundance ratio is that

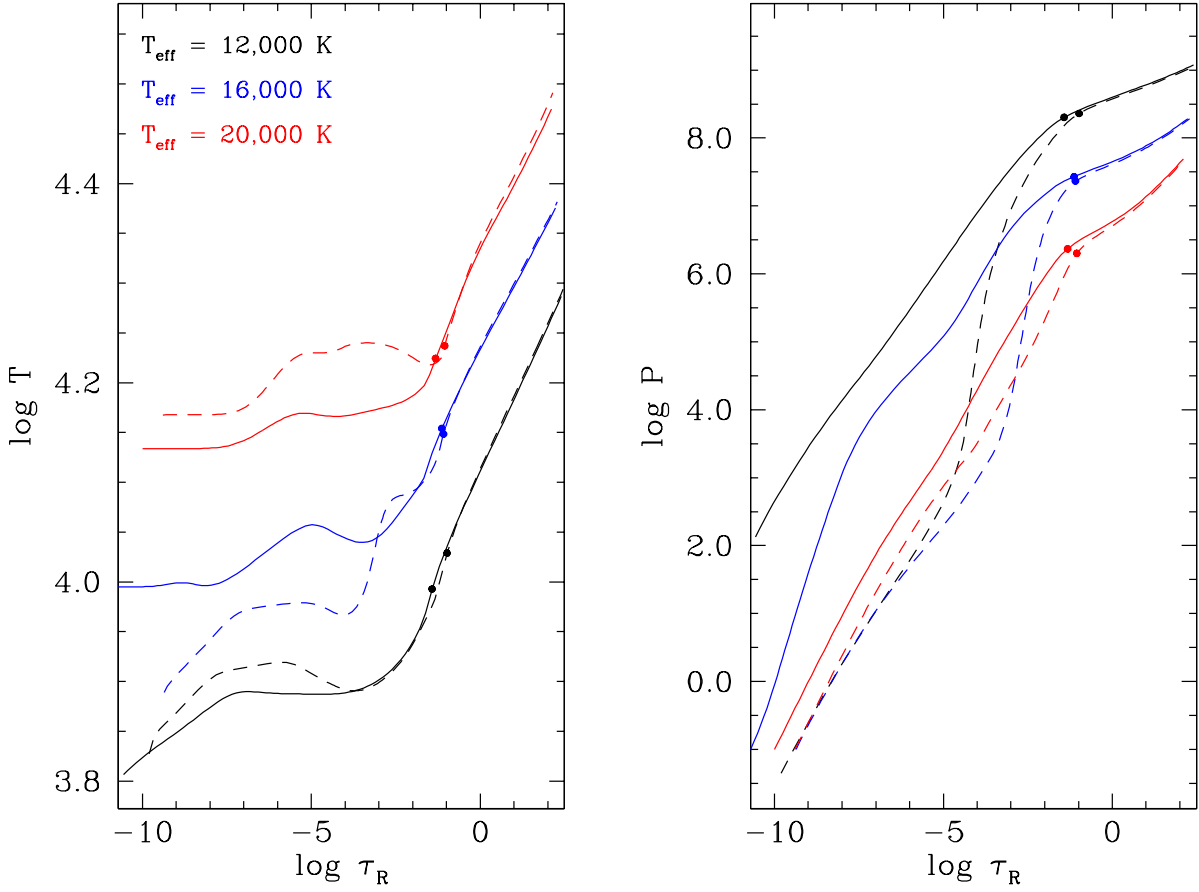


Figure 3.26. Temperature and pressure structures as a function of Rosseland optical depth for homogenous (solid lines) and chemically stratified (dashed lines) model atmospheres at $T_{\text{eff}} = 12,000 \text{ K}$, $16,000 \text{ K}$, and $20,000 \text{ K}$, $\log g = 8.0$, and $\log \text{H/He} = -4.0$. The transition between the convective and radiative zones is indicated by the full circles.

measured in the mixed H/He convection zone. This would in turn imply a smaller total amount of hydrogen inferred in the stellar envelope.

We show in Figure 3.28 our best fit to the DBA white dwarf WD 1822+410 (G256-18, taken from Rolland et al. 2018) using homogeneous model atmospheres. Also shown are stratified model spectra at fixed values of T_{eff} and $\log g$, and for two different hydrogen abundances, whose value is set in the mixed H/He convection zone, as discussed above. As can be seen, the stratified models with a H/He value even ~ 0.5 dex lower than the homogeneous value predict hydrogen lines that are significantly deeper than the observed profiles. Most surprisingly, however, the overall fit to the neutral helium lines appears quite reasonable. One way to match the observed hydrogen lines is to reduce the hydrogen abundance in the

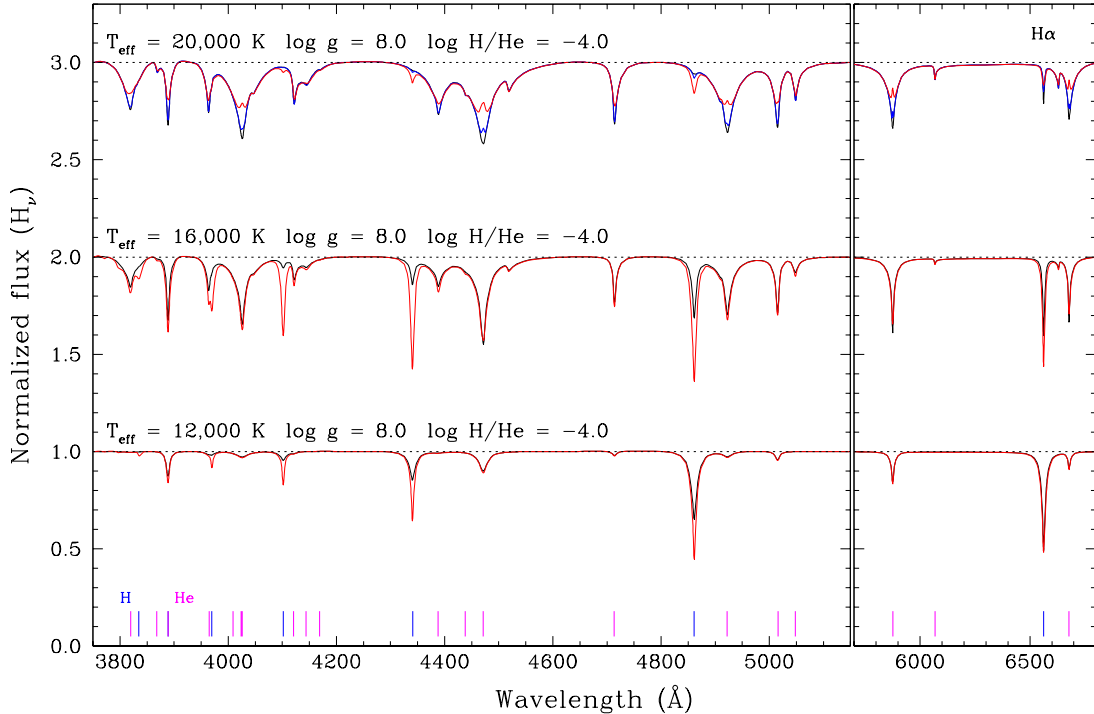


Figure 3.27. Synthetic spectra obtained from homogeneous (black) and chemically stratified (red) model atmospheres. Also shown at $T_{\text{eff}} = 20,000$ K only is a chemically stratified spectrum (blue) that includes convective overshooting two pressure scale heights. All spectra have been normalized to a continuum set to unity and convolved with a 3 Å FWHM Gaussian profile. The blue (magenta) tick marks indicate the location of the hydrogen (helium) lines. The location of $\text{H}\alpha$ is also shown.

mixed convection zone even further, by ~ 1 dex with respect to the homogeneous value. The corresponding synthetic spectrum, also displayed in Figure 3.28, provides an excellent fit to the observed spectrum, with the exception of the absorption lines in the red portion of the spectrum (shown in the inset), which are predicted too shallow, in particular $\text{H}\alpha$. Models including convective overshoot, not displayed here, improved this discrepancy, but only marginally. We would like to point out that some of the fits to DBA white dwarfs presented in Rolland et al. (2018, see online material) showed similar discrepancies between $\text{H}\alpha$ and $\text{H}\beta$, an excellent example of which is WD 0503+147 ($T_{\text{eff}} = 15,640$ K).

Stratified models such as those described in MacDonald & Vennes (1991), and calculated here, where hydrogen and helium sit in perfect diffusive equilibrium on top of the mixed H/He convection zone, are probably unrealistic from a physical point of view, especially given the

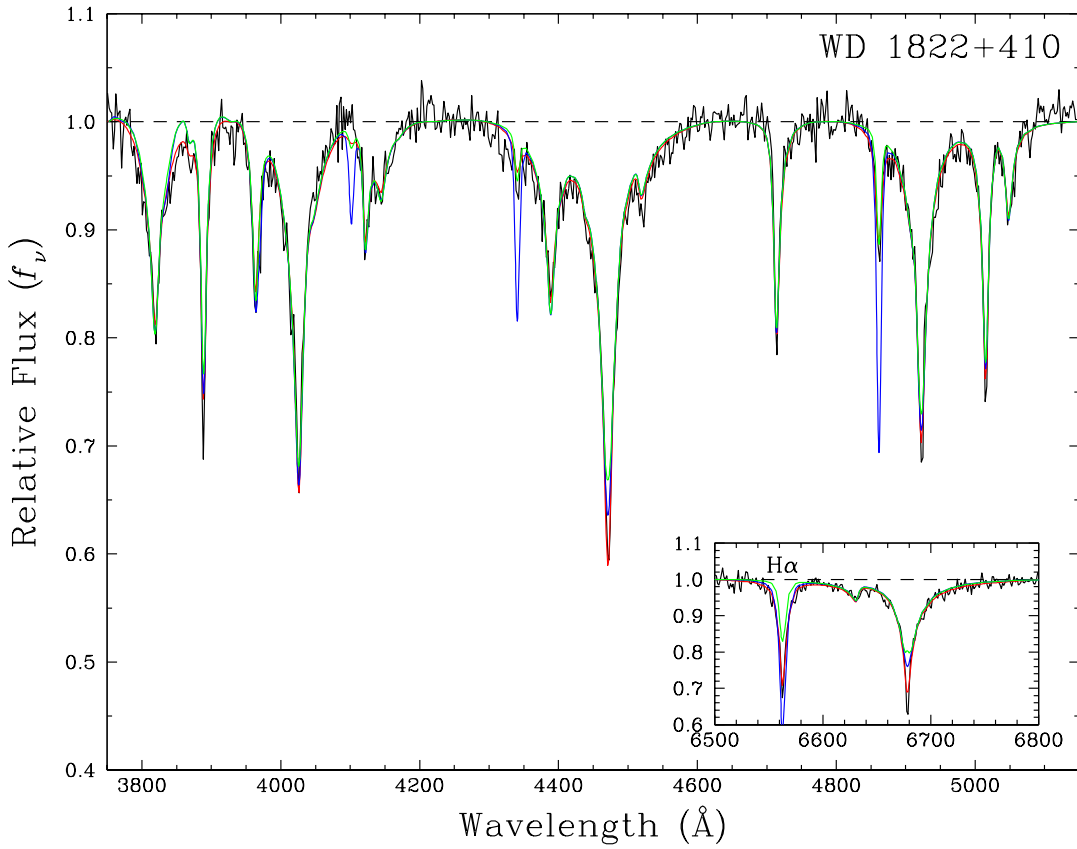


Figure 3.28. Normalized observed spectrum of WD 1822+410 (black), together with our best spectroscopic fit (red) using homogeneous models ($T_{\text{eff}} = 16,230$ K, $\log g = 8.01$, and $\log \text{H/He} = -4.45$). Also shown are synthetic spectra obtained from chemically stratified atmospheres at $T_{\text{eff}} = 16,000$ K, $\log g = 8.0$, and $\log \text{H/He} = -5.0$ (blue) and -5.5 (green). The location of $\text{H}\alpha$ is also indicated.

large velocities expected from convective overshooting in the uppermost layers of white dwarfs (see, e.g., Figure 2 of Tremblay et al. (2011b)). But our conclusion remains, namely that it is possible that the upper layers of DBA white dwarfs are chemically inhomogeneous, and that the hydrogen abundances measured in DBA stars using homogeneous model atmospheres may not be representative of the total hydrogen content in the star. In our experiment above, the total hydrogen mass could be at least of factor of 10 smaller than that inferred from models with homogeneous chemical compositions.

3.10. Discussion

We presented a detailed model atmosphere analysis of DB white dwarfs drawn from the SDSS database. The large set of optical spectra and *ugriz* photometry available from the SDSS, coupled with the exquisite trigonometric parallax measurements from the *Gaia* mission, allowed us to measure the fundamental parameters of DB white dwarfs using both the spectroscopic and photometric techniques. In turn, the results obtained from both fitting techniques provided us with a unique opportunity to assess the precision, but more importantly the *accuracy* of the measurements, in particular the effective temperature, stellar mass, and photospheric composition, which form the basic elements for understanding the origin and evolution of these stars.

We identified several problems in our analysis, both theoretical and observational. On the theoretical front, van der Waals broadening remains the largest source of uncertainty in the calculations of synthetic spectra for DB white dwarfs. Nevertheless, our mass comparison displayed in Figure 3.10 reveals that the spectroscopic masses at low temperatures appear fairly reasonable, if we exclude the objects with extremely weak helium lines. We also see some clear evidence for 3D hydrodynamical effects in our spectroscopic mass distributions in the 16,000–22,000 K temperature range, and additional work along the lines of Cukanovaite et al. (2018), but by including traces of hydrogen, should improve the spectroscopic mass measurements significantly. Finally, given the large spectroscopic data set available here, it would probably be worth revisiting the question of the convective efficiency in hot DB stars — which in all recent investigations, including ours, has been set to $ML2/\alpha = 1.25$ — by repeating the experiments performed in Section 4.4 of Bergeron et al. (2011).

We identified a few problems on the observational front as well. While the number of white dwarfs discovered by the SDSS has been increased by more than a factor of 10 since the latest version of the Villanova White Dwarf Catalog of McCook & Sion (1999), the optical spectra still appear to suffer from some residual flux calibration problems. This becomes apparent at high effective temperatures, where the spectroscopic masses are lower than those measured at cooler temperatures, or lower than those inferred from photometry for that matter. This problem is observed for both DA and DB stars. Furthermore, even though the large number of white dwarf spectra available in the SDSS has significantly improved our understanding of these objects, the generally low S/N of the SDSS spectra (see

Figure 3.1) still represents a strong limitation in terms of making more precise spectroscopic measurements of white dwarf parameters, and it is hoped that future spectroscopic surveys will improve the situation.

Our analysis has uncovered several interesting objects, including the existence of massive DB white dwarfs, mostly below $T_{\text{eff}} \sim 18,000$ K, whose progenitor might be the Hot DQ stars. We also identified a large population of unresolved double degenerate binaries composed of two DB white dwarfs, and even occasionally DB+DA double degenerates. As in previous investigations, we did not find any evidence for single low-mass ($M < 0.48M_{\odot}$) DB white dwarfs, obviously because nature does not produce such objects. All low-mass white dwarfs appear to have hydrogen-rich atmospheres. As discussed by Bergeron et al. (2011), common envelope evolution is required to produce such low mass white dwarfs, and this close-binary evolutionary channel must produce white dwarfs with hydrogen layers too massive to allow the DA to DB conversion at any temperature.

Probably the most important key result of our analysis is the hydrogen abundance (or limits) distribution as a function of effective temperature, summarized in Figure 3.24. This picture represents a static view, or a snapshot in time, of the current distribution of hydrogen abundances in DB and DBA white dwarfs, which detailed evolutionary calculations must eventually explain. In particular, DA white dwarfs must be able to turn into DB stars in the appropriate temperature range, and properly account for the observed DB-to-DA ratio. The residual amount of hydrogen expected from the DA-to-DB transition is much smaller than that inferred from current homogeneous envelope models (Rolland et al., 2018), unless the hydrogen-to-helium abundance ratio measured using homogeneous model atmospheres is somehow overestimated, for instance, if the atmosphere is chemically inhomogeneous, as discussed in Section 3.9. The alternative is to have an external source of hydrogen — either from the interstellar medium, disrupted asteroids, small planets, or even comets — polluting the atmosphere of DB white dwarfs after the DA-to-DB transition has occurred.

Yet, another alternative proposed by B. Rolland et al. (2019, in preparation) is to have an *internal* source of hydrogen. With this new paradigm, hydrogen is initially diluted in the deep stellar envelope of a hot PG1159 progenitor. With time, hydrogen slowly diffuses upward, slowly building a superficial hydrogen-rich atmosphere. However, calculations show that when the convective dilution process occurs, the resulting abundance profile is far from

equilibrium, and large amounts of hydrogen are still present in the deep interior. As the convection zone of the cooling DB stars grows, *large amounts of hydrogen is being dredged-up to the surface*, a phenomenon similar to that invoked in the context of DQ white dwarfs (Pelletier et al., 1986).

Also of importance in this context is the existence, and persistence, of pure DB stars, i.e. helium-atmosphere white dwarfs that show no hydrogen feature whatsoever. As discussed in our analysis, this is not a simple problem of detectability, because envelope models such as those displayed in Figure 3.24 do predict hydrogen abundances where H α simply becomes *undetectable*, even theoretically. White dwarfs with such small total amounts of hydrogen present in their envelope — in particular those discovered in the DB gap — can only be explained by the so-called born-again post-AGB (asymptotic giant branch) evolutionary scenario, involving a very late helium-shell flash, or an AGB final thermal pulse, as described in detail by Werner & Herwig (2006). As discussed in Bergeron et al. (2019), it is possible that in this process, the total mass of helium could also be significantly reduced. This could perhaps explain the origin of cool DQ white dwarfs, in which carbon is being dredged-up from the core, a process that occurs only if the helium envelope is not too thick according to Pelletier et al. (1986). If this interpretation is correct, the immediate progenitors of DQ stars could be the “pure” DB white dwarfs discussed above. By the same token, one could imagine that these very late helium-shell flashes are violent enough as to wipe out the stellar environment from any planetary debris, thus providing a natural explanation for the absence of metals in cool DQ stars.

Clearly, all these issues will require larger and better data sets — higher S/N spectra in particular — but most importantly, state-of-the-art evolutionary model calculations able to predict the spectral evolution of white dwarf stars as a function of their cooling age. Then perhaps one day, we will be able to map the range of total hydrogen mass (M_H) present in these stars — arguably the Holy Grail of white dwarf astrophysics.

We are grateful to Patrick Tremblay for useful discussions regarding the behavior of DB model spectra. This work is supported in part by the NSERC Canada and by the Fund FRQ-NT (Québec).

Chapitre 4

Conclusion

Cette thèse fut dédiée à l'étude des naines blanches de type DA et DB, avec une attention particulière accordée à ces dernières. L'étude des naines blanches repose principalement sur la détermination de leurs paramètres atmosphériques et physiques, tels que la température effective, la gravité de surface, la masse, la composition chimique, la luminosité et l'âge. Les deux méthodes principales pour obtenir ces quantités consistent en la comparaison des prédictions des modèles d'atmosphère à la distribution d'énergie de la naine blanche, contrainte par la photométrie, ou encore aux profils de raies d'absorption des spectres observés. Avant l'arrivée du SDSS et du relevé *Gaia*, les techniques photométrique et spectroscopique ne pouvaient être appliquées qu'à de petits échantillons, par manque de données accessibles. Ceci était particulièrement vrai dans le cas des naines blanches à atmosphère riche en hélium, car elles sont beaucoup moins nombreuses que leurs homologues riches en hydrogène. Grâce à ces relevés, une quantité phénoménale de données photométriques, spectroscopiques et de parallaxes trigonométriques sont maintenant accessibles, ce qui a fourni une opportunité unique de mettre à l'épreuve tant les modèles d'atmosphère que les outils techniques, tels que les techniques photométrique et spectroscopique. Cela permet aussi d'effectuer une analyse plus poussée de la population de naines blanches de type DB.

En ne gardant que les meilleures données disponibles, tant pour les naines blanches de type DA que de type DB, les paramètres atmosphériques obtenus à l'aide des techniques photométrique et spectroscopique ont pu être comparés. Ceci a permis de mettre en lumière certaines lacunes des présents modèles d'atmosphère.

La comparaison des températures effectives a révélé un effet systématique chez les DA plus chaudes qu'environ 14,000 K. Dans cette région en température, les températures effectives

spectroscopiques obtenues sont $\sim 10\%$ plus élevées que ce qui est prédict par la photométrie. L'effet n'étant pas vu dans le cas des naines blanches de type DB, cette disparité entre les températures a pu être reliée aux profils d'élargissement Stark présentement utilisés dans les modèles d'atmosphère riches en hydrogène. Cette lacune ne semble cependant pas affecter la détermination de la masse à l'aide de la technique spectroscopique, puisque M_{phot} et M_{spec} sont en bon accord, peu importe le régime de température dans lequel on se trouve.

Dans le cas des naines blanches de type DB, bien qu'il y ait un bon accord entre les températures photométrique et spectroscopique, pour les masses, la situation paraît différente. Sous $T_{\text{eff}} = 16,000$ K, les masses spectroscopiques semblent tendre vers des valeurs plus élevées que celles obtenues photométriquement. Cependant, en retirant les naines blanches pour lesquelles le spectres ne montrent que des raies marginales, les masses déterminées à l'aide de la technique spectroscopique semblent relativement raisonnables. Malgré tout, il est évident que le traitement de l'élargissement van der Waals demeure peu satisfaisant. Pour qu'une analyse spectroscopique fiable des DB froides soit accomplie, il est impératif de développer de nouvelles théories pour décrire l'élargissement des raies d'absorption par les particules neutres.

Il semble aussi que les distributions de masse spectroscopiques à haute température tendent vers des valeurs environ $0.05 M_{\odot}$ plus faibles, et ce, autant pour les DA que pour les DB. Ceci suggère que le problème ne provient pas des modèles d'atmosphère, qui sont différents pour ces deux types d'objets. Comme cet effet n'est pas observé dans les distributions de masse photométriques, il semble relié aux données spectroscopiques, ou plus précisément à la calibration en flux des spectres provenant du SDSS.

Finalement, la relation masse-rayon, un outil vital à l'étude des naines blanches a été mise à l'épreuve. Cette relation permet de relier la température effective et la gravité de surface (ou le rayon) aux autres paramètres atmosphériques et physiques. Bien qu'elle ait déjà été testée et validée par d'autres études, ce ne fut qu'à l'aide de petits échantillons et de parallaxes trigonométriques parfois imprécises ou même inexactes. L'abondance et la précision des parallaxes trigonométriques mesurées par le satellite *Gaia* ont permis de mettre la relation masse-rayon théorique à l'épreuve à nouveau à l'aide d'un échantillon beaucoup

plus volumineux. Pour environ 65% des naines blanches étudiées, la distance obtenue directement de la parallaxe et celle obtenue spectroscopiquement via la masse-rayon concordaient ($\leq 1 \sigma$), confirmant ainsi la validité de cette relation.

Une fois les lacunes associées aux modèles d'atmosphère et aux outils techniques identifiées et la validité de la relation masse-rayon confirmée, une étude plus approfondie des paramètres atmosphériques et physiques des naines blanches de type DB a pu être accomplie. Afin de caractériser le plus fidèlement cette population, aucun critère sur la qualité des données n'a été appliqué dans la sélection de l'échantillon.

L'analyse de la distribution des gravités de surface spectroscopiques a révélé une légère augmentation de $\langle \log g \rangle$ entre $T_{\text{eff}} = 17,000$ K et $22,000$ K qui n'est pas présente dans la distribution photométrique. Cette augmentation apparente des gravités de surface est causée par l'utilisation des modèles 1D, qui traitent la convection à l'aide de la théorie de la longueur de mélange. Bien que des corrections à appliquer aux paramètres atmosphériques déterminés à l'aide de modèles 1D soient disponibles, il a été montré qu'elles ne permettent pas de corriger entièrement le problème : les valeurs de $\log g$ corrigées entre $16,000$ K et $20,000$ K sont bien inférieures à celles déterminées à l'aide de la photométrie. Ces corrections 1D→3D ne sont cependant appropriées que pour des atmosphères pures en hélium et, comme la majorité des naines blanches de type DB ont une certaine quantité d'hydrogène dans leur atmosphère, il faudra attendre que les calculs de modèles 3D ayant une composition mixte H/He soient disponibles.

Conformément à ce qui avait été noté dans plusieurs études, l'analyse des distributions de masse photométriques et spectroscopiques a démontré l'absence de DB de faible masse. Cette analyse a cependant soulevé la présence de DB massives ($M \gtrsim 0.8M_{\odot}$). La présence de ces objets est habituellement contestée, puisque la plupart se trouvent sous 16,000 K, où le traitement inapproprié de l'élargissement van der Waals rend la détermination de la gravité de surface, donc de la masse, plus incertaine. La détermination de M de façon indépendante, via la photométrie et la parallaxe, a cependant permis de confirmer la présence de tels objets. Comme les DA massives sont souvent attribuées à la fusion de deux étoiles, ou encore comme le résultat de la relation masse initiale-masse finale, la présence de ces DB massives pourrait être attribuée à ces mécanismes. Il se pourrait aussi que ces objets aient comme progéniteur les *Hot DQ*, car ces objets sont plus massifs que la population de naines blanches en général

et la température à laquelle ces objets disparaissent correspond à celle où les DB massives commencent à apparaître. Dans un cas comme dans l'autre, ce ne sont que des hypothèses qui demeurent à être vérifiées.

La comparaison des masses obtenues grâce aux techniques photométrique et spectroscopique a permis de révéler la présence de plusieurs systèmes binaires non-résolus. Les systèmes binaires de type DA+DB sont facilement identifiables spectroscopiquement, car les spectres synthétiques produits à partir des modèles d'atmosphère ne réussissent pas à bien reproduire les raies du spectre observé. Les systèmes de type DB+DB, quant à eux, sont pratiquement impossibles à identifier à l'aide de la spectroscopie seule, car la contribution combinée des deux membres du système résulte en un spectre de DB ayant des paramètres intermédiaires. Il en va de même pour les systèmes composés de deux DA. Ces systèmes sont toutefois identifiables à leur faible masse photométrique. Dix systèmes DA+DB, ainsi que 55 candidats DB+DB ont pu être identifiés dans cette analyse. Cette liste n'est cependant pas complète, car des données de bonne qualité sont nécessaires afin de pouvoir identifier correctement ces systèmes. La présence de systèmes DA+DA ainsi que DA+DC a aussi été notée.

En se basant sur la présence de la raie H α , il a été déterminé que 61% des DB ont une certaine quantité d'hydrogène dans leur atmosphère. Il reste cependant quelques incertitudes quant à cette fraction, puisque la détermination de H/He repose sur la région H α du spectre. Bien que cette raie soit relativement forte dans le spectre des DB les plus froides, même à de faibles abondances, elle peut s'avérer difficilement détectable à plus haute température, ou lorsque le rapport signal-sur-bruit du spectre est relativement faible. Pour déterminer avec une plus grande précision la proportion de DB ayant des atmosphères pures en hélium, il serait nécessaire d'obtenir des spectres à très haut signal-sur-bruit, en particulier dans la région entre 6400–6800 Å.

L'analyse des abondances d'hydrogène a aussi montré que, sous $T_{\text{eff}} = 20,000$ K, H/He varie significativement d'un objet à l'autre. Pour certains objets, seule une limite supérieure sur H/He a pu être déterminée, basée sur l'absence de la raie H α , bien que celle-ci soit facilement détectable dans ce régime en température. Ces objets ne peuvent avoir effectué de transition DA→DB, M_H étant tout simplement trop faible. Dans d'autres cas cependant, les abondances déterminées impliquent une M_H suffisamment élevée pour que la naine blanche

soit apparue comme une DA *avant* l'épisode de dilution convective. Ces deux types d'objets doivent donc nécessairement avoir suivi des canaux évolutifs différents.

Afin d'avoir un portrait plus complet de l'évolution spectrale des naines blanches de type DB, le rapport $N_{\text{DB}}/(N_{\text{DA}} + N_{\text{DB}})$ à différentes températures a été calculé. Ceci a été possible encore une fois grâce à l'énorme quantité de données présentes dans les bases de données du SDSS. Il a été démontré que ce rapport varie énormément en fonction de la température effective, et donc de l'âge. En particulier, le rapport demeure relativement constant entre $T_{\text{eff}} = 40,000$ K et $T_{\text{eff}} \sim 27,000$ K, à une valeur de $\sim 5\%$, puis augmente de façon graduelle, jusqu'à atteindre 25% à 15,000 K. Ceci est cohérent avec le scénario de dilution convective qui prédit la dilution de la couche mince d'hydrogène dans la zone convective d'hélium, convertissant ainsi certaines naines blanches de type DA en DB.

Quelques doutes demeurent néanmoins quant à la valeur exacte de ces rapports. Une grande source d'incertitude, outre les lacunes associées aux modèles d'atmosphère (élargissement Stark, élargissement van der Waals, effets 3D, etc.) et aux données (faible signal-sur-bruit, problème de calibration en flux) susmentionnées, provient des critères de sélection des naines blanches dans le relevé SDSS. Bien qu'un poids plus élevé ait été accordé aux objets ne satisfaisant pas les critères de sélection des *hot standard* (objets rouges), il est fort probable qu'il y ait d'autres effets de sélection qui discriminent un type d'objet plutôt qu'un autre. De plus, l'estimation de la complétude du SDSS a été effectuée à l'aide des données du DR4, qui ne comprenait qu'environ 9000 naines blanches. Le catalogue le plus récent, tiré du DR14, en comprend environ 50,000. Une nouvelle étude sur la complétude du SDSS serait donc de mise.

De plus, l'étude présentée dans cette thèse s'est surtout concentrée sur les naines blanches de type DB, objets qui ne se trouvent qu'entre $T_{\text{eff}} \sim 10,000$ K et $\sim 40,000$ K. Pour avoir un portrait complet de l'évolution spectrale des naines blanches à atmosphère riche en hélium, il faudrait aussi inclure dans cette analyse les naines blanches de type DO ($120,000$ K $> T_{\text{eff}} > 40,000$ K) ainsi que les DC ($T_{\text{eff}} < 10,000$ K).

Tel que mentionné, il a été trouvé que 61% des naines blanches de type DB avaient une atmosphère contenant une certaine quantité d'hydrogène. L'origine de cet hydrogène atmosphérique n'est cependant toujours pas claire. Bien que l'origine résiduelle et le scénario de la dilution convective permettent de bien expliquer les faibles abondances notées dans

certaines naines blanches, dans d'autres cas il semble nécessaire d'invoquer une source d'hydrogène externe, telle que l'accrétion du milieu interstellaire ou encore de débris d'un ancien système planétaire. Si tel est le cas, il est fort probable que d'autres éléments, tels que des métaux, soient accrétés par la même occasion. Une analyse plus poussée de la composition atmosphérique des DBZ ainsi que la fraction de tels objets pourrait alors fournir quelques réponses. Dans ce cas, il faudrait des modèles d'atmosphère plus réalistes que ceux ayant été utilisés dans le cadre de cette thèse, qui n'incluent pas seulement les raies H & K du calcium, mais aussi d'autres métaux, comme l'oxygène et le magnésium. De nouveaux spectres à plus haut rapport signal-sur-bruit seraient aussi bienvenus, car, tout comme pour l'hydrogène, la détection des raies métalliques dépend de la qualité des données.

Finalement, de nouveaux modèles d'atmosphère chimiquement stratifiée ont été présentés. Ces modèles, ayant des profils d'abondance d'hydrogène en équilibre diffusif, permettent de produire des spectres synthétiques avec des raies d'hydrogène plus fortes que celles obtenues à l'aide des modèles homogènes, sans significativement affecter la largeur des raies d'hélium. La partie bleue du spectre observé de WD 1822+410 a pu être relativement bien reproduite à l'aide de modèles stratifiés ayant une abondance d'hydrogène 10 fois plus faible que ce qui est prévu par les modèles homogènes. Il est probablement peu réaliste de supposer que l'hydrogène et l'hélium dans l'atmosphère d'une naine blanche soient en parfait équilibre diffusif, notamment si l'on considère le dépassement convectif, cependant les résultats présentés ici montrent qu'il est possible qu'une mince couche d'hydrogène subsiste à la surface. Dans ce cas, les valeurs de M_H mesurées à l'aide des modèles d'atmosphère actuels ne seraient pas représentatives de la quantité réelle d'hydrogène contenue dans l'enveloppe des DBA. Des modèles incluant un traitement moins approximatif de la convection, des modèles 3D hydrodynamiques incluant du dépassement convectif par exemple, pourraient produire des profils d'abondances réalistes et potentiellement déterminer la quantité réelle d'hydrogène contenue dans l'enveloppe des naines blanches de type DBA.

Cette thèse a démontré que, malgré les meilleurs efforts de la communauté scientifique, beaucoup de questions demeurent toujours sans réponse au sujet des étoiles naines blanches et de leur évolution.

Bibliographie

- Abazajian, K., Adelman-McCarthy, J. K., Agüeros, M. A., et al. 2003, AJ, 126, 2081
- Ali, A. W., & Griem, H. R. 1965, Phys. Rev., 140, A1044. <https://link.aps.org/doi/10.1103/PhysRev.140.A1044>
- Beauchamp, A. 1995, PhD thesis, Université de Montréal
- Beauchamp, A., Wesemael, F., & Bergeron, P. 1997, ApJS, 108, 559
- Beauchamp, A., Wesemael, F., Bergeron, P., Liebert, J., & Saffer, R. A. 1996, in Astronomical Society of the Pacific Conference Series, Vol. 96, Hydrogen Deficient Stars, ed. C. S. Jeffery & U. Heber, 295
- Bédard, A., Bergeron, P., & Fontaine, G. 2017, ApJ, 848, 11
- Bergeron, P., Dufour, P., Fontaine, G., et al. 2019, arXiv e-prints, arXiv :1904.02022
- Bergeron, P., Leggett, S. K., & Ruiz, M. T. 2001, ApJS, 133, 413
- Bergeron, P., Ruiz, M. T., & Leggett, S. K. 1997, ApJS, 108, 339
- Bergeron, P., Saffer, R. A., & Liebert, J. 1992, ApJ, 394, 228
- Bergeron, P., Saumon, D., & Wesemael, F. 1995a, ApJ, 443, 764
- Bergeron, P., Wesemael, F., & Fontaine, G. 1991, ApJ, 367, 253
- Bergeron, P., Wesemael, F., Lamontagne, R., et al. 1995b, ApJ, 449, 258
- Bergeron, P., Wesemael, F., Dufour, P., et al. 2011, ApJ, 737, 28
- Cukanovaite, E., Tremblay, P. E., Freytag, B., Ludwig, H. G., & Bergeron, P. 2018, MNRAS, 481, 1522
- Dantona, F., & Mazzitelli, I. 1979, A&A, 74, 161
- Deridder, G., & van Rensbergen, W. 1976, A&AS, 23, 147
- Dreizler, S., & Werner, K. 1996, A&A, 314, 217
- Dufour, P., Bergeron, P., & Fontaine, G. 2005, ApJ, 627, 404

- Dufour, P., Blouin, S., Coutu, S., et al. 2017, in Astronomical Society of the Pacific Conference Series, Vol. 509, 20th European White Dwarf Workshop, ed. P.-E. Tremblay, B. Gaensicke, & T. Marsh, 3
- Dufour, P., Fontaine, G., Liebert, J., Schmidt, G. D., & Behara, N. 2008, *ApJ*, 683, 978
- Dufour, P., Kilic, M., Fontaine, G., et al. 2012, *ApJ*, 749, 6
- Dufour, P., Liebert, J., Fontaine, G., & Behara, N. 2007, *Nature*, 450, 522
- Dunlap, B. H., & Clemens, J. C. 2015, in Astronomical Society of the Pacific Conference Series, Vol. 493, 19th European Workshop on White Dwarfs, ed. P. Dufour, P. Bergeron, & G. Fontaine, 547
- Eisenstein, D. J., Liebert, J., Koester, D., et al. 2006a, *AJ*, 132, 676
- Eisenstein, D. J., Liebert, J., Harris, H. C., et al. 2006b, *ApJS*, 167, 40
- El-Badry, K., Rix, H.-W., & Weisz, D. R. 2018, *ApJ*, 860, L17
- Falcon, R. E., Winget, D. E., Montgomery, M. H., & Williams, K. A. 2012, *ApJ*, 757, 116
- Farihi, J., Koester, D., Zuckerman, B., et al. 2016, *MNRAS*, 463, 3186
- Ferrario, L., de Martino, D., & Gänsicke, B. T. 2015, *Space Sci. Rev.*, 191, 111
- Fontaine, G., & Brassard, P. 2005, in Astronomical Society of the Pacific Conference Series, Vol. 334, 14th European Workshop on White Dwarfs, ed. D. Koester & S. Moehler, 49
- Fontaine, G., Brassard, P., & Bergeron, P. 2001, *PASP*, 113, 409
- Fontaine, G., & Wesemael, F. 1987, in IAU Colloq. 95 : Second Conference on Faint Blue Stars, ed. A. G. D. Philip, D. S. Hayes, & J. W. Liebert, 319–326
- Gaia Collaboration, Brown, A. G. A., Vallenari, A., et al. 2018, *A&A*, 616, A1
- Gänsicke, B. T., Koester, D., Farihi, J., et al. 2012, *MNRAS*, 424, 333
- Genest-Beaulieu, C., & Bergeron, P. 2014, *ApJ*, 796, 128
- Genest-Beaulieu, C., & Bergeron, P. 2017, in 20th European White Dwarf Workshop, ed. P. E. Tremblay, B. Gaensicke, & T. Marsh, Vol. 509, 201
- . 2019, *ApJ*, 871, 169
- Gentile Fusillo, N. P., Gänsicke, B. T., Farihi, J., et al. 2017, *MNRAS*, 468, 971
- Gentile Fusillo, N. P., Tremblay, P.-E., Gänsicke, B. T., et al. 2019, *MNRAS*, 482, 4570
- Giammichele, N., Bergeron, P., & Dufour, P. 2012, *ApJS*, 199, 29
- Gianninas, A., Bergeron, P., & Ruiz, M. T. 2011, *ApJ*, 743, 138

- Gomez, T. A., Montgomery, M. H., Nagayama, T., Kilcrease, D. P., & Winget, D. E. 2017, in Astronomical Society of the Pacific Conference Series, Vol. 509, 20th European White Dwarf Workshop, ed. P.-E. Tremblay, B. Gaensicke, & T. Marsh, 143
- Harris, H. C., Munn, J. A., Kilic, M., et al. 2006, AJ, 131, 571
- Holberg, J. B., Oswalt, T. D., & Barstow, M. A. 2012, AJ, 143, 68
- Hubeny, I., & Lanz, T. 1995, ApJ, 439, 875
- Hügelmeyer, S. D., Dreizler, S., Werner, K., et al. 2005, A&A, 442, 309
- Iben, Jr., I. 1990, ApJ, 353, 215
- Kepler, S. O., Pelisoli, I., Koester, D., et al. 2015, MNRAS, 446, 4078
- . 2016, MNRAS, 455, 3413
- Kilic, M., Hambly, N. C., Bergeron, P., Genest-Beaulieu, C., & Rowell, N. 2018, MNRAS, 479, L113
- Kleinman, S. J., Kepler, S. O., Koester, D., et al. 2013, ApJS, 204, 5
- Koester, D. 1976, A&A, 52, 415
- Koester, D., & Kepler, S. O. 2015, A&A, 583, A86
- Koester, D., Kepler, S. O., Kleinman, S. J., & Nitta, A. 2009a, Journal of Physics Conference Series, 172, 012006
- Koester, D., Voss, B., Napiwotzki, R., et al. 2009b, A&A, 505, 441
- Lemke, M. 1997, A&AS, 122, 285
- Leo, P. J., Peach, G., & Whittingham, I. B. 1995, Journal of Physics B : Atomic, Molecular and Optical Physics, 28, 591
- Lewis, E. L. 1967, in Proc. Phys. Soc., Vol. 92, 817
- Liebert, J. 1988, Publications of the Astronomical Society of the Pacific, 100, 1302
- Liebert, J., Bergeron, P., & Holberg, J. B. 2005, ApJS, 156, 47
- Liebert, J., Bergeron, P., & Saffer, R. A. 1991, in NATO Advanced Science Institutes (ASI) Series C, Vol. 336, NATO Advanced Science Institutes (ASI) Series C, ed. G. Vauclair & E. Sion, 409
- Liebert, J., Fontaine, G., & Wesemael, F. 1987, Memorie della Societa Astronomica Italiana, 58, 17
- Liebert, J., Wesemael, F., Hansen, C. J., et al. 1986, ApJ, 309, 241
- Limoges, M.-M., & Bergeron, P. 2010, ApJ, 714, 1037

- Limoges, M. M., Bergeron, P., & Dufour, P. 2009, ApJ, 696, 1461
- Limoges, M.-M., Bergeron, P., & Lépine, S. 2015, ApJS, 219, 19
- MacDonald, J., & Vennes, S. 1991, ApJ, 371, 719
- Manseau, P. M., Bergeron, P., & Green, E. M. 2016, ApJ, 833, 127
- McCook, G. P., & Sion, E. M. 1999, The Astrophysical Journal Supplement Series, 121, 1
- Mullamphy, D. F. T., Peach, G., & Whittingham, I. B. 1991, Journal of Physics B : Atomic, Molecular and Optical Physics, 24, 3709
- Paquette, C., Pelletier, C., Fontaine, G., & Michaud, G. 1986, The Astrophysical Journal Supplement Series, 61, 197
- Parsons, S. G., Gänsicke, B. T., Marsh, T. R., et al. 2017, MNRAS, 470, 4473
- Pelletier, C., Fontaine, G., Wesemael, F., Michaud, G., & Wegner, G. 1986, ApJ, 307, 242
- Press, W. H., Flannery, B. P., Teukolsky, S. A., & Vetterling, W. T. 1992, Numerical Recipes in FORTRAN 77 : The Art of Scientific Computing, 2nd edn. (Cambridge University Press). <http://www.worldcat.org/isbn/052143064X>
- Preval, S. P., & Barstow, M. A. 2017, in Astronomical Society of the Pacific Conference Series, Vol. 509, 20th European White Dwarf Workshop, ed. P. E. Tremblay, B. Gaensicke, & T. Marsh, 195
- Provencal, J. L., Shipman, H. L., Høg, E., & Thejll, P. 1998, ApJ, 494, 759
- Raddi, R., Gänsicke, B. T., Koester, D., et al. 2015, MNRAS, 450, 2083
- Rolland, B., Bergeron, P., & Fontaine, G. 2018, ApJ, 857, 56
- Schlafly, E. F., & Finkbeiner, D. P. 2011, ApJ, 737, 103
- Tremblay, P.-E., & Bergeron, P. 2009, ApJ, 696, 1755
- Tremblay, P.-E., Bergeron, P., & Gianninas, A. 2011a, ApJ, 730, 128
- Tremblay, P. E., Cukanovaite, E., Gentile Fusillo, N. P., Cunningham, T., & Hollands, M. A. 2019, MNRAS, 482, 5222
- Tremblay, P.-E., Ludwig, H.-G., Steffen, M., Bergeron, P., & Freytag, B. 2011b, A&A, 531, L19
- Tremblay, P.-E., Ludwig, H.-G., Steffen, M., & Freytag, B. 2013a, A&A, 552, A13
- . 2013b, A&A, 559, A104
- Tremblay, P.-E., Gentile-Fusillo, N., Raddi, R., et al. 2017, MNRAS, 465, 2849
- Unsold, A. 1955, Physik der Sternatmosphären, MIT besonderer Berücksichtigung der Sonne.

- Van Grootel, V., Fontaine, G., Brassard, P., & Dupret, M. A. 2017, in Astronomical Society of the Pacific Conference Series, Vol. 509, 20th European White Dwarf Workshop, ed. P. E. Tremblay, B. Gaensicke, & T. Marsh, 321
- van Leeuwen, F. 2007, A&A, 474, 653
- Vauclair, G., & Reisse, C. 1977, A&A, 61, 415
- Vennes, S., Pelletier, C., Fontaine, G., & Wesemael, F. 1988, ApJ, 331, 876
- Veras, D., Shannon, A., & Gänsicke, B. T. 2014, MNRAS, 445, 4175
- Voss, B., Koester, D., Napiwotzki, R., Christlieb, N., & Reimers, D. 2007, A&A, 470, 1079
- Werner, K., & Herwig, F. 2006, PASP, 118, 183
- Wesemael, F., Greenstein, J. L., Liebert, J., et al. 1993, PASP, 105, 761
- Zuckerman, B., Koester, D., Melis, C., Hansen, B. M., & Jura, M. 2007, ApJ, 671, 872

Annexe A

Systèmes binaires de type DA+DB du Chapitre 3

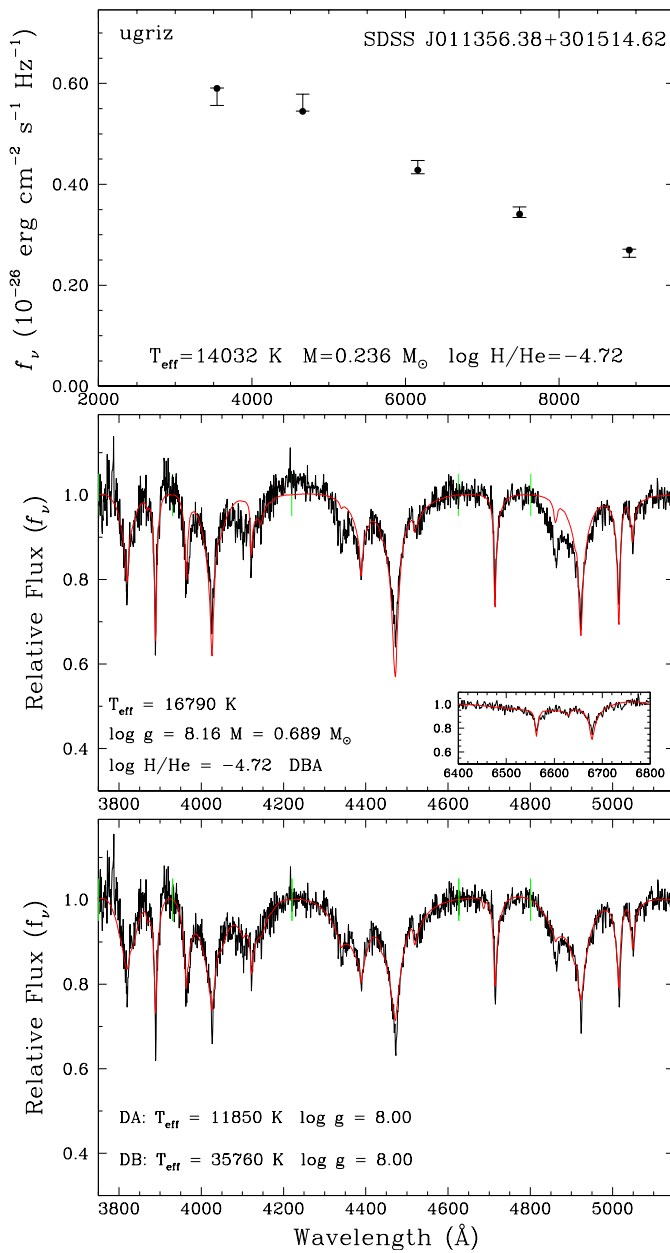


FIGURE A.1. SDSS J011356.38+301514.62

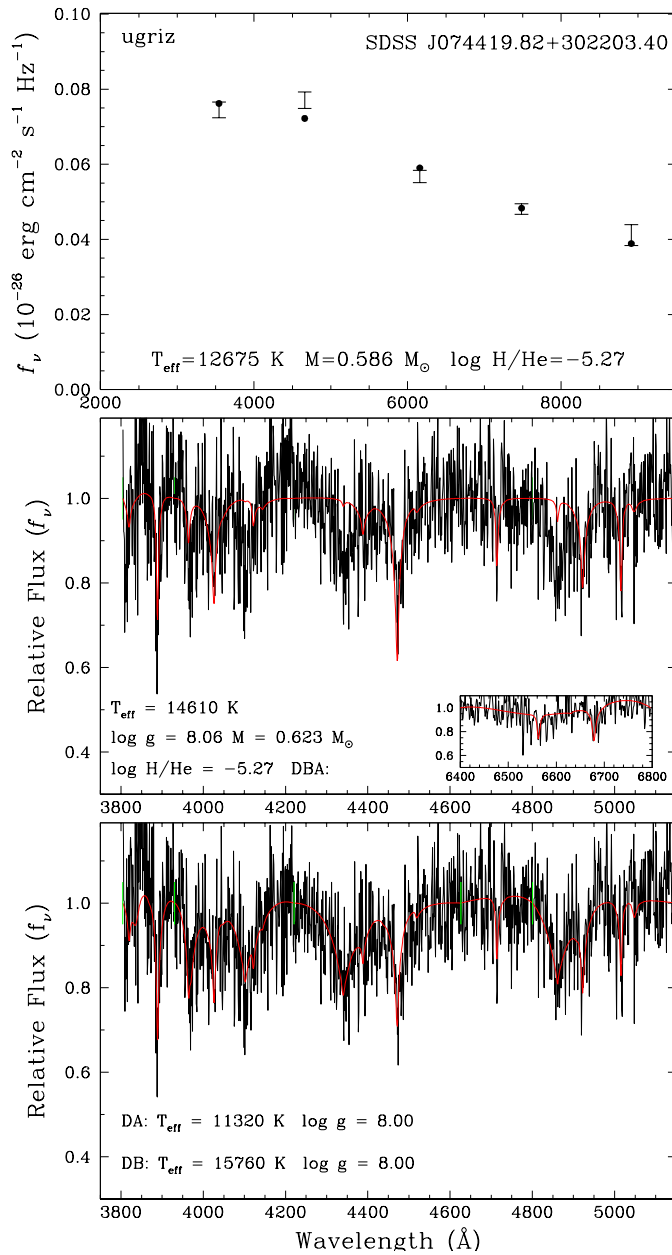


FIGURE A.2. SDSS J074419.82+302203.40. La gravité de surface forcée à $\log g = 8.0$ pour obtenir la solution photométrique.

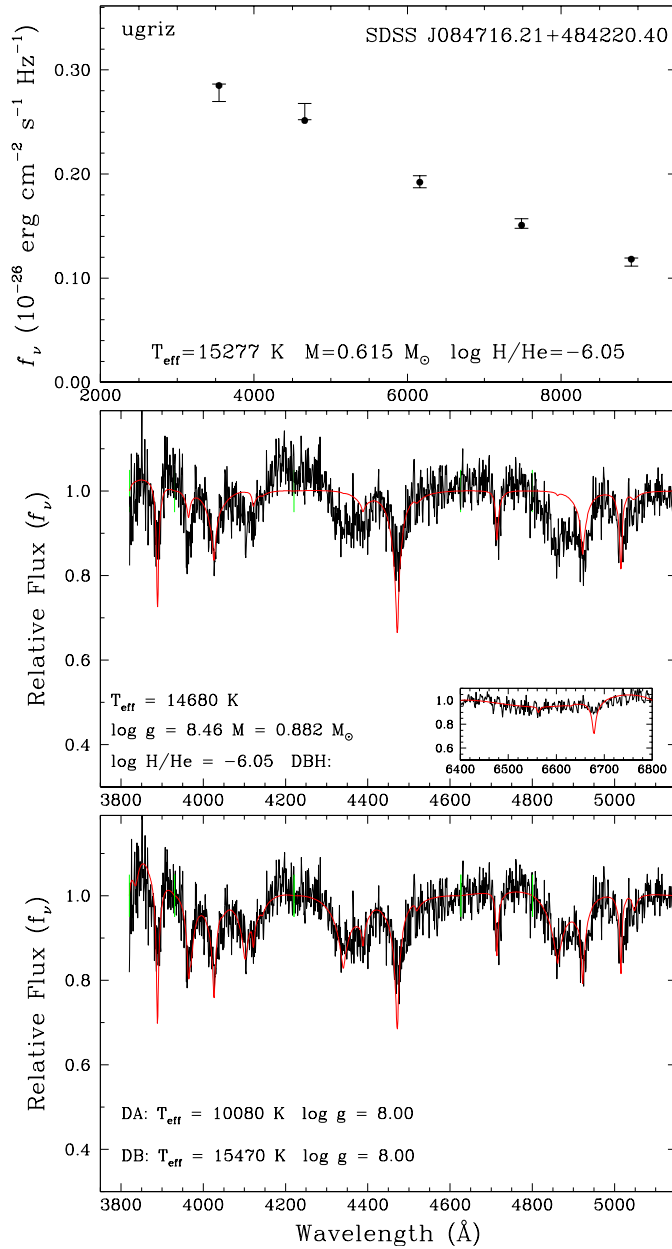


FIGURE A.3. SDSS J084716.21+484220.40.

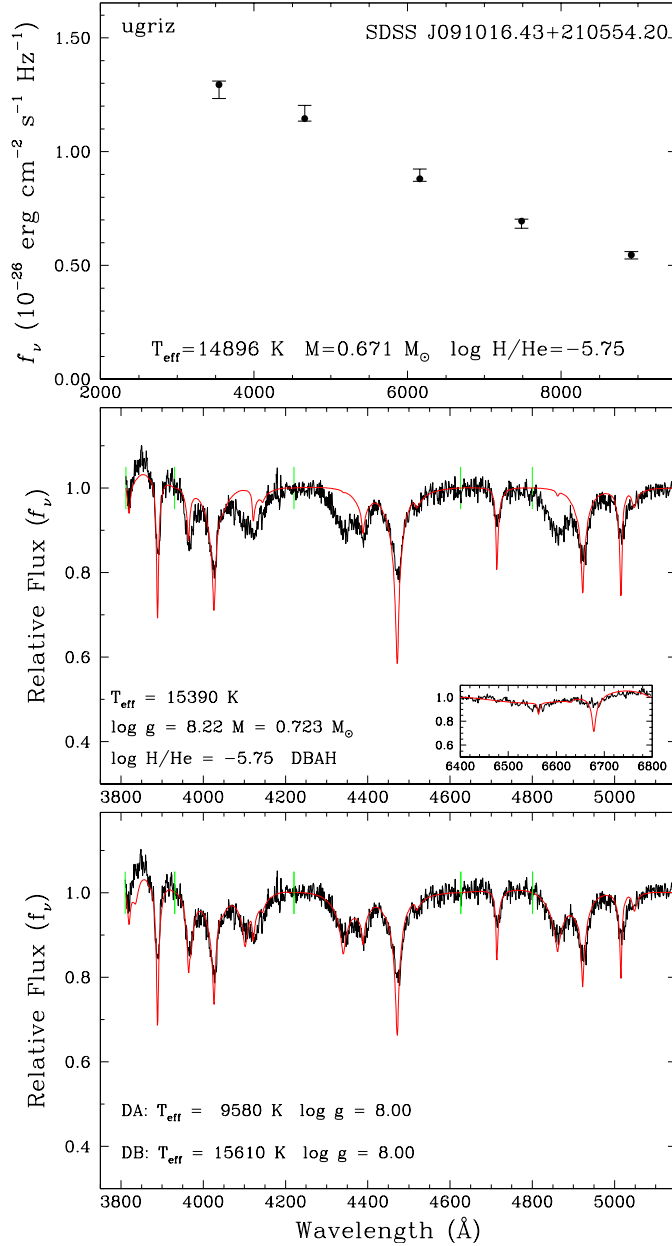


FIGURE A.4. SDSS J091016.43+210554.20. Les deux membres de ce système présentent un champ magnétique.

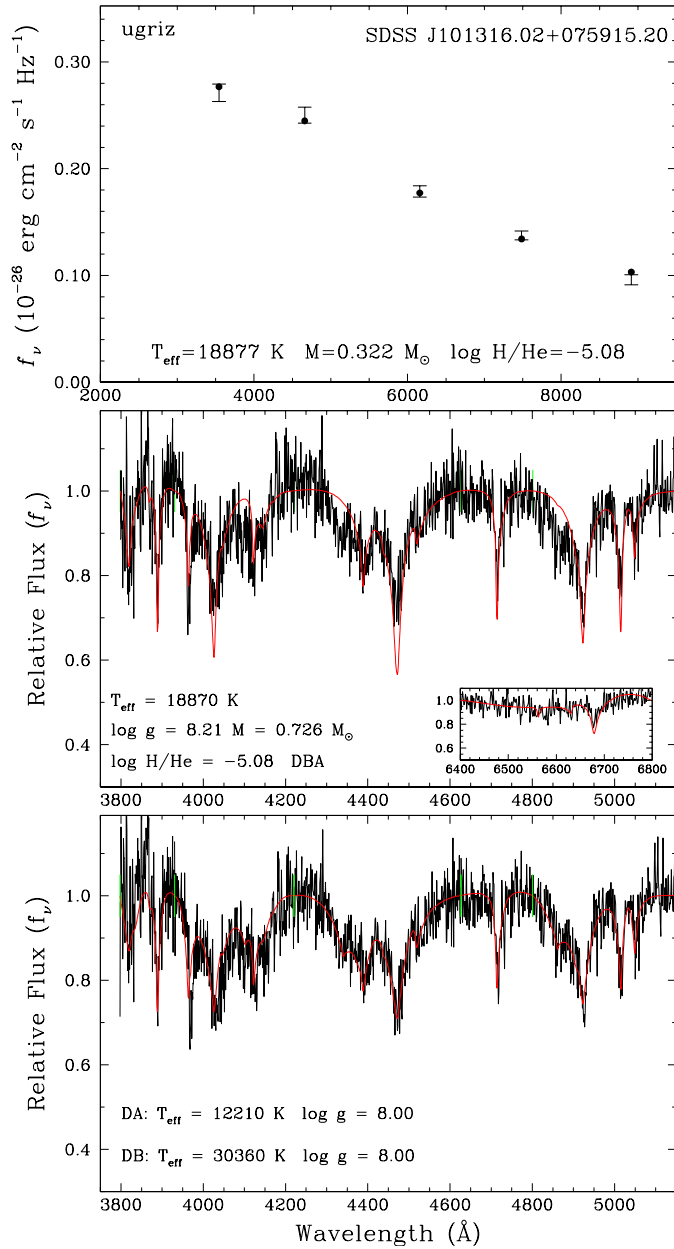


FIGURE A.5. SDSS J101316.02+075915.20

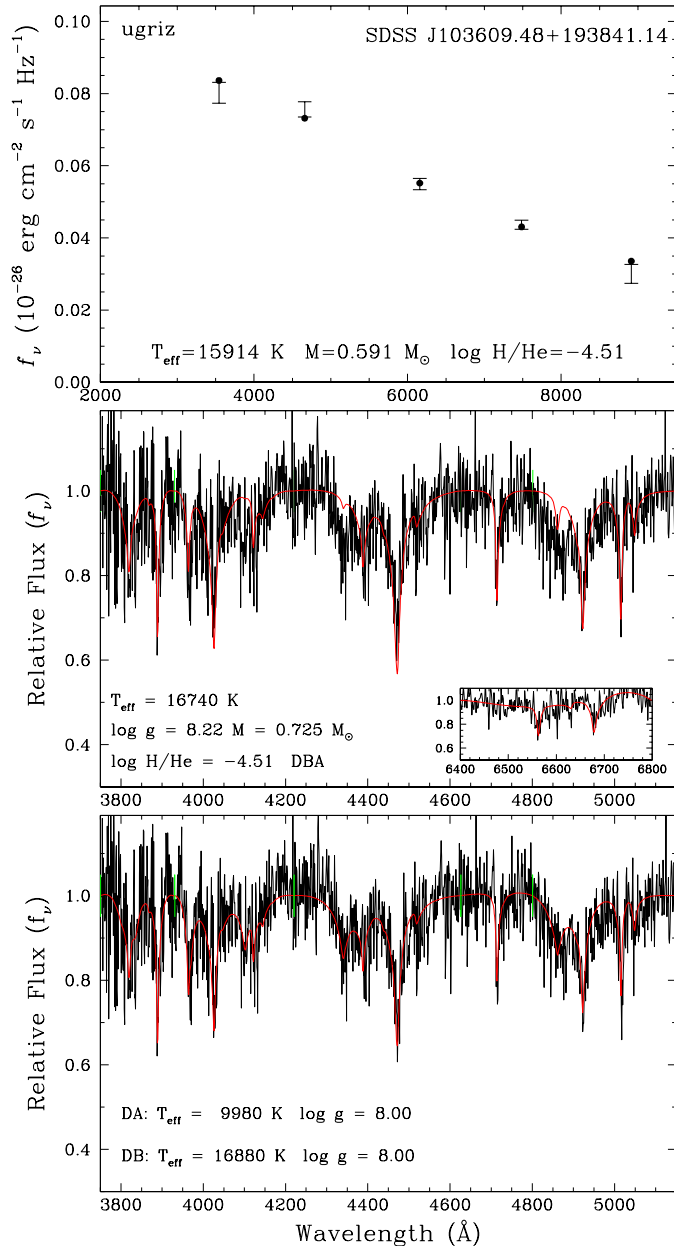


FIGURE A.6. SDSS J103609.48+193841.14. La gravité de surface forcée à $\log g = 8.0$ pour obtenir la solution photométrique.

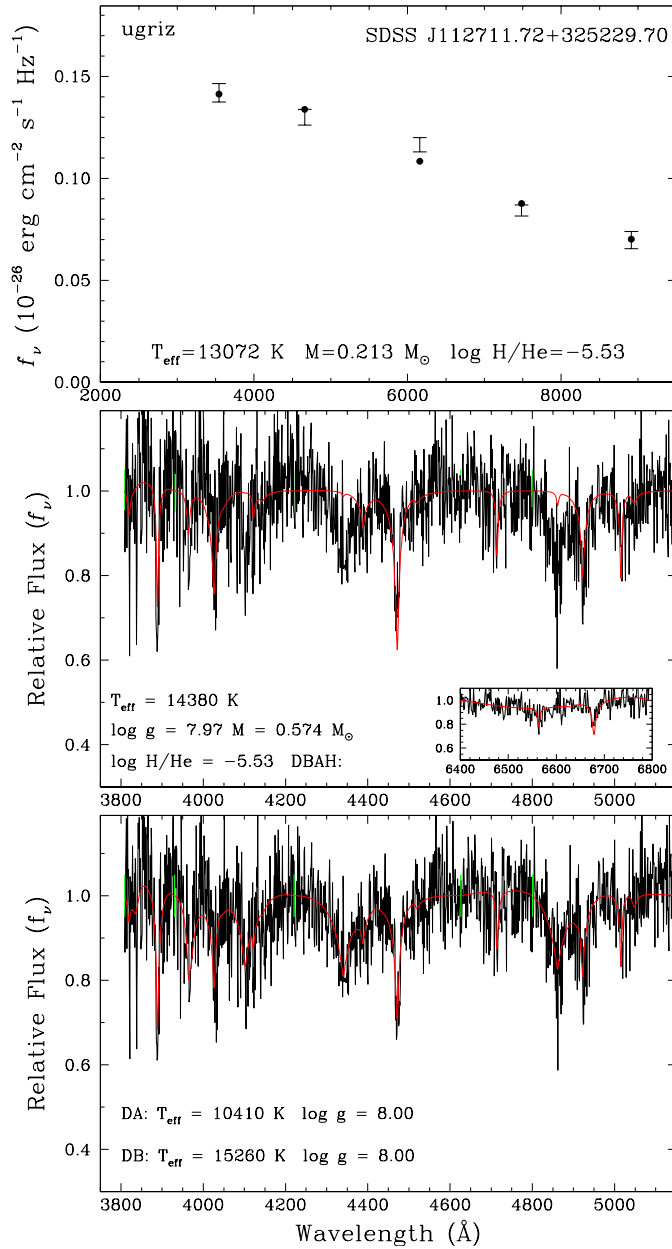


FIGURE A.7. SDSS J112711.72+325229.70

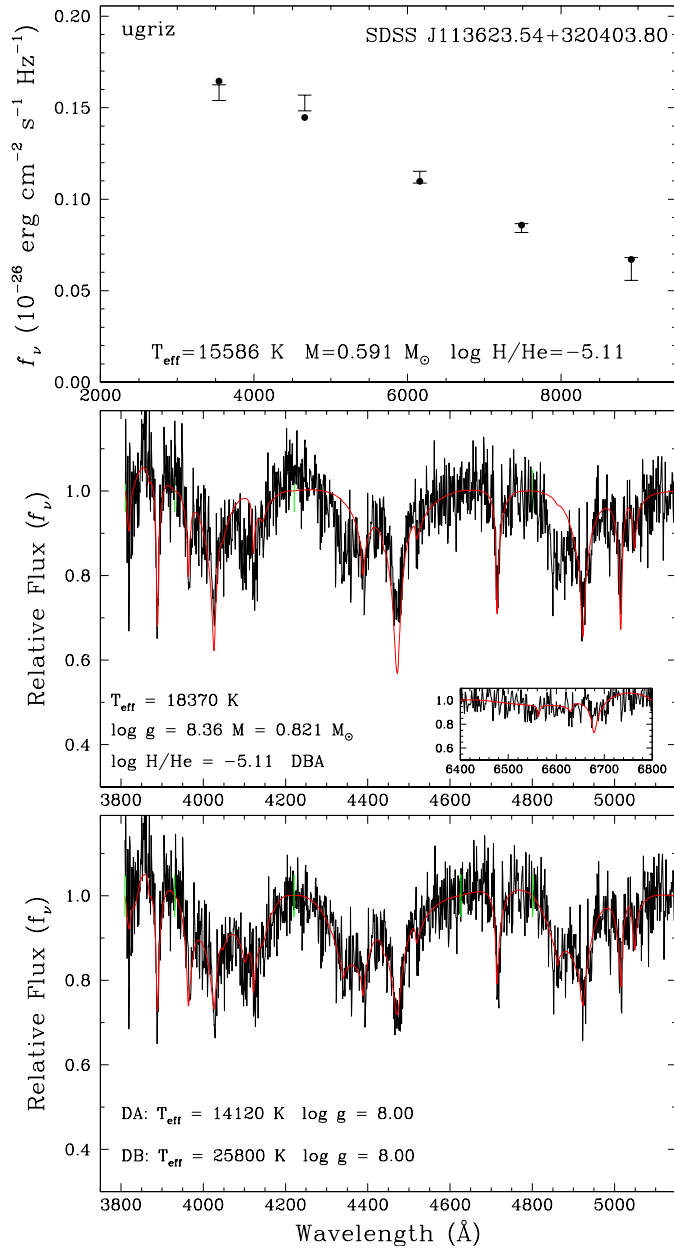


FIGURE A.8. SDSS J113623.54+320403.80. La gravité de surface forcée à $\log g = 8.0$ pour obtenir la solution photométrique.

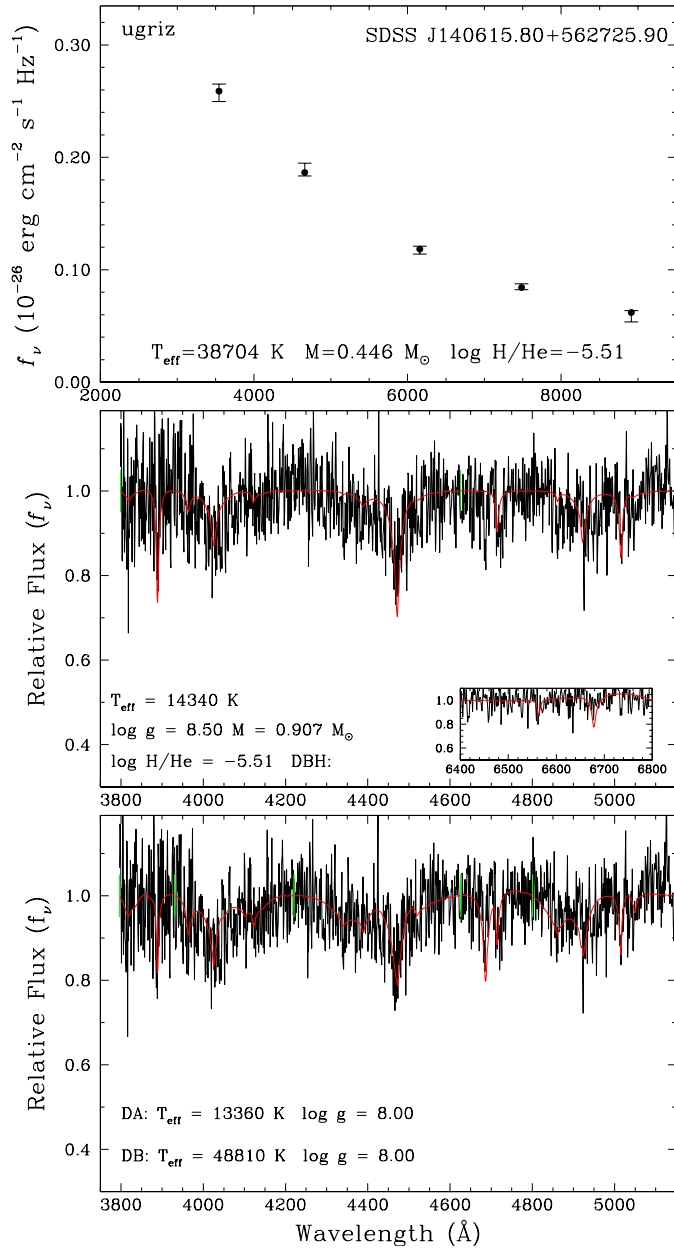


FIGURE A.9. SDSS J140615.80+562725.90

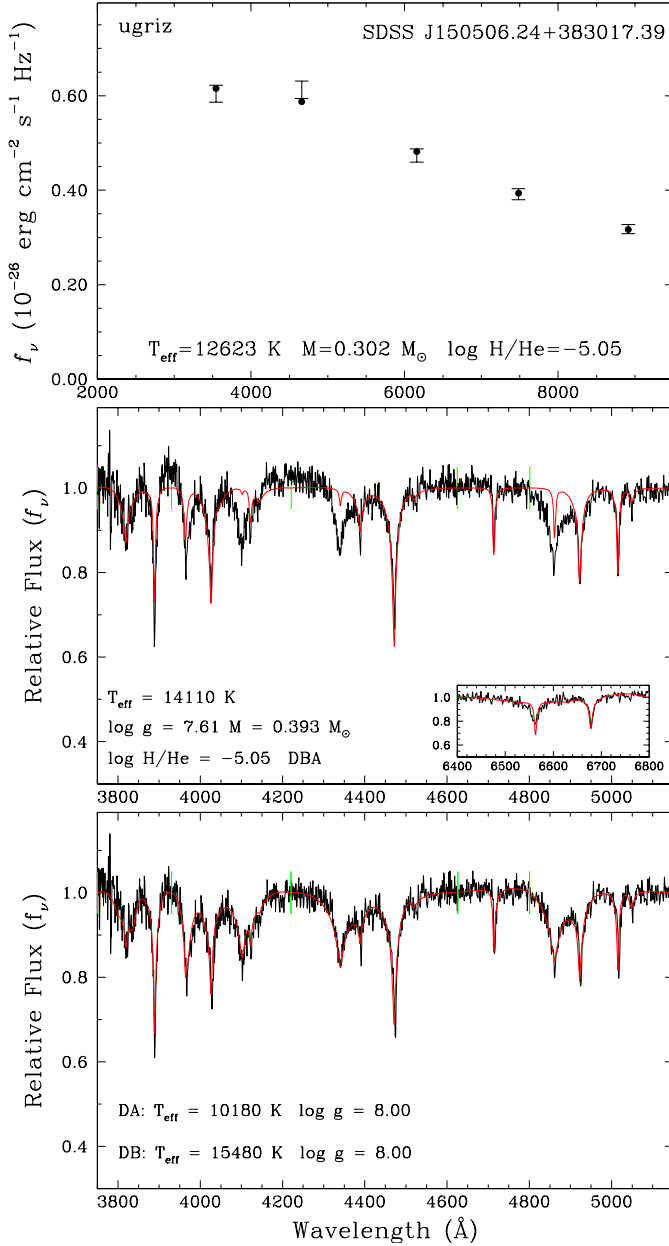


FIGURE A.10. SDSS J150506.24+383017.39

Annexe B

Procédure de stratification

L'article intitulé *A Photometric and Spectroscopic Investigation of the DB White Dwarf Population in the SDSS and Gaia*, présenté au chapitre 3 présente de nouveaux modèles d'atmosphère chimiquement stratifiées. Les équations d'équilibre diffusif, la méthode de Newton ainsi que la routine implémentée dans le code de modèle d'atmosphère sont décrits dans cette section.

B.1. Profil d'abondance en équilibre diffusif

Le profil d'abondance d'hydrogène $\frac{dy}{dP}$ dans les modèles d'atmosphère stratifiés est calculé en supposant l'équilibre diffusif. Le développement présenté ici est similaire à ce qui est présenté dans Pelletier et al. (1986) (voir aussi Vennes et al. 1988).

La vitesse de diffusion relative entre deux éléments ω_{12} de proportions arbitraires est donnée par

$$\omega_{12} = D_{12} (1 + y) \left[-\frac{\partial \ln c_2}{\partial r} + \left(\frac{A_1 Z_2 - A_2 Z_1}{Z_1 + y Z_2} \right) \frac{m_p g}{kT} + \left(\frac{Z_2 - Z_1}{Z_1 + y Z_2} \right) \frac{\partial \ln p_i}{\partial r} + \left(\frac{A_1 A_2}{A_1 + y A_2} \right) \frac{m_p g_r}{kT} \right] \quad (\text{B.1})$$

où D_{12} est le coefficient de diffusion, $y \equiv n_2/n_1$ est l'abondance en nombre, $c_2 = n_2/(n_1 + n_2)$, r la coordonnée radiale, A_x et Z_x le poids atomique et la charge moyenne de l'élément x ($=1,2$), respectivement, m_p la masse du proton, k la constante de Boltzmann, T la température, g est la gravité locale, $p_i = p_1 + p_2$ est la pression ionique et g_r est l'accélération radiative (vers le haut) appliquée sur l'élément 2 dans le plasma. Dans le cas présent, le gaz est composé d'hydrogène (élément 1) et d'hélium (élément 2). Il est à noter que l'équation B.1

ne considère pas la diffusion thermique, qui est négligeable dans les atmosphères de naines blanches (Paquette et al., 1986). Dans ce qui suit, l'accélération radiative sera supposée nulle ($g_r = 0$).

Lorsque l'équilibre diffusion est atteint, $\omega_{12} = 0$. Dans ce cas, l'équation B.1 devient

$$\frac{\partial \ln c_2}{\partial r} = \left(\frac{A_1 Z_2 - A_2 Z_1}{Z_1 + y Z_2} \right) \frac{m_p g}{kT} + \left(\frac{Z_2 - Z_1}{Z_1 + y Z_2} \right) \frac{\partial \ln P_i}{\partial r} \quad (\text{B.2})$$

En imposant la neutralité de charge

$$P = P_1(1 + Z_1) + P_2(1 + Z_2) \quad (\text{B.3})$$

ainsi qu'en supposant que les charges moyennes Z_1 et Z_2 ne varient pas en fonction de la profondeur, il peut être démontré que la pression ionique et la pression totale sont reliées par

$$\frac{\partial \ln P_i}{\partial r} = \frac{\partial \ln P}{\partial r} - \frac{(Z_2 - Z_1)}{(1 + Z_1) + y(1 + Z_2)} \frac{1}{(1 + y)} \frac{\partial y}{\partial r} \quad (\text{B.4})$$

En combinant les équations B.2 et B.4, on obtient

$$\frac{\partial \ln c_2}{\partial r} = \left(\frac{A_1 Z_2 - A_2 Z_1}{Z_1 + y Z_2} \right) \frac{m_p g}{kT} + \left(\frac{Z_2 - Z_1}{Z_1 + y Z_2} \right) \left[\frac{\partial \ln P}{\partial r} - \frac{(Z_2 - Z_1)}{(1 + Z_1) + y(1 + Z_2)} \frac{1}{(1 + y)} \frac{\partial y}{\partial r} \right] \quad (\text{B.5})$$

Il est possible de relier $m_p g / kT$ au gradient de pression total $\frac{\partial P}{\partial r}$ à l'aide de l'équilibre hydrostatique :

$$\frac{\partial P}{\partial r} = -\rho g \quad (\text{B.6})$$

ou encore

$$\frac{1}{P} \frac{\partial P}{\partial r} = -\frac{\rho g}{P} \quad (\text{B.7})$$

qui devient, en utilisant l'équation d'état $P = nkT$

$$\frac{\partial \ln P}{\partial r} = -\frac{\rho g}{nkT} \quad (\text{B.8})$$

La densité en nombre et en masse peuvent s'écrire $n = n_1(1 + Z_1) + n_2(1 + Z_2)$ et $\rho = n_1A_1m_p + n_2A_2m_p + n_e m_e$, où n_e et m_e sont la densité et la masse électronique. En supposant la contribution des électrons à ρ négligeable, l'équation B.8 devient

$$\begin{aligned}\frac{\partial \ln P}{\partial r} &= -\frac{(n_1A_1m_p + n_2A_2m_p)g}{[n_1(1 + Z_1) + n_2(1 + Z_2)] kT} \\ &= -\frac{(n_1A_1 + n_2A_2)m_pg}{[n_1(1 + Z_1) + n_2(1 + Z_2)] kT} \\ &= -\frac{n_1(A_1 + n_2/n_1A_1)m_pg}{n_1[n_1(1 + Z_1) + n_2/n_1(1 + Z_2)] kT}\end{aligned}\quad (\text{B.9})$$

En se rappelant que $n_2/n_1 \equiv y$,

$$\frac{\partial \ln P}{\partial r} = -\frac{(A_1 + yA_2)m_pg}{[(1 + Z_1) + y(1 + Z_2)] kT} \quad (\text{B.10})$$

Finalement, en réorganisant les termes, on obtient

$$\frac{m_pg}{kT} = -\frac{\partial \ln P [(1 + Z_1) + y(1 + Z_2)]}{\partial r (A_1 + yA_2)} \quad (\text{B.11})$$

En combinant les équations B.11 et B.5, on obtient une équation pour le profil d'abondance :

$$\frac{\partial y}{\partial \ln P} = \frac{[E(y)(A_2Z_1 - A_1Z_2) + D(y)(Z_2 - Z_1)]}{\left[\frac{C(y)D(y)}{yB(y)}\right] + \left[\frac{D(y)(Z_2 - Z_1)^2}{B(y)E(y)}\right]} \quad (\text{B.12})$$

où

$$\begin{aligned}B(y) &= 1 + y \\ C(y) &= Z_1 + yZ_2 \\ D(y) &= A_1 + yA_2 \\ E(y) &= (1 + Z_1) + y(1 + Z_2)\end{aligned}\quad (\text{B.13})$$

L'équation B.12 permet donc de calculer l'abondance d'hydrogène en fonction de la pression totale dans l'atmosphère d'une naine blanche.

B.2. Méthode de Newton

Si on suppose une fonction $f(x)$, son développement en série de Taylor est

$$f(x + \Delta x) = f(x_0) + (\Delta x) \frac{df}{dx} \Big|_{x_0} + \frac{(\Delta x)^2}{2!} \frac{d^2 f}{dx^2} \Big|_{x_0} + \frac{(\Delta x)^3}{3!} \frac{d^3 f}{dx^3} \Big|_{x_0} + \dots \quad (\text{B.14})$$

La méthode de Newton dit que, si $f(x)$ possède une racine à $x = r$, il est possible de définir Δx de sorte que $x_0 + \Delta x = r$. En ne gardant que les deux premiers termes de l'équation B.14, on obtient

$$f(r) = f(x_0) + (r - x_0) \frac{df}{dx} \Big|_{x_0} \quad (\text{B.15})$$

Comme r est une racine, $f(r) = 0$. Par conséquent, l'équation B.15 devient

$$r = x_0 - \frac{f(x_0)}{f'(x_0)} \quad (\text{B.16})$$

où $f'(x_0) = df(x)/dx \Big|_{x_0}$. Comme le développement en série de Taylor de la fonction $f(x)$ a été tronqué au deuxième terme, la valeur de r obtenue grâce à l'équation B.16 n'est qu'une approximation de la racine réelle. Une meilleure approximation de la racine peut être obtenue grâce à l'équation B.16 en réévaluant f et f' à $x = r$. Il s'agit ensuite de procéder par itération jusqu'à ce que la valeur de r ait convergé.

B.3. Implémentation du profil d'abondance d'hydrogène dans le code de modèle d'atmosphère

La méthode de Newton peut être utilisée pour calculer le profil d'abondance dans l'atmosphère d'une naine blanche. Bien que l'équation B.12 décrive ce profil d'abondance, elle ne peut être utilisée directement avec la méthode de Newton.

La première étape consiste à réorganiser les termes de l'équation B.12 (voir aussi les équations B.13),

$$d \ln P = \frac{\left(\frac{C(y)D(y)}{yB(y)} + \frac{D(y)(Z_2 - Z_1)^2}{B(y)E(y)} \right)}{[E(y)(A_2Z_1 - A_1Z_2) + D(y)(Z_2 - Z_1)]} dy \quad (\text{B.17})$$

qu'on peut ensuite intégrer :

$$\int d \ln P = \int \frac{C(y)D(y)dy}{yB(y)[E(y)(A_2Z_1 - A_1Z_2) + D(y)(Z_2 - Z_1)]} + \int \frac{D(y)(Z_2 - Z_1)^2 dy}{B(y)E(y)[E(y)(A_2Z_1 - A_1Z_2) + D(y)(Z_2 - Z_1)]} \quad (\text{B.18})$$

Dans le cas présent, le gaz est composé d'hydrogène et d'hélium, donc $A_1 = 1$ et $A_2 = 4$. En utilisant les équations B.13, l'équation B.18 devient

$$\begin{aligned} \ln P + K &= \int \frac{(Z_1 + yZ_2)(1 + 4y)dy}{y(1 + y)[(1 + Z_1 + y + yZ_2)(4Z_1 - Z_2) + (1 + 4y)(Z_2 - Z_1)]} \\ &+ \int \frac{(1 + 4y)(Z_2 - Z_1)^2 dy}{(1 + y)(1 + Z_1 + y + yZ_2)[(1 + Z_1 + y + yZ_2)(4Z_1 - Z_2) + (1 + 4y)(Z_2 - Z_1)]} \end{aligned} \quad (\text{B.19})$$

où K est la constante d'intégration. Finalement,

$$\begin{aligned} \ln P + K &= \frac{\ln y + 3 \ln(y + 1)}{4Z_1 - Z_2 + 3} \\ &+ \frac{(Z_2 - 4Z_1) \ln(Z_1 + Z_2y) + (4Z_1 - Z_2 + 3) \ln(Z_1 + Z_2y + y + 1) - 3 \ln(y + 1)}{4Z_1 - Z_2 + 3} \end{aligned} \quad (\text{B.20})$$

On définit ensuite la fonction $G(y)$:

$$\begin{aligned} G \equiv G(y) &= \ln y + (Z_2 - 4Z_1) \ln(Z_1 + Z_2y) + (4Z_1 - Z_2 + 3) \ln(Z_1 + Z_2y + y + 1) \\ &= (4Z_1 - Z_2 + 3)(\ln P + K) \end{aligned} \quad (\text{B.21})$$

L'équilibre diffusif ne peut s'établir qu'au-delà de la zone convective. Par conséquent, le point de référence est défini à la dernière couche de la zone de convection (iconv), de sorte que $y_0 \equiv y(\text{iconv})$ et $P_0 \equiv P(\text{iconv})$. Ainsi,

$$\begin{aligned} G_0 &= \ln y_0 + (Z_2 - 4Z_1) \ln(Z_1 + Z_2y_0) + (4Z_1 - Z_2 + 3) \ln(Z_1 + Z_2y_0 + y_0 + 1) \\ &= (4Z_1 - Z_2 + 3)(\ln P_0 + K) \end{aligned} \quad (\text{B.22})$$

La soustraction des équations B.21 et B.22 permet de se débarrasser de la constante K :

$$G - G_0 = (4Z_1 - Z_2 + 3) \ln(P/P_0) \quad (\text{B.23})$$

ou encore

$$G = (4Z_1 - Z_2 + 3) \ln(P/P_0) + G_0 \quad (\text{B.24})$$

Afin de pouvoir utiliser la méthode de Newton, il faut définir une fonction comportant une racine. On définit alors la fonction $f(y)$

$$f(y) = G - G_0 - (4Z_1 - Z_2 + 3) \ln(P/P_0) = 0 \quad (\text{B.25})$$

Il s'agit ensuite de déterminer l'abondance y qui satisfait $f(y) = 0$, ce qui satisfaira aussi l'équation de diffusion. Ceci peut être accompli en utilisant l'équation B.16, en sachant que :

$$f'(y) = \frac{df}{dy} = \frac{1}{y} + \frac{Z_2(Z_2 - 4Z_1)}{Z_1 + Z_2y} + \frac{(4Z_1 - Z_2 + 3)(Z_2 + 1)}{Z_1 + Z_2y + y + 1} \quad (\text{B.26})$$

Il est à noter que, comme la supposition que Z_1 et Z_2 ne varient pas en fonction de la profondeur a été faite (voir la section B.1), la moyenne, pondérée par la densité de masse,

$$Z_i = \frac{\sum_{j=1}^{\text{iconv}} Z_i(j)\rho(j)}{\sum_{j=1}^{\text{iconv}} \rho(j)} \quad (\text{B.27})$$

est adoptée.

De façon schématique, voici la procédure pour déterminer l'abondance d'hydrogène pour chaque couche de la zone radiative du modèle :

$$G_0 \leftarrow \ln(y_0) + (Z_2 - 4Z_1) \ln(Z_1 + Z_2y_0) + (4Z_1 - Z_2 + 3) \ln(Z_1 + Z_2y_0 + y_0 + 1)$$

$$\circlearrowleft \text{ tant que } \left(\frac{\Delta y}{y} > 10^{-6} \right)$$

$$G \leftarrow \ln(y) + (Z_2 - 4Z_1) \ln(Z_1 + Z_2y) + (4Z_1 - Z_2 + 3) \ln(Z_1 + Z_2y + y + 1)$$

$$f \leftarrow G - G_0 - (4Z_1 - Z_2 + 3) \ln\left(\frac{P}{P_0}\right)$$

$$f' \leftarrow \frac{1}{y} + \frac{Z_2(Z_2 - 4Z_1)}{Z_1 + Z_2y} + \frac{(4Z_1 - Z_2 + 3)(Z_2 + 1)}{Z_1 + Z_2y + y + 1}$$

$$\Delta y \leftarrow \frac{f}{f'}$$

$$y \leftarrow y - \Delta y$$

Fin de la boucle

Annexe C

Paramètres atmosphériques et physiques des naines blanches de type DB de l'échantillon du Chapitre 3

TABLE C.1. Listes des paramètres atmosphériques obtenus à l'aide des techniques photométrique et spectroscopique

Nom SDSS	Photométrie				Spectroscopie						Notes
	T_{eff} (K)	$\log g$	M (M_{\odot})	σ_{π}/π	T_{eff} (K)	$\log g$	M (M_{\odot})	$\log \text{H/He}$	$\log \text{Ca/He}$	S/N	
000055.12 – 042449.00	14,675	7.80	0.483	0.694	13,649	7.88	0.517	-5.111	—	10.16	
000106.22 + 250330.00	15,753	7.03	0.237	0.527	14,836	7.88	0.520	-4.748	-7.50	18.68	
000111.66 + 000342.55	—	—	—	—	11,205	6.32	0.022	-5.327	—	18.84	1
000116.49 + 000204.45	11,238	7.87	0.510	0.093	11,304	7.73	0.440	-5.965	—	31.52	1
000122.51 + 235934.20	—	—	—	—	12,339	6.88	0.194	< -5.672	—	7.63	1
000205.57 + 002041.80	19,926	7.11	0.266	1.388	18,108	8.16	0.693	-5.025	—	6.47	
000223.06 + 272358.50	16,437	8.08	0.637	0.033	16,830	8.00	0.594	< -6.133	—	49.67	
000407.15 + 264939.70	12,800	7.96	0.565	0.222	14,050	9.28	1.288	-5.263	—	9.47	
000426.95 + 243258.90	10,564	8.25	0.738	0.173	16,206	9.16	1.253	-5.090	-6.00	10.46	
000447.06 + 240703.60	—	—	—	—	15,328	7.75	0.457	-5.434	—	9.47	
000509.94 + 003809.60	47,176	7.68	0.503	0.278	50,033	7.68	0.509	< -3.280	—	16.24	
000515.58 + 071313.71	17,994	7.90	0.538	0.057	19,000	8.15	0.686	< -5.600	—	40.62	
000720.22 – 002325.40	19,434	8.10	0.658	0.096	19,099	7.90	0.540	< -5.383	—	18.67	
000730.75 + 275111.90	13,932	7.64	0.405	0.250	16,305	8.06	0.629	-5.880	—	11.92	2
000731.17 – 095849.10	18,651	7.90	0.541	0.326	20,170	8.05	0.625	< -4.849	—	6.32	
000742.62 + 252422.50	20,913	8.64	0.999	0.368	28,723	7.80	0.511	< -3.702	—	12.85	
001008.65 – 001841.80	—	—	—	—	16,342	7.86	0.517	-4.201	—	2.94	
001206.04 – 103005.00	19,920	7.37	0.327	0.965	17,274	7.98	0.580	< -5.480	—	4.63	
001510.77 + 074105.58	—	—	—	—	19,547	8.64	0.998	-4.321	—	8.11	
001529.75 + 010521.40	31,649	8.07	0.658	0.241	34,751	8.02	0.635	-2.429	—	9.58	
001742.44 + 004137.40	14,515	8.12	0.661	0.013	12,100	7.92	0.537	< -6.545	—	27.75	1
001756.52 – 091433.30	18,976	5.99	0.136	2.414	23,374	7.71	0.459	-3.575	—	4.57	
001830.96 – 095644.50	14,696	8.00	0.586	0.004	15,355	8.03	0.608	-4.120	—	86.29	
002001.81 + 135248.00	17,976	8.01	0.601	0.007	18,146	8.18	0.700	-4.613	—	69.04	
002150.57 – 005629.80	—	—	—	—	16,473	7.67	0.423	< -5.751	—	5.11	

TABLE C.1 (Suite)

Nom SDSS	T_{eff}	$\log g$	M	σ_{π}/π	T_{eff}	$\log g$	M	$\log \text{H/He}$	$\log \text{Ca/He}$	S/N	Notes
002153.33 + 083141.82	27,313	7.76	0.492	0.200	17,789	8.35	0.812	< -5.733	—	19.08	2
002202.49 – 003814.70	15,127	8.10	0.651	0.091	15,047	7.74	0.454	< -5.974	—	8.89	
002247.12 + 152831.90	—	—	—	—	18,529	8.08	0.644	< -5.275	—	6.51	
002458.42 + 245834.26	22,275	8.15	0.690	0.034	20,592	8.11	0.662	-4.739	—	40.15	
002633.89 + 005425.90	19,076	8.11	0.663	0.190	18,755	8.09	0.651	-4.419	—	10.78	
002639.47 – 000630.50	—	—	—	—	16,122	9.27	1.287	-4.651	-6.00	6.89	
002846.59 + 235312.16	18,453	8.13	0.675	0.233	21,608	7.99	0.597	< -4.646	—	14.43	
002857.53 + 135229.70	—	—	—	—	11,784	7.01	0.214	-5.605	—	3.94	1
003003.24 + 152629.30	17,619	8.24	0.740	0.027	15,470	8.11	0.656	-5.142	-7.50	36.03	
003115.10 + 083004.83	12,959	8.04	0.608	0.090	13,513	7.98	0.577	-5.678	—	18.00	
003230.11 + 001138.40	13,643	7.92	0.540	0.078	13,496	7.74	0.449	-5.940	—	10.29	
003340.91 – 182032.30	14,276	7.96	0.566	0.011	14,159	7.80	0.481	-5.713	—	64.42	
003436.33 + 072014.00	15,112	8.13	0.670	0.088	15,367	8.16	0.686	-5.614	—	21.05	
003436.66 + 003141.60	16,257	8.22	0.727	0.085	15,258	7.67	0.421	< -6.198	—	17.44	
003533.09 + 080324.26	10,866	8.02	0.596	0.084	11,888	7.42	0.315	-5.994	—	21.11	1
003816.32 + 005226.00	15,649	8.00	0.589	0.289	15,840	8.44	0.871	-5.232	—	8.66	
003833.66 + 242022.40	15,303	7.91	0.537	0.127	15,912	7.95	0.563	-6.039	—	31.02	
003855.69 + 140412.20	13,622	8.12	0.662	0.286	14,957	8.09	0.642	< -5.985	—	5.56	
004200.48 + 241647.20	16,993	7.94	0.558	0.118	15,974	8.06	0.629	< -6.284	—	26.83	
004232.65 + 254727.30	11,140	7.30	0.276	0.722	13,327	8.69	1.023	-5.364	—	8.68	1
004341.73 + 002324.40	12,098	8.59	0.966	0.291	13,757	8.07	0.628	-5.868	—	8.20	
004358.20 + 144619.20	15,301	8.39	0.833	0.304	15,386	7.60	0.392	< -5.932	—	8.07	
004613.38 + 064124.00	17,594	7.99	0.588	0.183	20,732	8.42	0.862	-4.311	—	7.42	
004900.48 – 094203.00	18,466	7.75	0.463	0.118	19,419	8.30	0.780	-4.434	—	11.66	2
005151.24 + 063935.49	—	—	—	—	14,597	7.53	0.363	< -6.272	—	15.68	
005232.04 + 134917.10	—	—	—	—	17,834	8.34	0.803	< -5.350	—	4.26	
005632.69 – 001815.10	19,333	7.85	0.518	0.261	26,329	8.18	0.713	< -4.019	—	11.18	
005904.58 – 001209.93	—	—	—	—	13,555	7.00	0.221	< -6.107	—	5.15	
010532.40 + 064234.18	13,368	7.54	0.363	0.185	13,404	7.65	0.406	-5.694	—	18.71	2
010608.43 + 063123.27	11,165	7.89	0.519	0.140	12,934	8.62	0.983	-5.591	—	22.29	
010723.42 + 010008.20	11,565	7.87	0.508	0.475	14,225	7.49	0.347	< -6.062	—	5.53	
010901.58 + 083354.67	14,234	8.05	0.616	0.096	15,807	7.89	0.529	< -6.310	—	22.28	
011023.82 + 223716.25	12,275	7.68	0.417	0.166	12,771	8.01	0.594	-5.714	—	19.10	2
011306.59 – 005041.60	16,818	8.30	0.777	0.200	18,932	8.06	0.629	< -5.168	—	9.07	
011341.04 + 190020.52	12,967	8.10	0.644	0.047	13,788	8.24	0.737	-6.007	—	37.92	
011356.38 + 301514.62	14,032	7.07	0.236	0.038	16,786	8.16	0.690	-4.719	—	43.06	3
011409.86 + 272739.42	15,833	7.46	0.344	0.239	17,540	8.14	0.677	-4.887	—	22.81	2
011420.50 + 312027.20	10,636	8.00	0.584	0.080	10,948	7.42	0.313	< -6.243	—	19.82	1
011535.52 + 004543.40	17,725	8.28	0.769	0.170	19,497	8.19	0.714	-4.658	—	15.20	
011607.92 + 330154.29	29,072	8.11	0.674	0.192	23,990	8.10	0.662	< -4.691	—	24.12	
011609.65 – 101514.30	11,709	8.64	0.995	0.266	13,683	8.32	0.788	-4.846	—	5.56	

TABLE C.1 (Suite)

Nom SDSS	T_{eff}	$\log g$	M	σ_{π}/π	T_{eff}	$\log g$	M	$\log \text{H/He}$	$\log \text{Ca/He}$	S/N	Notes
011721.58 + 061601.12	14,665	8.06	0.626	0.073	15,401	7.92	0.543	< -6.369	—	33.14	
011842.73 + 252207.90	11,664	8.86	1.119	0.446	14,085	6.70	0.176	-6.063	—	5.54	
011847.76 - 000142.10	16,153	7.93	0.553	0.135	15,164	7.77	0.466	< -5.960	—	9.23	
011919.89 + 301419.60	—	—	—	—	13,903	6.60	0.154	-5.711	—	5.60	
012016.16 - 004705.70	16,173	6.95	0.225	0.674	16,319	8.03	0.611	-4.128	-7.00	8.25	
012017.48 + 395927.50	13,561	7.55	0.368	0.517	13,407	8.50	0.905	< -6.114	—	9.86	1
012022.61 + 250503.40	14,749	6.71	0.184	1.550	15,646	8.72	1.045	-4.416	—	7.30	
012044.78 - 004159.10	12,170	7.89	0.525	0.061	13,340	7.57	0.374	-6.091	-7.50	16.06	
012118.42 + 384606.90	16,437	8.25	0.748	0.223	17,776	8.14	0.677	< -5.736	—	17.44	
012148.24 - 001053.00	17,288	8.16	0.693	0.011	15,508	7.83	0.499	< -6.355	—	57.96	
012413.08 + 072246.90	12,603	7.39	0.308	0.594	11,421	7.23	0.259	-5.204	—	13.92	1
012426.34 + 400357.40	17,964	8.41	0.855	0.194	23,375	8.68	1.027	-3.258	—	15.64	
012527.80 + 063048.80	—	—	—	—	18,523	8.36	0.820	< -5.390	—	11.76	
012732.97 + 133030.10	13,754	8.15	0.678	0.106	13,759	8.32	0.788	-5.731	—	10.66	
012839.65 + 394753.50	19,867	8.41	0.852	0.278	20,598	8.21	0.724	< -4.864	—	11.65	
012921.39 + 404428.50	10,916	8.04	0.609	0.044	12,299	8.49	0.896	-4.407	—	26.52	1
012940.05 + 384210.40	14,110	7.93	0.551	0.256	15,459	8.76	1.069	-5.211	—	8.28	
013025.42 + 232805.48	15,426	8.06	0.626	0.028	16,686	8.20	0.716	-4.655	—	54.69	
013044.09 + 151321.70	13,063	8.09	0.638	0.129	13,135	7.89	0.524	< -6.125	—	9.51	1
013101.91 + 142418.00	—	—	—	—	17,531	8.76	1.069	< -5.421	—	3.71	
013224.03 + 245612.52	15,165	8.01	0.596	0.019	16,584	8.04	0.617	-4.809	—	20.12	
013553.05 + 070315.10	17,194	7.30	0.298	0.257	19,532	8.13	0.677	< -5.270	—	18.23	
013824.21 - 094305.00	14,789	8.26	0.747	0.354	14,922	8.00	0.590	< -5.989	—	7.48	
013826.54 + 025634.59	—	—	—	—	12,228	8.62	0.983	< -6.051	—	4.53	1
014029.30 + 234445.10	—	—	—	—	19,816	8.23	0.736	< -4.936	—	6.28	
014049.00 - 010302.70	15,850	6.48	0.161	0.655	19,493	8.10	0.658	< -5.280	—	19.97	
014108.84 + 143819.00	12,225	8.12	0.656	0.276	13,929	8.07	0.628	< -5.996	—	4.81	
014147.15 + 071130.65	11,480	8.16	0.684	0.007	10,809	7.74	0.443	-5.811	—	84.18	1
014200.46 + 073350.69	15,050	7.98	0.580	0.056	15,820	8.00	0.593	-5.660	—	37.15	
014245.37 + 131546.30	14,731	8.26	0.750	0.030	13,880	8.93	1.157	< -6.517	—	29.48	
014320.44 - 085537.40	—	—	—	—	14,007	8.19	0.704	-5.985	—	14.44	
014618.90 - 005150.50	11,069	7.89	0.523	0.048	11,183	7.87	0.512	-6.198	—	22.67	1
014722.56 - 083059.60	14,279	8.21	0.715	0.021	14,400	8.11	0.653	-4.723	—	30.67	
014812.13 + 220558.52	13,569	8.18	0.694	0.012	14,352	8.10	0.649	-5.831	—	57.91	
014852.15 - 083137.40	17,058	7.95	0.567	0.058	16,609	7.88	0.527	< -6.174	—	21.30	
014945.65 + 223016.49	28,319	6.77	0.240	0.651	31,929	7.63	0.448	< -3.425	—	12.79	
015157.05 - 093341.80	13,496	7.94	0.555	0.165	14,457	8.61	0.977	-4.873	—	10.98	
015348.05 - 005929.30	13,604	8.46	0.878	0.142	14,169	8.09	0.642	-5.412	—	12.89	
015629.58 + 131744.70	17,954	8.17	0.695	0.054	17,474	8.29	0.776	-5.380	—	20.43	
015904.10 + 144151.04	15,177	8.31	0.784	0.091	14,650	8.75	1.061	< -6.458	—	25.73	
015935.01 + 130023.50	12,024	8.09	0.639	0.017	12,319	8.18	0.696	< -6.552	—	30.85	

TABLE C.1 (Suite)

Nom SDSS	T_{eff}	$\log g$	M	σ_{π}/π	T_{eff}	$\log g$	M	$\log \text{H/He}$	$\log \text{Ca/He}$	S/N	Notes
020349.41 + 221623.40	12,570	7.79	0.470	0.460	16,186	8.05	0.621	< -5.807	—	6.87	
020409.84 + 212948.58	15,071	8.01	0.595	0.045	20,605	8.38	0.831	-3.186	—	39.37	2
020527.47 + 143553.80	12,417	7.98	0.572	0.062	12,822	7.55	0.367	-5.900	—	19.73	
021103.00 + 074107.00	14,586	7.92	0.545	0.249	15,033	7.89	0.529	-5.870	—	10.47	
021258.62 + 074953.00	13,699	7.97	0.570	0.096	15,546	8.07	0.632	-5.571	—	20.61	
021358.82 + 060644.99	—	—	—	—	49,316	7.76	0.540	< -2.000	—	9.49	
021512.23 - 005626.70	—	—	—	—	15,627	7.77	0.470	< -6.008	—	10.26	
021614.17 - 001309.20	15,345	8.06	0.624	0.069	14,790	7.81	0.488	< -6.253	—	16.06	
022524.28 - 080301.80	13,936	8.16	0.683	0.105	13,662	7.88	0.519	< -6.341	—	15.52	
023016.93 - 010950.70	—	—	—	—	41,141	6.81	0.298	< -2.867	—	3.83	
023026.62 + 251758.30	—	—	—	—	16,764	8.61	0.981	-4.279	—	6.62	
023047.63 - 082132.20	20,722	8.25	0.752	0.383	19,531	8.06	0.633	< -5.125	—	12.13	
023333.41 - 092325.40	17,254	8.12	0.667	0.066	17,419	7.88	0.525	-3.310	—	26.27	
023344.36 - 062515.89	41,868	8.16	0.725	0.128	40,869	7.70	0.498	< -3.444	—	36.54	
023348.61 + 245542.70	—	—	—	—	14,905	9.00	1.188	-3.685	-6.00	6.33	
023402.50 + 243352.20	27,619	7.85	0.533	0.159	23,596	7.74	0.473	-2.720	—	19.59	
023514.51 + 284754.00	—	—	—	—	15,944	8.06	0.628	< -5.849	—	5.22	
023613.51 - 002407.30	—	—	—	—	15,019	7.61	0.396	-4.277	-6.00	5.35	
023614.44 - 080804.90	11,516	8.22	0.719	0.110	11,303	7.39	0.303	< -6.160	—	13.33	1
023617.32 - 073500.20	13,060	8.14	0.674	0.169	13,129	7.86	0.511	-6.122	—	16.71	
023823.22 + 271451.80	—	—	—	—	15,844	7.96	0.566	< -5.975	—	12.48	
024050.71 + 290744.30	—	—	—	—	22,280	7.91	0.552	< -4.428	—	5.24	
024103.10 - 074044.60	18,299	9.19	1.263	0.565	26,775	7.75	0.486	-2.000	—	3.99	
024227.13 - 080800.20	—	—	—	—	25,813	8.03	0.623	< -3.967	—	7.46	
024232.63 - 050954.75	12,181	7.63	0.398	0.100	14,438	7.94	0.557	-5.871	—	24.74	2
024433.59 - 042326.04	14,908	8.38	0.829	0.156	15,393	7.95	0.562	-5.973	—	14.92	
024443.69 - 005228.10	12,698	7.76	0.457	0.178	14,005	8.02	0.598	-6.066	—	9.91	
025005.76 - 022258.56	11,057	7.88	0.513	0.095	11,190	7.25	0.263	-5.944	—	14.26	1
025341.93 - 025658.59	12,837	7.84	0.499	0.050	13,606	8.24	0.733	-5.434	—	21.89	
025352.96 + 332803.60	26,464	7.80	0.509	0.179	29,072	7.83	0.525	< -4.021	—	20.45	
025758.04 + 341748.10	—	—	—	—	30,274	7.65	0.453	< -3.316	—	4.45	
025808.35 - 064838.50	16,007	6.73	0.196	1.482	16,676	9.59	1.391	< -5.610	—	2.98	
025934.98 - 072134.20	15,404	8.08	0.635	0.057	15,228	7.76	0.461	< -6.392	-6.50	20.02	
030127.13 - 002335.50	—	—	—	—	16,173	10.06	1.811	-4.503	—	3.04	
030253.10 - 010833.80	14,226	8.05	0.617	0.004	14,430	7.70	0.432	-6.254	—	73.84	
030254.32 - 081116.40	14,724	7.86	0.512	0.342	14,576	7.21	0.267	< -6.028	—	6.96	
030328.33 + 065327.50	—	—	—	—	16,754	8.00	0.593	< -5.693	—	6.07	
030415.19 + 000411.50	21,237	8.09	0.649	0.685	18,985	8.12	0.667	< -5.154	—	8.55	
030502.28 + 374747.20	12,468	6.99	0.213	0.744	17,275	8.43	0.863	-4.357	—	10.24	
030515.18 + 010745.20	26,118	6.33	0.148	2.732	25,131	7.83	0.518	< -4.070	—	7.51	
030922.05 + 010556.40	17,981	8.02	0.605	0.163	17,238	8.15	0.685	< -5.860	—	19.20	

TABLE C.1 (Suite)

Nom SDSS	T_{eff}	$\log g$	M	σ_{π}/π	T_{eff}	$\log g$	M	$\log \text{H/He}$	$\log \text{Ca/He}$	S/N	Notes
030941.17 + 403849.00	14,178	7.92	0.542	0.507	16,835	8.38	0.828	-5.057	—	9.49	
031134.00 + 001359.00	14,164	8.12	0.657	0.694	15,176	8.74	1.056	< -5.959	—	6.18	
031338.07 + 054411.00	—	—	—	—	18,099	8.17	0.698	-3.829	—	7.45	
031410.28 - 075126.00	14,602	8.19	0.704	0.156	14,765	7.92	0.547	< -6.007	—	7.93	
031438.94 - 001640.50	—	—	—	—	10,773	15.09	*****	< -5.900	—	0.92	1
031502.87 + 054647.40	—	—	—	—	15,247	8.14	0.673	< -5.849	—	3.45	
031609.12 - 062556.80	—	—	—	—	19,032	7.76	0.473	< -5.141	-6.00	6.42	
031639.27 + 001746.90	14,270	7.57	0.377	0.544	13,528	6.79	0.185	< -6.026	—	4.53	
031917.74 - 064026.20	17,457	6.53	0.183	1.920	16,496	7.94	0.559	< -5.747	—	7.21	
032222.14 + 005159.90	13,379	8.78	1.077	0.346	16,546	8.69	1.026	< -5.637	—	3.85	
032452.83 + 045106.70	14,696	8.01	0.593	0.340	15,276	8.02	0.600	< -6.056	—	13.03	
032645.91 + 043349.20	—	—	—	—	14,392	7.64	0.408	< -6.046	—	7.62	
032742.88 + 002503.00	13,607	8.09	0.643	0.100	12,310	7.39	0.306	-6.321	—	15.66	1
033137.37 - 064428.10	20,067	8.57	0.958	0.396	17,922	7.77	0.475	< -5.429	—	5.45	
033146.02 + 002232.50	14,269	8.47	0.886	0.278	17,048	8.11	0.655	< -5.629	—	7.55	
033319.84 - 003603.10	16,892	7.85	0.511	0.434	15,921	8.01	0.594	< -5.853	—	8.50	
033320.37 + 000720.70	9,038	8.62	0.978	0.003	12,750	9.41	1.328	-6.350	—	41.11	1
033328.47 - 000553.40	—	—	—	—	15,343	8.43	0.863	< -5.837	—	4.02	
033542.90 + 011542.10	15,797	7.41	0.324	0.634	32,284	7.67	0.465	< -3.171	—	4.23	
033553.86 - 074533.70	—	—	—	—	47,731	10.03	1.755	-2.000	—	4.12	
034153.03 - 054905.90	24,339	7.95	0.576	0.079	23,978	7.84	0.520	-3.924	—	29.96	
034227.62 - 072213.20	46,888	8.02	0.652	0.083	48,925	7.93	0.615	-2.328	—	37.88	
034741.96 + 010823.80	26,320	7.89	0.551	0.158	17,809	8.30	0.783	-4.844	—	10.10	2
035101.76 + 094110.00	—	—	—	—	23,752	8.45	0.885	< -4.150	—	4.65	
035617.50 - 063109.60	13,901	8.33	0.793	0.072	13,821	8.44	0.865	-5.862	-7.50	22.48	
040836.75 + 155149.40	15,379	7.56	0.376	0.206	18,780	8.37	0.829	-4.370	—	16.30	
040854.60 - 043354.70	36,873	7.42	0.394	0.630	39,954	7.87	0.566	-2.000	—	10.18	
041105.65 + 155011.40	—	—	—	—	16,287	9.51	1.360	-4.737	—	2.58	
041621.04 + 065613.50	35,143	7.84	0.542	0.529	13,902	8.23	0.730	< -6.197	—	11.37	
042042.78 + 072637.80	—	—	—	—	27,014	7.92	0.567	-3.329	—	13.77	
044109.80 - 050329.80	13,595	8.06	0.625	0.079	12,885	7.95	0.559	-5.324	—	20.99	
044252.11 + 113343.40	9,081	7.64	0.393	0.151	18,053	8.47	0.890	-4.459	—	7.01	
044420.12 - 002241.97	20,195	8.13	0.678	0.616	21,109	8.34	0.808	-3.798	—	8.34	
044425.84 - 070137.70	19,256	7.70	0.446	0.496	17,687	7.95	0.567	< -5.485	—	9.80	
044556.06 - 000419.40	41,759	8.85	1.127	0.461	45,732	7.69	0.504	-2.000	—	10.13	
044745.75 - 054215.00	19,337	8.21	0.722	0.103	17,765	8.19	0.710	-4.261	—	23.78	
045008.14 - 052456.20	13,597	7.98	0.577	0.459	19,392	8.72	1.044	< -5.046	—	8.72	
045111.20 - 002243.45	—	—	—	—	28,028	7.32	0.345	< -3.656	—	5.29	
045248.39 - 001034.13	14,761	8.96	1.169	0.386	29,800	8.56	0.957	< -3.458	—	5.94	
052941.58 + 603806.80	13,612	7.61	0.391	0.078	16,823	7.83	0.498	-5.665	—	16.96	2
053146.99 - 000853.70	—	—	—	—	52,031	8.19	0.757	< -3.470	—	23.19	

TABLE C.1 (Suite)

Nom SDSS	T_{eff}	$\log g$	M	σ_{π}/π	T_{eff}	$\log g$	M	$\log \text{H/He}$	$\log \text{Ca/He}$	S/N	Notes
053553.56 – 004003.90	11,988	8.61	0.976	0.117	18,126	9.29	1.293	< -5.497	-6.00	13.33	
053624.98 – 000227.50	—	—	—	—	32,480	6.13	0.177	< -3.159	—	2.12	
055420.64 + 834811.40	12,810	7.99	0.582	0.193	12,200	7.50	0.343	-5.608	—	9.90	1
055531.33 + 830732.80	26,142	7.97	0.590	0.249	30,377	7.79	0.513	-2.090	—	15.52	
060323.25 + 823549.10	14,953	7.73	0.448	0.459	16,947	8.39	0.840	< -5.652	—	8.35	
063524.65 + 835316.80	15,473	8.70	1.033	0.185	15,229	8.06	0.625	-5.433	—	9.62	
064452.30 + 371144.30	14,077	7.66	0.412	0.089	15,241	7.96	0.567	-6.030	—	26.93	2
064813.95 + 382042.20	18,018	8.17	0.697	0.222	19,250	8.17	0.697	-4.371	—	14.77	
065026.82 + 280419.30	16,802	7.98	0.582	0.212	16,396	7.92	0.548	-5.572	—	12.07	
065036.65 + 275533.20	17,489	8.53	0.929	0.309	17,732	9.05	1.212	< -5.475	—	7.00	
065146.32 + 271927.40	33,568	7.95	0.595	0.133	36,894	7.92	0.584	< -3.553	—	27.25	
065221.16 + 374917.90	14,999	7.84	0.501	0.117	16,580	7.91	0.540	-3.408	—	31.65	
065250.76 + 285253.60	18,596	7.72	0.450	3.021	21,558	8.04	0.622	< -4.547	—	7.07	
070916.40 + 394039.80	15,401	7.97	0.575	0.012	16,440	8.05	0.624	-6.062	—	79.67	
071159.16 + 382846.40	25,370	7.38	0.351	0.429	24,891	7.58	0.412	< -4.235	—	12.89	
071709.06 + 310626.60	15,179	8.76	1.067	0.467	17,947	8.10	0.652	-4.080	—	8.16	
072348.85 + 355230.50	14,621	7.45	0.333	0.784	14,370	8.24	0.734	-4.698	—	5.94	
072414.86 + 391003.36	15,637	7.76	0.464	0.186	13,996	7.81	0.483	-5.942	—	20.87	
072453.57 + 364010.60	17,867	8.13	0.672	0.569	18,082	8.33	0.801	< -5.390	—	5.02	
072459.83 + 365625.60	20,193	8.41	0.855	0.302	17,592	8.13	0.671	-5.232	—	13.30	
072621.21 + 363311.40	44,316	7.86	0.569	0.162	48,426	7.82	0.563	-2.000	—	38.68	
072707.40 + 351429.40	17,788	8.30	0.777	0.189	14,761	7.98	0.579	-5.712	-7.50	15.76	
072758.87 + 420714.48	11,779	7.96	0.559	0.144	11,984	7.77	0.461	-5.769	—	19.71	1
072943.05 + 352630.50	12,184	8.46	0.880	0.428	13,233	7.77	0.463	-5.415	—	5.20	
072959.11 + 455121.50	14,702	7.85	0.507	0.031	16,307	8.07	0.635	-5.507	—	27.68	
073106.08 + 345740.90	15,773	8.58	0.959	0.234	17,010	8.58	0.960	< -5.638	—	9.99	
073119.01 + 375814.30	20,345	8.03	0.617	0.962	18,779	8.60	0.973	< -5.209	—	9.16	
073149.99 + 414341.10	11,970	8.23	0.725	0.159	12,072	7.92	0.539	-5.822	—	10.76	1
073204.74 + 154641.60	12,576	9.02	1.194	0.329	12,115	6.62	0.139	-5.604	—	6.90	1
073217.01 + 274641.30	12,507	8.05	0.616	0.089	14,433	8.93	1.154	-5.369	-7.50	25.31	4
073223.60 + 433628.51	24,528	7.24	0.312	0.446	22,705	7.95	0.576	< -4.831	—	22.05	
073238.45 + 153536.20	19,003	8.34	0.805	0.453	16,952	8.85	1.117	-4.780	—	7.66	
073355.86 + 382020.60	13,916	8.77	1.072	0.359	15,138	8.48	0.895	< -5.963	—	6.70	
073416.92 + 444801.21	14,162	8.46	0.882	0.133	15,616	8.26	0.752	-5.240	-7.50	18.06	
073513.35 + 404943.30	13,353	7.67	0.418	0.545	11,275	8.95	1.164	< -6.050	—	6.21	1
073517.14 + 204022.50	12,758	8.17	0.691	0.202	14,236	7.99	0.582	-5.298	—	12.05	
073552.27 + 364634.80	17,532	8.38	0.833	0.234	18,683	8.70	1.033	< -5.234	—	9.15	
073552.64 + 210135.90	26,718	7.56	0.408	0.281	20,869	7.99	0.592	< -5.138	—	20.37	
073647.22 + 671240.50	13,117	8.59	0.966	0.341	14,455	9.33	1.304	-4.847	—	5.76	
073711.86 + 223402.00	13,016	7.08	0.232	1.035	14,390	9.29	1.291	< -6.156	—	10.17	
073737.20 + 154131.30	13,990	8.11	0.651	0.010	14,632	8.18	0.696	-5.950	-7.50	39.13	

TABLE C.1 (Suite)

Nom SDSS	T_{eff}	$\log g$	M	σ_{π}/π	T_{eff}	$\log g$	M	$\log \text{H/He}$	$\log \text{Ca/He}$	S/N	Notes
073739.87 + 413127.40	16,543	8.07	0.635	0.730	16,862	8.13	0.674	< -5.670	—	6.30	
073749.08 + 331558.70	16,296	8.91	1.148	0.235	17,745	8.22	0.730	-4.742	—	11.46	
073842.57 + 183509.60	13,991	8.05	0.619	0.035	15,213	7.80	0.482	-5.889	-6.00	33.84	
073843.91 + 333431.20	14,117	7.49	0.346	0.385	13,264	7.99	0.580	-4.968	—	7.95	
073847.48 + 463844.74	20,340	7.87	0.528	0.095	18,631	8.15	0.688	< -5.705	—	32.08	
073916.80 + 242513.69	11,547	7.84	0.492	0.134	12,269	7.71	0.431	-5.779	—	20.09	
073924.84 + 374612.90	15,867	8.20	0.715	0.284	16,168	8.21	0.719	-4.864	—	4.34	
073929.42 + 285219.00	19,243	8.96	1.170	0.487	18,600	8.53	0.929	-4.898	—	5.51	
073935.14 + 244505.27	22,778	8.03	0.619	0.032	25,305	7.83	0.516	< -4.529	—	49.28	
073939.13 + 670916.50	20,333	7.99	0.595	0.063	20,275	8.09	0.651	-4.650	—	32.04	
074120.74 + 281245.50	13,030	8.46	0.882	0.191	13,349	8.26	0.747	-5.660	—	15.80	
074208.41 + 425559.40	12,062	8.43	0.861	0.291	14,885	9.80	1.518	-4.806	—	3.89	
074225.39 + 200357.50	19,406	8.73	1.054	0.182	21,071	8.24	0.745	< -4.645	—	6.28	
074233.59 + 272238.80	13,496	7.44	0.327	0.460	13,107	7.54	0.363	-5.534	—	13.89	
074249.21 + 280745.70	21,154	7.50	0.374	0.549	16,893	8.22	0.729	-4.436	—	17.58	
074253.65 + 185306.70	14,278	7.93	0.550	0.039	15,099	7.96	0.569	-6.061	—	43.37	
074257.18 + 423029.44	13,052	8.32	0.788	0.139	14,139	9.00	1.187	-5.325	—	12.97	
074257.30 + 390618.20	14,055	7.89	0.524	0.119	14,451	8.05	0.616	-5.239	—	12.03	
074345.08 + 384953.51	15,645	8.24	0.741	0.121	14,716	7.96	0.565	-5.756	—	24.99	
074347.83 + 424023.30	—	—	—	—	16,667	9.43	1.333	-5.210	-6.00	4.45	
074349.10 + 423005.60	14,651	7.12	0.246	0.415	13,965	7.47	0.337	< -6.083	—	8.29	
074351.15 + 235322.10	—	—	—	—	17,404	8.02	0.604	-3.852	—	4.31	
074351.32 + 385615.80	17,815	8.05	0.622	0.072	17,633	8.04	0.618	< -5.968	—	20.64	
074419.82 + 302203.40	—	—	—	—	14,607	8.06	0.624	-5.270	—	12.55	3
074443.40 + 164851.10	16,310	8.01	0.596	0.081	17,508	8.11	0.657	-5.760	—	30.39	
074507.43 + 194000.40	15,594	8.13	0.666	0.261	17,371	8.14	0.679	< -5.831	—	17.06	
074508.80 + 311659.44	14,314	7.51	0.355	0.286	17,431	8.40	0.842	-5.028	—	15.34	
074538.17 + 312205.40	37,206	7.96	0.606	0.276	47,975	7.81	0.557	< -3.130	—	10.01	
074547.21 + 384836.00	18,903	7.19	0.280	1.607	27,447	7.68	0.455	< -3.625	—	4.84	
074624.34 + 335214.56	14,613	8.14	0.675	0.158	13,664	7.55	0.368	-6.034	—	17.68	
074638.03 + 663338.70	14,461	6.04	0.075	1.200	17,783	8.43	0.864	< -5.463	—	8.52	
074651.08 + 181430.18	11,484	8.22	0.723	0.297	11,032	6.98	0.205	< -6.015	—	6.94	1
074702.99 + 181825.40	12,491	8.18	0.698	0.096	13,479	8.75	1.063	< -6.222	—	10.54	
074713.07 + 184719.80	15,414	8.68	1.018	0.254	15,621	8.00	0.593	-4.694	—	13.72	
074733.42 + 213937.90	14,493	7.04	0.232	1.207	17,456	9.63	1.412	< -5.439	—	3.22	
074740.37 + 445811.70	—	—	—	—	22,133	8.56	0.954	< -4.449	—	5.39	
074823.27 + 221311.30	13,310	7.74	0.451	0.254	12,587	8.01	0.588	< -6.246	—	14.09	1
074903.16 + 273204.20	11,244	8.00	0.583	0.071	17,301	9.41	1.328	-4.193	-6.00	12.15	
074925.15 + 195039.94	19,850	7.93	0.560	0.060	20,186	8.09	0.651	< -5.295	—	45.17	
074946.23 + 450346.50	17,314	7.75	0.463	0.613	20,290	8.13	0.675	< -4.820	—	7.11	
075008.74 + 283032.90	17,267	8.49	0.902	0.600	13,483	7.92	0.544	-5.150	—	10.15	

TABLE C.1 (Suite)

Nom SDSS	T_{eff}	$\log g$	M	σ_{π}/π	T_{eff}	$\log g$	M	$\log \text{H/He}$	$\log \text{Ca/He}$	S/N	Notes
075033.95 + 433652.90	12,925	7.88	0.519	0.358	13,682	8.05	0.619	< -6.101	—	7.51	
075035.65 + 200332.20	15,447	8.02	0.603	0.077	14,869	8.17	0.695	-4.938	—	15.59	
075052.94 + 182955.10	15,795	7.06	0.241	1.193	16,031	8.56	0.950	-3.986	—	11.25	
075112.44 + 652641.30	14,178	7.80	0.482	0.395	15,318	8.85	1.115	-4.664	-7.00	7.90	
075113.92 + 221443.40	—	—	—	—	17,028	8.28	0.767	-5.452	—	9.91	
075121.46 + 335650.60	15,188	8.07	0.633	0.430	15,593	8.08	0.640	-5.630	—	4.65	
075123.32 + 261744.30	24,471	7.90	0.554	0.751	21,359	7.77	0.480	-3.535	—	3.97	
075129.01 + 460131.19	13,358	7.97	0.571	0.142	14,664	7.97	0.575	-5.905	—	22.15	
075132.16 + 200226.77	16,574	8.05	0.623	0.036	16,568	8.10	0.650	-5.242	—	31.13	
075136.85 + 232613.50	20,236	8.06	0.634	0.345	16,291	7.98	0.578	< -5.787	—	8.46	
075140.40 + 411244.50	17,194	7.92	0.547	0.165	15,415	7.79	0.480	< -6.178	—	15.88	
075152.10 + 230414.20	17,526	8.42	0.856	0.309	19,169	8.89	1.141	-3.281	—	11.05	
075212.14 + 141244.83	17,690	8.02	0.606	0.244	18,079	8.21	0.722	-4.854	—	18.06	
075224.32 + 150352.34	12,219	7.58	0.375	0.039	13,562	7.91	0.535	-6.373	—	39.86	2
075452.85 + 194907.00	20,140	8.14	0.679	0.075	22,636	7.94	0.571	< -4.839	—	35.67	
075453.20 + 192225.20	18,933	8.46	0.882	0.341	21,447	7.80	0.497	< -4.676	—	10.55	
075453.84 + 291114.17	13,751	8.52	0.921	0.123	13,845	8.07	0.627	-5.821	—	20.50	
075520.71 + 091757.70	—	—	—	—	14,101	8.71	1.035	< -6.182	—	13.16	
075523.87 + 172825.20	23,947	8.10	0.660	0.075	25,277	7.84	0.525	< -4.533	—	42.59	
075528.54 + 165346.60	21,128	8.29	0.774	0.382	21,280	7.88	0.534	< -4.602	—	9.69	
075538.21 + 233626.70	13,596	8.15	0.681	0.259	13,123	7.63	0.398	< -6.126	—	6.71	
075556.00 + 240113.70	16,093	8.03	0.608	0.218	14,987	7.56	0.374	< -6.231	—	18.21	
075608.44 + 490239.73	15,408	8.41	0.853	0.119	16,017	8.14	0.677	-5.682	—	22.87	
075635.45 + 323235.20	12,627	7.89	0.526	0.130	11,076	7.33	0.286	< -6.130	—	11.95	1
075706.19 + 414611.50	14,908	8.08	0.636	0.577	14,235	7.78	0.470	< -5.968	—	4.77	
075713.62 + 540941.30	21,950	7.95	0.574	0.207	28,475	7.62	0.436	< -3.731	—	10.55	
075832.89 + 160723.80	—	—	—	—	19,132	8.63	0.990	-4.313	—	7.40	
075901.95 + 260806.60	17,800	7.83	0.501	0.380	16,946	8.25	0.746	-4.963	—	9.45	
075907.56 + 433351.70	16,848	7.98	0.583	0.238	17,776	8.28	0.768	-4.470	—	10.24	
075907.80 + 164639.30	16,021	7.71	0.443	0.356	14,882	8.29	0.771	-4.821	—	6.30	
075938.20 + 235113.90	20,660	7.89	0.541	0.367	22,464	7.85	0.523	-3.674	—	8.76	
080013.25 + 383823.70	20,111	8.73	1.053	0.205	19,766	8.14	0.679	-4.849	—	7.29	
080016.55 + 350232.30	—	—	—	—	12,744	8.26	0.750	< -6.056	—	4.61	1
080104.29 + 110617.90	—	—	—	—	40,382	7.70	0.495	-2.710	—	6.89	
080124.48 + 144551.20	14,030	9.19	1.261	0.339	13,444	6.95	0.212	-5.990	—	4.93	
080127.11 + 141454.88	15,228	8.09	0.641	0.028	15,747	8.11	0.658	-5.504	-7.50	43.88	
080132.10 + 280143.30	20,892	7.95	0.569	0.225	17,861	8.20	0.718	-4.372	—	11.95	
080136.87 + 201011.13	15,332	7.82	0.494	0.299	15,974	8.10	0.653	< -6.094	—	17.75	
080234.16 + 405015.19	13,615	7.97	0.570	0.036	15,092	8.21	0.716	-4.910	-7.50	40.72	
080236.92 + 154813.58	20,907	8.03	0.618	0.039	23,526	8.04	0.628	-4.454	—	47.37	
080257.89 + 060740.40	20,194	8.10	0.655	0.091	21,926	8.23	0.740	-4.097	—	27.71	

TABLE C.1 (Suite)

Nom SDSS	T_{eff}	$\log g$	M	σ_{π}/π	T_{eff}	$\log g$	M	$\log \text{H/He}$	$\log \text{Ca/He}$	S/N	Notes
080330.78 + 360244.70	13,220	5.83	0.043	1.127	12,009	6.86	0.187	-5.785	—	5.06	1
080345.74 + 074422.00	17,737	8.11	0.660	0.038	17,563	8.22	0.726	-4.615	—	45.45	
080348.49 + 393115.00	19,342	7.98	0.584	0.044	18,920	7.90	0.540	-4.866	—	28.44	
080359.51 + 401400.20	18,056	8.44	0.873	0.351	19,562	8.20	0.718	< -5.001	—	6.32	
080413.06 + 390451.43	15,426	7.82	0.492	0.160	14,716	8.27	0.755	-5.241	—	16.34	
080414.92 + 471208.60	13,391	8.51	0.912	0.170	15,149	8.32	0.793	-5.418	—	10.95	
080421.52 + 165452.90	14,989	8.09	0.646	0.121	15,763	8.08	0.639	-4.283	—	12.28	
080459.55 + 351327.60	12,254	8.07	0.626	0.067	12,185	7.85	0.503	< -6.239	—	14.74	1
080513.13 + 540615.60	13,293	8.13	0.668	0.024	15,250	8.78	1.079	-5.699	-7.50	31.76	
080611.65 + 334425.80	15,153	8.03	0.610	0.007	15,538	8.09	0.641	-5.520	-7.50	53.95	
080630.85 + 271750.92	12,475	8.16	0.682	0.114	11,755	7.07	0.227	-6.182	—	14.28	1
080653.76 + 361014.20	16,675	7.62	0.402	0.326	17,591	8.16	0.693	-5.115	—	14.33	
080653.79 + 294432.50	15,962	8.35	0.813	0.501	16,781	7.07	0.249	< -5.687	—	7.05	
080709.36 + 435600.80	19,481	8.37	0.828	0.397	16,566	7.66	0.421	< -5.732	—	7.82	
080717.72 + 431241.80	12,016	7.91	0.532	0.088	12,580	7.92	0.540	-5.521	—	17.77	1
080747.86 + 081316.10	14,233	7.93	0.548	0.227	14,378	7.94	0.555	-5.653	—	6.80	
080748.38 + 340321.00	13,386	8.54	0.933	0.513	15,699	7.90	0.536	-4.133	—	3.54	
080830.78 + 264054.74	19,856	8.05	0.626	0.085	17,715	8.16	0.693	-5.346	—	29.92	
080833.56 + 241620.00	17,478	6.96	0.232	0.842	35,963	7.04	0.326	-2.000	—	5.42	
080841.72 - 072852.80	19,026	8.34	0.805	0.148	17,016	7.99	0.585	< -5.907	—	19.10	
080856.86 + 314615.50	12,210	8.79	1.083	0.223	12,120	7.41	0.311	-5.604	—	4.37	1
080902.06 + 202955.60	12,273	8.16	0.684	0.072	12,522	8.14	0.669	-5.263	—	29.16	
080916.50 + 201248.20	13,457	8.02	0.596	0.218	12,482	7.37	0.302	< -6.142	—	6.56	1
080939.34 + 334543.05	20,711	7.91	0.548	0.268	17,099	7.96	0.570	< -5.890	—	18.45	
080942.84 + 080853.50	15,619	7.74	0.455	0.071	16,007	7.84	0.503	-5.604	—	23.87	
080949.94 + 310642.00	11,764	7.85	0.500	0.051	16,592	9.27	1.286	-4.696	-6.00	15.38	4
081011.15 + 214540.40	24,595	7.82	0.513	0.140	22,028	8.17	0.703	< -4.726	—	18.22	
081029.20 + 341112.20	12,935	8.12	0.658	0.162	12,275	7.57	0.373	< -6.141	—	7.69	1
081040.75 + 191811.95	19,020	7.93	0.559	0.131	23,192	8.02	0.613	-2.000	—	21.91	
081058.71 + 501145.89	14,460	8.13	0.667	0.034	15,254	8.06	0.627	-6.300	—	41.72	
081137.18 + 162115.30	—	—	—	—	11,270	7.83	0.488	-5.234	—	28.46	1
081223.85 + 254843.00	20,541	8.04	0.621	0.304	18,785	7.90	0.541	-4.344	—	7.28	
081231.32 + 562221.20	—	—	—	—	16,072	8.42	0.856	-5.414	—	10.68	
081251.05 + 160728.70	14,743	7.98	0.580	0.380	14,356	7.52	0.357	-5.771	—	6.05	
081307.29 + 153635.81	12,077	8.10	0.645	0.111	11,278	7.27	0.270	< -6.286	—	17.55	1
081324.79 + 192414.40	13,920	9.10	1.229	0.377	22,590	7.84	0.520	< -4.289	—	4.32	
081345.43 + 365140.50	26,139	7.72	0.472	0.260	26,991	7.69	0.458	< -4.281	—	20.50	
081453.56 + 300734.90	22,968	8.16	0.699	0.124	24,145	8.00	0.602	-4.287	—	19.42	
081507.03 + 241638.50	22,392	8.28	0.774	1.140	20,410	8.94	1.162	-4.542	—	3.51	
081510.93 + 280346.60	15,623	8.20	0.710	0.370	15,049	8.30	0.775	-5.965	—	5.52	
081540.75 + 391056.80	14,566	8.84	1.111	0.336	13,203	7.58	0.376	< -6.042	—	3.15	

TABLE C.1 (Suite)

Nom SDSS	T_{eff}	$\log g$	M	σ_{π}/π	T_{eff}	$\log g$	M	$\log \text{H/He}$	$\log \text{Ca/He}$	S/N	Notes
081548.70 + 364950.80	—	—	—	—	14,555	8.72	1.043	-4.636	-7.50	8.03	
081627.93 + 005028.70	12,912	7.91	0.533	0.053	16,390	7.95	0.562	-5.958	—	22.29	
081635.77 + 124025.20	22,790	8.26	0.761	0.197	21,097	7.99	0.595	< -4.639	—	8.82	
081635.82 + 100536.90	15,023	6.89	0.211	0.895	14,559	8.21	0.715	-4.987	—	7.15	
081642.90 + 064740.60	35,775	7.65	0.467	1.505	44,814	8.20	0.752	-2.510	—	4.95	
081656.17 + 204946.10	24,425	8.08	0.651	0.024	25,712	8.00	0.606	< -4.472	—	47.52	
081721.43 + 465156.10	—	—	—	—	14,081	7.13	0.248	-5.482	—	2.96	
081739.38 + 134951.11	16,807	8.17	0.696	0.080	16,573	8.02	0.603	-5.967	—	27.97	
081742.70 + 333947.00	14,116	7.77	0.464	0.397	13,758	7.29	0.285	< -6.096	—	6.09	
081751.55 + 245923.27	12,284	8.06	0.621	0.162	12,838	8.61	0.975	-5.662	—	18.58	1
081835.10 - 000553.00	25,520	7.50	0.385	0.696	19,864	7.96	0.574	< -4.924	—	8.49	
081904.19 + 354255.80	18,398	8.17	0.700	0.077	24,461	8.00	0.605	-4.337	—	15.12	
081942.45 + 191512.60	13,930	8.28	0.763	0.376	14,437	8.06	0.624	-4.864	—	4.75	
081952.23 + 142013.40	23,976	8.30	0.785	0.119	18,620	7.74	0.461	-5.009	—	12.65	
081958.05 + 284109.28	12,147	7.98	0.574	0.057	12,027	7.68	0.417	-5.885	—	30.75	1
082004.96 + 213135.69	28,425	8.14	0.695	0.254	24,267	7.95	0.576	< -4.659	—	21.53	
082019.50 + 253035.15	12,692	8.07	0.629	0.022	13,294	8.07	0.626	-5.486	-6.50	46.44	
082041.50 + 062024.90	14,971	8.20	0.709	0.377	14,652	8.38	0.832	< -6.020	—	5.13	
082052.24 + 332550.10	16,058	8.53	0.927	0.338	16,338	8.45	0.875	< -5.778	—	5.51	
082140.73 + 081455.50	14,748	8.79	1.083	0.330	15,781	8.34	0.806	< -5.876	—	6.08	
082214.46 + 132501.60	13,522	8.23	0.730	0.303	15,589	7.87	0.516	-4.795	—	4.61	
082216.14 + 133822.60	14,327	7.87	0.517	0.064	14,547	8.10	0.648	-4.312	—	16.87	
082316.33 + 233317.70	19,076	7.98	0.586	0.047	19,831	8.19	0.711	-4.425	—	47.19	
082323.20 + 360834.79	14,876	7.59	0.387	0.186	15,180	8.09	0.645	< -6.208	—	19.35	2
082457.54 + 285241.73	—	—	—	—	20,340	8.29	0.773	-3.701	—	20.19	
082543.11 + 430640.93	15,555	8.12	0.663	0.042	15,352	8.02	0.599	< -6.376	—	39.63	
082614.97 + 402234.82	22,146	8.36	0.820	0.246	23,358	7.96	0.583	-3.579	—	19.44	
082623.76 + 474814.83	14,707	7.95	0.559	0.108	14,953	7.84	0.503	-5.678	—	27.43	
082647.69 - 042124.00	43,227	8.24	0.772	0.078	44,350	7.94	0.611	-2.769	—	41.62	
082659.83 + 111845.44	17,634	8.05	0.622	0.033	17,020	8.10	0.650	-5.517	—	43.95	
082710.07 + 442951.10	13,320	8.18	0.699	0.160	14,628	8.18	0.698	< -6.132	—	12.59	
082727.91 + 423304.70	—	—	—	—	32,834	7.89	0.565	< -3.248	—	6.88	
082829.17 + 363418.69	15,299	7.96	0.565	0.028	16,027	7.93	0.551	< -6.276	—	48.48	
082834.81 + 090547.80	14,971	7.87	0.519	0.072	15,361	8.18	0.699	-5.673	-7.50	21.70	
082852.54 + 084831.30	—	—	—	—	22,424	8.09	0.653	< -4.409	—	5.31	
082852.82 + 305603.49	17,130	7.58	0.390	0.286	14,804	7.95	0.562	< -6.113	—	14.90	
082916.83 + 123744.46	12,846	7.89	0.526	0.103	12,345	8.07	0.630	-5.848	—	21.94	
082931.60 + 282836.27	20,493	8.36	0.823	0.161	19,655	8.22	0.729	< -5.426	—	20.31	
082951.44 + 292623.00	13,844	8.25	0.742	0.192	13,051	8.35	0.807	< -6.128	—	6.86	1
083021.84 - 035805.90	15,710	7.88	0.525	0.300	17,199	8.07	0.633	< -5.869	—	16.94	
083024.17 + 455206.02	15,272	7.73	0.448	0.155	14,546	7.97	0.570	-5.296	—	19.70	2

TABLE C.1 (Suite)

Nom SDSS	T_{eff}	$\log g$	M	σ_{π}/π	T_{eff}	$\log g$	M	$\log \text{H/He}$	$\log \text{Ca/He}$	S/N	Notes
083035.14 + 564459.40	26,080	8.00	0.611	0.029	24,887	7.90	0.553	< -4.584	—	35.39	
083048.86 + 214033.40	15,151	7.17	0.260	1.059	15,968	9.05	1.209	< -5.745	—	3.86	
083056.94 + 253853.80	19,098	8.21	0.727	0.229	18,083	8.26	0.755	< -5.658	—	15.92	
083059.35 + 193214.30	15,859	7.98	0.580	0.138	14,938	7.50	0.351	-5.881	—	16.91	
083202.32 + 240133.50	19,866	7.77	0.480	0.451	18,638	8.27	0.762	-4.802	-6.00	13.21	
083231.47 + 443337.10	19,235	7.66	0.428	0.506	18,746	8.32	0.795	-3.652	—	6.88	
083314.08 + 175822.00	13,723	9.08	1.223	0.400	14,473	7.23	0.272	< -5.942	—	4.84	
083317.40 + 531335.50	—	—	—	—	11,857	8.12	0.660	-4.824	—	15.59	1
083317.64 + 051201.47	12,476	7.46	0.332	0.216	16,623	9.29	1.291	-4.900	-6.00	20.00	
083331.19 - 052335.90	18,897	6.42	0.187	2.353	19,667	8.43	0.869	< -4.974	—	8.92	
083334.35 + 554728.54	12,428	8.02	0.599	0.010	12,412	7.93	0.546	-5.313	—	52.98	
083342.06 + 045252.10	—	—	—	—	15,561	8.01	0.599	-5.855	—	13.42	
083344.04 + 252229.90	18,112	5.91	0.105	1.400	14,769	7.85	0.506	-5.941	—	15.13	
083345.84 + 434328.70	14,247	8.17	0.690	0.122	14,159	8.00	0.589	-5.078	—	18.35	
083355.68 + 082744.00	15,538	6.74	0.193	2.025	25,630	9.07	1.219	-2.466	—	3.50	
083407.27 + 385057.60	18,068	8.04	0.619	0.104	17,734	8.21	0.720	< -5.596	—	14.70	
083409.05 + 410700.90	12,968	8.31	0.782	0.029	12,969	8.34	0.801	-5.037	—	28.47	
083412.05 + 513707.60	12,572	8.08	0.635	0.067	13,221	8.15	0.675	-5.569	—	13.16	
083415.45 + 254819.90	26,404	8.07	0.648	0.125	24,094	7.94	0.574	< -4.679	—	20.83	
083420.39 + 231600.60	31,955	7.30	0.335	1.121	38,789	7.53	0.433	< -3.036	—	7.32	
083448.91 + 381414.50	12,415	8.04	0.607	0.356	13,084	7.54	0.364	< -6.047	—	4.05	1
083449.30 + 233608.10	14,125	8.00	0.588	0.241	13,599	7.95	0.561	< -6.216	—	10.10	
083450.81 + 160408.20	14,243	7.21	0.266	0.497	14,549	8.20	0.711	-6.006	—	7.33	
083457.61 + 081144.20	19,807	8.24	0.747	0.129	17,830	8.30	0.779	< -5.573	—	13.62	
083538.32 + 152626.37	9,854	8.27	0.750	0.048	9,727	9.01	1.190	-5.475	—	12.09	1
083542.23 + 040817.50	13,317	7.98	0.574	0.009	13,881	8.00	0.589	-4.951	—	51.08	
083550.58 + 045755.40	16,422	8.66	1.007	0.372	15,339	7.91	0.539	< -5.837	—	4.82	
083606.48 + 041005.46	16,483	7.87	0.519	0.169	16,584	8.15	0.681	< -6.179	—	22.33	
083629.27 - 040640.20	27,850	7.54	0.405	0.663	31,572	7.67	0.464	-3.191	—	13.18	
083647.58 + 045951.04	23,514	8.06	0.636	0.224	20,920	7.88	0.533	-3.860	—	18.28	
083709.90 + 240605.10	15,838	8.65	1.001	0.388	18,456	8.09	0.649	< -5.294	—	7.41	
083736.44 + 293825.00	19,889	7.53	0.378	0.556	19,556	8.48	0.898	< -5.003	—	6.26	
083754.83 + 533240.30	35,362	8.35	0.833	0.468	13,210	8.82	1.098	< -6.122	—	9.02	1
083855.76 + 184946.50	17,210	8.11	0.656	0.167	17,953	8.11	0.661	-4.719	—	13.91	
083905.08 + 255338.40	—	—	—	—	12,634	7.89	0.524	< -6.246	—	14.20	1
083906.11 + 432459.40	13,456	8.06	0.620	0.060	13,944	8.08	0.635	< -6.194	—	12.90	
083924.84 + 185402.30	17,011	7.62	0.406	0.254	15,913	8.28	0.762	< -5.855	—	6.91	
083930.08 + 261804.90	14,511	8.05	0.618	0.124	17,496	8.17	0.697	-3.462	-6.00	15.12	
083935.50 + 074507.70	17,247	7.88	0.530	0.647	18,823	8.10	0.655	< -5.097	—	4.17	
083936.97 + 145135.60	21,386	7.49	0.369	0.513	17,778	8.06	0.630	< -5.464	—	6.94	
084022.80 + 311620.60	16,026	8.71	1.037	0.201	15,016	7.53	0.362	-5.891	—	6.43	

TABLE C.1 (Suite)

Nom SDSS	T_{eff}	$\log g$	M	σ_{π}/π	T_{eff}	$\log g$	M	$\log \text{H/He}$	$\log \text{Ca/He}$	S/N	Notes
084036.73 + 063721.55	11,943	8.19	0.699	0.127	12,609	8.18	0.697	-5.436	—	16.26	1
084037.62 + 230452.00	—	—	—	—	15,669	7.53	0.366	-4.993	—	4.76	
084040.43 + 551113.40	17,293	7.92	0.549	0.186	16,600	8.15	0.685	-5.532	—	16.68	
084104.07 + 055406.16	12,675	7.89	0.522	0.173	12,373	7.93	0.544	-5.024	—	14.77	1
084115.19 + 103432.60	13,557	8.39	0.832	0.581	13,876	7.18	0.258	-4.559	—	4.45	
084155.03 + 372311.90	12,753	7.98	0.573	0.030	13,806	8.19	0.704	< -6.521	-7.00	28.80	
084211.30 + 461819.00	20,962	8.16	0.695	0.093	23,758	7.95	0.578	< -4.516	—	16.35	
084214.91 + 343850.60	13,298	8.94	1.159	0.264	14,871	7.78	0.473	-4.762	—	3.11	
084220.91 + 434444.60	18,353	8.21	0.721	0.270	18,050	8.62	0.987	-3.561	—	7.27	
084224.92 + 172402.50	22,984	8.70	1.038	0.675	19,750	8.04	0.620	< -4.953	—	5.36	
084244.93 + 295444.40	17,496	8.55	0.944	0.118	16,808	8.04	0.614	< -5.800	—	13.22	
084303.44 + 160719.40	16,546	8.07	0.633	0.131	15,625	8.14	0.673	-5.410	—	16.03	
084334.40 + 225408.20	18,721	7.04	0.249	0.744	18,320	8.01	0.599	-5.269	—	6.12	
084350.85 + 361419.50	20,345	8.03	0.615	0.029	20,297	8.10	0.655	< -5.269	—	35.25	
084424.51 + 105044.00	19,278	7.93	0.558	0.094	17,420	8.14	0.676	-4.927	—	19.60	
084430.69 + 105813.10	15,397	8.16	0.688	0.171	13,892	7.63	0.402	< -6.198	—	12.52	
084445.65 + 070848.20	18,072	8.32	0.791	0.412	16,703	8.68	1.020	-4.594	—	5.29	
084451.46 + 195948.80	16,832	8.91	1.147	0.220	20,648	7.84	0.513	-3.982	—	6.38	
084456.07 + 075132.60	13,260	8.09	0.642	0.209	12,416	7.36	0.299	-5.780	—	7.24	1
084521.51 + 511559.36	12,967	8.21	0.712	0.129	13,634	7.79	0.476	-5.799	—	14.56	
084539.18 + 225728.00	19,645	8.03	0.614	0.009	19,432	8.15	0.689	-5.163	-6.00	47.91	
084614.90 + 193515.40	16,968	7.85	0.509	0.065	18,026	8.15	0.682	-4.200	—	25.60	
084716.21 + 484220.40	15,277	8.04	0.615	0.047	14,678	8.46	0.882	-6.050	—	23.78	3
084717.71 + 322209.40	13,696	8.80	1.089	0.051	13,722	8.71	1.036	-4.672	—	12.86	
084728.33 + 081409.60	19,099	8.62	0.985	0.180	24,005	8.06	0.638	< -4.349	—	10.25	
084734.75 + 095706.70	22,176	8.11	0.664	0.153	17,315	8.12	0.668	-5.954	—	25.17	
084808.44 + 103345.60	—	—	—	—	22,175	7.40	0.345	-2.000	—	7.18	
084823.53 + 033216.70	35,202	8.05	0.652	0.519	30,753	7.76	0.501	-2.906	—	12.83	
084843.28 + 821949.50	15,089	8.31	0.781	0.220	14,732	8.11	0.656	-4.708	—	10.37	
084916.18 + 013721.30	24,329	7.68	0.449	0.403	28,924	7.75	0.488	< -3.548	—	8.94	
084925.35 + 415845.70	—	—	—	—	15,095	7.23	0.274	-5.034	—	4.55	
084952.82 + 471248.78	18,073	8.06	0.631	0.016	17,261	8.18	0.700	< -6.048	—	56.60	
084953.10 + 105621.20	27,106	8.23	0.746	0.066	30,185	8.16	0.710	-3.333	—	43.81	
084953.37 + 001043.10	13,963	7.80	0.481	0.639	15,317	8.44	0.871	-4.103	—	4.20	
085041.00 + 272221.20	—	—	—	—	15,848	8.61	0.977	< -5.865	—	7.48	
085047.18 + 370936.70	10,595	8.89	1.134	0.364	14,530	7.72	0.444	-4.821	—	5.55	
085116.63 + 250804.50	—	—	—	—	15,506	7.88	0.521	-4.887	—	8.76	
085134.88 + 114217.80	28,794	7.82	0.520	0.585	28,375	8.02	0.623	-2.303	—	13.48	
085154.45 + 075540.80	20,830	7.89	0.539	0.338	27,811	7.95	0.587	< -3.814	—	11.93	
085202.44 + 213036.50	21,656	8.01	0.607	0.075	26,496	7.96	0.586	-4.323	—	22.66	
085205.49 + 031414.00	14,974	8.20	0.714	0.061	14,706	7.80	0.479	< -6.452	—	43.55	

TABLE C.1 (Suite)

Nom SDSS	T_{eff}	$\log g$	M	σ_{π}/π	T_{eff}	$\log g$	M	$\log \text{H/He}$	$\log \text{Ca/He}$	S/N	Notes
085213.50 + 011706.90	25,931	7.14	0.297	0.782	36,355	7.37	0.381	< -3.109	—	7.79	
085216.78 + 610225.50	19,886	7.68	0.437	0.161	19,369	8.06	0.630	-4.647	—	9.43	
085237.68 + 344812.30	13,304	8.09	0.643	0.142	12,632	7.47	0.335	-5.185	—	7.47	1
085253.92 + 000739.23	23,076	8.17	0.703	0.168	22,862	8.01	0.607	< -4.616	—	19.33	
085318.61 + 032444.70	—	—	—	—	43,292	7.80	0.543	-2.557	—	12.08	
085427.99 + 380841.80	13,672	8.00	0.588	0.067	13,896	8.06	0.622	-5.701	—	28.33	
085434.16 + 563713.90	17,839	7.70	0.439	1.057	17,242	7.89	0.534	-5.069	—	4.89	
085444.87 + 152901.70	28,448	7.36	0.354	0.588	25,844	7.76	0.485	< -3.963	—	8.51	
085508.91 + 360925.20	11,996	7.71	0.430	0.160	13,012	8.66	1.007	-4.962	—	15.71	1
085551.54 + 013634.50	17,574	8.15	0.682	0.258	16,113	7.85	0.511	-4.545	—	6.94	
085618.94 + 161103.60	18,648	8.34	0.805	0.006	18,981	8.74	1.060	-5.002	—	96.81	
085707.25 + 120336.29	15,739	7.87	0.518	0.240	13,970	8.10	0.647	-6.125	—	15.81	
085717.08 + 380206.00	11,170	8.12	0.657	0.104	13,561	9.00	1.189	< -6.218	—	10.22	
085720.19 + 360142.80	18,191	8.35	0.809	0.121	16,814	8.20	0.712	< -6.136	—	22.83	
085748.04 + 332708.40	19,340	8.36	0.819	0.127	18,366	8.25	0.749	-4.298	—	18.12	
085819.37 + 290534.70	21,676	8.37	0.832	0.322	18,851	8.05	0.627	-4.572	—	8.48	
085822.12 + 131349.00	23,767	7.44	0.363	0.399	27,495	7.72	0.473	< -3.854	—	12.12	
085824.95 + 590012.90	26,086	7.80	0.505	0.185	29,753	7.92	0.572	< -3.593	—	10.58	
085919.96 + 350730.80	16,917	7.97	0.578	0.033	16,911	8.03	0.610	-5.686	—	38.21	
085934.17 + 112309.38	16,478	8.33	0.799	0.101	16,395	8.42	0.859	-4.508	-6.00	22.06	
085950.30 - 000339.60	—	—	—	—	17,576	7.75	0.461	-4.771	—	4.64	
085952.54 + 245509.40	—	—	—	—	32,111	7.97	0.602	< -3.284	—	7.74	
085953.78 + 464036.10	17,901	7.73	0.456	0.168	17,019	7.81	0.492	-4.991	—	12.31	
085955.92 + 080137.30	—	—	—	—	24,381	7.89	0.546	< -4.072	—	4.91	
085957.16 + 052853.70	20,038	8.34	0.807	0.583	18,904	8.19	0.712	-4.810	—	5.00	
085957.20 + 573249.90	13,788	8.13	0.664	0.120	14,902	7.50	0.351	< -6.102	-6.50	12.84	
090028.28 + 073445.70	17,224	7.99	0.589	0.427	14,811	7.86	0.514	-5.331	-6.00	7.29	
090038.20 - 004548.30	20,405	8.34	0.808	0.232	16,396	7.86	0.515	< -5.767	—	8.10	
090102.58 + 094333.30	—	—	—	—	14,268	9.33	1.304	-4.816	—	9.38	
090146.63 + 094029.80	14,832	7.86	0.512	0.117	14,813	7.79	0.475	-6.009	—	12.10	
090232.18 + 071930.00	31,226	8.15	0.703	0.156	27,193	7.55	0.409	-2.923	—	13.99	
090239.73 + 364458.00	16,957	7.91	0.540	0.031	16,972	7.97	0.573	-5.658	—	31.91	
090315.40 + 204743.80	18,850	7.94	0.562	0.035	17,281	7.86	0.515	-2.927	—	36.89	
090319.86 + 361532.90	18,124	7.75	0.466	0.978	30,628	7.67	0.459	-2.000	—	4.36	
090322.43 + 834550.00	25,405	7.88	0.546	0.083	29,950	7.77	0.503	< -3.925	—	30.42	
090331.28 + 140049.07	13,679	7.92	0.543	0.008	14,849	7.94	0.557	-6.205	—	75.40	
090336.00 + 212214.02	14,053	8.29	0.770	0.154	14,517	7.87	0.514	< -6.144	—	13.74	
090339.72 + 103213.09	16,391	8.03	0.608	0.020	16,604	8.07	0.634	-5.318	—	68.69	
090409.04 + 012741.00	21,518	8.05	0.631	0.072	24,581	7.93	0.570	< -4.622	—	21.58	
090441.85 + 433742.80	19,975	8.23	0.739	0.449	17,195	8.19	0.706	< -5.597	—	6.50	
090456.13 + 525029.90	34,293	6.79	0.180	0.536	38,034	7.89	0.573	< -3.329	—	16.21	

TABLE C.1 (Suite)

Nom SDSS	T_{eff}	$\log g$	M	σ_{π}/π	T_{eff}	$\log g$	M	$\log \text{H/He}$	$\log \text{Ca/He}$	S/N	Notes
090519.62 + 124503.00	—	—	—	—	15,897	8.70	1.035	-4.799	—	5.29	
090527.55 + 311037.51	—	—	—	—	15,997	7.96	0.568	< -6.281	—	20.74	
090529.44 + 104257.38	14,953	8.31	0.781	0.090	15,664	7.97	0.576	-5.818	—	25.71	
090538.46 + 290610.40	19,446	7.99	0.591	0.041	20,335	8.07	0.640	-5.146	—	40.25	
090542.42 + 510455.50	15,042	8.12	0.663	0.033	15,135	8.19	0.706	-5.006	—	32.21	
090557.47 + 525049.20	13,170	7.83	0.492	0.131	14,917	8.39	0.834	< -6.100	—	11.55	
090600.30 + 021325.10	15,149	7.38	0.314	0.573	14,446	7.15	0.254	< -6.041	—	5.74	
090703.37 + 043055.92	—	—	—	—	12,092	8.91	1.145	-5.902	—	17.04	1
090739.95 + 102629.90	16,383	7.80	0.484	0.632	18,003	7.84	0.510	-4.185	—	3.77	
090825.32 + 221848.70	—	—	—	—	19,508	8.78	1.081	-4.315	—	5.10	
090901.96 + 055619.80	—	—	—	—	16,841	8.15	0.685	< -5.674	—	9.57	
090929.24 + 335815.11	17,168	7.95	0.567	0.054	18,287	8.15	0.684	-5.272	—	34.91	
090957.47 + 111111.29	15,180	8.18	0.696	0.102	14,456	7.87	0.516	< -6.475	—	24.98	
091004.67 + 394153.50	14,804	8.88	1.134	0.166	11,369	7.58	0.373	-5.703	—	6.57	1
091015.75 + 394910.10	—	—	—	—	15,741	8.00	0.592	-5.304	—	7.16	
091016.43 + 210554.20	14,896	8.14	0.671	0.011	15,389	8.22	0.723	-5.745	—	54.68	3
091029.42 + 090205.10	15,345	7.96	0.569	0.019	15,840	8.02	0.600	< -6.305	—	42.47	
091058.73 + 044934.40	16,198	7.77	0.468	0.156	15,833	7.93	0.550	-4.426	—	13.73	
091113.01 + 031127.00	13,573	8.09	0.639	0.031	14,130	8.12	0.658	-5.916	—	26.21	
091125.32 + 193541.80	21,978	7.99	0.597	0.175	22,583	7.79	0.492	-3.774	—	13.81	
091131.38 + 302709.50	—	—	—	—	14,311	7.85	0.507	-5.561	—	15.79	
091234.45 + 351808.00	21,085	8.40	0.846	0.736	21,914	8.09	0.655	< -4.384	—	4.83	
091254.43 + 101102.90	12,138	8.37	0.819	0.461	14,808	9.16	1.252	-4.250	—	4.28	
091322.22 + 254514.70	15,021	7.91	0.539	0.139	15,047	8.00	0.591	-4.995	—	12.33	
091352.59 + 080246.00	15,225	8.43	0.860	0.180	14,813	7.52	0.361	< -6.112	—	10.08	
091403.55 + 192022.80	14,837	8.36	0.814	0.278	14,744	8.46	0.878	< -6.010	—	5.70	
091430.49 + 413627.30	13,622	7.77	0.465	0.331	15,007	8.55	0.941	-4.958	—	5.46	
091436.46 + 014514.50	—	—	—	—	15,616	8.89	1.135	< -5.800	—	3.56	
091448.53 + 424033.50	10,533	7.87	0.508	0.044	12,004	7.90	0.528	-5.594	—	22.05	1
091524.51 + 100824.40	—	—	—	—	12,272	6.84	0.186	< -6.053	—	3.48	1
091541.95 + 431250.20	12,278	7.98	0.572	0.071	12,728	7.85	0.503	-5.806	—	16.96	
091543.65 + 422344.10	—	—	—	—	17,176	8.49	0.901	-5.107	—	4.80	
091613.08 + 294207.20	14,895	8.05	0.620	0.726	14,720	7.57	0.378	-5.514	—	8.21	
091651.97 + 414703.80	13,244	8.03	0.604	0.081	14,803	8.09	0.643	-5.150	—	16.37	
091658.85 + 335914.50	23,886	9.01	1.194	0.665	19,787	7.76	0.472	-3.725	—	3.04	
091702.92 + 394913.60	—	—	—	—	25,847	7.30	0.333	-2.000	—	3.24	
091704.94 + 061834.30	19,732	8.34	0.806	0.464	18,636	7.98	0.583	< -5.147	—	4.90	
091707.51 + 635726.40	16,224	8.12	0.666	0.127	19,021	8.33	0.802	-4.687	—	10.77	
091719.37 + 110311.60	15,631	8.12	0.665	0.703	14,914	10.22	2.079	< -5.890	—	2.89	
091755.03 + 030338.60	—	—	—	—	21,239	8.24	0.747	< -4.510	—	4.29	
091755.64 + 003351.80	—	—	—	—	17,620	8.02	0.606	< -5.774	—	15.36	

TABLE C.1 (Suite)

Nom SDSS	T_{eff}	$\log g$	M	σ_{π}/π	T_{eff}	$\log g$	M	$\log \text{H/He}$	$\log \text{Ca/He}$	S/N	Notes
091804.27 + 222941.90	—	—	—	—	30,242	7.93	0.581	< -3.419	—	7.71	
091823.44 + 021805.30	17,934	8.53	0.929	0.307	18,352	8.12	0.663	< -5.321	—	9.17	
091827.89 + 305237.00	16,952	7.76	0.466	0.483	19,160	7.98	0.587	< -5.218	-6.00	14.05	
091828.56 + 224022.60	12,567	7.84	0.496	0.165	12,572	8.35	0.804	-6.209	—	19.12	1
091829.69 + 433810.60	13,341	8.18	0.695	0.147	14,478	7.88	0.520	-5.976	—	9.81	
091905.82 + 202316.70	18,781	8.10	0.653	0.035	17,740	8.07	0.636	-5.927	—	31.71	
091958.06 + 575341.80	12,589	7.65	0.407	0.183	13,278	8.20	0.708	< -6.120	—	7.76	
092001.29 + 404728.26	12,128	8.31	0.782	0.103	12,240	8.45	0.871	< -6.372	—	15.15	1
092017.92 + 243229.70	—	—	—	—	14,097	9.41	1.328	-4.814	—	8.32	
092023.80 + 254719.30	—	—	—	—	14,378	7.42	0.322	-5.035	—	5.23	
092024.08 + 083746.30	13,336	8.31	0.779	0.130	14,716	8.51	0.913	-5.468	—	10.93	
092035.73 + 014923.40	—	—	—	—	15,863	8.38	0.827	< -5.762	—	4.90	
092106.43 + 140736.70	20,077	8.17	0.700	0.078	18,963	8.32	0.791	-4.485	—	39.02	
092110.80 + 120411.10	14,024	8.01	0.594	0.197	14,856	8.92	1.151	-4.467	-7.50	9.59	
092111.85 + 304414.10	—	—	—	—	17,444	8.39	0.839	< -5.541	—	9.65	
092113.60 + 235152.20	18,406	8.41	0.855	0.165	17,533	8.10	0.651	-5.106	-6.00	10.70	
092114.76 + 223347.00	—	—	—	—	14,676	7.24	0.274	-5.231	—	8.03	
092116.04 + 372943.38	12,326	7.76	0.458	0.152	12,797	8.36	0.816	-5.082	—	18.65	1
092122.49 + 082805.60	—	—	—	—	27,818	7.66	0.448	-3.503	—	6.81	
092200.98 + 000834.40	21,038	8.10	0.661	0.104	22,664	7.91	0.556	-4.142	—	16.07	
092235.07 + 402059.30	12,294	7.96	0.564	0.053	12,631	8.15	0.678	-5.492	—	24.09	
092239.15 + 012726.00	12,565	7.89	0.522	0.127	12,978	8.40	0.842	-5.784	—	17.14	
092241.45 + 363818.20	18,660	8.88	1.130	0.716	18,280	7.56	0.383	-3.693	—	3.56	
092248.40 + 073639.00	—	—	—	—	17,773	8.00	0.593	< -5.465	—	8.44	
092310.58 + 202555.20	—	—	—	—	17,797	8.66	1.011	-4.351	—	5.66	
092313.66 + 112910.10	17,563	8.35	0.810	0.034	17,298	8.40	0.843	-5.281	—	28.99	
092326.10 + 230228.00	—	—	—	—	14,884	8.03	0.604	-4.912	—	29.21	
092401.04 + 053345.34	—	—	—	—	11,010	7.69	0.421	< -6.121	—	13.88	1
092410.60 + 401705.60	15,954	8.43	0.862	0.874	18,548	8.14	0.677	< -5.170	—	3.68	
092414.62 + 090940.20	14,504	8.14	0.675	0.103	14,906	7.48	0.344	< -6.101	—	13.34	
092427.30 + 604641.80	19,843	7.80	0.493	0.404	18,387	8.66	1.013	< -5.312	—	6.53	
092452.74 + 020712.30	13,100	8.13	0.666	0.110	13,878	8.01	0.596	-5.900	—	15.07	
092500.09 + 665953.80	14,678	7.97	0.571	0.132	19,536	7.97	0.581	-4.563	—	7.23	
092539.11 + 345445.70	14,507	7.47	0.339	0.124	16,824	7.94	0.560	-4.913	—	19.93	
092544.41 + 414803.20	42,877	7.52	0.443	0.844	40,356	7.50	0.428	< -3.004	—	9.76	
092558.91 + 592908.10	16,343	7.57	0.383	0.515	15,793	7.96	0.568	-5.815	—	6.39	
092628.07 + 230316.10	—	—	—	—	12,483	9.13	1.240	< -6.142	—	7.65	1
092634.09 + 512023.70	—	—	—	—	22,300	7.86	0.529	< -4.326	—	3.88	
092634.63 + 095141.20	14,845	7.45	0.336	0.717	14,760	6.87	0.207	-5.224	—	2.66	
092643.37 + 540406.90	13,623	8.33	0.793	0.374	14,511	8.26	0.752	-5.491	—	5.95	
092648.85 + 431109.20	11,984	7.11	0.235	0.428	11,995	6.82	0.179	< -6.040	—	4.74	1

TABLE C.1 (Suite)

Nom SDSS	T_{eff}	$\log g$	M	σ_{π}/π	T_{eff}	$\log g$	M	$\log \text{H/He}$	$\log \text{Ca/He}$	S/N	Notes
092654.51 – 013111.01	18,120	7.96	0.573	0.094	19,607	8.17	0.698	< -5.438	—	30.32	
092659.86 + 001457.70	—	—	—	—	18,030	8.65	1.005	-4.086	—	9.54	
092715.02 + 221042.90	13,689	8.57	0.951	0.451	13,264	6.36	0.084	< -6.040	—	4.10	
092818.94 + 224538.20	—	—	—	—	11,617	7.79	0.468	-5.166	—	10.99	1
092846.58 + 494209.30	14,708	8.09	0.641	0.125	14,460	7.59	0.386	< -6.040	—	9.43	
092903.70 + 382224.30	13,441	7.79	0.471	0.131	15,404	8.87	1.127	-4.939	—	12.42	
092903.80 + 595406.00	14,402	6.96	0.218	0.408	15,164	8.11	0.658	< -5.960	—	7.94	
092917.88 + 162637.46	—	—	—	—	15,368	7.98	0.581	< -6.374	—	21.56	
092951.38 + 072003.00	—	—	—	—	23,310	7.70	0.455	< -4.307	—	8.51	
093016.81 + 053802.30	19,861	7.82	0.504	0.866	20,150	8.42	0.861	< -4.753	—	4.94	
093024.62 + 083406.67	—	—	—	—	12,468	8.07	0.629	-5.752	—	29.04	
093040.10 + 054124.30	15,843	8.16	0.687	0.620	14,742	7.17	0.258	-5.495	—	6.09	
093041.80 + 011508.40	—	—	—	—	33,943	8.05	0.648	< -3.193	—	8.59	
093122.86 + 362209.40	20,334	7.83	0.508	0.800	20,675	7.82	0.505	< -4.731	—	6.38	
093130.31 + 073054.60	12,314	7.80	0.478	0.365	13,316	8.37	0.820	-5.450	-7.50	11.99	
093138.29 + 031012.70	21,433	8.82	1.104	0.177	20,386	8.38	0.832	< -4.797	—	6.62	
093329.42 + 090554.56	16,496	8.12	0.666	0.142	15,484	8.06	0.629	-6.055	—	27.67	
093416.09 + 483239.35	12,386	8.02	0.599	0.097	12,628	7.44	0.324	-5.507	—	15.17	
093429.31 + 351945.20	—	—	—	—	17,379	8.61	0.981	-4.272	—	7.97	
093429.98 + 565533.50	13,096	7.08	0.233	1.030	13,950	7.87	0.516	< -5.994	—	4.09	
093434.82 + 155343.70	—	—	—	—	25,412	7.05	0.274	-3.443	—	4.21	
093444.55 + 092443.31	15,671	7.97	0.575	0.036	16,993	8.23	0.736	-4.511	—	47.89	
093448.67 + 173651.30	15,776	8.35	0.811	0.518	14,700	8.14	0.677	< -6.014	—	5.83	
093454.24 + 304106.50	—	—	—	—	17,591	7.98	0.584	< -5.781	—	15.91	
093455.07 + 234213.10	15,081	6.48	0.151	2.901	15,067	7.29	0.287	-4.712	—	5.53	
093512.70 + 003857.12	12,472	7.54	0.359	0.068	12,853	8.03	0.601	-6.053	—	32.76	2
093512.70 + 104001.20	14,072	7.54	0.364	0.314	14,420	8.07	0.633	-6.010	—	17.95	
093529.43 + 133702.39	11,188	8.22	0.717	0.190	12,044	8.10	0.647	-5.526	—	18.75	1
093603.30 + 560257.80	13,173	7.86	0.509	0.371	13,077	7.70	0.428	-5.905	—	7.70	1
093610.22 + 303049.30	15,628	8.49	0.904	0.423	15,773	7.93	0.551	< -5.986	—	12.27	
093628.93 + 400451.10	16,850	8.03	0.612	0.135	16,976	8.02	0.604	-5.121	—	18.70	
093631.00 + 565637.90	—	—	—	—	15,397	7.83	0.496	< -5.930	—	6.36	
093708.92 + 284205.70	—	—	—	—	15,465	8.33	0.799	-4.858	-7.50	12.91	
093720.36 + 014803.50	15,154	7.96	0.570	0.156	14,898	8.01	0.595	-5.376	-6.00	8.65	
093759.52 + 091653.30	—	—	—	—	31,847	8.01	0.622	< -3.571	—	17.24	
093806.30 + 032242.53	20,190	7.80	0.492	0.137	18,864	8.24	0.742	-5.068	—	28.76	2
093819.20 + 253736.00	18,589	8.09	0.648	0.133	17,023	8.13	0.670	< -5.905	—	17.48	
093832.79 + 474050.61	10,430	8.54	0.930	0.050	10,446	6.96	0.196	< -6.180	—	15.42	1
093844.81 + 391321.67	13,250	8.10	0.649	0.046	13,676	8.29	0.771	-6.443	—	26.67	
093844.97 + 021755.60	—	—	—	—	17,661	8.21	0.724	< -5.391	—	3.64	
093846.06 + 531632.50	18,060	7.74	0.461	0.723	16,687	8.23	0.732	< -5.824	—	10.09	

TABLE C.1 (Suite)

Nom SDSS	T_{eff}	$\log g$	M	σ_{π}/π	T_{eff}	$\log g$	M	$\log \text{H/He}$	$\log \text{Ca/He}$	S/N	Notes
093849.35 + 414645.00	19,770	5.67	0.109	5.383	18,231	7.74	0.461	< -5.252	—	4.33	
093849.68 + 363839.88	20,845	8.19	0.715	0.087	19,074	8.12	0.669	-4.766	—	33.94	
093855.69 + 023657.10	12,423	8.89	1.138	0.231	16,702	9.13	1.240	-4.006	—	3.79	
093857.45 + 002428.80	16,219	7.48	0.350	0.540	13,779	7.60	0.387	< -6.095	—	6.11	
093921.05 + 384344.20	32,920	8.77	1.083	0.408	35,126	7.88	0.563	< -3.146	—	6.57	
093924.25 + 001145.70	—	—	—	—	18,747	8.10	0.655	-5.377	—	20.22	
094003.14 + 084049.20	—	—	—	—	18,160	8.13	0.674	-4.183	—	10.47	
094023.58 + 185837.24	12,891	7.45	0.330	0.129	13,449	7.90	0.530	-6.219	—	26.53	2
094026.86 - 021234.88	19,309	8.06	0.629	0.078	19,711	8.19	0.714	-5.284	—	40.12	
094029.90 + 221802.80	11,951	7.92	0.539	0.113	12,460	8.56	0.945	< -6.246	—	13.90	1
094038.33 + 285705.60	14,473	6.98	0.222	0.947	14,277	7.88	0.524	-5.970	—	9.39	
094049.57 + 335853.00	15,843	8.04	0.611	0.067	16,026	8.07	0.632	< -6.276	—	25.14	
094053.83 + 203334.90	13,445	8.59	0.965	0.214	12,932	7.02	0.223	< -6.132	—	8.33	1
094105.41 + 013140.60	14,964	7.93	0.548	0.058	15,743	8.04	0.611	-5.419	—	18.34	
094127.03 + 062113.70	19,032	8.14	0.681	0.217	18,587	7.73	0.458	-5.125	—	10.86	
094209.49 + 540157.50	36,052	9.28	1.344	0.146	52,702	7.52	0.466	< -3.280	—	15.58	1
094224.12 + 445453.30	18,198	7.22	0.283	1.041	15,648	7.34	0.304	-5.018	—	4.96	
094303.60 + 462913.70	40,986	8.77	1.082	0.405	44,065	7.81	0.547	< -2.759	—	6.41	
094329.03 + 392801.00	16,365	8.10	0.654	0.195	16,114	8.04	0.617	< -5.820	—	8.98	
094335.49 + 521836.50	—	—	—	—	21,645	7.79	0.489	-4.162	—	7.74	
094411.18 + 310334.00	15,531	7.92	0.545	0.167	15,209	7.94	0.556	-5.562	—	12.21	
094431.28 - 003933.70	13,307	8.16	0.687	0.028	14,265	8.30	0.775	-6.029	-7.00	29.41	
094447.51 + 062342.40	16,555	8.37	0.826	0.184	17,932	8.23	0.737	< -5.547	—	10.34	
094534.50 + 343455.50	18,880	8.22	0.731	0.090	19,467	8.14	0.678	-5.330	—	25.85	
094547.51 + 482314.57	11,647	8.16	0.682	0.075	11,865	8.30	0.775	< -6.350	—	16.06	1
094551.02 + 194013.19	20,398	7.08	0.262	1.037	19,865	8.23	0.737	< -5.373	—	20.74	
094638.77 + 621759.50	12,248	7.64	0.400	0.241	12,840	7.48	0.340	< -6.244	—	11.63	2
094726.37 + 075506.70	16,909	7.89	0.529	0.283	17,917	7.86	0.517	< -5.430	—	9.24	
094749.40 + 015501.90	—	—	—	—	27,517	8.08	0.654	-2.705	—	7.14	
094756.14 + 105757.50	11,908	8.49	0.902	0.112	11,390	7.19	0.251	< -6.067	—	8.01	1
094826.42 + 040730.80	—	—	—	—	14,245	8.05	0.620	-5.461	—	32.13	
094942.79 + 442922.60	14,648	8.38	0.830	0.232	13,498	7.13	0.246	-4.938	—	5.61	
094949.93 + 255028.52	12,535	8.04	0.608	0.088	13,549	8.45	0.873	-5.024	—	18.53	
094957.05 - 011609.45	16,900	8.05	0.620	0.071	15,984	8.11	0.657	-5.610	—	36.77	
095027.87 + 000535.70	23,966	7.81	0.508	0.148	20,397	8.05	0.629	< -5.050	—	18.47	
095035.51 + 483758.70	12,574	7.85	0.501	0.087	12,556	7.25	0.269	< -6.246	—	13.75	1
095046.79 + 444210.70	13,407	7.41	0.318	0.695	15,960	8.49	0.899	-4.658	—	3.77	
095102.23 + 010432.60	16,851	7.97	0.575	0.009	16,906	8.09	0.648	-5.324	—	74.61	
095117.15 + 472422.81	—	—	—	—	13,847	7.58	0.379	< -6.201	—	10.13	
095141.89 + 501715.80	17,049	8.05	0.625	0.058	17,292	8.14	0.675	-5.657	—	21.38	
095207.88 + 090953.40	17,523	8.04	0.619	0.044	18,762	8.21	0.724	-4.579	—	42.27	

TABLE C.1 (Suite)

Nom SDSS	T_{eff}	$\log g$	M	σ_{π}/π	T_{eff}	$\log g$	M	$\log \text{H/He}$	$\log \text{Ca/He}$	S/N	Notes
095229.04 + 455130.80	18,057	7.66	0.425	0.331	17,670	7.93	0.554	< -5.611	—	11.02	
095256.37 + 244851.66	10,934	8.05	0.612	0.031	12,619	8.89	1.137	-4.712	—	38.97	1
095256.69 + 015407.70	28,645	8.06	0.646	0.062	33,904	8.05	0.648	< -3.664	—	37.20	
095319.64 + 325104.00	12,840	8.07	0.627	0.106	12,693	8.29	0.769	-5.558	—	24.19	
095337.98 + 493439.80	21,078	7.78	0.484	0.211	20,524	7.88	0.535	< -4.881	—	12.49	
095346.94 + 431932.30	—	—	—	—	43,916	7.75	0.521	-2.422	—	3.86	
095353.91 + 074246.10	19,163	8.01	0.600	0.059	20,007	8.30	0.781	-4.371	—	23.99	
095356.63 + 412649.90	15,828	8.02	0.604	0.152	16,069	8.30	0.778	< -5.828	—	8.81	
095415.13 + 184405.80	13,665	9.60	1.398	0.318	14,671	7.84	0.503	< -5.920	—	4.13	
095424.84 + 230419.00	—	—	—	—	16,918	8.16	0.690	< -5.558	—	4.81	
095426.18 + 484700.50	16,220	7.86	0.516	0.034	17,227	7.86	0.518	-5.578	—	22.27	
095440.47 + 120917.20	37,635	7.72	0.496	0.408	34,242	7.80	0.524	< -3.302	—	11.04	
095449.30 + 181454.78	—	—	—	—	12,873	8.19	0.701	-5.371	-7.50	24.87	
095455.12 + 440330.30	18,398	7.99	0.588	0.125	23,829	8.30	0.788	-4.416	—	18.18	2
095515.28 + 351521.90	19,145	8.04	0.620	0.780	24,764	7.84	0.521	-3.657	—	5.19	
095600.58 + 224810.70	12,315	8.20	0.707	0.049	11,315	7.21	0.255	-5.717	—	17.11	1
095604.37 + 241848.60	16,846	7.56	0.382	0.480	15,664	8.01	0.598	-5.204	-7.50	12.19	
095649.55 + 010812.40	—	—	—	—	16,740	6.83	0.213	-4.702	—	3.80	
095723.13 + 571350.30	14,100	8.16	0.686	0.024	14,675	8.27	0.759	-5.067	—	28.62	
095749.40 + 335923.60	26,533	8.00	0.610	0.053	27,440	7.97	0.597	< -4.220	—	32.73	
095819.70 + 552514.30	18,044	8.24	0.744	0.155	22,569	8.02	0.614	-3.425	—	11.30	
095820.52 + 600234.91	14,045	8.09	0.639	0.033	14,167	8.10	0.650	-5.470	—	31.39	
095854.97 + 055020.83	—	—	—	—	13,125	8.66	1.005	-5.481	-7.50	31.58	
095855.57 + 432029.00	14,814	8.52	0.917	0.169	17,524	7.50	0.362	< -5.523	—	6.35	
095855.99 + 641039.10	18,138	7.99	0.589	0.243	16,762	7.75	0.460	-5.290	—	7.79	
095902.38 + 044653.02	17,973	8.21	0.723	0.186	20,442	8.23	0.736	-4.726	—	19.98	
095923.47 + 023143.62	14,774	8.24	0.735	0.223	15,575	7.99	0.584	-5.802	—	16.05	
095926.99 + 010327.90	—	—	—	—	17,121	8.24	0.739	-5.097	—	27.29	
100001.26 + 442015.72	13,963	7.91	0.539	0.092	14,781	8.21	0.717	-4.135	-7.50	27.62	
100011.82 + 364558.30	15,310	7.38	0.315	0.355	16,786	8.39	0.837	-5.493	—	8.93	
100015.28 + 240724.70	43,165	8.11	0.696	0.094	15,112	8.21	0.718	-5.850	—	22.78	
100100.10 + 313413.16	—	—	—	—	45,970	6.79	0.298	< -3.010	—	6.43	
100105.42 + 565157.00	18,056	7.90	0.541	0.575	31,091	9.36	1.314	-2.582	—	4.02	
100128.79 + 235346.90	—	—	—	—	20,860	8.20	0.719	-4.436	—	11.67	
100140.17 + 025853.19	16,397	7.87	0.520	0.095	18,526	8.22	0.727	-4.689	—	33.28	2
100209.64 + 035327.30	—	—	—	—	16,720	8.31	0.784	-5.295	—	21.71	
100218.27 + 273903.70	17,219	8.66	1.010	0.393	16,295	8.57	0.953	-4.942	—	4.67	
100242.41 + 700054.30	30,475	7.70	0.474	0.572	31,833	7.89	0.563	< -3.300	—	7.46	
100327.90 + 451625.50	15,542	7.22	0.274	4.240	30,161	8.51	0.926	< -3.326	—	3.39	
100442.48 + 533150.00	17,827	7.89	0.536	0.043	20,694	8.13	0.678	-4.600	—	26.84	
100442.59 + 021702.90	14,479	8.07	0.629	0.370	16,288	7.81	0.490	-4.609	—	10.79	

TABLE C.1 (Suite)

Nom SDSS	T_{eff}	$\log g$	M	σ_{π}/π	T_{eff}	$\log g$	M	$\log \text{H/He}$	$\log \text{Ca/He}$	S/N	Notes
100544.91 + 364838.50	15,172	7.96	0.566	0.139	14,495	7.87	0.518	-4.826	—	9.47	
100621.42 + 250445.00	14,590	8.45	0.874	0.234	15,699	7.99	0.585	-5.254	—	17.12	
100632.87 + 424352.30	20,052	7.57	0.393	0.266	21,350	8.17	0.704	< -4.695	—	11.74	
100646.07 + 413306.60	11,806	7.90	0.530	0.037	12,974	7.97	0.566	-6.081	—	17.35	
100700.19 + 611925.66	13,539	7.88	0.523	0.125	13,958	8.14	0.674	< -6.513	—	22.70	
100728.41 + 611103.40	15,513	7.87	0.520	0.211	15,470	7.99	0.585	-5.092	—	12.06	
100755.84 + 213117.40	23,994	7.86	0.531	0.349	25,406	8.11	0.673	< -4.311	—	19.50	
100809.13 + 425657.84	17,327	8.32	0.793	0.112	16,594	8.11	0.660	-5.414	—	21.18	
100817.04 + 434931.80	11,508	8.04	0.607	0.037	16,456	9.24	1.278	-4.935	-6.00	24.29	4
100852.01 + 225937.20	11,470	7.93	0.541	0.037	12,745	8.70	1.033	-6.118	—	26.57	1
100904.42 + 060817.50	18,565	7.72	0.450	0.168	18,325	8.37	0.827	-5.384	—	14.97	2
100922.96 + 410505.17	13,692	7.99	0.580	0.016	13,513	7.78	0.469	-5.350	—	50.75	
100926.60 + 154236.54	—	—	—	—	14,974	7.97	0.571	-4.804	—	19.52	
101022.15 + 030157.30	—	—	—	—	19,382	8.43	0.868	< -5.049	—	5.01	
101022.37 + 272239.30	17,118	7.56	0.381	0.223	16,028	7.99	0.588	< -6.085	—	15.93	2
101049.19 + 062143.70	15,457	8.46	0.884	0.098	15,622	8.26	0.749	-4.416	—	12.12	
101131.88 + 050729.30	—	—	—	—	25,979	7.76	0.488	< -3.943	—	9.58	
101149.93 + 024105.82	15,168	8.24	0.740	0.272	16,333	8.20	0.716	< -5.892	—	13.06	
101200.50 + 021732.10	18,194	7.51	0.368	0.719	16,001	8.15	0.685	< -5.950	—	10.49	
101208.09 + 283244.90	21,164	8.34	0.809	0.195	18,842	8.16	0.689	-4.858	—	9.32	
101226.17 + 003703.80	—	—	—	—	14,413	8.31	0.784	-5.387	—	5.09	
101249.63 + 412311.04	15,888	7.87	0.519	0.009	16,363	8.47	0.893	-5.260	—	82.64	2
101310.98 + 285407.60	15,910	7.30	0.294	1.763	15,069	8.23	0.733	-5.910	—	5.14	
101316.02 + 075915.20	18,877	7.36	0.322	0.109	18,870	8.21	0.726	-5.075	—	18.85	3
101320.07 + 354116.80	—	—	—	—	16,698	7.99	0.588	< -5.969	-7.50	17.02	
101342.58 + 085121.28	24,654	7.13	0.288	0.699	22,735	8.01	0.606	< -4.631	—	19.35	
101351.14 + 434851.00	12,808	7.97	0.571	0.444	13,890	7.79	0.473	-5.219	—	6.18	
101357.19 + 234533.00	—	—	—	—	12,439	8.11	0.653	-5.478	—	17.03	1
101427.06 + 132657.34	16,390	8.27	0.756	0.073	15,889	8.08	0.638	-5.709	—	32.16	
101502.95 + 464835.30	20,969	7.95	0.572	0.133	23,405	7.90	0.548	-3.797	—	16.56	
101526.56 + 524212.74	11,157	8.20	0.709	0.011	11,220	8.04	0.606	-5.734	—	58.09	1
101545.92 + 400214.99	20,295	8.31	0.790	0.111	18,993	8.15	0.684	-4.574	—	25.03	
101636.81 + 074951.40	21,035	7.94	0.569	0.211	22,384	8.02	0.615	-2.000	—	13.71	
101704.38 + 194848.30	16,008	8.54	0.935	0.256	15,683	8.06	0.624	-5.057	-7.00	9.62	
101706.30 + 465956.00	13,627	7.28	0.280	0.387	13,632	7.93	0.547	< -6.103	—	7.05	
101716.69 + 465232.40	12,111	7.83	0.491	0.108	12,269	7.17	0.248	-5.712	—	12.69	1
101727.85 + 184705.96	13,155	7.96	0.565	0.026	13,617	7.83	0.491	-6.106	—	38.19	
101800.81 + 370840.64	15,767	8.17	0.696	0.075	15,034	8.15	0.679	-5.489	-7.50	25.45	
101821.19 + 140507.00	13,293	8.13	0.663	0.071	14,304	8.07	0.633	< -6.297	—	16.89	
101904.85 + 052256.30	11,181	8.11	0.649	0.056	12,500	8.76	1.068	-5.448	—	27.67	1
101908.35 + 005514.60	15,534	8.41	0.852	0.309	15,314	7.78	0.470	< -5.941	—	6.86	

TABLE C.1 (Suite)

Nom SDSS	T_{eff}	$\log g$	M	σ_{π}/π	T_{eff}	$\log g$	M	$\log \text{H/He}$	$\log \text{Ca/He}$	S/N	Notes
101929.78 + 375218.90	12,963	8.08	0.635	0.105	16,822	9.26	1.284	-4.866	-6.00	16.79	
101951.55 + 290100.70	23,136	8.02	0.616	0.101	21,142	8.01	0.608	-4.510	—	21.27	
102044.06 + 090617.10	19,999	8.09	0.649	0.246	21,158	8.01	0.607	< -5.076	—	32.46	
102100.92 + 564644.70	19,416	7.97	0.580	0.065	18,624	8.07	0.636	-4.466	—	17.10	
102106.66 + 082724.48	23,475	8.00	0.605	0.036	25,328	7.96	0.587	< -4.526	—	46.94	
102218.91 + 261502.75	13,543	7.97	0.570	0.020	14,102	8.05	0.620	-6.071	—	50.23	
102251.33 + 520305.00	14,788	7.90	0.532	0.118	15,794	7.73	0.451	-4.550	-6.00	8.47	
102312.63 + 051039.60	18,599	7.76	0.472	0.066	19,317	8.09	0.649	-5.439	—	27.66	
102420.20 + 161912.50	28,492	8.39	0.851	0.319	24,962	8.11	0.671	< -4.225	—	12.75	
102600.35 + 591424.70	17,659	8.12	0.666	0.031	18,695	8.40	0.843	-5.022	—	29.33	
102615.54 + 005942.90	—	—	—	—	15,825	8.08	0.638	-4.778	—	5.71	
102616.80 + 081258.90	14,066	8.27	0.758	0.181	14,532	8.23	0.734	< -6.142	—	13.56	
102618.50 + 013646.46	—	—	—	—	18,932	8.14	0.679	< -5.428	—	18.55	
102626.04 + 513758.29	13,001	8.44	0.869	0.163	12,072	7.17	0.249	-5.910	—	5.25	1
102651.55 + 091347.50	26,132	7.73	0.475	0.286	25,573	7.83	0.518	-3.652	—	31.61	
102655.38 + 530610.09	36,530	7.99	0.624	0.120	37,939	7.84	0.550	< -3.531	—	28.59	
102701.87 + 583142.64	13,051	8.07	0.627	0.065	13,002	8.13	0.667	-5.885	—	21.87	
102706.20 + 304526.50	—	—	—	—	15,456	7.82	0.494	-4.890	—	3.27	
102718.79 + 275539.51	20,235	8.07	0.642	0.064	20,069	8.13	0.678	-3.241	—	31.27	
102738.24 + 351844.90	18,819	8.06	0.629	0.585	15,077	7.72	0.444	-5.066	—	5.49	
102807.83 - 013552.94	13,407	8.00	0.586	0.112	14,644	8.69	1.024	-5.302	-7.50	21.61	
102816.83 + 490200.70	15,019	7.67	0.422	0.040	17,195	7.91	0.545	-5.425	—	25.25	
102941.17 + 451810.20	12,135	7.66	0.411	0.158	11,426	6.83	0.177	< -6.175	—	10.77	1
102953.32 + 020812.45	14,963	7.61	0.393	0.201	14,201	8.18	0.699	-4.853	—	24.21	2
103026.29 + 075607.50	18,479	8.50	0.911	0.413	18,554	8.04	0.617	< -5.381	—	11.62	
103033.20 + 385447.59	21,194	7.67	0.438	0.246	20,387	8.33	0.800	-4.810	—	24.64	2
103036.14 + 212519.70	19,724	8.41	0.851	0.606	17,817	7.77	0.474	-5.306	—	4.77	
103056.39 + 233831.80	12,843	7.99	0.578	0.077	12,841	8.01	0.592	-5.754	—	12.44	
103110.42 + 080059.40	26,022	7.62	0.427	0.588	26,059	8.09	0.658	< -4.061	—	12.56	
103205.76 + 324005.55	12,690	8.02	0.596	0.006	12,753	7.96	0.561	-4.940	—	72.11	
103248.52 - 025520.46	10,920	8.06	0.619	0.014	16,474	9.22	1.273	-5.145	-6.00	70.02	4
103340.76 + 131159.53	13,072	8.16	0.684	0.178	15,341	8.51	0.915	-5.778	—	15.52	
103411.31 + 373336.70	15,215	7.90	0.533	0.168	15,112	8.31	0.783	-5.114	-7.50	10.99	
103455.91 + 240905.80	52,475	8.18	0.746	0.088	48,474	7.72	0.521	< -2.517	—	28.08	
103517.85 + 273934.30	—	—	—	—	14,231	8.79	1.085	-5.294	—	13.02	
103536.44 - 011849.17	29,189	8.12	0.683	0.307	24,367	8.00	0.605	-4.160	—	30.95	
103554.29 + 624851.40	15,646	7.83	0.499	0.304	16,540	7.81	0.488	< -5.738	—	5.94	
103555.52 + 421043.75	38,763	8.34	0.830	0.155	41,231	7.87	0.568	-2.782	—	28.27	
103609.48 + 193841.14	—	—	—	—	16,737	8.22	0.725	-4.509	—	14.75	3
103610.50 + 052329.57	17,956	8.55	0.942	0.180	17,644	8.11	0.658	< -5.768	—	16.50	
103611.53 + 181453.20	12,676	8.00	0.585	0.043	12,902	7.86	0.509	-5.733	—	22.96	

TABLE C.1 (Suite)

Nom SDSS	T_{eff}	$\log g$	M	σ_{π}/π	T_{eff}	$\log g$	M	$\log \text{H/He}$	$\log \text{Ca/He}$	S/N	Notes
103651.09 + 483754.00	11,697	7.73	0.439	0.128	14,554	9.00	1.187	-5.055	-6.50	8.75	
103710.16 + 663201.40	14,511	8.05	0.616	0.014	15,001	7.95	0.559	-5.810	—	38.13	
103728.49 + 372359.60	11,458	6.56	0.130	1.003	13,697	9.72	1.466	-5.040	—	6.33	1
103729.48 - 003111.17	16,675	8.10	0.650	0.030	15,805	7.88	0.525	< -6.311	—	55.00	
103729.83 + 070902.70	11,609	8.06	0.619	0.110	13,318	8.18	0.699	-4.430	-7.00	10.09	
103734.47 + 455025.83	—	—	—	—	14,048	9.55	1.377	< -6.076	—	5.19	
103742.80 + 515655.60	19,002	8.44	0.871	0.417	20,881	8.15	0.688	< -4.686	—	6.22	
103902.40 + 024326.62	13,010	7.95	0.557	0.152	13,388	8.34	0.799	-6.123	—	15.66	
103910.92 + 345235.95	11,743	7.95	0.552	0.120	11,211	7.23	0.259	-5.828	—	16.23	1
103917.11 + 055741.70	15,254	7.64	0.408	0.281	15,476	7.83	0.496	< -5.920	—	7.49	
103923.87 + 264822.90	13,774	8.03	0.605	0.051	14,959	8.36	0.817	-5.285	-7.50	24.75	
103942.95 + 422718.70	12,781	7.95	0.555	0.110	12,787	8.04	0.612	-5.829	—	14.49	
103955.45 + 310643.53	12,467	7.88	0.520	0.023	13,292	7.83	0.492	-4.554	—	24.76	
103959.55 + 400225.10	24,119	8.28	0.774	0.050	19,705	8.06	0.634	< -5.413	—	28.70	
104036.41 + 095358.60	12,556	7.71	0.431	0.151	11,761	7.25	0.267	-5.842	—	14.84	1
104043.86 + 375306.50	17,325	8.27	0.758	0.136	16,406	8.14	0.675	< -5.878	—	13.99	
104117.42 + 231036.40	25,880	7.60	0.420	0.207	21,596	8.06	0.634	-4.784	—	32.18	2
104219.93 - 015223.02	13,934	8.27	0.758	0.194	13,523	8.04	0.608	< -6.349	—	16.57	
104313.65 + 150754.00	—	—	—	—	17,783	9.91	1.620	-4.226	-6.00	4.76	
104318.16 + 492320.10	15,225	7.97	0.571	0.111	16,289	8.27	0.759	-5.882	—	12.21	
104318.44 + 415412.50	20,738	7.77	0.481	0.283	29,776	8.05	0.641	< -3.460	—	9.85	
104348.18 + 334451.30	18,640	7.82	0.501	0.427	26,521	7.92	0.565	-2.510	—	6.06	
104423.24 + 565506.78	25,702	8.30	0.792	0.205	29,735	7.82	0.522	< -3.947	—	20.82	
104441.54 + 011041.40	14,359	8.50	0.906	0.175	13,888	7.34	0.297	-6.098	—	12.48	
104504.99 + 525443.30	10,835	7.19	0.247	0.678	16,500	9.52	1.365	-4.283	-6.00	5.84	
104657.99 - 005045.70	21,238	8.11	0.663	0.058	18,664	8.05	0.625	< -5.696	—	47.46	
104706.72 + 281122.60	12,845	8.55	0.940	0.365	14,586	8.42	0.854	-5.279	—	3.75	
104739.51 + 604753.10	12,468	7.51	0.351	0.838	14,066	7.45	0.333	-4.736	—	3.57	
104806.83 + 025431.80	13,860	8.22	0.722	0.127	13,993	7.98	0.578	-5.612	—	9.34	
104819.30 + 180052.78	13,777	8.43	0.863	0.184	14,912	8.24	0.737	-5.270	—	15.65	
104832.64 - 020112.29	14,021	8.02	0.601	0.005	14,581	8.07	0.631	< -6.464	—	91.66	
104908.33 - 001529.30	22,653	7.90	0.550	0.657	21,468	8.03	0.615	< -4.672	—	14.21	
105001.57 + 000541.30	15,516	8.85	1.115	0.274	15,686	8.15	0.682	-5.800	—	12.17	
105058.17 + 095815.20	—	—	—	—	15,580	8.28	0.766	< -5.905	—	5.62	
105100.62 + 283715.40	—	—	—	—	14,991	8.06	0.628	-5.247	-7.00	18.92	
105113.66 + 043516.91	13,705	7.98	0.578	0.012	14,317	7.93	0.548	< -6.487	—	60.83	
105131.19 + 305355.50	—	—	—	—	15,525	7.55	0.372	< -5.812	—	4.28	
105149.10 + 110112.70	20,215	8.17	0.698	0.056	20,495	8.06	0.635	-4.823	—	24.68	
105327.66 + 000043.00	—	—	—	—	14,614	7.83	0.498	-4.666	—	5.59	
105344.44 + 201415.30	—	—	—	—	38,770	7.67	0.479	< -3.508	—	22.57	
105404.68 + 443819.90	27,769	7.76	0.494	0.096	25,493	7.98	0.595	-3.855	—	19.16	

TABLE C.1 (Suite)

Nom SDSS	T_{eff}	$\log g$	M	σ_{π}/π	T_{eff}	$\log g$	M	$\log \text{H/He}$	$\log \text{Ca/He}$	S/N	Notes
105423.95 + 211057.58	20,795	7.96	0.578	0.044	22,038	8.08	0.646	< -4.914	—	47.06	
105443.45 + 042923.70	18,422	8.13	0.676	0.084	16,416	8.01	0.600	< -6.020	—	16.36	
105459.92 + 473218.70	15,019	8.27	0.757	0.529	16,614	8.13	0.671	-4.907	—	11.41	
105604.14 + 045634.13	17,124	8.01	0.601	0.066	16,403	8.11	0.659	-4.323	—	36.65	
105635.40 + 391757.55	19,800	7.94	0.564	0.262	19,222	8.18	0.705	-4.850	—	21.26	
105715.58 + 102943.10	17,754	8.58	0.962	0.393	17,153	7.67	0.426	< -5.606	—	8.06	
105752.20 + 621301.60	15,738	7.43	0.333	0.870	15,796	7.84	0.502	< -5.773	—	3.44	
105829.24 + 655227.20	13,665	7.69	0.426	0.111	15,381	7.67	0.422	< -6.182	—	15.45	2
105925.46 + 341451.40	12,182	8.03	0.603	0.003	12,313	7.95	0.555	-5.469	—	78.04	
105929.60 + 554039.30	16,707	7.74	0.457	0.077	24,251	7.97	0.591	-2.645	—	12.69	
105931.76 + 333504.10	—	—	—	—	13,472	8.54	0.935	-4.917	—	5.65	1
110030.22 + 552238.00	12,103	8.08	0.633	0.028	11,011	7.21	0.254	-5.650	—	16.36	1
110147.19 + 592409.50	—	—	—	—	51,534	8.50	0.940	< -7.803	—	4.11	
110235.85 + 623416.10	22,069	8.09	0.655	0.041	24,224	7.86	0.530	-4.616	—	20.17	
110342.78 + 220333.80	21,795	8.02	0.614	0.091	18,889	8.29	0.773	-4.127	—	32.70	
110438.39 + 071129.80	11,231	8.03	0.598	0.028	16,488	9.34	1.307	-5.083	-6.00	19.13	4
110445.12 + 350004.91	19,345	7.58	0.395	0.343	21,110	8.22	0.734	-3.950	—	11.22	
110509.99 + 665757.90	27,161	7.78	0.501	0.711	25,332	7.53	0.394	< -4.040	—	8.47	
110520.35 + 092324.97	17,499	8.32	0.795	0.165	15,907	7.78	0.474	< -6.105	—	18.89	
110559.21 + 371725.50	12,687	8.12	0.657	0.121	11,765	7.83	0.491	< -6.523	—	20.98	1
110611.71 + 125835.00	19,372	8.15	0.685	0.147	19,158	8.14	0.683	-4.960	—	25.04	
110614.78 + 303726.90	26,724	7.82	0.516	0.519	23,671	8.18	0.709	< -4.268	—	9.65	
110649.88 + 374655.90	13,626	8.21	0.720	0.072	13,557	8.11	0.656	-6.265	—	26.92	
110700.55 - 164721.20	21,071	8.57	0.956	0.297	18,858	8.37	0.829	< -5.298	—	12.09	
110708.12 + 361631.57	22,215	8.03	0.621	0.143	22,173	8.12	0.672	-4.130	—	21.02	
110737.03 + 142527.20	12,499	7.88	0.515	0.052	13,142	8.32	0.788	-5.833	—	22.77	
110817.58 + 132049.10	17,372	8.23	0.736	0.086	16,879	7.98	0.583	-4.880	—	15.45	
110834.77 + 575403.40	14,989	8.15	0.680	0.017	15,627	8.25	0.743	-4.490	—	28.92	
110954.10 + 580630.80	21,939	8.49	0.909	0.478	22,874	8.24	0.747	< -4.354	—	7.09	
110957.82 + 131827.90	16,104	7.87	0.521	0.146	16,125	8.13	0.667	-4.044	—	13.03	
111004.40 + 300918.40	—	—	—	—	15,539	8.43	0.860	-5.023	-6.00	10.02	
111010.94 + 385700.30	—	—	—	—	16,160	8.11	0.655	-4.534	—	32.14	
111023.01 + 592234.10	12,567	8.21	0.715	0.062	12,459	8.02	0.596	-5.908	—	26.95	
111106.49 + 400203.20	14,738	9.46	1.344	0.406	17,588	7.85	0.514	-3.823	—	4.95	
111137.92 + 184938.63	11,248	8.14	0.670	0.112	12,152	8.28	0.759	-4.966	—	18.52	1
111157.31 + 061027.40	16,982	7.51	0.362	0.509	16,837	8.51	0.915	-4.735	—	7.17	
111158.10 - 153503.30	15,604	8.11	0.654	0.172	16,457	8.01	0.595	< -5.869	—	14.30	
111201.75 + 420403.52	13,638	8.03	0.605	0.170	13,903	7.87	0.517	-5.973	—	18.93	
111203.60 + 215747.46	—	—	—	—	13,571	7.88	0.522	-5.473	—	24.72	
111310.23 + 202916.40	13,182	8.21	0.715	0.011	13,433	8.03	0.607	-4.559	—	49.91	
111335.92 + 014534.05	—	—	—	—	32,052	8.00	0.620	-2.946	—	13.17	

TABLE C.1 (Suite)

Nom SDSS	T_{eff}	$\log g$	M	σ_{π}/π	T_{eff}	$\log g$	M	$\log \text{H/He}$	$\log \text{Ca/He}$	S/N	Notes
111348.39 + 600229.30	17,830	8.10	0.655	0.073	17,497	8.04	0.618	-3.640	-6.50	28.48	
111435.44 + 244743.03	16,673	7.95	0.562	0.117	15,681	7.97	0.574	< -6.330	—	20.51	
111447.80 + 293249.60	12,814	7.54	0.361	0.249	12,497	7.90	0.530	-5.974	—	11.76	1
111655.10 - 121343.70	14,529	8.70	1.034	0.831	14,832	6.98	0.225	-5.581	—	6.51	
111822.68 + 153334.50	21,339	7.92	0.557	0.028	24,685	7.88	0.542	-3.787	—	49.92	
111839.02 + 383333.40	13,796	6.78	0.187	0.845	16,995	7.84	0.504	< -5.641	—	8.11	
111911.27 - 130649.80	15,764	8.34	0.800	0.145	14,425	7.89	0.526	-5.731	—	17.52	
111946.75 + 673631.10	13,284	7.60	0.388	0.059	15,207	8.02	0.600	-5.625	—	45.32	2
112013.34 + 665259.90	16,054	7.96	0.568	0.112	15,669	8.21	0.721	-6.003	—	18.47	
112022.38 + 141026.70	12,563	8.03	0.604	0.087	12,095	7.88	0.518	-5.881	—	21.04	1
112154.14 + 542503.40	20,298	8.12	0.668	0.097	19,413	8.12	0.666	-5.144	—	13.07	
112223.42 + 113641.47	21,144	8.41	0.855	0.169	22,325	7.99	0.597	-4.320	—	17.12	
112225.21 + 153527.13	16,051	8.10	0.651	0.314	15,736	8.07	0.630	-3.786	—	20.64	
112340.06 + 674222.30	15,817	7.78	0.472	0.293	17,955	8.07	0.633	-5.532	—	11.45	
112355.86 + 563647.00	16,754	7.57	0.386	0.288	21,209	8.60	0.974	< -4.616	—	6.66	
112506.49 + 452814.00	15,184	8.12	0.664	0.044	14,118	7.95	0.561	-5.830	—	16.21	
112632.69 - 073837.30	14,094	8.55	0.938	0.309	15,602	7.65	0.415	< -6.011	—	13.87	
112711.72 + 325229.70	13,072	6.97	0.213	0.770	14,382	7.97	0.574	-5.532	—	14.22	3
112712.26 + 120227.38	—	—	—	—	14,694	8.25	0.742	-5.820	—	11.32	
112737.92 + 052905.20	—	—	—	—	14,494	7.42	0.324	-5.281	—	5.50	
112838.20 - 062146.70	12,696	7.94	0.554	0.851	12,496	6.62	0.144	-5.204	—	7.78	1
112839.69 + 415140.70	21,309	7.99	0.594	0.087	21,643	8.08	0.648	< -4.980	—	20.89	
112900.85 + 151119.75	16,296	7.89	0.532	0.050	16,052	8.02	0.602	-4.953	—	37.16	
112920.58 + 011604.71	16,932	7.88	0.524	0.110	16,540	7.99	0.585	< -6.187	—	27.37	
112944.19 + 471126.40	14,581	7.53	0.363	0.515	15,850	7.58	0.387	-5.292	—	3.52	
112956.37 + 474411.00	—	—	—	—	18,511	7.98	0.583	-3.484	-6.00	4.50	
113007.78 + 614340.30	15,298	8.78	1.079	0.266	17,771	8.70	1.034	-3.914	—	4.34	
113011.86 + 621926.20	18,267	8.17	0.698	0.020	16,801	8.12	0.665	-5.672	—	42.03	
113028.62 + 301120.70	14,678	8.32	0.791	0.164	14,404	8.27	0.757	-5.029	—	11.04	
113058.39 + 664712.25	8,988	8.49	0.893	0.010	12,107	8.32	0.789	-4.889	—	4.80	1
113131.97 - 022617.70	16,766	7.16	0.265	0.789	15,416	7.20	0.268	< -5.928	—	6.14	
113143.40 + 370128.10	12,965	8.02	0.598	0.006	12,760	7.83	0.495	-6.251	—	57.04	
113153.32 + 481852.30	17,235	7.90	0.536	0.024	18,474	8.12	0.666	< -5.750	—	35.20	
113158.48 - 012955.90	18,752	7.76	0.470	0.599	15,642	7.60	0.391	< -5.896	—	6.63	
113213.56 + 202518.50	20,485	8.13	0.674	0.066	19,236	8.10	0.654	-5.525	—	23.06	
113247.25 + 283519.00	21,395	7.55	0.392	0.259	23,747	8.01	0.611	-3.470	—	12.52	
113257.32 + 382544.90	—	—	—	—	13,907	8.62	0.986	-5.273	—	4.35	
113316.54 + 035652.59	14,136	7.97	0.572	0.025	15,023	7.94	0.558	-5.685	—	56.06	
113325.85 - 012829.24	12,877	7.92	0.543	0.022	14,140	7.88	0.519	-5.228	—	46.39	
113327.45 + 381621.80	20,459	8.64	1.002	0.438	17,135	7.76	0.465	< -5.610	—	5.87	
113348.88 + 262354.42	—	—	—	—	13,428	8.19	0.705	-5.540	—	9.08	

TABLE C.1 (Suite)

Nom SDSS	T_{eff}	$\log g$	M	σ_{π}/π	T_{eff}	$\log g$	M	$\log \text{H/He}$	$\log \text{Ca/He}$	S/N	Notes
113425.11 + 644305.35	16,917	8.19	0.707	0.034	15,903	8.01	0.595	-5.477	—	35.94	
113527.68 - 000844.40	19,852	8.06	0.630	0.144	20,486	8.13	0.678	< -5.225	—	21.46	
113529.60 + 425339.84	14,724	8.07	0.628	0.103	15,484	8.18	0.697	-5.412	—	18.35	
113623.54 + 320403.80	—	—	—	—	18,370	8.36	0.821	-5.111	—	18.53	3
113654.22 + 070336.18	17,004	8.20	0.715	0.018	18,724	8.42	0.861	-4.996	—	55.64	
113716.68 + 405527.30	17,438	8.29	0.770	0.681	18,821	8.68	1.023	< -5.098	—	4.43	
113747.78 + 354421.70	17,051	8.05	0.620	0.153	16,665	8.10	0.652	< -5.829	—	13.83	
113749.20 + 160355.50	19,918	7.88	0.530	0.200	22,637	7.90	0.546	-3.486	—	10.14	
113752.01 + 561715.59	12,604	8.09	0.638	0.029	12,551	8.28	0.762	-6.103	—	32.83	
113811.94 + 545947.60	17,954	8.22	0.728	0.094	18,160	8.09	0.648	-5.235	—	12.01	
114010.54 - 002935.50	13,670	6.96	0.214	0.734	14,808	8.46	0.879	-5.681	—	11.21	
114022.27 + 143002.77	13,407	8.08	0.635	0.048	13,128	7.86	0.508	< -6.547	—	26.64	
114039.37 - 004949.70	24,194	8.05	0.635	0.186	25,481	7.85	0.528	< -4.149	—	13.89	
114051.66 + 663950.10	18,470	8.03	0.614	0.083	17,436	8.08	0.642	-5.649	—	24.73	
114151.77 + 395854.70	14,113	9.09	1.227	0.372	14,669	6.95	0.218	-4.757	—	4.26	
114238.69 + 572747.50	19,547	8.30	0.779	0.051	18,788	8.45	0.876	-5.270	—	19.72	
114245.28 + 290432.60	12,979	8.16	0.684	0.075	13,434	8.88	1.128	-4.601	—	11.00	
114350.12 + 272733.22	—	—	—	—	18,507	8.06	0.633	< -5.545	—	18.44	
114356.86 + 052334.33	—	—	—	—	11,890	6.05	-1.106	-5.610	—	11.62	1
114428.49 + 143146.34	19,760	7.80	0.492	0.297	19,240	8.13	0.676	-4.670	—	19.92	
114446.39 + 254122.36	36,751	7.67	0.474	0.148	49,482	8.09	0.692	< -2.203	—	33.21	
114503.75 + 143736.60	—	—	—	—	18,365	8.05	0.627	< -5.318	—	5.58	
114546.58 + 150848.40	13,888	8.50	0.908	0.198	13,512	7.71	0.434	-5.951	—	11.54	
114552.73 + 033218.71	13,818	7.80	0.478	0.112	14,033	8.06	0.626	-5.826	—	22.83	
114605.39 + 001458.60	14,292	7.83	0.497	0.380	14,175	7.20	0.262	< -6.066	—	6.06	
114659.63 + 303243.54	—	—	—	—	44,244	6.20	0.206	-2.000	—	10.51	
114751.73 + 001701.20	—	—	—	—	25,892	7.53	0.395	< -3.956	—	6.68	
114850.90 + 350425.02	14,992	8.06	0.623	0.025	14,891	7.89	0.526	< -6.432	—	47.13	
114910.95 - 014444.10	15,970	7.07	0.244	0.643	16,072	9.75	1.485	< -5.728	—	4.51	
114912.80 + 304531.20	11,708	7.79	0.471	0.061	12,521	8.05	0.616	-4.948	—	22.57	
114933.01 + 451043.59	12,686	8.12	0.657	0.100	12,552	7.82	0.489	-5.611	—	15.05	1
114940.13 + 643223.10	14,952	8.16	0.685	0.186	14,976	7.45	0.334	< -5.883	—	4.76	
115114.92 + 194346.63	18,874	8.03	0.614	0.022	18,160	8.21	0.722	-5.155	—	52.46	
115130.77 + 403455.49	16,971	8.18	0.699	0.024	17,473	8.28	0.764	-5.169	—	56.40	
115141.89 + 593430.60	15,271	8.29	0.769	0.047	13,804	7.65	0.409	< -6.333	—	17.65	
115153.98 + 111809.04	13,064	8.30	0.777	0.179	13,696	8.54	0.930	-6.463	—	20.41	
115307.40 + 312737.73	23,157	6.74	0.203	0.362	22,983	7.92	0.561	-4.264	—	25.02	
115326.63 + 223752.23	17,401	8.57	0.955	0.112	16,316	8.06	0.625	-5.474	—	22.96	
115416.86 + 045104.10	16,714	8.00	0.592	0.019	17,369	8.25	0.747	-5.387	—	36.99	
115418.62 + 014137.90	19,802	8.08	0.645	0.067	20,235	8.12	0.670	-4.645	—	21.08	
115426.67 + 251755.60	21,458	7.94	0.568	0.043	22,604	7.97	0.584	-4.699	—	40.05	

TABLE C.1 (Suite)

Nom SDSS	T_{eff}	$\log g$	M	σ_{π}/π	T_{eff}	$\log g$	M	$\log \text{H/He}$	$\log \text{Ca/He}$	S/N	Notes
115440.17 + 425818.70	17,476	8.13	0.669	0.626	15,742	8.31	0.784	< -5.882	—	5.10	
115503.66 + 314825.80	17,015	8.13	0.671	0.041	15,668	7.62	0.401	-6.195	—	26.17	
115522.54 + 342524.50	19,793	7.92	0.556	0.267	19,973	8.33	0.803	-4.571	—	8.71	
115538.57 + 254135.20	39,460	8.12	0.697	0.262	35,311	7.75	0.505	< -3.268	—	12.71	
115553.69 + 242737.00	17,676	7.87	0.521	0.128	16,106	8.08	0.638	< -5.932	—	13.73	
115655.23 + 162147.50	15,616	8.29	0.772	0.136	15,407	8.13	0.669	-5.501	—	8.20	
115705.53 + 452011.10	19,378	8.06	0.633	0.183	18,984	8.47	0.890	< -5.154	—	8.19	
115800.08 + 162125.60	11,952	8.24	0.736	0.011	12,805	8.56	0.943	-5.368	—	30.78	
115808.54 - 030342.50	15,499	8.07	0.632	0.151	15,625	7.55	0.375	< -5.899	—	9.73	
115959.91 + 500554.20	13,226	8.20	0.708	0.048	12,764	8.16	0.682	-5.243	—	30.40	
120013.28 + 445154.40	16,449	8.36	0.816	0.292	15,481	8.07	0.634	< -5.919	—	5.29	
120043.67 + 592601.02	14,858	8.11	0.653	0.026	15,062	8.01	0.597	-6.351	—	26.22	
120101.04 + 673004.90	15,495	7.81	0.487	0.016	17,523	8.09	0.648	-5.727	—	40.24	
120203.13 + 285647.07	16,043	7.56	0.377	0.205	17,179	8.16	0.690	-5.231	—	16.37	2
120319.78 + 243955.70	14,397	8.23	0.728	0.011	15,300	8.60	0.969	-4.912	-7.50	40.55	
120349.82 - 005145.90	—	—	—	—	15,146	7.86	0.511	-4.969	—	8.81	
120350.03 + 102242.17	11,874	8.25	0.742	0.061	12,302	8.22	0.721	-5.571	—	16.40	1
120524.67 + 063010.00	19,628	8.08	0.645	0.048	21,282	8.23	0.737	-4.683	—	26.40	
120551.38 + 200602.04	11,182	7.60	0.380	0.155	11,062	8.06	0.622	< -6.258	—	16.36	1
120658.14 - 003336.80	24,145	7.92	0.564	0.101	24,045	7.87	0.536	< -4.685	—	35.94	
120706.08 + 314030.10	21,697	8.33	0.806	0.130	21,300	8.16	0.694	< -4.849	—	17.41	
120708.63 + 322155.70	15,403	8.49	0.900	0.370	18,468	8.17	0.696	< -5.291	—	7.13	
120735.19 + 225905.70	25,020	7.71	0.463	0.120	20,592	8.13	0.677	< -5.201	—	22.06	2
120753.27 + 223335.00	14,709	8.52	0.920	0.409	12,111	6.16	-.031	< -6.046	—	3.40	1
120936.87 - 023631.46	10,129	8.27	0.749	0.024	10,283	7.84	0.493	< -6.361	—	22.64	1
121029.29 + 283227.80	12,883	7.71	0.433	0.259	14,775	8.56	0.946	-5.664	—	7.13	
121031.40 + 214430.10	24,029	7.73	0.468	0.144	24,849	8.01	0.611	-4.511	—	21.27	
121037.50 + 193200.60	26,221	8.00	0.607	0.049	19,016	8.11	0.659	-5.060	—	43.62	
121108.46 + 053249.80	14,894	7.96	0.564	0.091	15,802	8.02	0.601	< -6.121	—	15.73	
121133.01 + 190727.30	17,559	8.29	0.772	0.478	14,049	7.75	0.457	< -6.076	—	8.13	
121135.65 + 181040.30	30,892	8.04	0.638	0.618	37,209	7.96	0.606	< -3.084	—	7.83	
121219.03 - 011536.00	13,439	8.46	0.881	0.216	14,469	8.28	0.763	-5.373	—	7.11	
121312.75 + 500441.60	19,670	8.11	0.660	0.137	16,774	8.01	0.598	< -6.144	—	24.91	
121439.61 + 351813.40	17,497	8.14	0.681	0.339	25,943	7.75	0.483	< -3.948	—	5.48	
121449.65 + 570903.10	—	—	—	—	15,819	10.22	2.078	< -5.769	—	3.86	
121527.51 + 373009.13	15,633	8.17	0.694	0.129	16,077	7.93	0.551	< -6.078	—	19.92	
121545.49 + 253634.40	21,803	8.32	0.797	0.336	23,146	8.29	0.777	-3.527	—	10.97	
121600.21 + 302328.82	9,267	8.64	0.992	0.028	12,158	9.83	1.544	-5.742	—	11.70	1
121620.09 + 421601.60	14,761	7.58	0.383	0.270	16,093	7.79	0.480	< -5.824	—	8.30	
121735.00 + 244308.50	13,430	8.10	0.645	0.099	12,324	7.35	0.294	< -6.244	—	14.21	1
121754.60 - 024323.40	19,113	8.35	0.816	0.076	17,595	8.29	0.771	-5.362	—	16.85	

TABLE C.1 (Suite)

Nom SDSS	T_{eff}	$\log g$	M	σ_{π}/π	T_{eff}	$\log g$	M	$\log \text{H/He}$	$\log \text{Ca/He}$	S/N	Notes
121813.58 + 461806.10	39,799	7.80	0.535	0.120	44,390	7.71	0.510	< -2.977	—	19.43	
121939.35 + 094956.42	25,397	8.07	0.648	0.078	31,524	7.79	0.513	-3.604	—	42.72	
122002.19 + 592643.69	13,590	8.01	0.594	0.047	14,224	7.82	0.491	-6.020	—	25.86	
122025.21 + 384127.90	—	—	—	—	16,958	7.93	0.555	-5.618	—	19.05	
122041.22 + 213729.60	15,683	7.45	0.338	0.353	14,876	8.10	0.648	< -5.995	—	7.59	
122112.33 + 402455.40	—	—	—	—	15,570	8.19	0.704	< -5.907	—	8.15	
122117.91 + 035440.10	—	—	—	—	17,973	8.29	0.776	-5.020	—	11.52	
122241.27 - 003614.40	22,215	7.91	0.553	0.075	19,547	8.17	0.700	-4.466	—	33.11	
122244.47 + 182259.80	19,626	7.17	0.279	0.399	22,328	8.22	0.736	-3.939	—	9.49	
122250.15 + 684314.25	13,439	7.93	0.548	0.040	14,007	8.00	0.586	-5.586	—	25.96	
122259.40 + 503645.30	18,040	8.16	0.689	0.066	17,946	8.36	0.818	-5.156	—	10.72	
122314.26 + 435009.20	20,712	7.88	0.536	0.182	25,084	7.80	0.503	-2.083	—	10.30	
122444.73 + 174145.85	15,967	7.62	0.400	0.163	14,527	8.04	0.610	-5.613	—	22.01	2
122526.22 + 621552.50	13,200	7.87	0.512	0.086	14,458	7.90	0.533	< -6.040	—	7.05	
122529.70 + 065033.43	21,871	8.44	0.871	0.204	19,803	8.22	0.733	-4.951	—	20.70	
122555.17 + 225057.30	19,108	8.05	0.626	0.105	17,848	8.11	0.661	-5.283	—	16.56	
122555.85 + 663903.47	19,725	8.18	0.703	0.149	20,977	8.19	0.716	< -4.915	—	15.18	
122632.58 - 004400.70	16,102	8.55	0.942	0.429	14,937	7.95	0.562	-5.621	—	8.95	
122649.96 + 444513.59	—	—	—	—	16,628	9.23	1.274	-4.964	-6.00	20.47	4
122655.92 - 010454.80	12,268	7.91	0.532	0.045	12,278	7.84	0.499	-6.017	—	19.59	1
122803.20 + 550339.40	19,998	8.54	0.938	0.286	18,980	8.06	0.632	< -5.055	—	4.31	
122833.66 + 385401.80	15,747	7.46	0.343	0.900	14,166	7.11	0.245	< -5.974	—	2.81	
122859.40 + 102319.80	20,656	8.28	0.771	0.164	17,070	8.21	0.724	-5.451	—	10.07	
122929.47 + 243544.00	13,745	8.04	0.614	0.038	13,563	7.80	0.477	-6.048	—	14.72	
123006.36 + 114826.53	16,003	8.05	0.619	0.170	15,355	8.19	0.706	-5.868	—	18.15	
123032.75 + 443729.90	12,972	7.93	0.545	0.059	13,109	7.46	0.331	< -6.237	—	11.41	
123032.96 + 044608.00	15,764	7.75	0.459	0.167	16,213	8.00	0.590	-4.225	—	12.40	
123045.65 + 162138.59	14,163	8.08	0.636	0.127	14,347	8.12	0.663	-6.107	—	21.79	
123051.52 + 532721.90	15,784	7.95	0.562	0.066	15,935	8.01	0.595	-5.312	—	14.27	
123108.33 - 011438.10	—	—	—	—	11,639	7.95	0.555	-5.359	—	22.92	1
123114.72 + 321352.00	11,456	8.10	0.647	0.057	11,579	7.99	0.578	-5.829	—	12.16	1
123130.21 + 302621.23	11,123	8.01	0.588	0.031	11,532	7.98	0.572	-5.975	—	34.86	1
123140.49 + 404241.60	16,381	7.87	0.522	0.163	16,679	7.82	0.495	-5.603	—	12.99	
123143.74 + 172511.30	14,868	8.03	0.604	0.467	14,850	9.02	1.196	-5.502	—	5.53	
123157.03 + 253355.45	17,938	8.23	0.737	0.109	16,506	8.13	0.672	-6.153	—	26.13	
123217.92 + 580553.40	13,153	7.97	0.569	0.214	15,212	8.96	1.170	-4.802	—	5.23	
123230.41 + 035036.70	19,349	7.53	0.377	0.129	18,295	7.96	0.573	< -5.801	—	20.39	2
123341.16 + 451642.80	13,216	8.06	0.622	0.038	13,047	7.73	0.442	-4.962	—	21.35	
123345.52 + 570344.00	13,505	6.26	0.099	1.396	13,962	8.29	0.771	< -5.993	—	2.81	
123407.08 + 482011.22	18,470	8.00	0.595	0.239	22,371	8.21	0.727	-4.358	—	14.53	
123427.23 + 033900.30	15,999	8.10	0.653	0.078	14,957	7.75	0.455	< -6.235	—	18.14	

TABLE C.1 (Suite)

Nom SDSS	T_{eff}	$\log g$	M	σ_{π}/π	T_{eff}	$\log g$	M	$\log \text{H/He}$	$\log \text{Ca/He}$	S/N	Notes
123432.64 + 560643.10	12,515	8.30	0.775	0.021	13,193	8.19	0.701	-5.691	-7.00	22.31	
123544.36 + 623414.40	15,856	8.28	0.763	0.116	14,955	8.23	0.729	< -5.985	—	8.69	
123552.27 + 073134.30	—	—	—	—	13,791	7.93	0.550	-5.015	—	17.90	
123652.94 + 475350.00	15,404	6.67	0.183	1.620	15,997	9.08	1.223	-4.804	—	3.28	
123654.96 + 170918.70	—	—	—	—	27,350	7.67	0.454	< -4.232	—	23.42	
123735.52 + 602833.00	12,195	7.02	0.218	0.155	15,863	7.79	0.477	-5.649	—	13.35	2
123750.47 + 085526.00	29,909	8.14	0.698	0.179	29,566	7.97	0.600	< -3.481	—	9.61	
123753.42 + 190725.10	13,869	8.09	0.639	0.433	12,949	7.69	0.423	-5.797	—	7.55	1
123758.46 + 525045.80	17,004	7.73	0.454	0.330	15,953	7.34	0.304	< -5.848	—	5.58	
123819.28 + 080309.70	13,648	8.01	0.595	0.010	13,980	7.89	0.526	-5.335	—	58.98	
123914.29 + 321058.60	14,020	7.97	0.573	0.074	14,909	8.00	0.591	-4.585	—	9.61	
124058.65 + 532623.60	16,327	7.97	0.572	0.117	17,591	8.47	0.888	-5.271	—	11.93	2
124112.99 + 122613.70	14,189	8.00	0.590	0.017	15,003	7.78	0.472	< -6.420	—	38.25	
124129.86 + 210321.90	15,676	7.94	0.555	0.125	16,194	8.26	0.753	< -5.917	—	12.37	
124206.06 + 194305.63	16,163	8.06	0.627	0.044	16,165	8.08	0.638	-5.631	—	30.69	
124241.43 + 192232.00	18,388	8.98	1.183	0.249	30,718	8.16	0.709	-2.000	—	5.87	
124304.32 + 500928.60	16,485	7.94	0.559	0.070	17,002	8.29	0.775	-5.397	-7.50	27.98	
124306.09 + 205708.86	13,533	7.93	0.550	0.014	14,614	7.94	0.553	-6.353	—	56.57	
124331.37 - 063455.40	29,736	7.85	0.537	0.775	28,126	7.63	0.438	-3.470	—	11.64	
124341.18 + 615422.95	12,152	7.87	0.510	0.118	13,322	8.93	1.157	-5.163	—	19.12	1
124356.53 + 153727.60	27,677	8.16	0.702	0.401	24,445	8.31	0.791	< -4.171	—	7.91	
124403.03 + 444532.01	14,801	8.10	0.647	0.097	15,107	7.97	0.572	-6.234	—	23.75	
124415.10 + 201657.29	15,140	8.09	0.644	0.068	15,554	8.00	0.589	-5.302	—	30.48	
124451.37 - 001045.70	13,249	8.16	0.684	0.276	13,695	7.42	0.322	< -6.100	—	5.08	
124519.55 - 084525.70	16,431	7.80	0.485	0.151	16,951	7.81	0.490	-5.883	—	18.31	
124634.59 + 160542.00	15,965	8.29	0.769	0.506	17,120	7.86	0.514	-4.643	—	4.57	
124703.28 + 493423.60	15,419	7.97	0.576	0.009	15,734	7.97	0.575	-5.178	-7.50	64.12	
124746.77 + 470550.80	20,345	8.01	0.605	0.150	17,676	7.98	0.581	< -5.488	—	9.37	
124805.25 + 515830.30	15,668	8.02	0.604	0.114	15,449	8.39	0.837	< -5.924	—	8.05	
124810.23 + 100541.20	15,677	8.10	0.651	0.022	15,210	7.79	0.479	-5.170	-7.00	35.65	
124845.85 + 365937.40	15,977	8.86	1.120	0.253	16,517	8.57	0.957	< -5.643	—	3.78	
124847.81 - 001846.03	23,239	7.74	0.470	0.233	22,383	8.09	0.652	< -4.676	—	17.72	
124854.93 + 015908.70	24,983	7.74	0.476	0.203	19,614	7.98	0.585	< -5.105	—	13.11	
124920.37 + 290454.20	17,429	8.31	0.788	0.081	16,314	8.01	0.598	< -6.038	—	17.88	
125019.38 + 324910.80	18,909	7.05	0.252	0.994	15,323	7.45	0.336	< -5.839	—	4.69	
125030.21 + 594932.90	14,844	7.67	0.421	0.141	15,831	8.00	0.588	-5.963	—	16.94	2
125132.70 + 621918.30	15,878	7.86	0.515	0.034	16,483	8.09	0.646	-5.914	—	16.42	
125138.06 + 490053.60	15,115	7.96	0.564	0.087	16,055	8.12	0.666	< -5.941	—	13.35	
125140.10 + 284955.16	14,999	7.95	0.561	0.046	15,881	8.11	0.657	-3.913	—	45.00	
125205.66 + 662902.80	12,717	8.05	0.613	0.041	11,487	7.48	0.336	< -6.182	—	11.55	1
125218.69 + 563727.40	20,351	8.65	1.003	0.291	18,708	8.18	0.702	-4.178	—	4.12	

TABLE C.1 (Suite)

Nom SDSS	T_{eff}	$\log g$	M	σ_{π}/π	T_{eff}	$\log g$	M	$\log \text{H/He}$	$\log \text{Ca/He}$	S/N	Notes
125246.32 + 035347.80	16,951	8.10	0.650	0.217	17,554	8.00	0.594	-5.054	—	9.15	
125304.22 + 093855.80	—	—	—	—	17,405	8.21	0.721	< -5.550	—	9.21	
125305.82 + 612955.40	17,196	8.08	0.639	0.179	16,249	7.95	0.560	-5.261	—	9.24	
125337.68 + 393725.30	—	—	—	—	18,569	7.88	0.532	< -5.164	—	4.30	
125410.02 + 121406.58	14,539	8.08	0.637	0.038	14,378	8.00	0.591	-5.768	—	38.09	
125424.62 + 582500.14	15,264	8.25	0.745	0.102	15,678	8.38	0.830	-5.262	—	21.35	
125433.77 + 423738.40	15,115	8.05	0.621	0.628	13,758	8.31	0.780	< -6.010	—	3.61	
125503.10 + 252221.79	11,581	7.98	0.572	0.071	11,865	8.46	0.878	< -6.531	—	27.55	1
125511.88 + 485117.60	18,374	8.00	0.594	0.345	16,784	7.72	0.445	< -5.805	—	13.82	
125524.52 + 151758.00	11,829	8.03	0.603	0.028	10,853	7.41	0.310	-5.894	—	21.17	1
125533.02 + 195253.00	12,734	8.54	0.932	0.239	13,223	7.91	0.535	-5.998	—	8.17	
125609.61 + 552209.60	15,884	8.09	0.647	0.236	16,554	8.03	0.610	< -5.635	—	3.81	
125634.22 + 181348.90	12,165	8.15	0.674	0.303	12,785	8.20	0.706	-5.790	—	5.07	1
125724.13 + 592236.00	13,108	8.00	0.584	0.024	14,233	8.22	0.725	-5.314	—	40.57	
125743.69 + 252846.60	14,673	8.82	1.103	0.190	14,445	7.13	0.250	-4.052	—	6.24	
125751.83 + 263621.50	19,659	7.88	0.529	0.199	20,780	7.98	0.589	< -4.820	—	13.61	
125752.77 + 425255.10	16,065	8.10	0.648	0.013	16,015	8.07	0.633	-5.576	-7.50	45.27	
125759.04 - 021313.40	26,740	7.88	0.546	0.304	21,785	7.89	0.541	-3.678	—	8.22	
125901.54 + 303238.80	13,011	8.00	0.583	0.062	12,917	7.71	0.433	-5.129	—	16.93	
125905.60 + 021918.10	14,262	8.99	1.183	0.238	15,387	7.32	0.298	< -5.831	—	4.90	
125914.25 + 505218.59	—	—	—	—	12,707	6.89	0.197	< -6.139	—	5.15	1
125955.17 + 240541.71	12,079	8.14	0.673	0.056	11,276	7.62	0.390	< -6.473	—	20.51	1
130041.85 + 234038.30	—	—	—	—	15,269	7.75	0.458	-3.875	—	19.38	
130106.26 + 023455.30	17,660	7.73	0.454	0.189	17,706	8.29	0.773	-5.570	—	11.84	2
130153.12 + 233106.13	15,181	7.85	0.508	0.107	15,324	7.99	0.586	-5.933	—	25.47	
130217.70 + 165008.60	20,757	8.53	0.930	0.098	19,848	8.34	0.810	-4.402	—	10.04	
130219.93 + 020322.80	17,238	8.16	0.692	0.139	15,466	7.58	0.383	-5.937	—	11.17	
130338.01 - 031348.60	13,301	7.52	0.354	0.179	12,350	7.84	0.495	-5.751	—	9.74	1
130423.67 + 425331.40	12,791	8.60	0.968	0.331	14,233	6.47	0.131	-5.151	—	2.31	
130435.24 + 281821.50	19,148	6.52	0.197	1.768	17,515	8.36	0.821	< -5.525	—	6.00	
130516.52 + 405640.90	23,730	7.97	0.590	0.030	21,672	8.09	0.651	< -4.975	—	23.88	
130541.22 + 081540.90	21,932	7.99	0.597	0.027	24,027	7.92	0.562	< -4.687	—	37.02	
130547.70 + 423837.80	—	—	—	—	17,936	9.03	1.201	< -5.326	—	3.30	
130633.62 + 645233.90	27,702	7.65	0.445	0.976	38,546	7.31	0.376	-2.732	—	5.14	
130728.60 + 144417.05	14,357	8.03	0.607	0.014	14,563	7.93	0.547	-4.894	—	60.15	
130742.44 + 622956.80	23,103	8.04	0.625	0.092	22,975	7.87	0.532	< -4.463	—	13.61	
130805.80 + 211817.10	25,711	7.96	0.588	0.321	23,411	7.57	0.405	< -4.296	—	6.74	
130805.82 + 024409.40	12,949	8.08	0.634	0.356	13,087	8.29	0.768	-5.592	—	5.92	1
130830.53 + 470017.90	14,705	7.68	0.423	0.099	17,109	7.90	0.539	< -5.737	—	14.48	2
130911.16 - 013946.80	18,840	7.97	0.582	0.062	18,072	8.21	0.721	< -5.661	—	17.52	
130947.54 + 121241.80	12,528	8.08	0.636	0.061	13,389	8.73	1.047	-5.702	—	19.62	

TABLE C.1 (Suite)

Nom SDSS	T_{eff}	$\log g$	M	σ_{π}/π	T_{eff}	$\log g$	M	$\log \text{H/He}$	$\log \text{Ca/He}$	S/N	Notes
131009.73 + 240357.40	13,131	7.99	0.583	0.057	12,709	7.67	0.415	< -6.246	—	14.87	
131012.29 + 444728.40	12,110	8.18	0.697	0.018	12,656	8.36	0.813	-5.343	—	20.56	
131038.32 + 063406.60	14,434	8.02	0.599	0.062	14,405	8.06	0.627	< -6.289	—	18.68	
131055.30 + 680255.23	12,226	8.12	0.659	0.060	12,328	8.06	0.624	-5.371	—	17.93	1
131119.92 + 275812.65	16,355	7.97	0.574	0.123	17,712	8.04	0.616	< -5.950	—	23.59	
131130.50 + 124843.42	10,779	8.08	0.628	0.011	11,647	8.36	0.809	-5.963	—	45.80	1
131133.00 + 485812.20	12,257	7.99	0.576	0.038	13,721	8.90	1.141	-6.220	—	15.25	
131148.50 + 053847.60	20,450	8.13	0.674	0.040	23,470	8.14	0.687	-4.734	—	27.66	
131303.43 + 621432.40	16,277	8.68	1.021	0.269	35,995	7.43	0.396	-2.000	—	4.64	
131329.44 + 613359.72	19,620	8.26	0.753	0.070	17,358	8.19	0.707	-4.865	—	26.08	
131343.91 + 570404.05	18,453	8.23	0.733	0.041	17,413	8.18	0.704	-3.924	—	35.76	
131349.21 + 503724.09	17,964	8.07	0.634	0.094	18,014	8.13	0.671	< -5.876	—	21.85	
131350.38 + 254457.50	14,760	7.87	0.515	0.121	15,108	7.77	0.465	< -6.077	—	11.86	
131351.28 + 124009.20	31,694	8.45	0.889	0.008	18,120	7.97	0.578	-3.345	—	58.44	
131351.71 + 051054.42	32,476	7.99	0.614	0.220	32,393	7.86	0.549	-3.293	—	30.80	
131402.01 + 635552.00	13,164	8.02	0.600	0.019	13,426	7.90	0.529	-6.003	—	24.59	
131425.19 + 083648.88	11,883	7.77	0.458	0.106	12,187	8.10	0.645	-5.532	—	17.35	1
131426.25 + 341028.90	18,345	8.17	0.696	0.123	20,467	8.04	0.624	< -4.778	—	8.79	
131446.17 + 483124.90	19,803	8.10	0.655	0.097	16,920	8.13	0.672	< -5.777	—	11.22	
131536.30 + 162415.40	16,297	7.72	0.445	0.026	17,524	8.41	0.849	-5.044	—	20.52	
131618.55 + 161332.05	20,306	8.01	0.602	0.050	19,009	8.14	0.681	-5.451	—	27.27	
131646.02 + 414639.00	22,227	8.01	0.606	0.022	22,743	8.03	0.620	< -4.827	—	35.84	
131658.16 + 305148.00	18,987	7.85	0.517	0.163	19,635	8.27	0.759	-4.448	—	13.36	2
131717.02 - 021945.60	19,262	8.11	0.659	0.086	17,861	8.13	0.673	< -5.565	—	14.74	
131717.75 + 391719.60	19,752	7.43	0.345	0.800	20,454	7.99	0.590	< -4.898	—	10.70	
131730.99 + 014314.80	15,951	8.08	0.637	0.546	15,237	7.74	0.453	< -5.850	—	4.82	
131754.12 + 023741.90	25,345	5.59	0.054	2.337	28,566	8.05	0.639	< -3.589	—	7.37	
131826.31 + 290934.06	11,524	8.01	0.590	0.052	11,903	7.93	0.544	-6.136	—	42.39	1
131905.61 + 145123.50	15,581	8.22	0.728	0.158	15,905	8.34	0.801	-4.738	—	10.65	
131928.37 + 411825.80	14,106	7.69	0.426	0.075	15,162	8.62	0.987	-4.021	—	12.09	
131930.81 + 333554.53	15,224	8.06	0.627	0.064	15,165	8.05	0.620	-5.824	—	29.35	
131953.38 + 430202.00	17,182	8.04	0.615	0.113	17,379	7.93	0.555	< -5.678	—	11.30	
132004.27 + 664535.70	15,951	8.09	0.641	0.051	16,037	8.09	0.646	< -6.274	—	23.17	
132016.62 + 504005.40	19,512	7.85	0.515	0.144	17,833	8.17	0.694	-5.536	—	11.97	
132029.02 + 174756.18	15,141	7.98	0.576	0.105	14,747	7.71	0.437	-5.725	—	24.03	
132048.84 + 221210.98	11,935	8.66	1.007	0.141	14,169	9.32	1.302	< -6.067	—	5.97	
132053.99 + 135043.10	13,255	7.98	0.574	0.015	13,514	7.88	0.519	-5.646	—	35.69	
132251.69 + 165604.20	16,235	8.03	0.606	0.024	16,437	8.09	0.646	-5.716	—	34.99	
132301.28 + 355924.50	15,555	8.30	0.776	0.074	15,902	8.13	0.667	-5.533	—	14.66	
132303.26 + 332628.43	19,548	8.08	0.645	0.193	18,475	8.08	0.643	-5.277	—	19.33	
132332.78 + 362032.00	18,577	8.07	0.634	0.047	17,854	8.15	0.683	< -5.916	—	23.54	

TABLE C.1 (Suite)

Nom SDSS	T_{eff}	$\log g$	M	σ_{π}/π	T_{eff}	$\log g$	M	$\log \text{H/He}$	$\log \text{Ca/He}$	S/N	Notes
132350.28 + 272744.14	18,035	8.09	0.650	0.087	18,571	8.19	0.707	-5.003	—	28.98	
132358.62 + 280330.42	23,555	7.39	0.349	0.298	24,054	8.16	0.697	< -4.484	—	16.72	
132430.42 + 055316.33	—	—	—	—	16,693	8.04	0.613	-5.942	—	31.41	
132452.67 + 144135.30	13,489	8.09	0.638	0.063	13,622	7.75	0.453	-6.127	—	21.79	
132517.97 + 463208.00	18,371	8.17	0.696	0.253	15,687	7.19	0.268	-5.423	—	5.40	
132644.21 + 314402.66	16,467	7.79	0.479	0.134	17,077	8.07	0.632	< -5.894	—	19.89	
132712.19 + 631044.91	22,727	7.94	0.571	0.166	18,432	8.15	0.684	-3.788	—	21.25	
132732.31 + 111956.42	—	—	—	—	12,175	7.86	0.509	< -6.049	—	2.55	1
132742.39 + 153118.48	13,058	8.14	0.668	0.130	14,020	8.57	0.949	-5.334	—	19.37	
132752.91 + 253145.00	40,128	7.77	0.522	0.284	39,063	7.60	0.457	-3.046	—	12.04	
132800.53 + 061542.01	16,474	7.99	0.586	0.014	17,312	8.13	0.672	-5.331	—	72.99	
132833.43 + 045637.40	11,833	8.02	0.596	0.061	11,631	7.50	0.344	-5.845	—	18.03	1
132840.62 + 260458.10	11,533	7.93	0.545	0.036	12,178	8.44	0.864	-5.612	—	30.80	1
132909.67 + 231454.35	19,721	8.18	0.706	0.104	20,439	8.07	0.638	-4.076	—	24.02	
132941.36 + 375322.10	18,288	8.25	0.749	0.113	17,583	8.12	0.668	-5.438	—	19.16	
132944.39 + 002836.40	21,793	7.75	0.471	0.551	16,811	7.92	0.550	-4.966	—	3.98	
133015.67 + 354742.14	11,583	8.04	0.608	0.007	11,935	8.07	0.627	-5.586	—	80.93	1
133021.16 + 222904.74	18,595	8.06	0.630	0.101	17,016	7.96	0.570	-6.001	—	26.85	
133025.03 + 284811.70	12,908	8.34	0.802	0.189	14,406	7.80	0.481	< -6.045	—	7.55	
133032.11 + 551635.00	13,188	8.03	0.603	0.126	14,732	8.82	1.101	< -6.011	—	5.68	
133048.27 + 560805.80	19,877	8.10	0.654	0.067	17,811	7.93	0.558	< -5.577	—	14.86	
133127.86 + 420044.50	18,830	8.38	0.835	0.111	18,666	8.33	0.802	-4.522	—	9.80	
133152.50 - 000445.21	13,024	7.79	0.472	0.137	11,854	7.96	0.562	-5.291	—	19.74	1
133159.27 + 574508.87	13,508	7.95	0.558	0.005	14,301	7.91	0.539	-5.190	—	61.29	
133208.34 + 211709.28	11,669	8.05	0.613	0.022	11,295	7.67	0.413	-5.916	—	38.31	1
133215.95 + 640656.30	21,271	8.23	0.737	0.077	20,182	7.92	0.553	-4.896	—	15.14	
133236.47 + 185734.90	17,873	8.21	0.723	0.588	17,070	8.17	0.696	< -5.625	—	5.77	
133245.33 + 185012.90	18,090	7.67	0.429	0.458	17,700	7.63	0.412	-4.762	—	8.65	
133305.34 + 325360.00	—	—	—	—	13,845	8.13	0.668	< -6.201	-6.50	10.66	
133306.98 + 634936.40	15,519	7.95	0.560	0.059	15,611	8.40	0.841	-5.052	-7.00	14.64	
133439.60 + 155948.80	16,850	8.04	0.618	0.008	17,023	8.13	0.670	-5.003	—	53.19	
133503.64 + 235900.70	13,125	8.19	0.703	0.102	12,697	7.25	0.270	< -6.246	—	10.95	
133717.52 + 083044.90	11,949	8.17	0.691	0.198	11,562	7.45	0.326	< -6.191	—	13.34	1
133740.75 + 213216.80	18,905	7.97	0.579	0.025	18,329	8.05	0.622	< -5.791	—	28.76	
133754.88 + 344911.20	19,019	8.04	0.620	0.062	22,494	8.18	0.707	-4.166	—	17.20	
133818.00 + 602254.71	18,469	7.92	0.552	0.047	18,559	8.10	0.657	< -5.726	—	27.96	
133819.07 + 624018.70	11,465	8.02	0.593	0.032	12,248	8.19	0.704	< -6.372	—	17.15	1
133834.97 + 505111.40	12,789	7.98	0.577	0.082	13,914	8.00	0.589	-5.554	—	8.50	
133836.18 + 133360.00	13,774	8.11	0.651	0.069	14,421	7.89	0.526	-5.094	-7.50	15.81	
133840.45 + 451543.21	12,528	7.76	0.456	0.092	13,044	8.11	0.653	-5.722	—	16.94	
134120.88 + 004204.70	15,365	8.76	1.064	0.391	14,771	7.68	0.426	-4.416	—	7.50	

TABLE C.1 (Suite)

Nom SDSS	T_{eff}	$\log g$	M	σ_{π}/π	T_{eff}	$\log g$	M	$\log \text{H/He}$	$\log \text{Ca/He}$	S/N	Notes
134126.36 + 570556.60	19,353	6.43	0.192	2.822	19,160	8.88	1.134	< -5.007	—	3.01	
134157.73 + 032424.17	17,825	7.98	0.581	0.142	16,927	8.16	0.689	-5.398	—	24.09	
134213.99 + 452055.20	17,573	8.20	0.718	0.012	16,499	8.08	0.641	-6.090	—	36.19	
134246.52 + 521921.20	14,411	7.90	0.532	0.119	14,310	7.47	0.341	-5.715	—	7.74	
134255.34 + 140131.90	17,985	7.24	0.287	0.958	18,171	8.24	0.740	< -5.367	—	6.91	
134257.98 + 415259.90	18,744	9.16	1.251	0.214	15,049	10.41	2.551	-5.591	—	3.15	
134311.80 + 224543.85	17,686	8.02	0.608	0.085	16,851	8.03	0.611	-6.068	—	37.49	
134315.81 + 100838.80	—	—	—	—	21,201	8.00	0.601	< -4.726	—	13.87	
134329.61 + 670733.10	13,216	8.15	0.680	0.076	14,300	8.11	0.654	-5.101	-7.50	18.49	
134417.06 + 281511.20	13,491	7.75	0.456	0.349	12,426	6.87	0.192	< -6.142	—	9.69	1
134437.65 + 183714.40	14,324	8.06	0.625	0.015	14,724	7.99	0.583	-5.356	—	50.30	
134449.10 + 105500.80	13,614	8.05	0.619	0.078	12,912	8.25	0.740	-5.274	—	12.27	
134510.51 + 215558.30	16,195	8.15	0.685	0.187	16,365	7.97	0.574	-5.604	—	8.91	
134524.92 - 023714.20	39,619	7.54	0.438	0.931	40,116	7.70	0.496	< -3.008	—	9.02	
134603.15 - 025727.90	16,252	8.15	0.685	0.190	15,643	7.82	0.493	-5.852	—	8.86	
134712.54 + 562110.70	11,232	7.95	0.555	0.020	11,056	7.56	0.365	-6.064	—	23.49	1
134839.62 + 645746.68	13,147	7.93	0.545	0.040	14,042	8.18	0.699	-6.254	—	24.46	
134849.25 + 203011.38	14,287	8.07	0.633	0.028	14,009	7.74	0.450	< -6.509	—	33.61	
134956.22 + 024309.40	13,964	8.11	0.653	0.048	14,253	8.05	0.617	-5.655	-7.50	18.23	
135008.57 + 051425.40	—	—	—	—	18,242	8.87	1.128	< -5.349	—	5.18	
135015.08 + 145408.00	20,158	7.87	0.527	0.324	17,263	7.89	0.534	< -5.704	—	11.02	
135042.51 + 615223.40	16,624	8.50	0.908	0.496	21,566	9.70	1.447	-2.000	—	3.04	
135115.58 + 395749.20	18,755	7.72	0.453	0.425	25,249	7.21	0.309	-2.000	—	4.43	
135116.60 + 190006.30	14,803	7.55	0.370	0.439	15,148	7.93	0.551	-5.891	-7.50	11.78	
135121.92 + 180411.90	18,840	7.84	0.511	0.150	20,083	8.08	0.647	< -5.320	—	33.44	
135142.59 + 342144.96	—	—	—	—	13,426	8.07	0.632	< -6.538	—	21.62	
135150.63 + 035718.07	—	—	—	—	13,866	6.52	0.138	-5.948	—	19.74	
135152.46 + 544627.50	16,360	7.78	0.474	0.323	18,286	8.60	0.975	-5.123	—	3.22	
135153.48 + 385652.30	15,280	8.15	0.682	0.115	14,979	7.76	0.461	< -6.093	—	13.57	
135224.27 + 203005.98	16,372	8.03	0.610	0.037	16,779	7.97	0.578	-5.991	—	38.96	
135228.45 + 342906.04	11,928	8.03	0.601	0.010	12,479	8.26	0.747	< -6.555	—	55.68	
135240.39 + 630901.90	12,451	8.33	0.791	0.274	14,601	6.95	0.218	< -5.928	-6.00	3.98	
135240.43 + 411943.23	12,115	8.13	0.666	0.059	12,977	8.62	0.982	< -6.241	—	14.92	1
135352.51 + 604918.60	18,621	8.24	0.742	0.306	18,006	7.88	0.526	< -5.408	—	6.69	
135532.42 + 001124.00	13,417	7.97	0.571	0.004	13,855	7.86	0.509	-5.372	—	83.75	
135541.21 + 351441.60	13,699	8.18	0.698	0.071	13,578	8.06	0.622	< -6.217	—	13.52	
135541.70 + 110031.80	21,224	7.80	0.497	0.093	24,295	7.75	0.479	-3.822	—	24.64	
135610.31 - 002230.60	20,737	8.22	0.729	0.197	18,230	8.28	0.765	-4.449	—	8.52	
135723.99 + 495903.30	14,684	7.89	0.528	0.012	15,293	7.91	0.541	-5.964	—	51.43	
135832.14 - 014519.90	13,918	7.60	0.389	0.299	14,278	8.34	0.804	< -6.057	—	5.83	
135908.14 + 411619.70	15,932	8.74	1.057	0.235	18,025	8.68	1.023	-3.909	—	3.41	

TABLE C.1 (Suite)

Nom SDSS	T_{eff}	$\log g$	M	σ_{π}/π	T_{eff}	$\log g$	M	$\log \text{H/He}$	$\log \text{Ca/He}$	S/N	Notes
135911.39 + 225212.32	22,236	8.49	0.905	0.190	21,729	8.14	0.681	-3.913	—	16.88	
135933.24 - 021715.20	16,372	8.04	0.615	0.033	16,304	7.70	0.438	-3.455	—	25.17	
135934.49 + 045942.30	19,413	7.40	0.336	0.316	19,183	8.14	0.680	< -5.212	—	11.41	
140001.73 + 363139.90	14,718	7.82	0.492	0.133	14,644	7.84	0.502	< -6.130	—	10.53	
140020.18 + 641237.00	17,438	8.01	0.596	0.173	16,110	8.11	0.656	-5.011	—	6.03	
140028.40 + 475644.56	27,933	7.91	0.565	0.022	32,229	8.02	0.630	< -3.755	—	46.95	
140035.81 + 341440.40	12,654	7.47	0.335	0.095	15,723	7.86	0.512	-5.338	—	17.41	
140115.57 + 601313.90	16,791	6.93	0.225	1.320	15,421	7.72	0.445	< -5.826	—	3.45	
140129.62 + 050130.79	16,870	8.08	0.642	0.089	17,170	8.06	0.630	-5.864	—	21.15	
140151.43 + 032946.60	19,974	8.72	1.047	0.504	35,023	7.99	0.616	-2.000	—	5.31	
140159.09 + 022126.70	34,863	7.97	0.609	0.470	37,878	7.45	0.407	-2.629	—	10.65	
140227.20 + 403922.30	16,271	7.98	0.579	0.028	16,075	7.86	0.513	< -6.268	—	33.12	
140229.38 + 602117.40	15,697	7.92	0.547	0.073	15,372	7.90	0.532	-5.633	—	13.72	
140235.99 - 014925.66	20,815	7.95	0.573	0.050	18,894	8.13	0.672	< -5.630	—	32.74	
140255.43 + 245313.49	12,621	7.85	0.501	0.126	13,023	8.05	0.613	< -6.549	—	20.05	
140255.58 + 573157.10	19,573	8.15	0.685	0.102	19,908	8.22	0.733	< -5.032	—	14.36	
140315.35 + 180437.10	13,683	7.75	0.455	0.264	13,835	7.45	0.330	-5.994	—	8.73	
140325.11 + 272533.02	10,995	8.07	0.625	0.015	11,396	8.05	0.612	-5.131	—	40.82	1
140336.35 + 195455.20	13,677	8.21	0.713	0.100	15,298	8.90	1.142	-3.979	-7.50	11.91	
140356.97 + 082047.08	16,512	8.00	0.593	0.074	15,844	7.94	0.558	< -6.305	—	34.14	
140404.37 + 030718.30	14,631	8.17	0.695	0.260	15,744	7.74	0.456	-5.061	—	7.08	
140438.26 + 275747.27	21,466	8.12	0.668	0.146	23,631	8.14	0.686	-3.258	—	17.20	
140441.32 + 182437.58	12,656	8.02	0.598	0.052	12,769	7.90	0.529	-5.515	—	24.20	
140458.60 + 175804.40	12,713	8.28	0.758	0.077	13,052	8.47	0.885	-5.281	—	21.29	
140502.10 + 380957.70	15,621	7.92	0.547	0.006	16,805	8.05	0.625	-5.626	—	55.95	
140555.56 + 110336.94	15,389	8.01	0.596	0.078	15,679	7.89	0.527	< -6.330	—	24.01	
140615.80 + 562725.90	38,704	7.57	0.446	0.135	14,342	8.50	0.907	-5.512	—	15.71	3
140616.63 + 194628.90	16,209	8.31	0.783	0.153	17,350	8.02	0.602	-4.972	—	8.96	
140619.96 - 011932.50	14,361	7.92	0.542	0.005	15,224	7.96	0.564	-6.168	—	82.87	
140645.47 + 552340.20	14,917	8.21	0.720	0.075	14,601	7.68	0.426	-5.613	—	12.70	
140647.76 + 314858.40	16,731	8.28	0.762	0.205	16,415	8.12	0.662	-5.498	—	7.29	
140733.05 + 620540.30	12,689	8.12	0.657	0.115	13,919	8.50	0.905	< -6.086	—	6.12	
140759.50 + 121533.95	19,574	8.26	0.758	0.074	18,411	8.10	0.652	-5.457	—	40.11	
140805.16 + 062326.45	15,381	7.93	0.549	0.124	14,729	8.06	0.628	-4.563	—	22.28	
140814.64 + 003838.90	27,797	8.00	0.611	0.287	26,078	7.85	0.531	-3.769	—	12.08	
140832.57 + 125426.39	13,892	8.02	0.602	0.067	13,250	7.65	0.408	-6.045	—	22.85	
140957.76 + 124352.80	14,419	8.00	0.590	0.068	14,263	7.74	0.452	-5.723	—	12.90	
141001.58 + 523842.05	18,033	7.65	0.421	0.743	17,545	8.22	0.726	< -5.518	—	8.49	
141023.40 + 120552.81	12,158	8.02	0.599	0.078	12,618	7.72	0.438	-6.071	—	23.48	
141029.97 + 285146.90	21,454	8.10	0.658	0.090	24,812	7.92	0.563	< -4.246	—	14.60	
141037.54 + 144544.78	13,546	8.17	0.691	0.110	14,928	8.75	1.062	-5.251	-7.50	16.29	

TABLE C.1 (Suite)

Nom SDSS	T_{eff}	$\log g$	M	σ_{π}/π	T_{eff}	$\log g$	M	$\log \text{H/He}$	$\log \text{Ca/He}$	S/N	Notes
141044.61 + 373544.80	—	—	—	—	29,593	7.77	0.499	< -3.962	—	23.49	
141048.84 + 342746.60	15,108	7.87	0.519	0.235	14,899	7.78	0.471	< -6.102	—	10.85	
141122.50 + 183036.97	19,041	7.92	0.550	0.204	16,896	8.21	0.723	-5.306	—	16.81	
141127.09 + 035429.70	38,245	8.00	0.631	0.052	37,068	7.70	0.486	< -3.548	—	48.09	
141214.58 + 544829.20	17,439	8.46	0.882	0.143	16,069	8.11	0.656	< -5.828	—	8.20	
141214.94 + 012422.70	19,670	8.22	0.731	0.174	24,074	7.87	0.537	< -4.341	—	10.93	
141218.72 + 102157.64	18,774	8.40	0.846	0.146	16,873	8.26	0.752	-5.190	—	17.84	
141258.17 + 045602.20	27,980	8.17	0.709	0.055	30,690	7.84	0.537	< -3.863	—	31.67	
141301.64 + 493957.40	16,572	7.94	0.556	0.013	17,135	8.01	0.601	< -6.073	—	41.40	
141306.65 + 354928.10	13,982	7.84	0.499	0.158	15,140	8.42	0.854	-4.402	-7.50	15.28	
141322.31 + 343047.10	19,831	8.18	0.706	0.096	20,092	8.04	0.620	< -4.987	—	13.20	
141329.16 + 422522.90	13,160	8.35	0.807	0.156	14,713	8.45	0.872	< -6.013	—	5.74	
141337.74 + 450431.60	19,841	7.46	0.356	0.168	24,983	8.01	0.611	< -4.222	—	10.95	2
141349.46 + 571716.40	27,625	8.18	0.718	0.069	30,058	7.88	0.552	< -3.915	—	29.38	
141431.59 - 024008.10	11,185	8.07	0.625	0.039	13,451	9.19	1.260	< -6.352	—	18.76	1
141445.48 + 563345.00	15,408	8.04	0.611	0.029	15,183	7.92	0.544	< -6.398	—	37.52	
141539.63 + 185851.50	—	—	—	—	12,804	7.47	0.337	-4.606	—	28.61	
141551.69 + 603308.00	13,551	8.05	0.615	0.111	13,181	7.83	0.490	-3.956	—	8.44	
141621.79 + 322638.60	31,289	7.50	0.402	0.122	35,428	7.65	0.466	< -3.407	—	19.12	2
141739.30 + 081541.26	26,677	8.29	0.784	0.215	22,828	7.91	0.554	< -4.818	—	20.56	
141755.35 + 231136.90	17,031	8.11	0.661	0.013	17,836	8.26	0.755	-4.959	—	44.95	
141759.32 + 010725.64	16,434	7.96	0.571	0.145	17,326	8.02	0.604	< -6.035	—	22.37	
141803.55 + 200053.70	19,958	8.30	0.785	0.137	17,089	8.11	0.661	< -5.741	—	14.76	
141825.85 + 224132.39	16,366	7.97	0.577	0.017	17,516	8.09	0.644	-5.887	—	61.14	
141834.59 + 304215.30	13,824	7.53	0.359	0.414	13,313	8.06	0.625	< -6.118	—	7.24	
141844.96 + 563225.90	19,843	8.01	0.606	0.528	18,416	8.28	0.769	-4.602	—	8.32	
141854.18 + 125404.60	17,551	8.09	0.649	0.060	15,970	8.01	0.596	< -6.095	—	18.48	
141859.77 + 034026.76	13,776	8.06	0.622	0.031	14,313	7.91	0.535	-5.413	—	31.21	
141915.95 + 204535.60	16,422	7.15	0.261	2.111	16,734	7.71	0.441	< -5.597	—	4.68	
141920.96 + 411254.76	14,398	8.09	0.641	0.067	14,153	7.84	0.500	< -6.309	—	19.64	
142016.53 + 142618.70	16,158	8.28	0.764	0.239	16,118	8.11	0.658	< -5.819	—	7.97	
142028.89 + 303042.50	17,482	8.86	1.120	0.205	18,098	8.54	0.936	< -5.386	—	6.83	
142202.88 - 020251.90	15,851	8.18	0.699	0.051	15,900	7.96	0.565	-5.536	—	25.63	
142204.29 + 345457.49	12,101	8.12	0.655	0.007	12,634	8.27	0.752	-5.348	—	68.79	
142240.81 + 334807.95	23,964	7.85	0.526	0.068	23,211	8.02	0.615	-4.643	—	27.87	
142258.01 + 522925.80	12,090	7.54	0.359	0.120	15,356	7.80	0.483	-4.408	-6.00	7.64	
142307.87 + 362454.00	13,197	8.01	0.594	0.026	13,428	8.01	0.592	-5.336	—	43.17	
142321.79 + 592307.10	15,530	8.04	0.613	0.071	15,495	8.30	0.775	-5.484	—	11.17	
142352.93 + 141133.50	14,056	8.16	0.687	0.631	14,425	6.95	0.217	< -5.948	—	3.40	
142356.36 + 362336.00	22,547	8.02	0.616	0.035	22,522	8.09	0.655	-4.705	—	28.12	
142405.54 + 181807.40	24,781	8.07	0.644	0.149	30,234	7.97	0.597	< -3.700	—	15.17	

TABLE C.1 (Suite)

Nom SDSS	T_{eff}	$\log g$	M	σ_{π}/π	T_{eff}	$\log g$	M	$\log \text{H/He}$	$\log \text{Ca/He}$	S/N	Notes
142437.63 + 600650.20	15,390	7.90	0.533	0.168	15,916	8.55	0.939	-5.437	—	6.22	
142446.24 + 322930.37	21,974	8.36	0.824	0.104	19,376	8.41	0.854	-5.093	—	21.25	
142455.90 + 491420.00	12,194	7.94	0.551	0.170	11,919	7.10	0.233	-5.078	—	5.41	1
142505.18 + 335948.50	14,597	8.30	0.775	0.320	14,408	7.49	0.349	< -6.045	—	5.56	
142516.05 + 500926.00	25,833	7.99	0.604	0.121	20,846	8.07	0.640	< -4.805	—	10.75	
142608.21 + 182059.75	12,041	8.03	0.600	0.164	14,184	9.12	1.237	-5.202	—	15.42	
142632.08 + 455639.70	12,165	7.98	0.573	0.089	12,294	7.95	0.558	-5.891	—	14.83	1
142640.91 + 101816.40	—	—	—	—	15,096	7.67	0.421	< -6.078	—	10.98	
142810.12 + 103953.70	14,857	7.89	0.531	0.024	16,341	8.01	0.598	-5.778	—	21.78	
142825.08 + 051031.10	16,401	7.92	0.550	0.024	17,555	8.17	0.694	-4.985	—	47.12	
142833.01 + 161922.94	15,816	8.34	0.806	0.163	15,159	8.02	0.604	-5.735	—	19.51	
142842.83 + 600300.63	14,527	8.05	0.618	0.051	14,207	8.06	0.621	< -6.173	—	14.99	
142851.08 - 005717.30	20,941	7.62	0.417	0.486	21,833	8.43	0.871	< -4.397	—	3.85	
142907.91 + 254214.16	11,121	8.27	0.750	0.046	11,352	7.98	0.573	-6.348	—	22.49	1
142925.02 + 083218.70	—	—	—	—	26,232	7.83	0.522	< -4.034	—	12.06	
142959.75 + 143958.30	23,947	8.26	0.758	0.250	21,877	7.78	0.488	-3.152	—	10.97	
143149.25 + 235100.11	24,064	8.13	0.679	0.046	22,928	7.99	0.595	< -4.808	—	35.92	
143227.25 + 363215.20	27,829	8.20	0.730	0.116	32,041	7.75	0.496	< -3.417	—	12.48	
143235.28 + 525748.22	—	—	—	—	17,287	8.61	0.979	< -5.477	—	4.18	
143239.60 - 020315.83	14,169	8.15	0.676	0.117	13,289	7.96	0.565	-5.910	—	18.38	
143350.80 + 071452.22	11,449	7.99	0.578	0.013	16,220	9.38	1.317	-4.964	-6.00	53.90	4
143452.22 + 091835.35	13,206	7.88	0.520	0.091	13,281	8.06	0.620	< -6.543	—	26.55	
143458.86 + 121404.99	17,518	7.93	0.552	0.113	17,236	8.10	0.651	-5.390	—	23.54	
143638.26 + 320523.70	13,697	7.91	0.539	0.140	15,914	8.52	0.918	< -5.854	—	8.02	
143639.51 - 011517.80	12,715	8.33	0.791	0.113	13,209	8.16	0.682	< -6.233	—	12.91	
143732.94 + 172557.04	17,472	8.04	0.616	0.010	17,789	8.18	0.701	-5.333	—	60.08	
143739.13 + 315248.80	25,443	9.23	1.276	0.141	51,647	8.36	0.855	< -3.010	—	5.73	
143744.78 + 333656.26	12,079	7.83	0.492	0.175	11,697	7.58	0.372	-5.587	—	7.72	1
143802.78 + 144137.54	18,567	8.08	0.641	0.104	18,470	8.15	0.688	-4.759	—	28.67	
143846.21 + 280455.90	15,325	7.83	0.498	0.130	16,362	7.95	0.565	< -5.886	—	13.14	
143903.94 - 003119.40	19,014	7.63	0.415	0.803	15,148	7.73	0.449	< -5.962	—	8.03	
143936.57 + 571414.80	12,650	7.83	0.489	0.224	16,599	9.94	1.654	< -5.726	—	5.09	
144021.59 + 172033.17	8,837	8.78	1.076	0.047	12,679	8.79	1.083	-5.440	—	11.20	1
144100.60 + 043047.20	18,503	8.29	0.771	0.242	17,680	7.97	0.580	-4.198	—	9.27	
144139.08 + 485448.33	19,734	8.16	0.694	0.060	18,184	8.14	0.682	< -5.831	—	21.75	
144205.41 + 122926.80	33,645	7.99	0.618	0.091	32,824	7.79	0.514	< -3.720	—	26.51	
144212.69 + 105107.30	14,862	8.13	0.666	0.026	14,771	8.10	0.648	-6.376	—	24.78	
144230.11 + 083147.20	—	—	—	—	16,902	8.10	0.651	-5.554	—	17.94	
144316.83 + 471335.90	13,312	8.00	0.584	0.217	11,885	7.16	0.245	< -6.122	—	5.97	1
144412.83 + 035807.80	13,268	8.01	0.595	0.238	13,956	8.96	1.172	-5.437	—	9.02	
144426.39 + 413521.44	12,885	7.97	0.569	0.090	13,333	8.07	0.627	-5.803	—	19.54	

TABLE C.1 (Suite)

Nom SDSS	T_{eff}	$\log g$	M	σ_{π}/π	T_{eff}	$\log g$	M	$\log \text{H/He}$	$\log \text{Ca/He}$	S/N	Notes
144428.15 + 162717.60	14,748	7.86	0.511	0.184	15,512	8.05	0.619	-5.980	—	13.67	
144518.03 + 585032.20	13,527	8.01	0.593	0.022	14,185	7.87	0.517	< -6.497	-7.50	25.27	
144601.02 + 625733.80	20,878	8.20	0.720	0.175	17,922	8.34	0.806	< -5.429	—	7.00	
144650.87 + 285142.30	22,944	7.22	0.303	0.231	22,817	7.94	0.569	< -4.479	—	12.47	2
144651.48 - 002942.00	17,853	8.12	0.665	0.179	15,814	8.25	0.748	-4.631	—	18.86	
144700.58 + 112613.14	11,147	7.95	0.554	0.058	13,225	9.25	1.280	-4.941	—	22.66	
144814.33 + 150449.70	19,143	7.95	0.565	0.007	21,020	8.08	0.648	< -5.106	—	66.91	
144816.68 + 632419.27	20,308	8.02	0.610	0.026	19,022	8.14	0.678	-5.545	—	28.13	
144819.48 + 322500.89	18,609	7.80	0.488	0.226	23,561	8.05	0.631	-2.000	—	17.66	
144824.12 + 101501.58	—	—	—	—	12,575	6.42	0.090	-5.760	—	15.06	1
144826.45 + 630835.30	14,930	8.09	0.643	0.017	15,125	7.98	0.580	< -6.405	—	21.83	
144837.56 + 150538.29	15,324	8.21	0.720	0.035	15,205	8.13	0.669	-5.381	—	32.71	
144912.54 + 170150.56	20,041	7.90	0.541	0.057	22,293	8.06	0.634	-4.712	—	39.31	
144930.58 + 445719.44	18,101	8.09	0.648	0.119	17,688	7.79	0.480	-5.172	—	16.45	
144936.84 + 093739.80	19,204	7.90	0.540	0.143	19,265	8.15	0.689	-4.909	—	17.94	
144939.14 + 494436.72	14,605	8.13	0.670	0.082	14,368	7.97	0.572	-5.987	—	16.23	
144947.79 + 205254.30	19,569	8.04	0.622	0.185	23,804	7.84	0.520	-3.898	—	11.92	
144952.03 + 133817.92	11,458	8.12	0.654	0.040	12,365	8.52	0.921	-6.181	—	25.14	1
145023.39 - 005441.00	13,090	8.02	0.600	0.074	14,061	8.40	0.845	-6.181	—	18.63	
145030.62 - 020301.80	21,510	8.49	0.910	0.191	20,127	8.13	0.678	-4.773	—	7.19	
145031.30 + 600101.40	14,827	7.95	0.559	0.076	15,143	8.02	0.603	< -6.213	—	15.40	
145213.98 + 134633.50	12,551	8.23	0.728	0.117	14,770	8.99	1.185	-5.653	-7.50	11.49	
145240.49 + 614526.40	17,185	7.96	0.568	0.038	18,469	8.26	0.752	-4.419	—	21.47	
145325.98 + 294912.80	13,835	8.00	0.587	0.021	14,517	7.84	0.502	-5.968	—	25.29	
145329.41 + 363612.90	12,761	7.96	0.562	0.042	12,745	7.88	0.521	< -6.376	—	16.48	
145334.46 + 020840.40	19,440	8.20	0.715	0.368	15,372	8.05	0.621	-4.794	—	7.07	
145349.09 + 195201.60	16,705	7.95	0.566	0.093	16,975	7.86	0.516	< -5.915	—	15.52	
145437.06 + 445523.59	11,698	8.05	0.613	0.091	12,273	8.16	0.685	-5.614	—	16.77	1
145448.79 + 434644.40	15,888	8.34	0.801	0.295	18,156	9.20	1.266	-4.062	—	3.62	
145452.84 + 084640.66	14,632	8.03	0.606	0.017	15,287	7.91	0.541	-6.303	—	53.70	
145514.37 + 044153.40	17,460	8.26	0.756	0.144	16,014	7.92	0.545	< -5.948	—	13.31	
145534.04 + 103846.68	12,907	8.09	0.640	0.100	12,296	7.76	0.455	-6.183	—	18.80	1
145553.96 + 130123.50	16,569	7.87	0.523	0.251	17,532	7.94	0.558	< -5.521	—	7.26	
145634.43 + 413407.40	12,898	7.67	0.415	0.162	14,433	8.68	1.021	< -6.042	—	6.22	
145644.91 + 011017.50	17,052	7.92	0.547	0.239	17,189	7.99	0.586	< -5.720	—	12.93	
145649.52 + 573029.80	17,262	6.95	0.231	0.911	29,611	7.80	0.512	< -3.377	—	4.67	
145746.31 + 330944.95	15,029	6.76	0.192	0.269	19,655	8.15	0.689	-4.207	—	28.62	
145755.43 + 015442.95	19,092	7.86	0.523	0.125	20,272	8.15	0.686	-5.181	—	47.86	
145818.51 + 102632.96	11,868	8.06	0.622	0.060	12,377	8.05	0.616	-5.330	—	36.38	
145822.52 + 435905.80	18,988	8.17	0.698	0.014	20,326	8.26	0.755	-4.237	—	32.52	
145832.12 + 471955.80	13,574	8.07	0.629	0.102	13,996	7.99	0.582	-4.631	-7.00	9.56	

TABLE C.1 (Suite)

Nom SDSS	T_{eff}	$\log g$	M	σ_{π}/π	T_{eff}	$\log g$	M	$\log \text{H/He}$	$\log \text{Ca/He}$	S/N	Notes
145832.63 + 100818.10	23,738	8.00	0.606	0.017	24,370	7.87	0.537	-3.192	—	52.03	
145900.87 + 202221.20	15,125	7.51	0.356	0.100	16,318	8.03	0.608	-5.628	—	16.53	
145907.71 + 553116.50	13,779	8.04	0.609	0.047	14,333	8.25	0.742	-4.943	—	15.43	
145931.20 + 613502.77	18,543	8.04	0.621	0.085	18,082	8.29	0.776	-5.209	—	22.84	
145935.23 + 192818.59	12,970	8.13	0.668	0.056	12,333	8.06	0.623	-6.106	—	27.35	
145940.78 + 244554.20	12,535	7.99	0.577	0.006	13,300	7.91	0.534	-5.922	—	60.30	
145944.22 + 013654.50	14,059	8.67	1.016	0.572	18,651	8.65	1.005	-4.099	—	3.64	
145947.04 - 003954.60	16,861	8.04	0.617	0.090	16,068	7.89	0.531	< -6.079	—	17.17	
145955.85 + 484401.20	12,276	7.97	0.567	0.056	13,442	8.26	0.751	< -6.224	—	11.16	
145959.63 + 103131.48	—	—	—	—	10,276	6.02	-1.197	-5.301	—	7.68	1
150003.86 + 002420.00	12,663	8.18	0.693	0.089	14,118	8.33	0.794	< -6.181	—	14.34	
150042.53 + 061304.30	11,614	8.11	0.652	0.092	12,228	8.32	0.786	-5.400	—	18.31	1
150101.49 + 272338.32	12,680	8.18	0.693	0.023	12,305	8.88	1.131	-5.379	—	26.54	1
150224.02 + 510229.00	13,178	8.45	0.875	0.141	12,775	7.49	0.342	< -6.137	—	5.85	1
150247.75 + 604020.20	12,313	7.71	0.435	0.158	12,651	7.30	0.283	-5.278	—	6.69	1
150300.35 - 021947.30	—	—	—	—	13,704	6.66	0.164	-5.479	—	9.54	
150301.95 + 053414.05	13,681	7.73	0.445	0.228	13,120	8.27	0.752	-5.705	—	16.42	2
150347.30 + 615847.40	15,354	8.16	0.689	0.179	17,244	7.97	0.577	-4.932	—	6.95	
150418.55 + 120026.30	14,225	8.03	0.605	0.021	14,910	8.02	0.603	-5.150	—	36.45	
150431.69 + 162453.50	15,364	7.90	0.533	0.019	17,096	8.06	0.630	< -6.081	—	33.37	
150435.35 + 013707.97	—	—	—	—	15,325	8.11	0.656	-5.708	—	14.86	
150506.24 + 383017.39	12,623	7.37	0.302	0.013	14,112	7.61	0.393	-5.049	—	43.53	3
150633.90 + 531929.60	15,934	8.03	0.611	0.076	16,077	8.27	0.756	-5.482	—	11.27	
150647.60 + 310313.30	18,682	7.65	0.420	0.170	18,530	8.00	0.593	< -5.388	—	10.79	2
150657.27 - 004610.59	13,831	8.05	0.615	0.086	13,474	7.91	0.535	-5.626	—	30.83	
150704.70 + 522941.80	15,003	8.07	0.634	0.200	14,502	7.80	0.480	< -6.035	—	5.35	
150850.96 + 013518.47	13,294	8.49	0.902	0.094	14,388	8.29	0.772	-5.300	—	21.76	
151005.05 + 050905.80	12,610	8.08	0.631	0.051	13,206	7.99	0.581	< -6.545	—	21.31	
151057.26 + 244332.30	15,871	8.09	0.643	0.161	17,736	8.38	0.829	< -5.474	—	9.11	
151212.40 + 155742.31	11,979	8.17	0.687	0.094	12,735	8.15	0.679	< -6.245	—	14.63	1
151248.06 + 575549.70	18,883	8.16	0.689	0.343	17,181	7.88	0.529	-4.837	—	5.20	
151317.27 - 003523.06	12,840	8.11	0.651	0.016	14,757	8.32	0.793	-3.984	—	53.88	
151428.74 + 112417.00	20,936	8.23	0.736	0.183	21,487	8.07	0.644	-4.525	—	13.59	
151451.36 + 123714.20	14,820	8.00	0.588	0.147	15,335	8.40	0.846	-5.077	—	10.38	
151549.79 + 463745.90	16,945	8.23	0.736	0.192	16,841	8.70	1.035	-3.948	—	7.07	
151642.97 - 004042.71	13,496	8.00	0.589	0.017	14,788	8.05	0.617	-4.534	-7.50	51.79	
151711.26 + 062035.50	18,580	6.82	0.219	1.897	24,410	8.18	0.709	< -4.176	—	9.80	
151729.46 + 433028.70	26,203	8.12	0.676	0.060	25,112	8.01	0.612	-4.045	—	21.64	
151800.52 + 370303.40	12,683	8.02	0.595	0.016	12,908	7.97	0.568	-5.625	—	29.28	
151840.51 + 491602.70	12,856	7.19	0.255	0.308	13,838	7.23	0.269	< -6.091	—	6.13	
151844.33 + 481713.50	21,789	7.34	0.328	0.732	23,037	8.65	1.006	< -4.236	—	3.51	

TABLE C.1 (Suite)

Nom SDSS	T_{eff}	$\log g$	M	σ_{π}/π	T_{eff}	$\log g$	M	$\log \text{H/He}$	$\log \text{Ca/He}$	S/N	Notes
151907.02 + 464521.50	19,837	8.03	0.615	0.142	25,285	8.00	0.608	< -4.179	—	10.66	
151911.88 + 373605.40	51,850	8.67	1.036	0.595	47,933	6.78	0.313	< -2.000	—	5.17	1
151954.85 + 375604.70	18,387	8.15	0.685	0.391	21,733	7.98	0.592	< -4.415	—	4.43	
152006.05 + 580037.00	17,509	7.60	0.398	0.168	18,172	7.95	0.564	< -5.367	—	7.91	
152048.23 + 153013.70	18,319	7.97	0.579	0.102	17,135	7.87	0.523	< -5.882	—	15.31	
152123.36 + 382519.25	11,254	8.01	0.591	0.054	12,361	7.79	0.471	-5.874	—	26.25	
152135.91 + 481508.00	19,120	8.04	0.620	0.114	19,826	8.03	0.614	< -4.934	—	9.32	
152211.51 + 404455.70	—	—	—	—	12,175	7.87	0.513	-5.505	—	19.41	1
152223.24 + 401021.40	17,755	8.65	1.005	0.321	19,254	8.55	0.945	-4.647	—	8.97	
152228.41 + 354908.44	12,213	8.08	0.632	0.096	12,417	8.24	0.734	-6.272	—	15.09	1
152235.04 + 165117.80	13,434	8.00	0.589	0.071	14,265	7.89	0.525	< -6.491	—	24.41	
152249.56 + 553354.00	15,118	7.79	0.479	0.100	15,348	7.86	0.515	-6.013	—	18.20	
152304.84 + 051157.60	13,345	8.12	0.661	0.043	14,277	7.98	0.577	< -6.300	—	17.81	
152320.96 + 005525.10	13,317	7.50	0.348	0.155	13,758	8.30	0.777	< -6.207	—	10.74	2
152338.21 + 381104.90	21,800	7.81	0.500	0.662	18,589	7.97	0.577	< -5.259	—	8.06	
152512.52 + 020305.73	16,397	7.80	0.485	0.361	15,514	7.93	0.551	-5.530	—	11.48	
152518.41 + 173349.00	12,342	7.88	0.518	0.024	13,542	7.75	0.454	-6.513	—	31.34	
152521.13 + 042111.02	14,656	8.07	0.631	0.243	14,802	8.02	0.602	-5.917	—	19.62	
152624.35 + 385239.90	—	—	—	—	23,647	8.42	0.865	-3.653	—	9.63	
152634.97 + 485801.30	—	—	—	—	12,640	8.28	0.763	-4.834	—	29.94	
152717.28 + 523358.70	24,318	7.66	0.440	0.321	27,329	8.31	0.796	< -3.642	—	4.99	
152718.20 + 414835.70	14,255	8.07	0.631	0.035	14,466	8.08	0.637	-6.057	—	14.50	
152727.08 + 233351.25	14,212	7.93	0.548	0.016	16,119	7.91	0.539	-5.987	—	56.95	
152728.84 + 204010.80	11,760	8.16	0.682	0.067	12,335	8.60	0.968	-5.511	—	17.44	1
152738.99 + 390552.20	11,898	7.08	0.228	0.750	15,290	8.14	0.676	< -5.944	—	7.53	
152739.56 + 314242.00	18,219	8.19	0.707	0.058	18,209	8.43	0.862	-5.208	—	15.39	
152808.20 + 213847.00	31,666	7.72	0.485	0.152	33,452	7.82	0.532	-2.660	—	11.95	
152836.18 + 362609.40	15,885	8.29	0.768	0.143	15,854	8.57	0.953	-5.679	—	7.60	
152843.28 + 412426.70	—	—	—	—	12,220	7.49	0.340	-5.471	—	6.21	1
152959.49 + 571548.70	19,321	8.25	0.751	0.401	27,558	8.65	1.010	< -3.609	—	3.80	
153006.10 + 264923.91	15,058	7.86	0.510	0.043	15,991	8.09	0.642	-4.884	—	40.81	
153010.84 + 362750.20	18,716	7.38	0.327	0.764	18,227	8.24	0.742	< -5.253	—	4.06	
153011.34 + 025129.90	27,631	8.15	0.701	0.236	29,151	7.98	0.605	-3.124	—	8.02	
153024.23 + 331549.72	18,154	7.77	0.475	0.096	17,544	8.18	0.704	-4.340	—	19.04	2
153035.52 + 072800.06	10,933	8.14	0.671	0.072	13,063	9.31	1.298	< -6.368	—	18.64	1
153104.46 + 150117.40	16,434	8.40	0.843	0.447	14,904	6.62	0.168	< -5.892	—	4.51	
153124.48 + 440420.21	12,955	8.00	0.584	0.049	13,501	7.79	0.474	-6.289	—	25.70	
153148.42 + 383911.00	17,527	8.08	0.641	0.152	18,267	8.35	0.814	-4.259	-6.00	14.02	
153223.82 + 272503.60	11,267	7.98	0.571	0.011	12,134	8.30	0.773	-5.051	—	39.74	1
153224.23 + 491454.10	—	—	—	—	14,087	8.10	0.648	-5.628	—	14.00	
153225.49 + 472700.90	16,038	7.33	0.302	0.236	16,514	8.09	0.647	-5.238	—	5.66	

TABLE C.1 (Suite)

Nom SDSS	T_{eff}	$\log g$	M	σ_{π}/π	T_{eff}	$\log g$	M	$\log \text{H/He}$	$\log \text{Ca/He}$	S/N	Notes
153236.90 + 491011.10	—	—	—	—	13,751	7.84	0.501	< -6.207	—	10.82	
153243.73 + 350052.90	—	—	—	—	11,645	7.20	0.253	< -6.200	—	10.86	1
153255.11 + 171901.86	12,449	7.96	0.561	0.101	12,941	8.28	0.764	< -6.372	—	18.01	
153303.95 + 503245.54	11,899	8.13	0.663	0.050	12,644	8.46	0.878	-5.625	—	22.09	
153316.76 + 340803.70	16,636	7.51	0.363	0.028	16,223	7.99	0.585	< -6.243	—	25.21	2
153321.59 + 514057.20	41,184	7.68	0.490	0.417	47,050	7.77	0.538	< -2.000	—	6.68	
153325.60 + 132537.07	20,476	8.18	0.707	0.110	19,629	7.96	0.576	< -5.432	—	24.78	
153417.60 + 134515.60	14,111	8.14	0.670	0.109	14,829	7.98	0.577	< -6.000	-7.00	9.57	
153454.99 + 224918.70	18,135	7.90	0.538	0.042	21,460	8.10	0.660	< -5.015	—	27.34	
153615.72 + 574902.70	14,168	7.95	0.560	0.084	15,249	7.86	0.514	-5.643	—	10.18	
153725.51 + 233719.60	12,519	7.98	0.576	0.085	14,102	8.87	1.124	-5.365	—	11.35	
153725.72 + 515126.90	18,850	7.95	0.568	0.023	20,199	7.87	0.527	-2.157	—	33.56	
153735.17 + 063848.07	20,498	7.80	0.494	0.185	19,785	8.32	0.794	-3.663	—	18.31	2
153755.31 + 093249.50	15,910	8.12	0.665	0.086	14,656	7.88	0.523	-5.963	—	12.10	
153821.66 + 092006.76	18,754	8.20	0.717	0.049	17,631	8.03	0.613	-3.519	—	51.48	
153852.35 - 012133.80	33,678	8.15	0.712	0.342	16,974	8.25	0.746	-4.289	—	7.90	
153905.51 + 442951.86	13,230	8.14	0.669	0.075	14,395	8.84	1.110	-5.437	—	18.77	
153925.73 + 572640.40	12,952	7.87	0.514	0.456	16,310	10.23	2.103	< -5.684	—	1.96	
153935.03 + 145050.80	—	—	—	—	19,049	8.16	0.691	-4.832	—	4.94	
153953.06 + 385520.74	17,482	8.34	0.805	0.069	16,499	9.18	1.259	-5.066	-6.00	13.60	
154049.20 + 453322.60	13,084	8.16	0.682	0.261	14,929	7.38	0.312	-5.319	—	3.03	
154100.78 + 431112.30	17,543	8.24	0.744	0.079	16,128	8.07	0.632	-5.484	—	11.17	
154134.50 + 252329.98	11,491	7.98	0.571	0.003	11,566	7.91	0.531	-5.813	—	50.06	1
154152.20 + 475253.75	17,394	8.17	0.696	0.077	16,219	8.00	0.593	-5.669	—	20.77	
154157.75 + 124743.20	19,433	8.15	0.690	0.165	17,265	8.12	0.666	< -5.703	—	12.26	
154201.50 + 502532.10	32,141	8.04	0.644	0.017	31,766	7.81	0.524	< -3.786	—	48.50	
154205.10 + 304929.40	12,430	7.93	0.547	0.198	13,902	8.85	1.117	< -6.087	—	7.37	
154313.54 + 002957.50	16,261	8.18	0.703	0.143	16,111	8.20	0.716	< -5.821	—	9.38	
154330.60 + 290431.00	15,386	8.01	0.594	0.108	15,237	8.15	0.684	-5.422	—	9.82	
154446.06 + 204654.27	10,801	8.03	0.602	0.019	12,389	8.77	1.072	-5.657	—	48.99	1
154544.06 + 311528.90	—	—	—	—	14,478	8.93	1.155	-5.287	—	4.44	
154550.28 + 115958.70	15,860	7.84	0.506	0.024	17,781	8.13	0.672	-5.348	—	39.20	
154606.04 + 255543.69	12,411	7.90	0.529	0.055	13,105	7.97	0.567	-6.251	—	25.40	
154606.89 + 565059.10	11,980	8.07	0.626	0.025	11,363	7.81	0.477	-6.004	—	18.61	1
154648.77 + 312142.50	—	—	—	—	13,161	6.57	0.140	-4.407	—	6.11	
154703.53 + 450053.35	14,320	8.20	0.708	0.087	14,512	8.10	0.648	< -6.280	—	18.82	
154734.59 + 415530.60	23,804	8.11	0.670	0.481	19,951	8.60	0.974	-4.380	—	4.90	
154811.34 + 083613.21	21,175	7.75	0.472	0.135	19,480	8.18	0.704	-4.802	—	26.35	2
154844.43 + 410519.90	15,564	8.17	0.694	0.112	15,889	8.70	1.032	< -5.858	—	8.51	
154938.64 - 001318.20	12,332	8.24	0.736	0.361	14,576	8.62	0.984	< -5.931	—	3.93	
154955.24 + 285209.00	13,917	8.10	0.648	0.089	15,757	9.04	1.205	< -5.879	—	9.30	

TABLE C.1 (Suite)

Nom SDSS	T_{eff}	$\log g$	M	σ_{π}/π	T_{eff}	$\log g$	M	$\log \text{H/He}$	$\log \text{Ca/He}$	S/N	Notes
155014.63 + 334802.00	16,792	8.38	0.829	0.218	17,075	7.75	0.461	< -5.624	—	6.41	
155026.70 + 201951.80	—	—	—	—	12,653	7.98	0.574	-5.700	—	13.27	1
155051.40 + 022511.12	15,059	7.62	0.400	0.439	14,206	7.76	0.461	< -6.305	—	15.39	
155115.33 + 363742.00	15,147	7.93	0.551	0.024	16,077	7.99	0.584	-6.227	—	20.93	
155225.07 + 081919.88	13,998	8.40	0.843	0.115	14,305	7.98	0.579	-5.736	—	18.69	
155253.52 + 141334.50	18,433	8.07	0.636	0.055	16,675	8.23	0.733	-5.697	—	24.01	
155311.26 + 391401.90	14,297	8.65	1.003	0.457	13,183	7.26	0.275	< -6.043	—	3.49	
155327.56 + 150545.70	30,506	8.14	0.698	0.061	26,388	7.87	0.538	< -4.371	—	22.24	
155333.61 + 024460.00	14,107	8.12	0.658	0.112	14,783	7.27	0.281	< -6.005	—	6.57	
155340.36 + 011335.30	14,076	7.89	0.525	0.182	15,302	8.50	0.907	-5.501	—	8.47	
155400.09 + 094738.10	16,290	8.68	1.020	0.410	17,494	7.51	0.363	< -5.430	—	4.07	
155409.03 + 172124.10	15,221	8.02	0.601	0.020	16,252	8.08	0.641	-4.196	-6.00	35.98	
155420.97 + 253746.90	23,531	7.72	0.462	0.803	17,591	8.02	0.604	< -5.508	—	7.51	
155435.18 + 063949.10	15,605	7.56	0.377	0.271	16,431	8.67	1.015	-5.382	—	5.36	
155511.87 + 343350.58	17,372	8.08	0.643	0.027	17,103	8.18	0.701	-4.265	—	14.26	
155713.74 + 280339.10	15,508	8.09	0.641	0.098	15,261	8.18	0.696	-5.912	—	6.26	
155717.36 + 525623.10	14,156	7.98	0.579	0.057	15,280	8.20	0.711	-4.706	—	16.98	
155747.14 + 064500.40	14,710	8.29	0.769	0.160	15,262	7.88	0.525	-4.076	—	6.09	
155756.04 + 333603.74	13,256	7.86	0.509	0.080	14,741	8.10	0.650	< -6.258	—	19.81	
155813.61 + 402229.90	—	—	—	—	14,301	8.12	0.657	< -6.055	—	5.98	
155847.35 + 353113.39	13,612	8.05	0.614	0.091	13,121	7.91	0.534	< -6.236	—	14.70	
155921.08 + 190407.86	18,549	7.99	0.588	0.010	21,382	8.08	0.647	-3.870	—	62.14	
155924.30 + 135260.00	15,435	7.84	0.501	0.378	15,149	7.97	0.572	< -5.962	—	8.04	
155959.03 + 105842.10	13,842	7.86	0.510	0.395	13,555	7.99	0.580	< -6.107	—	5.83	
160030.97 + 195734.50	18,016	8.05	0.621	0.102	16,951	7.95	0.563	< -5.920	—	15.24	
160046.56 + 362937.10	25,214	8.11	0.668	0.221	18,134	8.58	0.963	< -5.377	—	8.58	
160051.35 + 402058.00	13,485	8.39	0.836	0.072	13,430	8.11	0.650	-5.798	—	8.87	
160157.26 + 125133.41	12,718	8.02	0.598	0.011	13,402	8.08	0.632	-5.594	—	59.86	
160205.60 + 320419.56	15,238	7.95	0.562	0.007	15,650	7.97	0.575	< -6.334	—	72.15	
160223.11 + 052239.80	18,649	8.03	0.614	0.138	16,995	8.23	0.734	-5.620	—	21.46	
160241.83 + 035814.93	14,819	7.97	0.571	0.177	15,764	7.90	0.533	-5.590	—	16.90	
160319.39 + 524935.90	17,523	9.00	1.191	0.189	10,772	7.22	0.254	< -6.090	—	10.19	1
160339.51 + 500955.47	—	—	—	—	14,562	9.52	1.363	< -6.029	—	7.51	
160401.31 + 083109.01	11,986	7.91	0.535	0.067	16,280	9.27	1.287	-4.854	-6.00	26.81	4
160424.75 + 404950.90	15,132	7.81	0.486	0.446	14,719	7.75	0.455	-5.848	—	4.33	
160437.77 + 005206.70	22,771	7.36	0.335	0.630	25,780	7.63	0.434	-3.396	—	6.76	
160444.12 + 033649.00	12,576	8.08	0.636	0.136	13,466	8.08	0.634	-6.029	—	10.44	
160457.25 + 392340.10	17,175	8.18	0.704	0.227	24,479	7.63	0.430	< -4.166	—	7.03	
160512.71 + 082324.20	15,007	9.07	1.219	0.270	21,385	7.96	0.579	< -4.480	—	3.82	
160522.47 + 532220.00	14,773	7.92	0.543	0.053	16,567	8.06	0.627	< -6.182	—	25.88	
160548.97 + 222547.20	17,442	8.17	0.698	0.105	15,078	8.05	0.617	-5.363	—	9.17	

TABLE C.1 (Suite)

Nom SDSS	T_{eff}	$\log g$	M	σ_{π}/π	T_{eff}	$\log g$	M	$\log \text{H/He}$	$\log \text{Ca/He}$	S/N	Notes
160622.04 + 272017.00	12,266	8.05	0.616	0.082	13,558	8.47	0.885	-5.402	—	18.66	
160625.19 + 052821.30	20,855	7.68	0.439	0.125	22,080	7.87	0.529	-4.280	—	26.28	
160651.52 + 074752.12	12,018	8.16	0.681	0.059	13,499	8.66	1.006	-5.635	—	19.92	
160714.84 + 391027.10	17,396	8.03	0.609	0.138	20,448	8.08	0.646	< -4.900	—	10.17	
160735.79 + 532100.70	15,903	7.98	0.582	0.271	17,753	8.02	0.606	< -5.591	—	10.43	
160836.24 + 271132.06	15,882	7.93	0.550	0.007	17,893	8.18	0.701	-4.684	—	76.49	
160904.90 + 500555.14	12,054	8.07	0.628	0.135	12,692	7.91	0.533	< -6.376	—	15.19	
160911.61 + 392150.40	15,194	8.12	0.661	0.041	15,056	8.22	0.722	-5.639	—	16.12	
160915.42 + 122515.90	30,939	7.91	0.570	0.501	29,765	7.69	0.468	< -3.591	—	10.56	
160936.00 + 043734.10	11,808	8.61	0.974	0.330	12,700	8.01	0.589	< -6.139	—	9.16	1
160942.44 + 063049.40	14,374	8.09	0.642	0.125	14,730	7.83	0.498	-5.148	—	20.82	
161000.72 + 370009.00	18,494	7.98	0.584	0.071	18,563	8.02	0.605	< -5.379	—	12.70	
161003.24 + 113004.50	16,053	7.96	0.571	0.029	17,466	8.26	0.755	-5.763	—	29.93	
161009.85 + 550211.46	28,954	8.04	0.635	0.208	33,430	7.74	0.494	< -3.687	—	22.59	
161030.17 + 401334.90	20,473	8.91	1.148	0.126	27,747	7.99	0.608	-2.000	—	7.21	
161038.93 + 371403.23	12,075	8.24	0.737	0.071	13,576	8.65	1.002	-4.783	-7.00	17.97	
161044.47 + 004650.51	9,993	8.21	0.710	0.025	13,142	9.50	1.356	< -6.547	—	27.29	
161054.23 + 521137.70	18,773	8.19	0.709	0.053	16,659	7.97	0.575	-4.476	—	29.25	
161126.34 + 052357.70	47,381	7.39	0.426	0.409	15,043	7.82	0.494	-5.714	-7.50	23.66	
161134.25 + 173817.20	18,849	8.95	1.166	0.452	17,099	8.20	0.713	< -5.618	—	8.76	
161152.90 + 421400.30	15,084	8.09	0.642	0.072	16,416	8.17	0.693	-5.691	—	11.75	
161157.73 + 282258.90	17,403	7.58	0.388	0.474	18,598	8.17	0.700	-4.524	—	6.56	
161159.82 + 092134.10	—	—	—	—	54,151	6.91	6.660	< -3.010	—	5.86	1
161200.33 + 151804.60	20,571	8.08	0.645	0.036	20,273	8.14	0.682	-4.363	—	29.67	
161213.39 + 254945.40	12,401	6.91	0.199	0.483	15,371	8.40	0.841	-4.866	—	3.81	
161218.32 + 450920.90	13,069	8.01	0.593	0.074	13,306	7.98	0.576	< -6.230	—	12.87	
161243.19 + 370803.66	15,845	7.94	0.559	0.124	15,112	8.20	0.710	-5.442	—	15.42	
161252.34 + 424856.30	18,656	7.91	0.545	0.033	19,531	8.09	0.647	-3.727	—	22.35	
161301.55 + 234830.80	13,687	8.09	0.638	0.003	13,158	7.79	0.475	-5.985	—	79.14	
161320.02 + 533752.90	—	—	—	—	12,409	7.73	0.441	-5.779	—	20.48	
161331.31 + 182406.80	14,030	8.00	0.590	0.066	14,274	7.71	0.436	< -6.167	—	14.69	
161437.93 + 231705.82	—	—	—	—	12,829	6.53	0.125	-6.081	—	29.62	
161448.58 + 243506.90	22,999	8.13	0.682	0.161	27,398	7.91	0.563	< -3.743	—	9.39	
161527.95 + 503841.43	—	—	—	—	14,755	8.11	0.657	-4.712	—	7.90	
161544.76 + 480241.02	18,552	8.55	0.944	0.101	20,521	8.29	0.779	< -5.020	—	16.66	
161610.23 + 353209.50	17,387	8.06	0.627	0.393	22,003	8.00	0.600	< -4.370	—	3.64	
161620.75 + 183255.70	20,717	7.20	0.288	1.735	19,092	7.99	0.590	< -5.025	—	4.41	
161643.67 + 171453.20	12,472	7.96	0.563	0.025	13,156	7.99	0.583	-6.217	—	49.25	
161701.34 + 352319.64	17,408	7.98	0.581	0.060	16,478	7.91	0.541	< -6.198	—	24.42	
161735.37 + 311645.41	18,860	7.32	0.310	0.248	18,470	8.01	0.599	-3.593	—	19.06	2
161756.83 + 301751.79	17,325	8.03	0.613	0.049	17,471	8.15	0.684	-5.102	—	29.94	

TABLE C.1 (Suite)

Nom SDSS	T_{eff}	$\log g$	M	σ_{π}/π	T_{eff}	$\log g$	M	$\log \text{H/He}$	$\log \text{Ca/He}$	S/N	Notes
161806.86 + 365048.70	17,216	7.62	0.407	0.343	19,881	8.77	1.077	-3.990	—	6.15	
161834.01 + 093358.14	20,651	7.99	0.595	0.067	19,563	8.19	0.713	-4.495	—	32.84	
161853.48 + 414143.01	12,255	7.99	0.579	0.025	12,621	8.12	0.661	-5.734	—	35.53	
161859.55 + 472323.78	12,725	8.21	0.716	0.074	13,271	7.92	0.541	-5.921	—	16.35	
161927.56 + 165145.00	14,121	8.07	0.632	0.028	14,301	7.86	0.510	-6.083	—	44.32	
161932.55 + 310941.47	18,846	7.96	0.572	0.039	19,177	8.08	0.644	-5.152	—	37.24	
161941.07 + 294353.51	18,628	7.87	0.523	0.098	18,506	8.04	0.620	< -5.545	—	19.62	
161953.99 + 493350.80	—	—	—	—	16,203	8.26	0.751	-5.855	—	10.60	
162008.75 + 184100.90	16,535	8.05	0.622	0.394	16,328	8.24	0.739	-4.539	-6.00	5.87	
162017.83 + 153351.90	—	—	—	—	14,141	7.75	0.454	< -5.977	—	3.10	
162040.54 + 003144.00	18,077	7.64	0.417	0.546	17,856	8.65	1.005	-3.209	—	7.44	
162218.64 + 325408.70	21,566	8.23	0.741	0.310	20,722	8.17	0.700	-3.647	—	8.11	
162332.63 + 542130.28	18,542	8.04	0.620	0.063	20,924	7.99	0.593	-5.046	—	25.08	
162359.48 + 250346.90	17,484	7.69	0.437	0.203	19,714	8.35	0.812	< -4.962	—	9.16	
162425.01 + 295511.86	28,038	8.09	0.663	0.059	23,381	7.89	0.547	< -4.759	—	28.94	
162516.28 + 331710.80	17,042	7.63	0.408	0.362	15,717	8.65	1.006	-5.205	—	4.79	
162545.54 + 000053.70	15,498	8.00	0.592	0.473	21,876	8.14	0.685	< -4.490	—	5.79	
162546.32 + 251144.00	11,830	8.03	0.604	0.022	12,425	8.39	0.836	-5.395	—	21.91	1
162550.54 + 122342.10	24,557	9.01	1.193	0.409	54,438	6.63	0.451	-2.486	—	3.33	1
162621.56 + 181439.98	13,264	8.06	0.620	0.031	13,612	7.97	0.572	-6.235	—	36.38	
162635.84 + 130544.70	20,061	8.07	0.642	0.090	17,658	8.03	0.610	< -5.765	—	18.46	
162646.92 + 313627.94	13,020	8.16	0.682	0.125	13,544	7.15	0.249	-4.813	-6.00	12.38	
162650.27 + 083026.28	10,871	8.14	0.670	0.043	12,481	8.65	1.000	-5.674	—	25.62	1
162703.33 + 172327.60	16,459	8.22	0.729	0.065	15,785	8.00	0.589	-5.576	—	12.78	
162710.78 + 270332.00	18,006	7.92	0.551	0.096	16,745	8.22	0.729	-4.645	—	8.52	
162711.17 + 253108.50	15,911	7.95	0.564	0.082	17,596	8.08	0.642	< -5.779	—	15.67	
162740.27 + 130354.71	26,910	7.67	0.454	0.259	21,987	8.06	0.635	-4.824	—	21.95	
162752.24 + 121654.50	16,757	8.31	0.788	0.064	15,654	8.13	0.671	-5.189	—	10.76	
162824.03 + 634510.00	23,121	8.24	0.749	0.234	25,963	7.90	0.556	< -4.076	—	11.59	
162844.43 + 191059.15	21,958	7.98	0.592	0.074	22,789	8.00	0.604	-3.944	—	31.15	
162852.16 + 080105.60	12,914	8.27	0.755	0.104	12,737	7.63	0.399	-5.626	—	8.95	1
162854.27 + 230124.10	11,002	8.03	0.597	0.046	10,995	7.69	0.421	< -6.119	—	13.31	1
162856.09 + 151328.10	19,993	8.02	0.608	0.499	17,231	7.40	0.327	-5.317	—	5.15	
162913.03 + 341325.00	15,654	8.01	0.598	0.148	16,465	8.32	0.790	-4.906	—	6.09	
162957.75 + 154011.60	15,610	8.37	0.825	0.273	14,706	7.72	0.441	< -6.014	—	6.15	
163014.61 + 165856.40	45,111	7.95	0.615	0.447	50,777	8.52	0.948	< -2.000	—	8.36	
163100.45 + 452710.44	20,422	7.95	0.569	0.029	22,377	8.02	0.614	-4.631	—	41.79	
163133.89 + 374053.98	18,443	8.25	0.749	0.078	19,474	8.06	0.629	< -5.472	—	24.45	
163259.40 + 523405.96	13,207	7.95	0.557	0.069	13,446	7.97	0.570	-6.237	—	15.57	
163322.86 + 341835.46	19,144	8.15	0.685	0.077	18,899	7.96	0.575	< -5.628	—	23.12	
163329.73 + 262104.20	18,396	7.71	0.446	0.369	16,998	7.95	0.564	-4.465	—	3.79	

TABLE C.1 (Suite)

Nom SDSS	T_{eff}	$\log g$	M	σ_{π}/π	T_{eff}	$\log g$	M	$\log \text{H/He}$	$\log \text{Ca/He}$	S/N	Notes
163334.09 + 480802.40	11,995	7.92	0.540	0.057	12,646	7.86	0.506	-5.359	—	20.09	
163349.59 + 615623.70	—	—	—	—	16,138	7.99	0.583	-5.109	—	7.83	
163353.45 + 394102.40	—	—	—	—	32,443	7.69	0.473	< -3.266	—	7.94	
163400.51 + 273003.60	14,537	8.17	0.689	0.373	15,934	7.58	0.384	< -5.751	—	3.58	
163411.27 + 281212.13	16,025	7.94	0.557	0.011	17,371	8.09	0.649	-5.366	—	75.18	
163415.68 + 195414.30	12,786	8.09	0.642	0.079	14,224	8.25	0.746	< -6.172	—	10.95	
163520.15 + 260852.94	14,361	7.90	0.531	0.026	14,862	8.01	0.596	-5.754	—	35.91	
163553.09 + 352947.10	13,341	7.72	0.442	0.234	13,578	8.03	0.605	-5.736	—	8.70	
163621.11 + 503757.26	12,117	7.98	0.571	0.026	12,113	7.82	0.485	< -6.546	—	26.58	
163654.12 + 345801.20	12,877	8.00	0.587	0.008	15,488	8.93	1.158	-5.310	-7.50	51.87	
163654.42 + 230236.10	17,718	8.07	0.634	0.031	18,689	8.10	0.656	-5.607	—	25.82	
163702.79 + 365517.10	14,063	8.04	0.615	0.013	14,695	8.01	0.597	-5.372	—	35.18	
163757.58 + 190526.02	24,039	8.07	0.648	0.086	40,662	8.63	1.009	-2.000	—	24.11	
163807.33 - 000837.60	14,737	7.17	0.259	0.568	17,153	8.20	0.715	-4.084	—	7.84	
163838.24 - 005417.50	—	—	—	—	15,523	6.96	0.225	-3.375	—	7.90	
163841.63 + 262336.49	11,871	8.02	0.593	0.048	11,885	7.83	0.490	-6.508	—	25.33	1
163908.82 + 381913.50	—	—	—	—	15,952	8.67	1.013	< -5.748	—	4.59	
163956.42 + 230459.70	13,265	8.31	0.785	0.226	13,259	7.69	0.424	< -6.121	—	6.41	
164007.85 + 453007.09	15,994	7.94	0.556	0.079	15,908	7.98	0.577	-5.737	—	19.98	
164030.46 + 243514.50	14,939	8.34	0.803	0.207	13,942	8.16	0.683	< -5.995	—	4.55	
164056.84 + 462448.10	11,167	7.94	0.547	0.022	12,968	8.91	1.147	-5.649	—	20.74	1
164240.42 + 391731.40	14,057	8.19	0.704	0.046	15,411	8.85	1.114	-4.682	-7.50	13.62	
164340.45 + 415532.41	20,339	8.31	0.791	0.107	20,417	8.07	0.638	< -5.045	—	19.00	
164432.15 + 403926.21	16,659	7.90	0.537	0.058	15,896	7.71	0.441	-3.389	—	27.79	
164500.53 + 211457.10	14,927	8.23	0.733	0.396	17,252	8.98	1.182	-4.916	—	4.62	
164612.06 + 634650.00	20,635	8.15	0.690	0.207	27,512	7.61	0.431	< -3.727	—	8.19	
164703.44 + 245129.10	32,615	8.07	0.660	0.359	27,488	7.71	0.471	< -3.731	—	8.09	
164751.77 + 221138.90	15,009	8.56	0.949	0.310	11,285	6.41	0.060	< -5.967	—	3.11	1
164756.71 + 364108.10	20,714	8.20	0.719	0.453	21,161	8.51	0.921	< -4.626	—	5.48	
164814.79 + 194520.50	23,175	8.01	0.606	0.115	17,576	8.01	0.602	-5.875	—	20.22	
164839.86 + 435153.80	20,121	8.01	0.605	0.097	18,332	8.03	0.613	-4.856	—	12.74	
164936.08 + 385048.20	17,601	8.16	0.689	0.112	17,064	7.77	0.471	< -5.626	—	8.24	
165003.55 + 274309.08	18,103	6.90	0.227	0.410	17,980	8.17	0.696	< -5.685	—	19.18	
165006.93 + 205049.60	21,694	8.14	0.683	0.346	17,557	7.95	0.565	-5.033	—	6.28	
165015.58 + 400129.46	—	—	—	—	14,702	7.59	0.386	-6.148	—	20.30	
165052.52 + 174636.59	14,040	7.94	0.555	0.056	14,653	7.97	0.575	-4.405	—	26.67	
165057.16 + 404327.30	18,566	8.09	0.649	0.026	19,095	8.27	0.764	-5.008	—	21.45	
165103.57 + 290820.67	12,598	7.99	0.577	0.027	12,908	8.12	0.660	-5.896	—	32.34	
165117.04 + 432757.35	16,235	7.91	0.543	0.067	19,076	8.01	0.601	-5.165	—	24.74	
165143.46 + 364647.70	—	—	—	—	13,019	6.57	0.137	-5.786	—	12.27	
165155.97 + 182112.80	—	—	—	—	14,277	8.00	0.588	-5.699	—	17.02	

TABLE C.1 (Suite)

Nom SDSS	T_{eff}	$\log g$	M	σ_{π}/π	T_{eff}	$\log g$	M	$\log \text{H/He}$	$\log \text{Ca/He}$	S/N	Notes
165222.17 + 322214.10	15,329	8.02	0.604	0.022	16,557	8.15	0.685	-6.148	—	25.89	
165245.82 + 290053.20	12,855	8.21	0.716	0.042	12,655	8.35	0.804	< -6.376	—	16.07	1
165321.37 + 331352.85	13,304	8.00	0.589	0.095	13,926	7.93	0.550	< -6.325	—	19.25	
165339.17 + 174838.84	16,633	7.63	0.407	0.236	18,714	8.17	0.697	-4.916	—	18.24	2
165349.38 + 274647.30	20,228	8.19	0.712	0.069	23,916	7.95	0.578	< -4.360	—	12.61	
165417.27 + 193857.80	12,982	8.03	0.604	0.074	14,174	8.32	0.791	-5.139	—	9.01	
165513.16 + 333313.60	18,502	7.83	0.503	0.148	18,434	8.15	0.684	-5.025	—	18.75	
165522.00 + 433638.56	13,922	7.93	0.547	0.038	14,533	7.71	0.436	-6.143	—	27.94	
165555.80 + 264549.00	—	—	—	—	15,270	7.33	0.300	< -6.056	—	10.49	
165603.96 + 372858.30	13,339	7.65	0.409	0.126	14,878	8.44	0.868	-5.783	—	9.65	
165858.70 + 180627.60	16,523	7.92	0.549	0.090	16,852	8.21	0.719	-4.956	—	12.16	
165938.54 + 614101.20	12,623	8.06	0.620	0.018	12,617	7.72	0.436	< -6.555	—	27.75	
165946.51 + 393418.30	19,311	7.56	0.388	0.175	24,325	7.79	0.498	< -4.454	—	18.41	2
170142.11 + 643720.70	—	—	—	—	12,199	7.76	0.458	-5.960	—	28.99	
170143.67 + 384953.50	18,084	7.97	0.579	0.078	18,595	8.04	0.622	-5.041	—	25.85	
170300.67 + 363248.30	—	—	—	—	17,545	8.08	0.642	-5.047	—	6.70	
170345.85 + 212506.20	23,742	7.99	0.598	0.073	22,212	8.14	0.686	-4.584	—	19.38	
170539.46 + 241945.10	15,020	7.89	0.528	0.032	16,654	8.07	0.636	-4.860	—	26.37	
170547.14 + 315007.70	13,860	8.22	0.722	0.005	14,449	8.30	0.777	-5.577	—	63.91	
170559.94 + 383115.60	10,379	7.90	0.524	0.022	12,125	8.15	0.674	-6.394	—	36.24	1
170611.93 + 404656.64	15,523	7.98	0.578	0.077	16,163	8.04	0.616	-4.304	—	19.79	
170727.11 + 203153.25	46,369	7.86	0.572	0.118	44,327	7.77	0.533	< -3.251	—	28.01	
170731.42 + 395755.04	16,799	8.12	0.662	0.049	16,474	7.97	0.573	< -6.199	—	25.37	
170741.85 + 390032.10	12,273	8.00	0.583	0.081	13,284	7.72	0.441	-6.001	—	16.34	
171143.72 + 232101.62	—	—	—	—	46,694	7.00	0.344	< -3.710	—	4.04	1
171323.16 + 280954.20	16,963	8.32	0.789	0.075	15,537	7.99	0.584	< -6.020	—	11.85	
171350.40 + 380843.14	18,716	8.23	0.735	0.056	17,123	7.99	0.586	-5.790	—	19.82	
171403.75 + 365810.56	10,986	7.80	0.475	0.055	13,400	8.50	0.908	-5.045	-7.50	21.22	
171514.21 + 280732.80	19,140	8.08	0.645	0.169	15,992	7.72	0.444	< -5.841	—	8.24	
171607.71 + 285006.98	10,022	8.31	0.775	0.033	13,969	9.08	1.223	< -6.192	—	11.45	
171616.20 + 410110.70	17,262	7.72	0.450	0.646	16,587	8.97	1.176	-4.622	—	3.64	
171643.99 + 305817.80	14,744	8.15	0.678	0.021	14,107	7.91	0.538	-5.720	—	30.06	
171709.25 + 300521.60	22,105	8.11	0.665	0.489	18,579	7.75	0.466	< -5.162	—	4.92	
171839.90 + 283317.60	20,829	8.31	0.790	0.200	19,162	8.29	0.777	-5.060	—	5.40	
172243.19 + 603059.70	16,614	7.81	0.491	0.035	18,921	8.28	0.765	< -5.622	—	20.84	2
172330.08 + 601504.90	16,720	7.75	0.462	0.295	16,267	7.36	0.313	< -5.792	—	6.08	
172505.57 + 312909.49	37,762	7.07	0.291	0.442	41,018	8.05	0.659	< -3.260	—	19.27	
172520.14 + 244604.94	18,243	7.87	0.522	0.261	15,881	8.24	0.740	-5.619	—	18.05	
172520.20 + 345910.86	13,910	7.99	0.581	0.066	14,943	8.10	0.651	-6.038	—	21.99	
172551.69 + 633142.50	21,164	8.24	0.743	0.112	17,643	8.29	0.774	-5.210	—	20.38	
172822.61 + 081549.30	10,854	8.59	0.963	0.251	14,318	7.58	0.381	-4.099	-7.00	7.30	

TABLE C.1 (Suite)

Nom SDSS	T_{eff}	$\log g$	M	σ_{π}/π	T_{eff}	$\log g$	M	$\log \text{H/He}$	$\log \text{Ca/He}$	S/N	Notes
172909.38 + 354704.13	—	—	—	—	12,995	6.54	0.132	-5.427	—	18.79	
173042.25 + 540313.30	14,299	7.86	0.512	0.061	15,183	7.90	0.533	< -6.068	—	13.68	
173232.09 + 335610.40	27,380	7.43	0.372	0.386	24,084	7.79	0.496	-4.298	—	14.29	
173304.07 + 645606.00	12,449	8.45	0.876	0.096	13,060	7.97	0.568	-5.429	—	12.08	
173529.67 + 431233.30	19,346	7.97	0.581	0.468	24,733	7.35	0.341	-3.642	—	7.43	
173635.42 + 642113.90	11,518	8.09	0.637	0.028	12,046	8.13	0.666	-5.117	—	27.01	1
173946.40 + 543842.40	14,306	9.00	1.189	0.295	15,331	9.53	1.369	-5.436	—	3.71	
174025.00 + 245704.50	15,694	7.74	0.456	0.024	17,997	8.31	0.788	-4.065	—	25.97	
174248.07 + 550528.10	19,716	7.76	0.473	0.410	29,013	7.26	0.334	< -3.539	—	5.40	
180326.53 + 243656.80	18,397	8.11	0.661	0.069	19,983	8.22	0.733	< -5.344	—	21.38	
180520.65 + 225608.40	11,850	8.01	0.591	0.005	12,892	8.05	0.617	-5.026	—	53.65	
180834.26 + 225604.50	—	—	—	—	25,011	7.45	0.370	< -3.988	—	3.74	
183131.64 + 420220.30	20,146	5.30	0.072	0.125	12,470	7.14	0.243	< -6.555	—	36.09	
183200.07 + 420029.80	17,022	8.15	0.681	0.133	16,134	7.99	0.584	< -6.068	—	18.22	
183252.20 + 421526.10	23,736	8.21	0.727	0.032	23,715	8.06	0.642	< -4.722	—	32.31	
183511.51 + 405752.10	21,437	8.02	0.610	0.177	18,349	8.01	0.601	< -5.588	—	16.99	
193318.29 + 613512.00	14,486	7.79	0.476	0.742	15,616	8.70	1.031	< -5.800	—	3.16	
194253.97 + 780521.53	—	—	—	—	10,079	9.21	1.265	< -6.015	—	10.17	1
195428.81 + 780053.60	24,276	6.82	0.223	5.102	18,036	8.99	1.185	< -5.301	—	3.44	
195746.78 + 772033.20	15,566	8.11	0.657	0.383	19,083	7.92	0.554	< -5.028	—	3.72	
200757.10 - 120832.00	12,365	7.99	0.576	0.011	14,824	8.21	0.721	-4.573	-7.50	51.13	
201001.60 - 124126.10	12,736	7.75	0.452	0.097	17,628	8.02	0.608	-5.378	—	21.31	
201313.81 - 112718.60	12,914	6.78	0.181	1.278	15,806	7.29	0.291	< -5.872	—	5.16	
202217.53 + 130146.00	—	—	—	—	26,632	8.11	0.674	-2.444	—	5.86	
202718.52 + 763446.60	12,649	8.09	0.640	0.025	13,160	8.67	1.011	< -6.365	—	16.92	1
203517.50 - 064539.90	21,118	8.32	0.797	0.129	18,281	8.70	1.035	< -5.456	—	11.88	
203821.24 - 053413.30	12,557	8.06	0.624	0.045	13,629	8.08	0.634	-6.271	—	19.35	
204140.74 - 045234.90	17,390	7.88	0.527	0.192	16,407	8.30	0.781	-5.303	—	9.57	
204213.01 + 764041.10	15,522	8.13	0.666	0.092	14,545	7.99	0.585	-5.295	—	14.04	
204347.70 + 005924.20	13,303	8.20	0.709	0.382	15,148	8.20	0.713	-5.808	—	8.24	
204349.78 - 060511.50	17,056	8.06	0.626	0.427	17,186	8.35	0.810	< -5.599	—	9.73	
204919.49 + 765828.90	26,183	8.41	0.857	0.052	9,830	10.10	1.870	-5.546	—	13.89	1
205301.70 + 004142.70	13,308	8.15	0.680	0.167	15,387	8.60	0.974	-5.457	—	7.98	
205336.69 + 764511.20	13,177	8.06	0.620	0.078	11,487	7.53	0.353	-5.357	—	14.66	1
205348.32 + 161620.30	16,536	7.30	0.296	0.836	14,818	7.53	0.362	< -6.001	—	8.01	
205348.45 - 002942.90	28,302	8.06	0.649	0.237	22,071	8.02	0.613	-4.223	—	10.02	
210328.68 - 004640.60	25,745	8.06	0.645	0.300	20,971	8.32	0.794	-4.461	—	14.09	
210429.88 - 062842.80	12,796	7.92	0.543	0.152	12,718	7.30	0.281	-5.652	—	11.35	
210454.70 - 000043.40	—	—	—	—	27,081	7.65	0.444	< -3.789	—	6.16	
210742.30 + 102611.70	12,473	8.02	0.596	0.054	14,053	8.36	0.816	-5.763	—	18.50	
211149.60 - 053938.40	36,068	8.34	0.829	0.201	37,517	7.52	0.425	-2.000	—	8.21	

TABLE C.1 (Suite)

Nom SDSS	T_{eff}	$\log g$	M	σ_{π}/π	T_{eff}	$\log g$	M	$\log \text{H/He}$	$\log \text{Ca/He}$	S/N	Notes
211252.07 + 102931.40	18,220	8.15	0.684	0.174	18,307	8.32	0.797	-4.211	-6.50	19.73	
211515.22 - 063618.50	23,229	8.24	0.747	0.153	15,906	7.72	0.447	-5.361	—	7.99	
211711.78 + 112304.30	—	—	—	—	13,488	7.47	0.339	< -6.111	—	5.72	
211845.17 + 045226.02	—	—	—	—	45,393	6.66	0.272	-2.413	—	20.68	
211950.84 - 064056.20	29,236	8.36	0.833	0.280	22,837	7.86	0.530	-3.982	—	15.28	
212310.79 + 003518.85	—	—	—	—	13,394	8.26	0.747	-5.873	—	20.50	
212403.12 + 114230.20	25,125	8.35	0.822	0.196	28,813	7.91	0.565	-3.474	—	13.28	
212448.91 + 112445.20	—	—	—	—	24,646	8.03	0.624	-2.983	—	5.38	
212552.77 + 001918.62	31,676	8.01	0.627	0.366	21,982	8.03	0.620	< -4.923	—	23.16	
212645.06 + 043138.36	19,065	7.94	0.563	0.355	15,971	7.77	0.468	< -6.095	—	15.98	
212656.72 - 002423.90	18,444	8.07	0.639	0.054	17,989	8.25	0.748	-4.846	—	21.89	
212841.49 + 001231.40	20,513	7.93	0.563	0.104	17,957	8.13	0.674	-5.344	—	24.28	
212901.32 - 062924.60	19,206	8.05	0.624	0.041	18,199	8.19	0.707	-5.053	—	25.34	
213103.40 + 105956.10	13,794	8.04	0.609	0.083	13,579	8.13	0.664	-6.093	—	24.64	
213401.58 + 010804.70	—	—	—	—	17,126	8.55	0.941	-5.139	—	6.47	
213840.11 - 003337.70	15,445	8.01	0.594	0.019	15,436	7.85	0.506	-4.811	—	35.50	
214116.86 - 062959.70	12,545	7.99	0.580	0.068	12,262	7.65	0.405	< -6.242	—	11.57	1
214441.71 + 010029.88	20,726	7.92	0.553	0.104	20,310	8.08	0.643	-4.352	—	39.50	
214527.11 + 125256.00	—	—	—	—	13,797	6.44	0.118	-6.349	—	20.03	
214541.77 + 003147.50	14,169	8.50	0.909	0.057	16,419	8.63	0.993	-4.127	—	17.63	
214712.52 + 001903.70	14,747	7.95	0.561	0.084	16,572	8.14	0.679	-5.411	—	16.29	
215107.29 - 084829.40	12,176	7.96	0.560	0.080	11,733	7.85	0.500	-6.026	—	19.29	1
215514.44 - 075833.80	32,339	8.12	0.686	0.143	35,459	8.14	0.704	-3.236	—	19.34	
215553.90 + 202802.92	—	—	—	—	47,137	6.77	0.304	-2.000	—	43.40	
215859.87 - 002845.20	—	—	—	—	30,436	8.02	0.625	< -3.303	—	4.44	
220203.15 - 002054.00	14,112	8.28	0.762	0.226	16,801	9.03	1.202	< -5.683	—	6.89	
220250.26 + 213120.21	19,859	8.10	0.656	0.018	21,258	8.07	0.638	-4.917	—	64.58	
220419.27 - 011525.30	—	—	—	—	16,022	8.75	1.060	< -5.836	—	5.71	
220507.32 + 010546.80	—	—	—	—	15,161	6.87	0.209	< -5.860	—	2.69	
220554.02 + 055252.90	11,459	8.07	0.628	0.053	11,935	8.20	0.709	< -6.536	—	25.50	1
220623.74 + 132556.50	16,303	7.80	0.487	0.054	16,184	8.00	0.589	-6.177	—	29.60	
220633.03 + 125911.10	14,104	7.82	0.489	0.107	15,099	8.02	0.603	-4.431	—	16.75	
220640.33 + 053312.70	—	—	—	—	16,264	7.75	0.462	-5.380	—	8.42	
220827.84 + 223636.90	11,958	8.04	0.611	0.009	12,538	8.17	0.688	-6.046	—	27.82	
220934.85 + 122336.60	15,131	7.96	0.569	0.023	17,356	8.23	0.737	< -6.028	-6.00	35.59	
221000.09 + 213719.06	11,684	8.15	0.673	0.042	12,123	8.26	0.746	-5.852	—	33.29	1
221150.49 + 222139.60	15,328	8.15	0.680	0.137	16,079	8.02	0.604	-5.507	—	18.39	
221513.63 + 230059.79	14,930	7.94	0.556	0.209	15,383	8.07	0.633	-5.571	—	20.09	
221517.83 + 062846.40	—	—	—	—	13,648	7.88	0.518	-5.828	—	10.23	
221729.25 + 000833.40	16,255	8.27	0.758	0.086	20,116	7.99	0.592	-4.932	—	13.12	
221921.99 - 005202.08	—	—	—	—	12,906	7.86	0.509	-6.191	—	20.08	

TABLE C.1 (Suite)

Nom SDSS	T_{eff}	$\log g$	M	σ_{π}/π	T_{eff}	$\log g$	M	$\log \text{H/He}$	$\log \text{Ca/He}$	S/N	Notes
221945.63 + 123554.05	12,569	8.02	0.598	0.014	12,725	8.03	0.606	-4.970	—	88.92	
223255.40 - 084044.20	12,676	8.09	0.638	0.049	12,936	7.86	0.510	-6.239	—	47.49	
223648.13 + 135537.40	—	—	—	—	17,477	7.61	0.400	< -5.434	—	4.39	
223652.97 + 010938.40	13,433	8.34	0.800	0.175	16,316	7.78	0.476	-4.084	-6.00	9.54	
223858.01 + 010353.70	12,468	8.67	1.015	0.207	17,144	8.21	0.722	< -5.608	—	8.49	
224009.33 + 320828.55	13,246	7.96	0.565	0.183	14,537	8.10	0.646	< -6.142	—	13.62	
224027.11 - 005945.60	13,800	8.01	0.594	0.109	15,352	8.66	1.010	-5.188	—	9.38	
224031.66 + 001237.00	13,508	7.59	0.383	0.584	13,818	7.91	0.537	-5.775	—	7.43	
224138.26 + 231240.70	—	—	—	—	16,126	8.13	0.668	-5.000	—	7.27	
224209.86 - 085735.50	—	—	—	—	12,908	8.60	0.971	-5.873	—	7.84	1
224239.71 + 135445.20	13,985	8.45	0.876	0.772	15,187	8.10	0.646	-5.043	-7.50	9.36	
224348.66 + 312239.74	11,688	7.91	0.533	0.094	11,237	7.67	0.412	< -6.468	—	21.85	1
224459.20 + 310443.20	12,684	8.58	0.956	0.333	14,043	7.27	0.279	< -5.986	—	4.25	
224600.40 - 080424.20	14,741	7.95	0.562	0.114	15,864	8.31	0.782	-5.105	—	20.26	
224748.78 + 302251.65	21,402	8.07	0.642	0.230	18,840	8.05	0.627	-4.543	—	17.03	
224828.65 + 131838.50	12,031	8.28	0.759	0.081	16,269	9.31	1.298	-5.337	-6.00	9.10	
224913.64 + 064410.04	—	—	—	—	17,228	8.20	0.714	-5.460	—	21.06	
224930.38 - 001623.00	13,096	8.02	0.596	0.049	15,526	8.75	1.063	-5.121	-7.50	24.65	
225020.91 - 091425.60	22,984	7.82	0.508	0.299	27,476	7.82	0.518	< -3.856	—	13.88	
225122.13 + 315628.90	16,855	8.02	0.605	0.048	17,505	8.11	0.662	< -5.997	—	24.10	
225158.75 + 314936.45	11,890	8.08	0.632	0.057	12,955	8.26	0.747	-6.270	—	24.00	
225206.14 + 130831.20	12,362	8.09	0.640	0.108	13,564	9.08	1.220	-5.873	—	12.85	
225410.48 + 054419.46	13,042	7.92	0.542	0.180	15,603	8.13	0.667	-5.735	—	15.54	
225424.73 + 231515.82	26,097	8.10	0.664	0.174	25,576	7.84	0.527	< -4.492	—	22.07	
225652.76 + 225738.28	11,637	8.01	0.589	0.083	12,609	8.87	1.126	-5.662	—	29.19	1
225809.37 - 082920.10	14,581	8.57	0.952	0.221	14,766	8.19	0.703	-5.204	-7.50	8.59	
230201.47 - 002531.90	18,352	7.71	0.444	0.722	16,999	8.21	0.722	< -5.540	—	4.40	
230419.08 + 232518.17	19,602	7.96	0.577	0.272	22,011	8.08	0.647	< -4.578	—	14.49	
230526.90 - 000030.10	18,677	8.10	0.655	2.546	21,337	7.59	0.405	-3.799	—	3.45	
230620.01 + 211118.50	10,045	7.80	0.469	0.145	15,249	8.19	0.703	-4.886	-6.50	14.03	
230656.38 + 135928.70	14,002	7.89	0.529	0.118	17,721	8.31	0.784	-4.781	—	8.65	
230842.14 + 243753.22	12,526	8.06	0.619	0.031	12,451	7.97	0.565	-5.298	—	32.68	
230924.78 + 213532.70	18,941	8.52	0.925	0.881	16,289	8.25	0.744	< -5.788	-6.00	6.87	
230953.03 + 060820.02	12,584	7.93	0.547	0.031	14,427	8.28	0.762	-3.925	-6.50	38.21	
231026.38 + 211204.80	28,550	7.93	0.573	0.166	18,516	8.04	0.620	-4.473	—	29.82	
231041.15 + 141600.80	15,781	7.67	0.423	0.137	14,938	7.82	0.492	< -6.097	—	10.97	2
231141.44 + 232707.00	—	—	—	—	16,607	7.92	0.550	< -6.175	—	23.63	
231141.59 - 004100.60	13,513	8.20	0.708	0.058	14,299	8.62	0.985	< -6.165	-7.00	14.00	
231324.25 - 001636.80	18,390	8.65	1.008	0.291	17,972	7.38	0.323	< -5.417	—	5.76	
231431.77 - 004937.80	13,532	7.32	0.291	0.352	13,800	7.85	0.504	-5.862	—	7.54	
231940.36 - 085037.20	12,941	8.11	0.652	0.112	12,856	7.81	0.482	-5.836	—	12.82	

TABLE C.1 (Suite)

Nom SDSS	T_{eff}	$\log g$	M	σ_{π}/π	T_{eff}	$\log g$	M	$\log \text{H/He}$	$\log \text{Ca/He}$	S/N	Notes
231952.98 + 132242.12	15,245	7.97	0.574	0.076	20,045	8.16	0.693	-4.968	—	24.77	
232015.20 + 004726.30	17,005	8.13	0.672	0.251	18,472	8.10	0.653	< -5.290	—	7.38	
232108.40 + 010433.50	18,813	8.00	0.597	0.073	19,440	8.15	0.685	< -5.294	—	15.13	
232344.88 + 150858.80	14,800	7.42	0.325	0.170	19,707	8.45	0.882	-4.321	—	12.96	2
232543.21 + 520825.90	—	—	—	—	16,328	7.03	0.239	< -5.680	—	3.20	
232548.14 + 125120.57	12,578	8.02	0.598	0.061	13,989	8.10	0.649	-5.835	—	28.64	
232647.35 + 533625.00	—	—	—	—	15,322	8.29	0.768	-5.377	—	3.61	
232711.11 + 515344.70	16,640	7.95	0.562	0.022	18,968	8.12	0.670	-5.356	—	28.25	
232808.03 - 002051.32	—	—	—	—	12,189	8.23	0.730	-5.524	—	13.74	1
233232.24 + 080229.90	17,281	8.12	0.664	0.061	16,369	8.10	0.650	-4.630	—	33.59	
233305.10 + 005155.90	17,239	7.48	0.354	0.136	21,506	8.13	0.675	-4.405	—	16.16	2
233550.82 + 143031.90	13,699	7.71	0.437	0.338	17,829	8.01	0.598	< -5.451	—	5.47	
233708.40 + 491124.20	—	—	—	—	40,719	8.29	0.798	< -2.877	—	2.98	
233725.94 + 145711.40	13,658	8.20	0.710	0.120	15,584	7.60	0.391	< -6.014	—	10.19	
233817.93 + 083732.70	10,839	8.03	0.598	0.032	12,164	8.33	0.792	-5.784	—	35.22	1
233849.05 + 011138.90	24,568	7.53	0.395	0.874	23,486	7.66	0.440	< -4.288	—	5.75	
233858.56 - 094816.10	19,699	7.54	0.381	0.394	24,053	8.11	0.669	< -4.344	—	10.62	
233907.99 - 091445.80	15,685	7.40	0.321	0.636	15,760	7.74	0.452	-5.694	—	6.53	
233913.27 + 152838.30	15,866	7.96	0.569	0.016	16,184	8.07	0.635	-5.650	—	30.45	
233931.34 - 000156.40	14,198	6.06	0.075	4.040	16,607	9.39	1.320	< -5.624	—	3.04	
234119.58 + 422723.80	11,484	7.89	0.523	0.307	12,967	7.71	0.435	-5.981	—	7.01	1
234124.56 + 154511.10	14,571	7.66	0.413	0.168	16,241	8.07	0.636	-5.465	—	8.43	
234137.40 + 082559.30	12,715	7.88	0.517	0.046	13,875	7.81	0.486	-4.867	—	32.28	
234326.57 - 005749.40	13,877	7.26	0.277	0.504	14,372	7.78	0.470	-5.704	—	11.73	
234352.56 + 002733.20	16,149	8.30	0.781	0.700	15,837	7.68	0.428	< -5.867	—	7.65	
234459.45 + 024108.93	16,415	7.95	0.564	0.036	17,038	7.99	0.587	-5.669	—	54.67	
234621.24 - 092415.20	18,605	8.82	1.100	0.220	18,238	8.10	0.655	< -5.350	—	8.00	
234625.31 + 153358.40	15,133	6.82	0.202	0.945	14,448	7.96	0.567	-5.599	—	7.56	
234709.29 + 001858.00	31,711	7.48	0.397	0.404	33,809	7.84	0.540	< -3.318	—	10.66	
234718.15 - 100729.60	11,526	7.94	0.551	0.281	12,491	8.38	0.823	-5.380	—	7.08	1
234754.18 + 032451.50	12,810	7.88	0.520	0.185	12,275	7.84	0.498	-4.745	—	22.10	
234814.03 - 094850.70	18,908	8.70	1.035	0.176	21,884	8.28	0.771	-3.716	—	10.01	
234820.10 + 023417.65	14,466	8.28	0.765	0.021	11,237	7.40	0.306	-5.879	—	41.25	1
234848.77 + 381754.60	16,455	7.96	0.569	0.031	25,198	8.09	0.659	-4.096	—	24.15	
234906.12 + 010022.10	15,394	8.05	0.618	0.554	14,917	6.66	0.176	< -5.890	—	3.72	
234920.03 + 045019.56	16,980	8.42	0.854	0.164	19,992	7.99	0.589	< -5.012	—	14.71	
234923.88 + 424739.20	11,520	7.83	0.491	0.088	13,431	8.32	0.789	< -6.224	—	11.75	
235245.19 + 030706.30	12,620	7.96	0.565	0.151	11,769	7.98	0.573	-5.478	—	12.86	1
235322.16 + 002653.90	21,353	7.55	0.391	0.968	28,941	7.96	0.595	< -3.546	—	5.76	
235336.08 + 372055.30	15,364	8.15	0.679	0.225	16,225	8.05	0.621	-5.166	-7.00	14.25	
235410.39 - 010728.50	14,345	7.61	0.394	0.073	16,114	8.08	0.641	-5.369	—	21.52	

TABLE C.1 (Suite)

Nom SDSS	T_{eff}	$\log g$	M	σ_{π}/π	T_{eff}	$\log g$	M	$\log \text{H/He}$	$\log \text{Ca/He}$	S/N	Notes
235658.20 + 353317.50	16,387	9.15	1.247	0.410	23,010	8.44	0.877	< -4.239	—	4.81	
235719.20 + 244111.52	14,037	7.86	0.509	0.132	14,041	8.02	0.599	-4.761	—	21.75	
235825.61 + 254824.52	13,362	8.16	0.685	0.078	12,651	7.74	0.449	-6.028	—	23.12	
235844.21 - 102202.24	17,952	7.80	0.488	0.449	17,953	8.01	0.601	-5.346	—	16.54	
235959.48 + 082813.01	15,653	8.25	0.747	0.051	15,858	8.40	0.841	-4.622	—	25.00	

Notes : (1) Raies d'hélium marginales (2) Candidat système binaire DB+DB (3) Système binaire DA+DB (4) Objets exclus

